

**Morphology control of
poly(3-hexylthiophene) with tailored
supramolecular nucleating agents**

Dissertation

zur Erlangung des akademischen Grades

eines Doktors der Naturwissenschaften (Dr. rer. nat.)

in der Bayreuther Graduiertenschule für Mathematik und Naturwissenschaften

(BayNAT)

der Universität Bayreuth

vorgelegt von

Hannes Gerhard Welz

aus Coburg

Bayreuth, 2019

Die vorliegende Arbeit wurde in der Zeit von Januar 2013 bis Januar 2018 am Lehrstuhl für Makromolekulare Chemie I der Universität Bayreuth unter der Betreuung von Herrn Professor Dr. Hans-Werner Schmidt angefertigt und bei der Bayreuther Graduiertenschule für Mathematik und Naturwissenschaften (BayNAT) der Universität Bayreuth im Promotionsprogramm *Polymer Science* eingereicht.

Dissertation eingereicht am: 17. Mai 2019

Zulassung durch das Leitungsgremium: 24. Juni 2019

Wissenschaftliches Kolloquium: 05. Dezember 2019

Amtierender Direktor der Graduiertenschule BayNAT: Prof. Dr. Markus Lippitz

Prüfungsausschuss:

Prof. Dr. Hans-Werner Schmidt (Gutachter)

Prof. Dr. Seema Agarwal (Gutachterin)

Prof. Dr. Mukundan Thelakkat (Vorsitz)

Prof. Dr. Georg Papastavrou

“Nimm das Leben nicht zu Ernst, denn du kommst da eh nicht lebend raus“

Van Wilder (2002)

Danksagung

Zuallererst möchte ich meinem Doktorvater, Herrn Prof. Dr. Hans-Werner Schmidt, für die Möglichkeit danken, dass ich die vorliegende Doktorarbeit an dem Lehrstuhl Makromolekulare Chemie I der Universität Bayreuth anfertigen durfte. Dabei bedanke ich mich vor Allem für die sehr interessante Aufgabenstellung, für die Bereitstellung eines gut ausgestatteten Labors und seine stete Bereitschaft zu wissenschaftlichen Diskussionen. Für die fortwährende Unterstützung und Motivation danke ich ihm herzlich.

Darüber hinaus bedanke ich mich für die finanzielle Unterstützung beim Bayrischen Staatsministerium für Bildung und Kultus, Wissenschaft und Kunst im Rahmen des interdisziplinären Forschungsverbunds „Solar Technologies go Hybrid (SolTech)“.

Ganz besonderer Dank gilt Dr. Klaus Kreger für seine stete Diskussions- und Hilfsbereitschaft, sowie für das Teilen seiner herausragenden fachlichen Kompetenz, welche zum Gelingen dieser Arbeit beigetragen hat.

Dr. Richard Hildner und Sebastian Stäter vom Lehrstuhl für Spektroskopie weicher Materie der Universität Bayreuth danke ich für die hervorragende Zusammenarbeit, sowie die Beantwortung auch schwieriger physikalischer Fragestellungen. Ich danke auch für die Durchführung der orts aufgelösten Spektroskopieaufnahmen an meinen Proben.

Prof. Dr. Mukundan Thelakkat von der Gruppe Applied Functional Polymers (AFuPo) danke ich recht herzlich für die Bereitstellung eines ganz besonderen von Dr. Ruth Lohwasser synthetisierten P3HT-Typs.

Bei den technischen Angestellten Doris Hanft, Sandra Ganzleben, Jutta Failner und Rika Schneider bedanke ich mich ganz herzlich für die Synthese der Additive. An dieser Stelle bedanke ich mich auch bei Alexander Kern und Jonas Mayer für ihre Unterstützung bei IT Fragestellungen.

Dr. Beate Förster und Martina Heider möchte ich für die Einweisung und stete Unterstützung im Bereich der Rasterelektronenmikroskopie danken.

Bei Petra Weiss und Christina Wunderlich bedanke ich mich für ihre unermüdliche Unterstützung bei verwaltungstechnischen Problemen.

Für unzählige produktive Diskussionen bedanke ich mich bei folgenden Kollegen: Dr. Christian Neuber, Dr. Philipp Knauer, Dr. Johannes Heigl, Dr. Christian Probst, Dr. Tristan Kolb, Christian Bartz, Bastian Klose, Tina Weller, Eva Fürsattel und Christoph Steinlein.

Dank gebührt allen Mitarbeitern des Lehrstuhls Makromolekulare Chemie I, die durch ihre fachliche Kompetenz und Freundschaft zum Gelingen dieser Arbeit beigetragen haben.

Mein größter Dank gilt meiner Familie und meiner Freundin. Meiner Mutter Elfi, meinem Vater Arno, meiner Oma Käthe, meiner Schwester Mareike und meiner Freundin Yvonne. Ihr alle habt mir in allen Situationen helfend zur Seite gestanden. Ohne Euch wäre all dies nicht möglich gewesen.

Table of Contents

Summary	1
Zusammenfassung	3
1 Introduction	7
1.1 Supramolecular chemistry.....	9
1.1.1 Supramolecular interactions	10
1.1.2 The self-assembly process.....	17
1.2 Conjugated polymers	20
1.2.1 Poly(3-alkylthiophene) (P3AT)	20
1.2.2 Poly(3-hexylthiophene)(P3HT).....	22
1.3 Nucleation of semi-crystalline polymers.....	28
1.3.1 Crystallization of semi-crystalline polymers.....	29
1.3.2 Supramolecular nucleating agents.....	33
2 Aim of the thesis	35
3 Self-assembly of bis- and trisamides with pyridine substituents	39
3.1 Versatile building blocks in supramolecular chemistry.....	39
3.1.2 Research fields and applications of bis- and trisamides	41
3.1.3 Functional bis- and trisamides	42
3.2 Selection, synthesis and self-assembly of pyridine-containing trisamides.....	51
3.2.1 Trisamide selection and their structural variation.....	51
3.2.2 Trisamide synthesis	52
3.2.3 Analytical characterization.....	54
3.2.4 Thermal characterization.....	56
3.2.5 Self-assembly investigations of trisamides in organic solvents	59
3.2.6 Self-assembly investigations of trisamides in aqueous solutions.....	74
3.3 Selection, synthesis and self-assembly of pyridine-containing bisamides.....	77
3.3.1 Bisamide selection and their structural variation	77
3.3.2 Bisamide synthesis	78

3.3.3 Analytical characterization	80
3.3.4 Thermal characterization	82
3.3.5 Self-assembly investigations of bisamides in organic solvents	84
3.3.6 Summary of the determined nanostructures.....	99
4 Nucleation of poly(3-hexylthiophene) with supramolecular additives	101
4.1 Characterization of different P3HT grades	101
4.1.1 Analytical characterization of different P3HT grades	101
4.1.2 Thermal characterization of the different P3HT grades	102
4.2 Preparation of P3HT spherulites via melt annealing	111
4.3 Nucleating agents for P3HT	119
4.4 Nucleation investigations of P3HT with pyridine-containing bis- and trisamides.....	123
4.4.1 Evaluation of suitable and highly efficient nucleating agents for P3HT	123
4.4.2 Nucleation of P3HT with BA 1-4 in dependency of the additive concentrations .	125
4.4.3 Isothermal crystallization behaviors of P3HT-bisamide compounds.....	132
4.4.4 Polarized optical microscopy investigations on P3HT-bisamide films	137
5 Highly ordered shish-kebab superstructures	145
5.1 Nanofiber formation of P3HT in solution	145
5.2 Shish-kebab-superstructures with P3HT	148
5.3 Preparation of P3HT nanofibers with shish-kebab-like superstructures.....	152
5.3.1 Material selection.....	152
5.3.2 Procedure for shish-kebab preparation.....	153
5.3.3 Microscopic investigations of shish-kebab superstructures	154
5.4 Spatially resolved spectroscopy along P3HT nanofibers	165
5.4.1 Setup for spatially resolved spectroscopy	165
5.4.2 Photophysical properties of P3HT superstructures	167
6 Extended summary	173
7 Experimental	179
7.1 Materials and methods.....	179

7.2 Synthesis and characterization of pyridine-containing trisamides	182
7.2.1 N ¹ ,N ³ ,N ⁵ -Tri(pyridin-4-yl)benzene-1,3,5-tricarboxamide (TA 1)	182
7.2.2 N,N',N''(Benzene-1,3,5-triyl)triisonicotinamide (TA 2)	183
7.2.3 N ¹ ,N ³ ,N ⁵ -Tri(pyridin-4-yl)cyclohexane-1,3,5-tricarboxamide (TA 3).....	184
7.2.4 N,N',N''(Cyclohexane-1,3,5-triyl)triisonicotinamide (TA 4).....	185
7.2.5 N ¹ ,N ³ ,N ⁵ -Tri(pyridin-2-yl)cyclohexane-1,3,5-tricarboxamide (TA 5).....	186
7.2.6 N ¹ ,N ³ ,N ⁵ -Tri(pyridin-3-yl)cyclohexane-1,3,5-tricarboxamide (TA 6).....	187
7.3 Synthesis and characterization of pyridine-containing bisamides.....	188
7.3.1 N ¹ ,N ⁴ -Di(pyridin-4-yl)terephthalamide (BA 1).....	188
7.3.2 N,N'-(1,4-Phenylene)diisonicotinamide (BA 2)	189
7.3.3 N ¹ ,N ⁴ -Di(pyridin-4-yl)cyclohexane-1,4-dicarboxamide (BA 3).....	190
7.3.4 N,N'-(Cyclohexane-1,4-diyl)diisonicotinamide (BA 4)	191
7.3.5 N ¹ ,N ⁴ -Di(pyridin-2-yl)cyclohexane-1,4-dicarboxamide (BA 5).....	192
7.3.6 N ¹ ,N ⁴ -Di(pyridin-3-yl)cyclohexane-1,4-dicarboxamide (BA 6).....	193
8 Appendix	195
8.1 ¹ H-NMR spectra of bis- and trisamides	195
8.2 Mass spectra of bis- and trisamides	200
8.3 Fourier-transform infrared spectra	202
8.4 TGA and SDTA thermograms.....	203
9 References	205
(Eidesstattliche) Versicherungen und Erklärungen	225

Summary

Poly(3-hexylthiophene) (P3HT) as highly used semiconducting polymer has been an integral part in the field of organic electronics for decades and emerged as the reference material. Despite the intensive research, however, not all existing issues have been clarified till date. For example, controlling the solid-state morphology and order of semi-crystalline films still represents a challenge today. A promising and straightforward approach to control the polymer solid-state morphology is nucleation. Therefore, this work is dedicated to the nucleation of P3HT with supramolecular nucleating agents.

The first chapter describes the design, synthesis and characterization of *pyridine-containing C₂-symmetric bisamides* and *C₃-symmetric trisamides*, which serve as nucleating agents for P3HT. These supramolecular building blocks were selected as they feature sufficient thermal stability and have a potential to self-assembly under certain conditions into supramolecular nanostructures in a controlled manner. The structural variations of the investigated compounds involve the central core, the orientation of the amide bond, and the pyridine-containing peripheral substituents. Analytical methods confirmed that all desired compounds were successfully synthesized in high purity. Thermal characterizations showed that nine of the twelve synthesized compounds have sufficient thermal stability to potentially be used as nucleating agent for P3HT. Comprehensive self-assembly investigations in chlorobenzene and ortho-dichlorobenzene resulted in fibrous supramolecular nanostructures of the trisamides and fibrous as well as sheet-like supramolecular nanostructures of the bisamides.

The second chapter deals with the *nucleation of P3HT* without and with various additives. Three different commercially available P3HT grades were selected, which vary with respect to molecular weight, regioregularity and polydispersity. Self-nucleation tests in bulk were performed to determine the maximum polymer crystallization temperature of each P3HT grade. The largest difference between the standard crystallization temperature and the maximum crystallization temperature of one grade was 9.1 °C. This grade was selected to investigate the nucleation behavior and the nucleation efficiency of the different pyridine-containing additives. It was found that the pyridine-containing trisamides are not capable of nucleating P3HT. In contrast, for some of the investigated 1,4-bisamides it could be shown that they are highly efficient nucleating agents for P3HT already at additive concentrations as low as 0.025 wt.-%. Notably, the highest nucleation efficiency with an appealing value of about 94 % could be observed for the bisamide N,N'-(1,4-phenylene)-diisonicotinamide at a

concentration of 0.25 wt.-%. In conclusion, this thesis presents for the first time very efficient nucleating agents for P3HT.

The third chapter deals with *highly ordered shish kebab superstructures* based on rigid fiber-like self-assembled 1,4-bisamides acting as shish and self-assembled P3HT nanofibers acting as kebabs. The preparation of these shish-kebab superstructures was realized via a dispersion-based nucleation process at room temperature. Hereby, the dissolved P3HT crystallizes in a fibrous manner from the solid bisamide surface of a supramolecular nanofiber. Several processing parameters, such as the molecular weight of P3HT, the concentration of the P3HT in solution and aging time of the P3HT-additive dispersion were systematically varied to reveal their influences on the resulting P3HT nanofiber length. The results showed that P3HT with a lower molecular weight and at higher solution concentrations as well as extended aging times lead to significant longer kebab fibers and higher kebab densities. By systematically tuning these parameters, it was possible to prepare highly oriented and aligned P3HT nanofibers that were over five micrometer long. These unique shish kebab superstructures never realized before allowed us for the very first time, to perform spatially resolved photophysical spectroscopic investigations along P3HT nanofibers. Unexpectedly, these spectroscopic investigations revealed, that all emission spectra feature variations of relative peak intensities as function of distance from the shish. These different intensities are equivalent to variations of the structural and electronic order along P3HT nanofibers and are also dependent on the preparation process of the samples. These findings indicate that an energy gradient along the P3HT nanofiber can be formed just using one single species of conjugated polymers and by applying suitable processing conditions.

In summary, this work presents tailored supramolecular nucleating agents based on pyridine-containing bisamides which are highly efficient for the nucleation of P3HT in melted state and also in solution. Moreover, the formation of highly oriented P3HT nanofibers with a shish-kebab-like superstructure was demonstrated for the first time. Employing confocal imaging and spectroscopy, it could be found that the structural and electronic order along the P3HT nanofibers varies in a directed manner. Moreover, it was shown that this order can be controlled by applying proper processing protocols. Thus, controlling of the morphology of P3HT by means of nucleating agents paves the way to study and understand the charge and energy transport processes of P3HT shish-kebab superstructures.

Zusammenfassung

Poly(3-hexylthiophen) (P3HT) als vielfach verwendetes halbleitendes Polymer ist seit Jahrzehnten ein fester Bestandteil der organischen Elektronik und hat sich hierbei als Referenzmaterial etabliert. Trotz intensiver Forschung sind jedoch bis heute nicht alle bestehenden Probleme geklärt. Beispielsweise stellt die Kontrolle der Festkörpermorphologie und -ordnung von teilkristallinen Filmen auch heute noch eine Herausforderung dar. Ein vielversprechender und direkter Ansatz zur Kontrolle der Polymer-Festkörpermorphologie ist die Nukleierung. Aus diesem Grund befasst sich diese Arbeit mit der Nukleierung von P3HT mittels supramolekularen Nukleierungsmitteln.

Das erste Kapitel beschreibt das Design, die Synthese und die Charakterisierung *pyridin-haltiger C₂-symmetrischer Bisamide* und *C₃-symmetrischer Trisamide*, welche als *Nukleierungsmittel für P3HT* dienen. Diese supramolekularen Bausteine wurden ausgewählt, da sie eine ausreichende thermische Stabilität aufweisen und das Potential haben unter bestimmten Bedingungen kontrolliert zu supramolekularen Nanostrukturen selbstzu-assemblyen. Die Strukturvariationen der untersuchten Verbindungen betreffen den zentralen Kern, die Orientierung der Amidbindung und die pyridinhaltigen äußeren Substituenten. Analytische Methoden bestätigten, dass alle gewünschten Verbindungen erfolgreich und in hoher Reinheit synthetisiert wurden. Thermische Charakterisierungen zeigten, dass neun der zwölf synthetisierten Verbindungen eine ausreichende thermische Stabilität aufweisen, um potentiell als Nukleierungsmittel für P3HT verwendet werden zu können. Umfangreiche Selbstassemblierungsuntersuchungen in Chlorbenzol und ortho-Dichlorbenzol zeigten faserige supramolekulare Nanostrukturen für die Trisamide und faserige als auch schichtartige supramolekulare Nanostrukturen für die Bisamide.

Das zweite Kapitel beschäftigt sich mit der Nukleierung von P3HT ohne und mit verschiedenen Additiven. Hierbei wurden drei unterschiedliche kommerziell erhältliche P3HT-Typen ausgewählt, welche in Bezug auf ihr Molekulargewicht, ihrer Regioregularität und ihrer Polydispersität variieren. Zur Bestimmung der maximalen Polymerkristallisationstemperatur wurden mit jedem dieser P3HT-Typen Selbstnukleierungsuntersuchungen im Bulk durchgeführt. Der größte Unterschied zwischen der Standardkristallisationstemperatur und der maximalen Kristallisationstemperatur eines Typs betrug 9,1 °C. Dieser Typ wurde schließlich ausgewählt, um das Nukleierungsverhalten und die Nukleierungseffizienz der verschiedenen pyridinhaltigen Additive zu untersuchen. Hierbei wurde festgestellt, dass die pyridinhaltigen Trisamide nicht in der Lage sind P3HT zu nukleieren. Im Gegensatz dazu

konnte für einige der untersuchten pyridinhaltigen 1,4-Bisamide gezeigt werden, dass diese hocheffiziente Nukleierungsmittel für P3HT sind und dies bereits bei Additivkonzentrationen von nur 0,025 Gew.-%. Bemerkenswert ist die höchste Nukleierungseffizienz mit einem herausragenden Wert von 94 %, welche für das Bisamid N,N'-(1,4-Phenyl)-diisonicotinamid bei einer Konzentration von 0,25 Gew.-% beobachtet werden konnte. Schließlich präsentiert diese Arbeit zum ersten Mal hoch effiziente Nukleierungsmittel für P3HT.

Das dritte Kapitel befasst sich mit *hochgeordneten Shish-Kebab-Überstrukturen*, die auf starren, faserähnlichen, selbstassemblierten 1,4-Bisamiden basieren, welche als Shish fungieren, und selbstassemblierten P3HT-Nanofasern, die die Kebabs darstellen. Die Herstellung dieser Shish-Kebab-Superstrukturen erfolgte über einen zweistufigen dispersionsbasierten Nukleierungsprozess bei Raumtemperatur. Hierbei kristallisiert das gelöste P3HT faserartig von der im ersten Schritt hergestellten festen Bisamidnanofaseroberfläche weg. Verschiedene Prozessparameter, wie das Molekulargewicht von P3HT, die Konzentration des P3HT's in Lösung und die Alterungszeit der P3HT-Additiv-Dispersion wurden systematisch variiert, um deren Einfluss auf die Länge der resultierenden P3HT-Nanofasern zu untersuchen. Die Ergebnisse zeigten, dass ein niedrigeres Molekulargewicht von P3HT, sowie höhere Lösungskonzentrationen und verlängerte Alterungszeiten zu deutlich längeren Kebab-Fasern und höheren Kebab-Dichten führen. Durch systematische Anpassungen dieser Parameter konnten parallel ausgerichtete P3HT-Kebabs mit einer Länge von mehr als fünf Mikrometern und einer enormen Wachstumsdichte hergestellt werden. Diese einzigartigen Shish-Kebab-Strukturen, welche in dieser Fassung noch nie zuvor realisiert werden konnten, ermöglichten es uns erstmals, ortsaufgelöste photophysikalische Spektroskopieuntersuchungen entlang von P3HT-Nanofasern durchzuführen. Unerwarteterweise zeigten diese spektroskopischen Untersuchungen, dass alle Emissionsspektren Variationen der relativen Peakintensitäten als Funktion der Entfernung vom Shish zeigten. Diese unterschiedlichen Intensitäten sind gleichzusetzen mit Variationen der strukturellen und elektronischen Ordnung entlang der P3HT Nanofasern und obliegen dem Herstellungsprozess der Proben. Diese Ergebnisse zeigen, dass ein Energiegradient entlang der P3HT-Nanofaser lediglich unter Verwendung einer konjugierten Polymerspezies und durch Anwendung geeigneter Verarbeitungsbedingungen gebildet werden kann.

Zusammenfassend wurden in dieser Arbeit maßgeschneiderte supramolekulare Nukleierungsmittel auf Basis von pyridinhaltigen Bisamiden gefunden, welche sowohl für die Nukleierung von P3HT aus der Schmelze als auch in Lösung hocheffizient sind. Des Weiteren wurde

erstmalig die Herstellung von hochorientierten P3HT-Nanofasern mit einer shish-kebab-artigen Überstruktur gezeigt. Durch konfokale Mikroskopie und Spektroskopie konnte ermittelt werden, dass die strukturelle und elektronische Ordnung entlang der P3HT-Nanofasern gezielt variiert. Darüber hinaus wurde gezeigt, dass diese Ordnung durch die Verwendung geeigneter Prozessparameter gezielt gesteuert werden kann. Diese Kontrolle der Morphologie von P3HT mithilfe von Nukleierungsmitteln ebnet den Weg, um die Ladungs- und Energietransportprozesse von P3HT-Shish-Kebab-Superstrukturen zu untersuchen und zu verstehen.



1 Introduction

In times of global warming and climate change, mankind is forced to rethink its energy production. This means replacing the conventional, finite fossil energy sources with alternative clean sources of energy. Theoretically, the sun provides in one hour sufficient energy to cover the annual energy consumption of the entire earth population.^[1] That is why solar energy nowadays is one of the most important renewable sources of energy apart from on- and off-shore windpower and hydropower.^[2] With the help of photovoltaic cells, the solar energy can be converted easily and efficiently into electricity. Nowadays, a large number of commercially available photovoltaic cells are on the market. These mainly consist of mono- and multicrystalline silicon, which can achieve efficiencies of up to approximately 25 %.^[3] Just a few years ago, the costs for production and installation with around 1-2 US \$ per generated watt at maximum irradiance were relatively high for this kind of solar cells.^[4] Meanwhile the increased production volumes and associated maturity of the technology have brought the cost of photovoltaic modules down to about 0.6 US \$ per generated watt (average price in 2015 according to the International Technology Roadmap for Photovoltaics).^[5] Therefore, a goal of current research is to minimize these costs further to about 0.2 US \$ per watt.^[1]

A promising approach to reduce manufacturing and maintenance costs is to use polymer-based organic solar cells. Advantages of this type of thin-film devices are low production costs, a low payback time, very low weight and mechanical flexibility. In addition, the photoactive materials can be coated from solution so that the manufacturing process is very short and relatively simple. Regarding the efficiency, however, polymer solar cells cannot yet match the silicon cells. The maximum efficiency of a laboratory cell is about 13 %.^[6]

An important subset of organic solar cells are "bulk heterojunction" (BHJ) solar cells. In these devices donor and acceptor materials are mixed together in the active layer and are arranged on nanoscale to form an interpenetrating network. Optimum efficiency is obtained for sizes of the individual phases in the range of the exciton diffusion wavelength (10-20 nm). This results in an enormously enlarged interface between the donor and acceptor phases, enabling more efficient charge generation and improved charge transport characteristics. If a perfect nanomorphology is present, a quantum yield of 100 % is theoretically possible.^[1] The active layer of BHJ solar cells generally consists of an interpenetrating network of a polymeric electron donor such as P3HT and usually a fullerene-based electron acceptor. The resulting nanomorphology is crucial for the resulting photovoltaic performance.^[1,7] However, a

compromise between two critical aspects of the nanomorphology must be achieved. On the one hand, a large boundary surface is desired with regard to charge generation, on the other hand, phase-pure donor and acceptor domains must be present in order to transport the generated charges to the respective electrodes.^[8] However, the general problem of such BHJ solar cells is that, from thermodynamic point of view, the blend morphology is metastable. This means that the nanomorphology evolves and changes with time. This also has enormous effects on the efficiency of such solar cells. Blend systems consisting of poly(3-hexylthiophene) (P3HT) (electron donator) and phenyl-C₆₁-butyric acid methyl ester (PCBM) (electron acceptor), which are until today the most frequently studied blend systems for organic solar cells, are the best example to illustrate the metastability of the nanomorphology. The parameter, which is very difficult to control in this system, is the distribution of the fullerene derivative in the blend.^[9] At temperatures above the glass transition temperature of this system (about 40 °C), the fullerene molecules begin to diffuse through the amorphous phases of the polymer matrix, forming partial micrometer-sized agglomerates.^[10] This dramatic change in the blend nanomorphology significantly reduces the efficiency of the solar cell.^[11] However, these systems are typically exposed to higher temperatures, both during the production (roll-to-roll process) and in the later outdoor operation.^[12]

To address this issue, there are a lot of approaches to stabilize the blend structures and thus to increase the long-term stability of the organic solar cells. These include the crosslinking of the polymer donor^[13,14] or the fullerene acceptor^[15], the use of fullerene containing compatibilizers^[16,17], the use of non-crystalline fullerene additives^[18] and the use of materials with very high glass temperatures.^[19,20] The nanomorphology and the efficiency of the solar cells can also be improved by post-processing methods.^[21] All these approaches, however, involve chemical modifications, increase the complexity of the system and, consequently, increase costs.^[22]

A further promising approach to stabilize the blend morphology is the nucleation of the individual components of the active layer by means of nucleating agents.^[23] In general, nucleating agents increase the crystallization temperatures of semi-crystalline polymers and, thus, reduce the cycle times during melt processing.^[24,25] This can lead to considerable cost savings. Furthermore, nucleating agents can also improve the physical and optical properties of polymers.^[26-31]

1.1 Supramolecular chemistry

Supramolecular chemistry is a lively and prominent research field. It is based on one hand on the development of the chemistry of crown ethers and cryptands, on the other hand, on progress in studying the self-organization of molecules. Jean-Marie Lehn, a pioneer in this research area, has defined supramolecular chemistry as “the chemistry of molecular assemblies and intermolecular bonds”.^[32] More colloquially, this can also be referred to as “the chemistry of the non-covalent bond”, “the chemistry beyond the molecule” and “the non-molecular chemistry”.^[33] In contrast to molecular chemistry, which is overwhelmingly based upon covalent bonding of atoms, supramolecular chemistry is based upon intermolecular interactions.^[34] For their pioneering work, Jean-Marie Lehn, Donald J. Cram and Charles J. Pederson has been honored with the Nobel Prize in 1987.^[32,33,35–38] Previous work concerning supramolecular chemistry dealt with only two components, a host and a guest. This so called “lock-and-key” model was defined by Emil Fischer for enzyme-substrate interactions in 1894.^[39] In this model the host and the guest interact non-covalently and build a host-guest complex or a supermolecule. The host is usually a large cyclic molecule or an aggregate possessing a accessible, central hole and so the convergent binding site. In 1891 Villiers and Hebd discovered cyclodextrins, the first synthetic host molecules.^[40] The guest, a simple inorganic anion, a monoatomic cation, an ion pair or a more complex molecule such as for example a neurotransmitter, possesses the divergent binding site and can be integrated into the intrinsic molecular cavity of the host. Interaction of two or more compounds via various intermolecular interactions such as metal coordination, H-bonding, π - π -interactions etc., result in large entity, “a supermolecule”. **Figure 1** shows some of the first supermolecules.^[41] Note the term supermolecules were introduced later on.

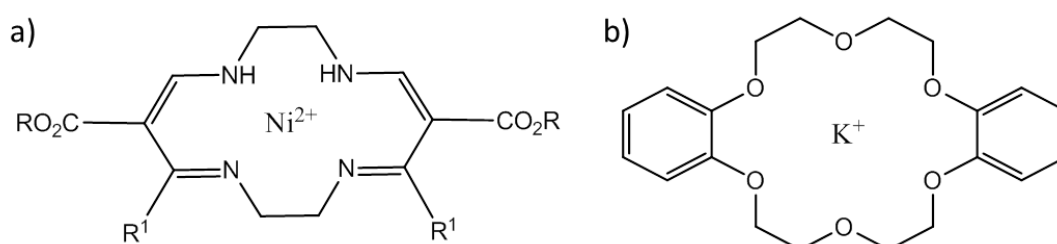


Figure 1: Some of the first supermolecules based on heterocyclic structures and intercalated ions: Jäger 1964 (a), Pedersen 1967 (b).^[41]

Supramolecular host-guest compounds can be classified into two major groups according to the type of the host-guest aggregate (**Figure 2**). If intramolecular cavities are present, the host-guest aggregate is called *cavitate*. *Clathrates* denote a host-guest aggregate which has extramolecular cavities. Recent research works dealing with host-guest aggregates focus

predominantly on mixed metal-organic frameworks, so called MOFs, and on inorganic hosts, e.g. polyoxometallates.^[34,35,41]

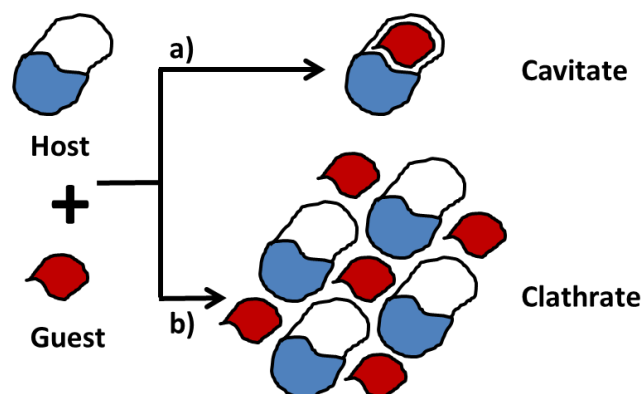


Figure 2: Schematic illustration of cavitates and clathrates: a) conversion of a cavitand into a cavitate by inclusion of the guest in the cavity of a host molecule; b) inclusion of guest molecules in cavities formed between the host molecules in the lattice: conversion of a clathrand into a clathrate.^[42]

Nowadays supramolecular chemistry is not just limited to host-guest chemistry, but it includes all aspects of self-assembly principles. That means single molecules or smaller units self-assemble by the formation of non-covalent bonds spontaneously and reversibly into nanoscale objects.^[41]

1.1.1 Supramolecular interactions

Since the beginning of scientifically based chemistry, the chemical approach has increasingly shifted from the macroscopic to the molecular level. The reason for this is the realization that the chemical properties of the substances depend decisively on the existing binding conditions and the structure.^[43] In general, molecular forces can be divided into two classes: short-range forces – these are primarily of the coulombic and exchange-type that include covalent bonds and result from molecule orbital overlap. They can be attractive or repulsive in nature and in certain situations may represent the strongest forces present in a molecular system. On the other hand there are the long-range forces. These are those forces that can be widely characterized as being proportional to r^{-m} (where r is the intranuclear distances and m is a positive integer). These include electrostatic, van-der-Waals-, and π - π interactions.^[44–47]

Besides the covalent bonding, similar strong interactions are also observed in the ordered lattice structures of metals and their salts. However, these are ionic interactions between two differently charged atoms or molecules. Commonly, supramolecular chemistry refers to non-covalent bonding interactions. These weak non-covalent interactions include a huge range of attractive and repulsive effects and are often dominated by hydrogen bonding and, if aromatic components are present, by π -cloud interactions. Furthermore, other weak

interactions (both attractive and/or repulsive) may play a role. These include for example Coulomb interactions between ions and dipoles or dipoles and dipoles. Additionally, charge-transfer, dispersion and polarisation interactions belong to this group. Combined, these describe the so called van der Waals forces.^[44,48] All these interactions can be directional, slightly directional or non-directional by constructing molecular assemblies.^[49] **Figure 3** shows an overview of some inter- and intramolecular forces and their corresponding energy values.

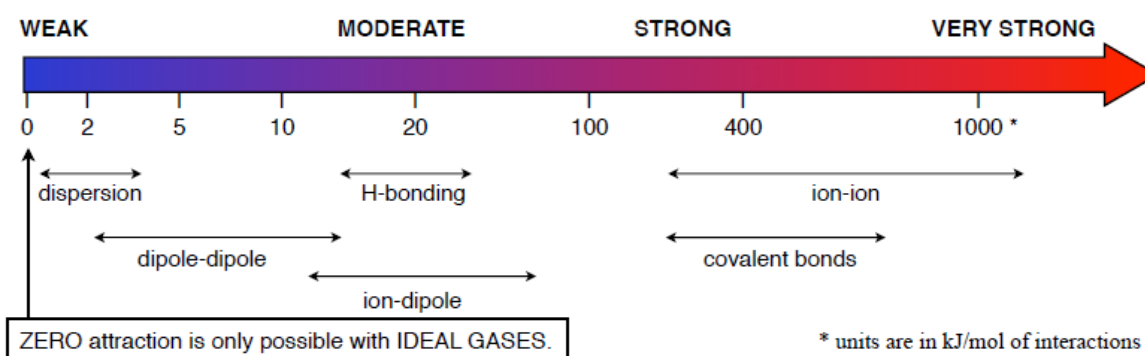


Figure 3: Inter- and intramolecular forces and their energy values.^[50]

Ion-Ion-interactions

Interactions of atoms or molecules which have permanent opposing charges are called *ion-ion-interactions*. The cations and anions attract electrostatically, resulting in the formation of a so-called *ion crystal*. The energy released during this process is referred to as *lattice energy*. Thereby, the attraction of the opposing charges is so strong that the strength of ionic bonds is comparable or beyond to covalent bonds.^[48] A typical example of an ionic solid is NaCl. By combining the ions NaCl forms a cubic lattice in which each Na^+ ion is surrounded by 6 Cl^- ions and vice versa (**Figure 4a**). Moreover, host-guest-complexes can also be formed by means of ionic bonds. A supramolecular example represents the complex of tris(diazabicyclooctane) (host) with $[\text{Fe}(\text{CN})_6]^{3-}$ anions (guest) (**Figure 4b**).^[41,51] In general, the smaller the ionic radius and the larger the ionic charge, the higher is the binding energy. Accordingly, the distance of the charges and the extent of delocalization over the whole molecule have a great influence on the strength of the interactions.^[48]

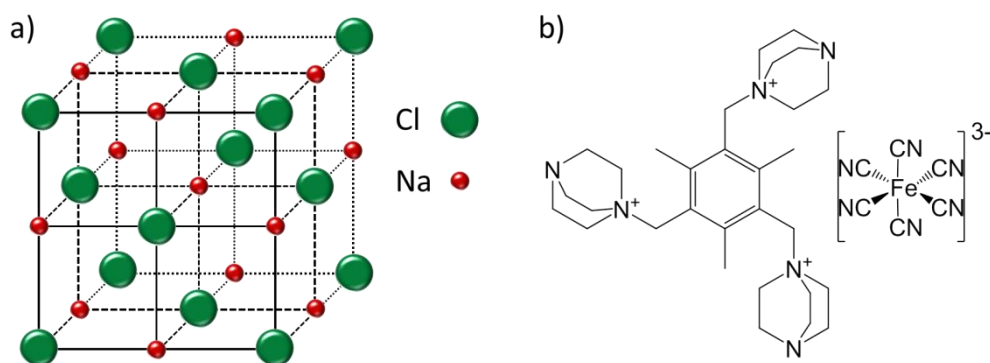


Figure 4: (a) NaCl ionic lattice. (b) Supramolecular ion-ion-interactions exemplified by the interaction of $[\text{Fe}(\text{CN})_6]^{3-}$ with the organic cation tris(diazabicyclooctane).^[51]

The interaction potential between ions is approximately proportional to r^{-1} (for short distances). For large distances, however, the interaction potential is approximately proportional to r^{-2} . Furthermore, the dielectric constant has a great influence on the bond strength. Thus, the interaction in the vacuum can be reduced by two orders of magnitude by the addition of aqueous or highly polar solvents; consequently the bond can easily be broken.^[44]

Ion-dipole-interactions

Interactions of an ion (e.g. Na^+) with the polar part of another uncharged polar molecule (e.g. H_2O) are regarded as ion-dipole-interactions. This type of binding can be present in solution as well as in the solid state and has a binding strength in the range of $50\text{-}200\text{ kJ}\cdot\text{mol}^{-1}$. Typical supramolecular examples are alkali metal-crown ether complexes (**Figure 5a**). In this case, the lone electron pairs of the oxygen interact with the positive charge of the alkali metal.^[41,48]

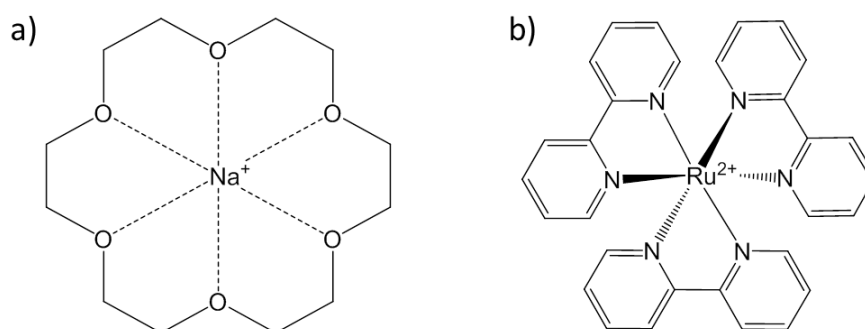


Figure 5: (a) Chemical structure of the Na^+ crown ether complex. (b) Chemical structure of $[\text{Ru}(\text{2,2}'\text{-bipyridyl})_3]^{2+}$.^[41]

Ion-dipole-interactions also involve coordinative bonds between non-polarizable metal cations and hard bases. The number of bonds can vary between 2 and 8 bonds; and are usually between 2 and 6. In this way, well-defined structures can be realized. An example of such a coordination complex with 6 bonds is $[\text{Ru}(\text{bpy})_3]^{2+}$, with ruthenium as Lewis acid (metal cation) and 2,2'-bipyridyl as Lewis base (ligand) (**Figure 5b**). The coordinative bonds are

relatively strong, which results in stable complexes. However, they are kinetically labile, which may give rise to reorganization processes.^[41]

Dipole-Dipole-interactions

Organic carbonyl compounds in solid state forms so-called dipole-dipole-interactions, which are also referred to as Keesom forces. Dipole-dipole-interactions are electrostatic forces with binding energies of about $5\text{-}50\text{ kJ}\cdot\text{mol}^{-1}$.^[41,48] The relative orientation of the two dipoles plays a decisive role.^[48] In general, a distinction can be made between two attachment types: the attachment of a dipole to an adjacent dipole (type I) and the opposite attachment from one dipole to another (type II) (**Figure 6**).^[41] The magnitude of the Keesom forces varies with the distance between the interacting molecules. Dipole interactions are often caused by strongly electronegative atoms such as oxygen, nitrogen, sulfur or halogens. However, many molecules bearing dipolar groups have no dipole moment. This is due to the fact that the dipole moment is cancelled symmetrically within the molecule, e.g. in tetrachloromethane. In the liquid state, the dipole-dipole-interactions are very weak, which is why acetone has only a boiling point of $56\text{ }^\circ\text{C}$.^[41,44]

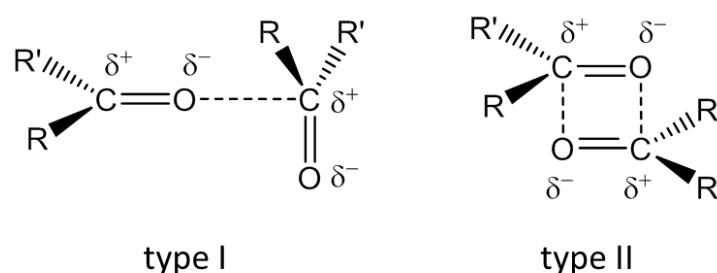


Figure 6: The two different types of dipole-dipole interactions in carbonyls.^[41]

π -interactions

Further types of non-covalent interactions are π -interactions. These include cation- π -, anion- π - and π - π -interactions. Cation- π -interactions occur between organic or metallic cations and aromatic or double/triple bonds, which can be very strong ($5\text{-}80\text{ kJ}\cdot\text{mol}^{-1}$).^[41,48,52] The resulting bonding takes place via the partially occupied d-orbitals of the metal and can therefore be regarded as non-covalent.^[41] Aromatics have a so-called quadrupole moment, which is due to the partially positive σ -scaffold and the partially negatively charged π -clouds above and below the ring plane. As soon as alkali metal or other cations are delocalized above or below the aromatic ring center, they can have attractive interactions with the aromatics.^[48] Examples of such cation- π -complexes are ferrocenes and Zeise's salts. Furthermore, cation- π -interactions play an important role in biochemistry and for chemical sensors.^[52,53]

Anion- π -interactions are similar to those of the cation- π -interactions, just reversed. Regarding the cation- π -interactions above, one can conclude that anions are repelled by the partial negative charge of the π -cloud and, therefore, no attractive anion- π -interaction can occur. However, due to the charge carrier difference between a neutral aromatic ring and an anion, the possibility for electrostatic attraction is in principle given.^[54,55] Work by Kochi et al.^[56] shows that anions can form stable charge carrier complexes with electron-deficient compounds such as 1,2,4,5-tetracyanobenzene. Furthermore, anion- π -interactions determine self-assembly reactions of Ag(I) complexes with π -acidic aromatic rings.^[57]

Interactions between aromatic rings are referred to as π - π -interactions or π - π -stacking-interactions. They are directional, electrostatic and attractive forces. First attempts to describe the occurrence of these interactions based on solvophobic^[58], electron donor-acceptor^[59] as well as atomic models.^[60] However, none of these models was satisfactory enough to describe the structures of π - π -complexes. In 1990, Sanders and Hunter supplied a model proposal that included both electrostatic and van-der-Waals-interactions.^[61] Their model proved successfully, that many observed geometries could be explained. The main feature of this model is that it considers the π -electrons separated from the σ -network. It concludes that *“apparently net favorable π - π -interactions are not due, in fact, to attractive electronic interactions between the two π -systems, but rather occur when the attractive interactions between the π -electrons and the σ -framework (namely, π - σ -attractions) outweigh the unfavorable π - π -repulsions that are present”*.^[44] By means of their model, Hunter and Sanders could establish six simple rules that apply to all π -stacked aromatics.^[61]

Figure 7 shows the most common types of geometries, which can be observed by interactions between the prototypical π - π -system of a benzene dimer.^[62] For this π - π -system three favored structural alignments are present. These are ‘face-to-face’ (stacked), ‘edge-to-face’ (T-shape) and ‘offset’ (parallel displaced). On the basis of the existing quadrupole moment in benzene, T-shape and the parallel displaced alignment are the preferred geometries. In this case a face-to-face parallel stacked alignment is not possible, due to repulsive interactions caused of identically partially negative charges above and below the ring plane. However, the quadrupole moment can be reversed by polarization of one ring by means of strongly electron-withdrawing substituents. Hereby, stable face-to-face parallel stacked geometries can be realized. Apart from these described geometries, there also exist a number of other intermediate alignments. π - π -interactions have been observed in crystal structures of

aromatics for a long time.^[35,41,49,61,62] They are, for example, the reason why benzene crystallizes in a herringbone motif. Furthermore, these π - π -interactions also ensure DNA stabilization and are involved in the intercalation of drugs into the grooves of the DNA.^[41,44]

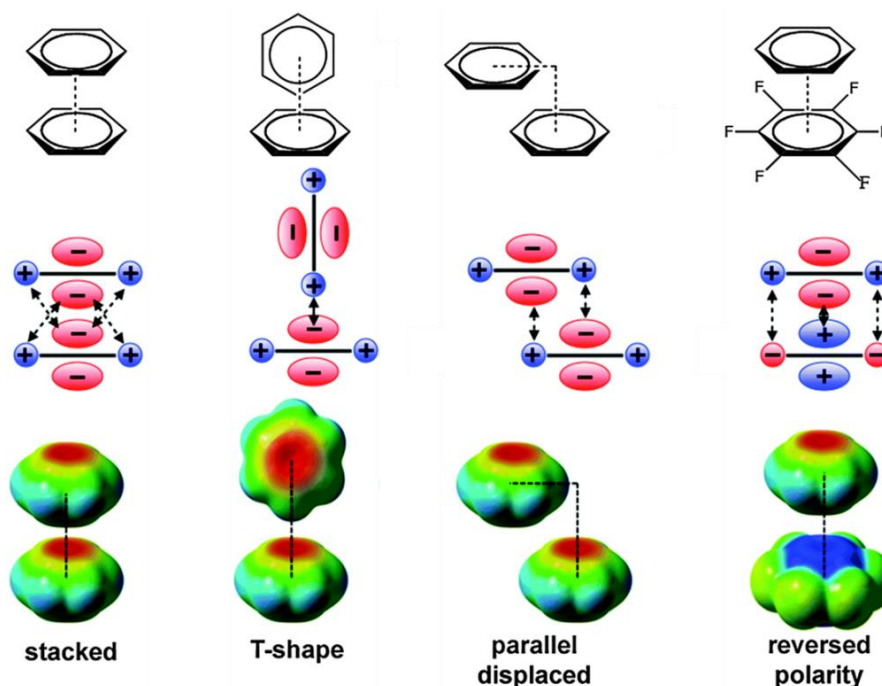


Figure 7: Geometries, quadrupole moments and electrostatic potentials (blue is positive and red is negative) of typical π - π -aromatic interactions.^[62]

A further peculiarity, which can be observed when two aromatics interact, one of which is electron-rich (e.g. hydroquinone) and the other electron-poor (e.g. quinone), is the so-called charge-transfer-interaction. This kind of interaction can be quite strong and can be identified by means UV/vis spectroscopy.^[48]

Hydrogen bonding

In the 1920s, the term hydrogen bonding was used to explain the structure of water.^[44] Finally, hydrogen bonds are also responsible for the fact that water is present as a liquid at room temperature and not as a gas.^[63] Meanwhile, however, an exact definition is difficult. In the classical book of Pimentel and McClellan, the concept of hydrogen bonds is discussed in detail.^[64] Simply put, attractive interactions between a proton donor and a proton acceptor are present in hydrogen bonds. Thus, a hydrogen atom is ligated to a more electronegative atom (or more electronegative group) and is attracted by an adjacent dipole or functional group. Both the donor and the acceptor (often with a lone electron pair) have an electronegative character and share the proton ligated in the middle. Hydrogen bonds exist in a wide range of lengths, strengths and geometries. Moderate strength hydrogen bonds with binding energies of $15 - 60 \text{ kJ}\cdot\text{mol}^{-1}$ are the most common species. They have no linear

geometry but are slightly bent ($130^\circ - 179^\circ$). Weak hydrogen bonds mainly include unconventional donors and acceptors, such as C-H groups or π -systems of aromatics. Due to their high bond angles, they have more geometric degrees of freedom and are, therefore, flexible. The donor-acceptor distances range up to 4 Å. Therefore, the weak hydrogen bonds are more electrostatic in nature ($<15 \text{ kJ}\cdot\text{mol}^{-1}$). In general, donor groups consist predominantly of C-H, N-H, O-H, S-H and halogen-H bonds. Acceptor groups include N, O, P, S, halogens, aromatic π -clouds and transition metals. N-H \cdots H bonds are more bent than O-H \cdots H bonds, since the oxygen is more electronegative than the nitrogen, and the binding interactions are stronger.^[41,44,48,63]

Figure 8 shows common arrangements of hydrogen bonding geometries. They may be described as *linear*, *bent*, *accepting bifurcated*, *bridging*, *donating bifurcated*, *cyclic dimer*, *trifurcated* and *three-centre bifurcated*. Since there is a direct interaction between donor and acceptor, these geometries are also referred to as *primary hydrogen bonding interactions*.^[41,44,63]

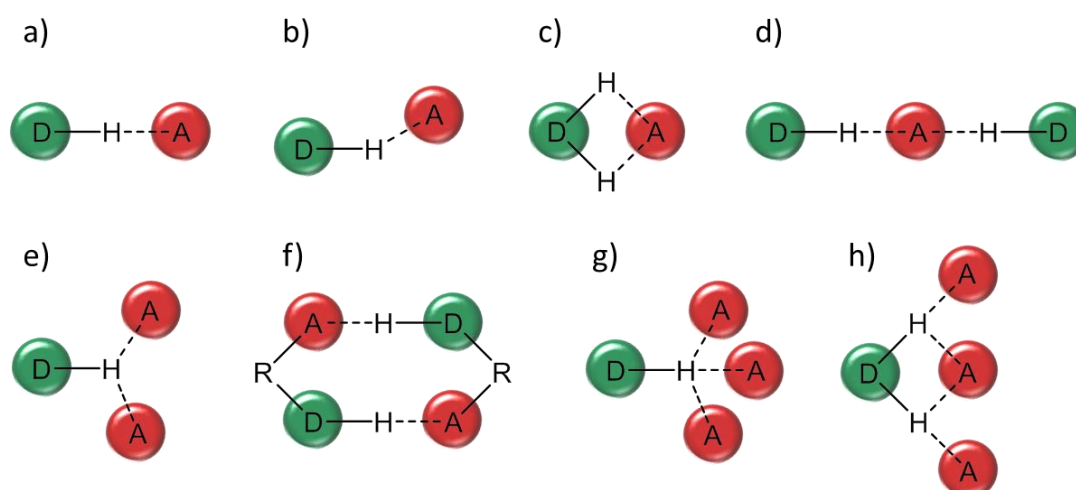


Figure 8: Common arrangements of hydrogen bonding geometries: (a) linear (b) bent (c) accepting bifurcated (cyclic) (d) bridging (e) donating bifurcated (f) cyclic dimer (g) trifurcated (h) three-centre bifurcated.^[49]

However, secondary interactions between adjacent donor and acceptor groups must also be considered. These interactions can have a positive or negative impact on the binding strength. **Figure 9** shows exemplarily this situation for three donor and acceptor groups. For an arrangement, in which three donors are present on one side and three acceptors are on the opposite side, only attractive interactions occur resulting in increased bonding strengths (**Figure 9a**). In the case of the mixed donor/acceptor systems, there are, besides the attractive interactions, also repulsive interactions (**Figure 9b**). Such a system, for example,

can be found in the DNA. There are three primary interactions between the base pair cytosine and guanine. In addition, there are both attractive and repulsive secondary interactions.^[41,63]

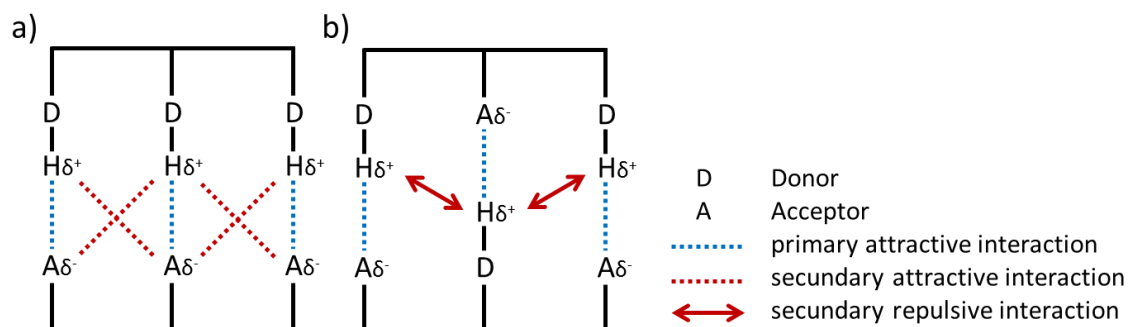


Figure 9: (a) Attractive secondary interactions for an DDD and AAA array and (b) attractive and repulsive interactions for a mixed donor/acceptor system (DAD and ADA).^[41]

Van der Waals interactions

Van der Waals interactions, named after the Dutch physicist Johannes Diderik van der Waals, are quite weak interactions ($<5 \text{ kJ}\cdot\text{mol}^{-1}$) between atoms or molecules whose interaction energy decreases for spherical particles with about the sixth power of the distance. The interactions can be attractive or repulsive and can be divided into three components: The force between permanent-permanent dipoles (Keesom interaction), the force between permanent-induced dipoles (Debye interaction), and the force between induced dipole-induced dipoles (London dispersion force). The main contribution of the van der Waals interactions make the London dispersion forces, since it does not require a permanent dipole. The London dispersion forces describe weak attractive forces between non-polar molecules and atoms. These attractive forces result from the spontaneous polarization of a particle whose polarization induces further dipoles in neighboring particles. According to that, London dispersion interactions are caused by accidental fluctuations in the electron density in an electron cloud. As the number of electrons in an atom increases, the associated London dispersion force increases too.^[41,48,65–67]

1.1.2 The self-assembly process

A fundamental feature of supramolecular chemistry is the self-assembly to objects, which is based on intermolecular non-covalent interactions.^[68] In general, the self-assembly describes a molecular arrangement in which two or more molecules interact with each other via different intermolecular interactions (e.g. H-bonding, π -interactions, metal coordination etc.), resulting in a large entity.^[49] Simple building blocks with suitable binding sites are mixed together, which may assemble spontaneously without any further contributions.^[48] However, self-assembly of supramolecular building blocks into supramolecular aggregates is a complex

process, in which several requirements must be fulfilled: (i) the building blocks must be mobile. On the basis of the Brownian motion of molecules in solution, however, this requirement is almost always fulfilled; (ii) after synthesis the individual components must have the corresponding geometric and electronic information in their structure. Self-assembly can only take place with suitable binding sites in the right places. According to this, self-assembly is a matter of well-designed building blocks; (iii) the bonds formed between different components must be reversible, i.e. they must be easily formed and broken. It means that a thermodynamic control is under equilibrium conditions and thus damaged or poorly defined structures can be easily repaired. This possibility of self-healing is not present in kinetically controlled processes.^[48,69,70]

Interacting molecules may complement each other in terms of their geometry and their interaction sites in such a way that they form non-covalent bindings with one another but not with themselves.^[38] Thus, two different mutually complementary molecules can aggregate (**Figure 10a**), or two complementary molecular moieties can be combined in one molecule (**Figure 10b**). The latter are also referred to as self-complementary molecules. These molecules can then form long chains with themselves.

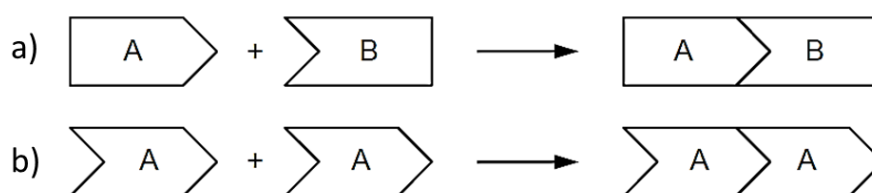


Figure 10: Schematic representation of the self-assembly process of complementary molecular building blocks: (a) aggregation of two differently complementary molecules; (b) aggregation of two identical self-complementary molecules.

In addition to the geometric structure of the building blocks, many other parameters have a great influence on the self-assembly process (self-assembly or disassembly) and can channel it in a certain direction. These include, inter alia, the present temperature or temperature changes during the process, the concentration of the components, the solvent, etc.^[71-75] In order to consciously control the self-assembly result, these triggers must be understood and carefully adapted. According to Maggini et al., these parameters can be divided into three main groups: (i) kinetic and thermodynamic considerations; (ii) internal factors such as molecular structure and non-covalent interactions; and (iii) external factors, e.g. solvent, temperature and pH-value.^[76] All three groups are not independent, but affect each other. Accordingly, the resulting supramolecular structure formed is based on a combination of all these factors.

Self-assembly is very far from a unique idiosyncrasy of supramolecular systems – it is ubiquitous throughout in nature. It is found in flora and fauna, in water and in viruses.^[77] For instance, collagen, the major extracellular structural element, which is responsible for the mechanical stability and elasticity of all tissues, organs and bones, is a classic example of a hierarchically self-assembled structure (**Figure 11**). The smallest subunits are amino acids, which are covalently linked forming polypeptides. The next larger hierarchical element is collagen, representing a triple helix, which is formed from three self-assembled polypeptide chains. The collagen formed, in turn, self-assembled into collagen nanofibrils, which subsequently bundle together into collagen microfibrils.^[78]

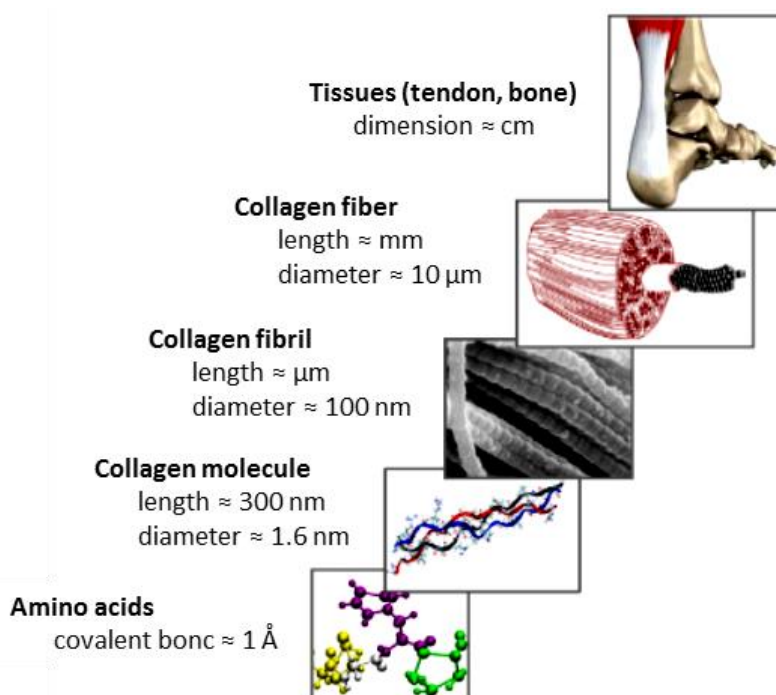


Figure 11: Hierarchical structure of collagen protein materials.^[78]

Further examples of supramolecular chemistry in nature are ribosomes^[70], the key moiety of every living cell, cellulose^[79], the main component of all plant cell walls, the tobacco mosaic virus^[80] or even snow flakes among others.^[77,81]

Biological systems aside, supramolecular systems are commonplace throughout chemistry. Self-assembly in chemical systems can be found, for example, in crystal growth, in the formation of liquid crystals, in the synthesis of metal coordination complexes, in the spontaneous formation of synthetic lipid bilayers, and in the alignment of molecules on surfaces, to name but a few.^[82] Therefore, it is not surprising that the field of supramolecular chemistry is an interdisciplinary field explored by chemists, biologists, physicists, materials scientists and theoreticians.^[83]

1.2 Conjugated polymers

Since the discovery of highly conductive polyacetylene by Shirakawa^[84], conjugated polymers have become more and more important in research. Both, their good semiconducting properties and potential processability from solution, which is associated with low-cost manufacturing methods, nourish the vision of inexpensive electronic components. Moreover, compared to inorganic semiconductors, conjugated polymers have significant advantages in terms of their light-weight and their corrosion resistance.^[85] **Figure 12** shows the basic chemical structures of the most commonly used conjugated polymers.

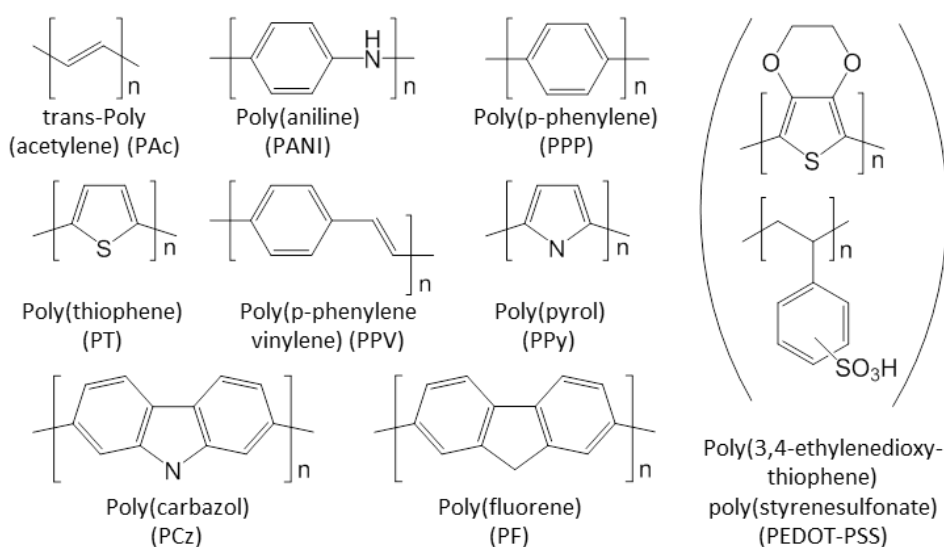


Figure 12: Chemical structures of the most commonly used conjugated polymers.

1.2.1 Poly(3-alkylthiophene) (P3AT)

An important class of organic semiconductors are polythiophenes. In addition to their good semiconducting properties, these feature a good resistance behaviour.^[86] As early as 1884, the acid-catalyzed polymerization of thiophenes was reported. In the middle of the 20th century it was also shown that polythiophene oligomers can be synthesized by means of one hundred percent ortho-phosphoric acid, Lewis acids, montmorillonite and aluminum silicate catalysts. Moreover, the electrochemical oxidation also represents a possibility for synthesizing polythiophenes. However, only insoluble oligomers with three to five repeating units could be prepared by the methods mentioned.^[85] Yamamoto et al. synthesized polythiophenes with several repeating units by initially producing a mono-Grignard reagent via the reaction of 2,5-dibromothiophene with metallic magnesium and subsequently polymerizing the activated monomer with a transition metal catalyst.^[87] The polythiophene obtained had a molecular weight of $1370 \text{ g}\cdot\text{mol}^{-1}$, but was predominantly insoluble. Further optimization of the catalyst ligands, the variation of the metals for the Grignard production,

the solvent and the reaction temperature, and the use of halogenated thiophenes led to remarkable improvements in the synthesis of polythiophenes.^[85] However, the soluble fractions of the polymers produced still had only a very low molecular weight. One finding of the previous syntheses was that the polymers obtained from methyl-substituted monomers were both higher in molecular weight and more soluble than the polymers prepared from unsubstituted thiophenes. This led to the assumption that the methyl substituent at the beta position of the thiophene ring increases the solubility of the polymer.^[88]

Yamamoto et al. reported first the presence of different regioisomers which arise during the polymerization of the unsymmetrical 3-methylthiophene monomer species.^[88] These regioisomers lead to polymeric structures with different regioregularities and thus to differences in their optoelectronic properties. The typical chemical polymerization of 3-alkylthiophenes involves the Kumada cross-coupling reaction of 2,5-dibromo-3-alkylthiophenes in the presence of nickel catalysts. The first step of this reaction involves the formation of a Grignard reagent from dibromo-3-alkylthiophenes with one equivalent of magnesium. During this formation, two different isomers are formed: 2-bromo-5-bromomagnesium-3-alkylthiophene and 5-bromo-2-bromomagnesium-3-alkylthiophene. In unsymmetrical 3-alkylthiophenes, the α -carbon atom is generally referred to as position "2", between the sulfur atom and the alkyl chain, as the "head" position (H), the α -carbon atom at position "5" as the "tail" position (T). During the first coupling reaction and the formation of dimers, three different regioisomers are possible (HH, HT, TT). In the further coupling of an alkylthiophene monomer, 4 different regioisomers can be formed (HH-TH, HH-TT, TT-HT, HT-HT) (see **Figure 13**). By means of ¹H-NMR spectroscopy, it is possible to determine the individual regioisomeric triads based on the chemical shift of the aromatic proton at position 4 of the thiophene ring.^[89] The HT-HT isomer is the regioregular isomer, while the other three are the regioirregular isomers. In a completely regioregular polymer chain, which means that only HT linkages are present, the side chains are more planar to the sp²-hybridized carbon atoms of the thiophene ring. This planarity allows efficient π -stacking interactions between adjacent polymer chains. In contrast, the presence of HH and TT linkages induces steric hindrance between the alkyl chains and, consequently, increases a tilting between the thiophene units.^[85,88]

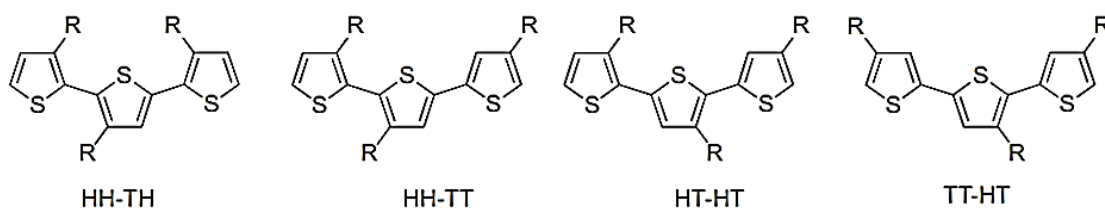


Figure 13: Chemical structures of the four possible regioisomeric triads of 3-alkylthiophene.^[85]

McCullough and Rieke published the first reports on the synthesis of regioregular poly(3-alkylthiophenes) (P3ATs) with mainly HT linkages.^[90,91] These two reports are also considered to be a significant breakthrough in the synthesis of regioregular P3ATs. However, a large-scale production turns out to be difficult due to the necessary cryogenic temperatures during the synthesis. In 1999, McCullough developed a simpler and more convenient synthetic route by using the so-called Grignard metathesis (GRIM), which could be performed at room temperature.^[92] This method allows the synthesis of high molecular weight regioregular P3ATs with very low PDIs. Yokozawa termed the polymerization a catalyst transfer polycondensation reaction, which was later named the Kumada catalyst transfer polycondensation (KCTP).^[93] However, the reaction mechanism involves a TT coupling reaction, resulting in at least one regiodeflect in the polymer chain.^[85] Nevertheless, by using an “external initiator”, this single regiodeflect can also be eliminated.^[94]

1.2.2 Poly(3-hexylthiophene)(P3HT)

One of the most prominent semiconducting polymer is P3HT. With the advancement of syntheses of P3ATs, P3HT has become a leader in the field of research of conjugated polymers. This organic semiconductor is nowadays used in various optoelectronic components, such as organic solar cells, field effect transistors or light emitting diodes. Furthermore, P3HT is often also used as a comparative model polymer for novel conjugated polymers. One reason for that is the relative simple synthesis by now.^[95–100] The chemical structure of P3HT is shown in **Figure 14**. The p_z molecular orbitals projecting perpendicularly from the thiophene plane overlap along the thiophene ring backbone. They form the π -electron system along the main chain, which is characterized by delocalized electronic states depending on the chain structure.^[85]

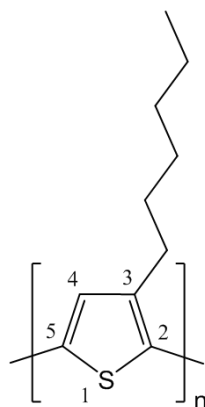


Figure 14: Chemical structure of poly(3-hexylthiophene) P3HT.

The hexyl side chain is located at position 3 of the thiophene ring. Since 3-hexylthiophene has an unsymmetrical structure, different regioisomers are formed during synthesis. The chemical structures of these regioisomers are shown in **Figure 15**. The regioregularity can be controlled by the synthesis method.^[85] In general, with decreasing regioregularity the melting temperature and the crystallinity decrease.^[101] Typical melting temperatures T_m of semi-crystalline P3HT are in the range of 225 – 235 °C.

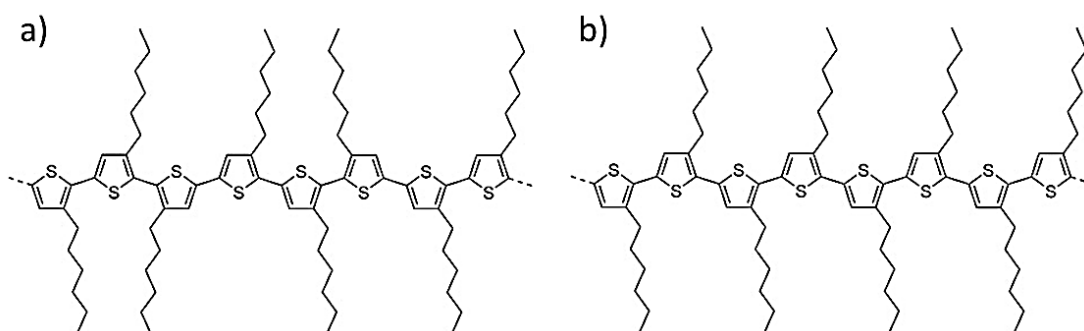


Figure 15: Chemical structures of regiorregular (a) and regioregular (b) P3HT.

The semi-crystalline structure of P3HT was determined by small and wide angle scattering (SAXS, WAXS), atomic force microscopy (AFM) and transmission electron microscopy (TEM). It consists of the crystalline areas in the form of lamellae or hairpin crystals and the amorphous intermediate areas.^[102–104] Initially, an orthorhombic unit cell was proposed for the crystal structure, but recent studies indicate a monoclinic unit cell.^[104–106] Frequently, P3HT has been studied with particularly short chain lengths, close to an oligomeric system where two crystal modifications are present.^[107]

Crystal structures of P3HT

The rigid and rather planar conformation of the conjugated backbone of P3HT allows efficient packing and crystallization. However, since P3HT single crystals are very difficult to generate, there are very few publications on this subject.^[108,109] The same applies for the degree of

crystallinity of P3HT. This is seldom discussed in the literature, as it is difficult to determine the reference melting enthalpy of an ideal P3HT crystal. A first value of $99 \text{ J}\cdot\text{g}^{-1}$ was given by Malik and Nandi.^[110] Recent research suggests values between 37 and $50 \text{ J}\cdot\text{g}^{-1}$.^[104,111,112] The investigations of the crystal structure of P3HT was mainly conducted via electron and X-ray diffraction on thin semi-crystalline films and accordingly not on single crystals.^[113] **Figure 16** shows the typical crystal structure of regioregular P3HT, with the lattice parameters a , b and c ; the “curvy lines” represent segments of amorphous domains.^[111] From a crystallographic point of view, the a -axis (100) is pointing in the direction of the alkyl chains and the b -axis (010) corresponds to the π - π -stacking direction between the planar backbones. The c -axis (001) describes the layer periodicity of the larger lamellar structure and matches to the direction along the polymer chains.^[112,114]

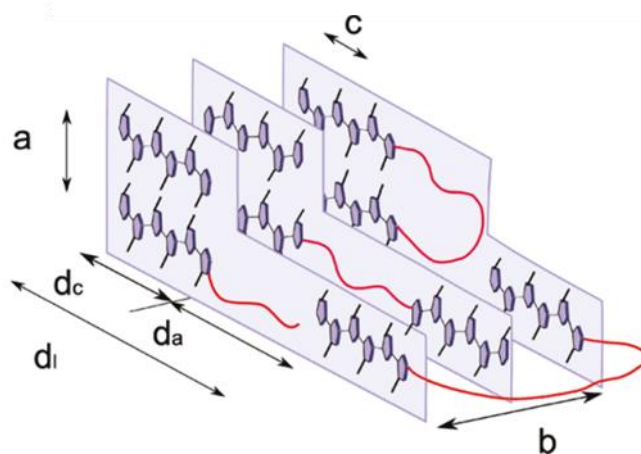


Figure 16: Typical microstructure of regioregular P3HT, with curvy lines representing segments in the amorphous domain. Crystal lattice parameters a , b , c ; thickness of the lamellar crystals d_c ; thickness of the amorphous layers d_a ; long period $d_l = d_a + d_c$.^[111]

In general, the unit cell is described as orthorhombic, although some reports showed a monoclinic structure.^[106] The dominant mechanism during crystallization is the π - π -stacking along the b -axis. The π - π -stacking between two molecules is caused by Van der Waals interactions between the two electron systems. Dipole moments in one P3HT molecule are formed by quantum mechanical fluctuations, which in turn induce a dipole moment in the adjacent P3HT molecule. This mechanism leads to an electromagnetic attraction of the two non-polar molecules (London dispersion forces). These forces also cause a parallel alignment of the molecules, which maximizes the overlap of the interacting electron systems. These attractive forces are opposed by the electromagnetic repulsion of the π -electron systems of the molecules.^[41,61] The balance between the two forces results in a packing distance of 3.8 \AA along the b -axis.^[113,115]

Figure 16 shows that a lamellar structure is formed along the c-axis in which crystalline and amorphous areas alternate. The crystalline areas are represented as blue rectangles. The amorphous regions, which describe P3HT chains in irregular and non-planar arrangement, are shown as red lines. If a P3HT chain is longer than the width of the crystal lamellae (d_c), it can be incorporated in crystal lamellae several times. For this purpose, it can fold back into its own crystal or penetrate into another crystalline region.^[111,113] The width of a crystalline lamella is in the range of 10-15 nm and depends on the molecular weight of the P3HT (**Figure 17**). Zhai and co-workers showed that the P3HT fibril width increases with molecular weight, but saturates above a critical value of around $10 \text{ kg}\cdot\text{mol}^{-1}$. Below the critical M_n the nanofibrils are assumed to be formed by extended chains that span the width of the fibrils. Above the critical M_n chain folding takes place and leads to a saturation of fibril width.^[116,117]

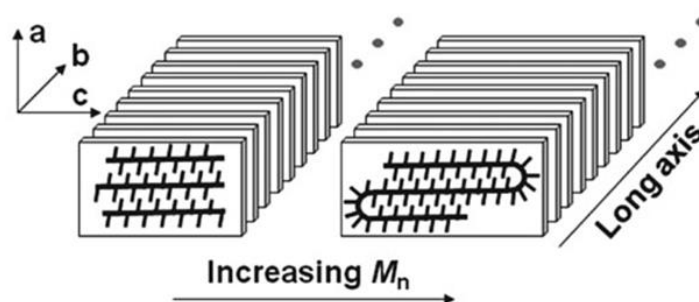


Figure 17: Schematic illustration of extended (left) and folded (right) P3HT backbone stacking in nanowhiskers prepared by low M_n (left) and high M_n (right) P3HT, respectively. The U-turn of the polymer includes 6-7 alkythiophene rings.^[116]

For the model of the crystal structure of P3HT as shown in **Figure 16** it has to be considered, however, that certain simplifications have been made. Experimental results indicate that the molecules in the crystal domains are slightly tilted so that the blue rectangles continue to be parallel to the c-axis, but no longer perpendicular to the b-axis. Furthermore, the crystallization of P3HT leads to a planarization of the backbone, but the side chains are usually not in the same plane.^[118]

For the arrangement of P3HT crystallites on a substrate, three arrangements are discussed in the literature. Considering the plane spanned from the b- and c-axis (**Figure 18a**) as a substrate plane, the π -stacking takes place in the film plane and the side chains point perpendicularly to the substrate. This arrangement is called edge-on orientation. Moreover, the alignment of the crystals on the substrate can also occur in a way in which the polymer chains lie flat on the substrate (**Figure 18b**). In this case π -stacking takes place perpendicular to the substrate. This arrangement is called face-on orientation. In a third possible

arrangement, the polymer backbone stands vertically on the substrate (**Figure 18c**). This arrangement is seldom reported in the literature.^[114,113,118]

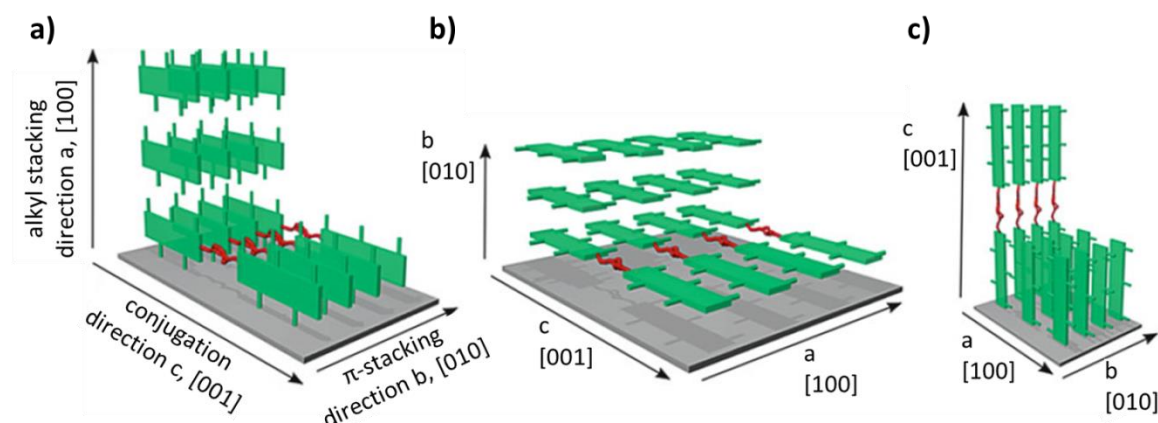


Figure 18: Molecular orientation of P3HT in thin layers: (a) edge-on orientation, (b) face-on orientation and (c) standing chains.^[114]

Which of these arrangements of P3HT is present depends strongly on the preparation conditions and the substrate surface. The edge-on orientation is the thermodynamically favored one, whereas the face-on orientation can be regarded as a kinetically trapped arrangement.^[114] DeLongchamp et al. reported that an edge-on texture develops for slow spinning speeds during spin-coating of P3HT from chlorobenzene. By increasing the rotational speed, face-on textures formed more often. With regard to the charge transport, it can be assumed that this will be faster in the c- (polymer chain axis) and b- (π -stacking axis) direction than in the a-direction of the isolating side chains. Therefore, the edge-on orientation represents for OFETs the desirable morphology.

Crystal structure studies of Prosa et al. revealed the presence of two polymorphic forms of P3HT (**Figure 19**).^[105,119] Form I has a packing distance of 1.6 nm and is present, if the P3HT molecules lie on top of each other along the a-axis in such a way that the P3HT side chains do not interdigitate. In general, the packing distance of the crystalline domains of P3ATs depends on the length of the side chains. Longer side chains increase the distances between the backbones. An arrangement in which the P3HT side chains interdigitate, leads to smaller package distances and is called Form II. This form is thermodynamically more unstable and can only be observed for P3HT with low molecular weights.^[118,120,121]

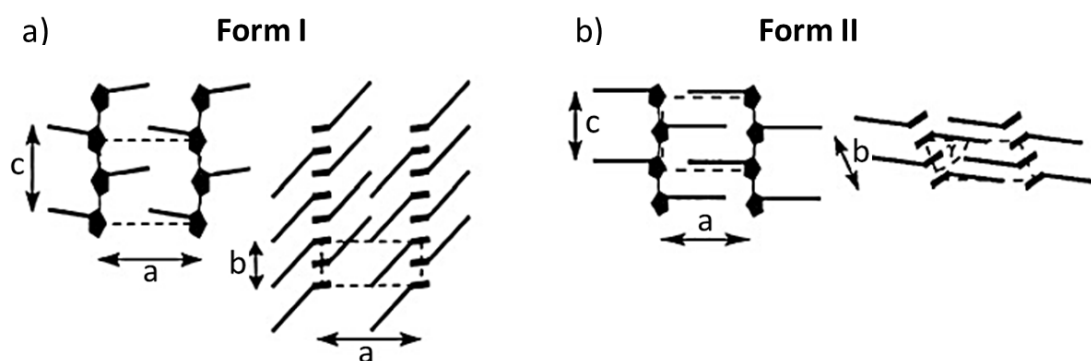


Figure 19: Crystal structure of P3HT in Form I (a) and Form II (b).^[119]

Properties of P3HT

P3HT is a conjugated, semiconducting polymer. Only by chemical or electronic doping does it become a radical-ionic polaron species and thus conductive.^[114] For the determination of its energy levels, usually cyclic voltammetry is used. Thereby, the onset of the oxidation- and reduction potentials are determined, which are closely related to the highest occupied molecular orbital (HOMO) and lowest unoccupied molecular orbital (LUMO) energies, since the oxidation is due to the removal of one electron from the HOMO and the reduction is due to the addition of one electron to the LUMO.^[122] The difference between these energy levels is referred to as the electrochemical band gap, which is an important parameter for polymer-based organic photovoltaics.^[114] Detailed characterizations regarding the electrochemical properties of P3HT have been reported by Trznadel et al. and Skompska et al.^[123,124]

Due to the good semiconducting properties and the processability from solution, P3HT is used today in various optoelectronic applications, among others in bulk-heterojunction solar cells.^[96,100] The active layer is very often a blend consisting of a polymeric electron donor (hole-conductor) and a fullerene-based electron acceptor (electron-conductor). P3HT:PCBM-blends are, to date, the most-studied active layer material in BHJ solar cells. Various power-conversion efficiencies are reported which can reach values of up to approximately 5%.^[125] In a BHJ solar cell, the active layer absorbs photons, which leads to the formation of excitons. These excitons must then be split at a donor-acceptor heterojunction in order to generate both types of charge carriers. The charges are then transported through the respective component (hole-conductor or electron-conductor) of the active layer to the electrodes, whereby an electric current is generated.^[126–128] In terms of device performance, the BHJ nanomorphology, i.e., the distribution of donor and acceptor molecules, has the most significant impact.^[1,129] Here, a compromise between two critical factors must be made. On the one hand, the contact area between the donor and acceptor molecules must be very

large in order to generate as many charges as possible. Therefore, a very well intermixed blend structure is desirable. On the other hand, however, the generated charges must be transported to the respective electrodes. This can be realized by the percolation of separated, relatively phase pure donor and acceptor domains. Considering these two aspects, the ideal nanomorphology exhibits an intermediate degree of phase separation.^[22] Meanwhile, a variety of processing techniques have been developed in order to control the blend nanostructures and thus to increase the long-term stability of the organic solar cells.^[13-20] All these approaches, however, increase the complexity of the system, often involve chemical modifications and increase the overall costs.^[22]

Recent work suggests that nucleation of one of the active layer components can also stabilize the BHJ morphology.^[22,23] Lindquist et al. showed that the nucleation of PCBM allowed a certain control of the blend morphology. It was shown that by adding appropriate nucleating agents, the PCBM crystallite size, at temperatures above the glass transition temperature of the blend, is significantly reduced and the number of crystallites is greatly increased without affecting the electrical properties.^[22] Chabinyk et al. have used commercial nucleating agents to manipulate the solidification kinetics of various organic semiconductors without adversely affecting the electronic properties.^[23,130-132]

These results show that it may be possible to positively influence the BHJ morphology by means of nucleating agents. Therefore, in the following, details of nucleating agents and their principle of operation will be discussed.

1.3 Nucleation of semi-crystalline polymers

Polymers are nowadays ubiquitous and indispensable in our daily lives. This is partly due to their excellent mechanical, optical and electronic properties, which qualified them for a variety of applications. Moreover, the plethora of processing methods and their low production costs render polymers to an intensively used material class. Consequently, in order to remain competitive within this vast industrial sector, specific properties of the polymers must steadily be advanced. This is achieved, for example, by the addition of so-called polymer additives. These include, among others, processing aids, UV-stabilizers, colorants, flame retardants, and nucleating agents.^[133]

In particular, nucleating agents play a major role for the processing and property profile of semi-crystalline polymers, since these properties are largely governed by their crystalline

domains. In general, nucleating agents increase the crystallization temperatures of semi-crystalline polymers and thus reduce the cycle times during melt processing.^[24,25] This can lead to considerable cost savings. Furthermore, nucleating agents can improve the physical and optical properties of semi-crystalline polymers.^[26–31]

1.3.1 Crystallization of semi-crystalline polymers

As is known for small molecules, the crystallization of polymers is initiated with the nucleation. Individual segments of macromolecules deposit themselves parallel to each other in very small formations, the nuclei. These nuclei form the basis for the following crystal growth. First, however, the entangled polymer chains must disentangle before they can be incorporated into the growing crystal. Since disentanglement is typically incomplete due to the length of the polymer chains an ideal, fully crystalline state is not achievable for polymers in the solid-state. The crystal growth in polymers thus proceeds as follows: the crystallizable sequence of a chain is separated, stretched and depending on the primary structure incorporated in a helical or zigzag shape in the growing nuclei. The remaining polyene chain can (1) fold back into the same crystal instantly, (2) remain mostly in the amorphous phase, and eventually return to the same crystal (loop molecules), (3) remain completely in the amorphous phase (cilia molecules), (4) can participate in the formation of another crystal (tie molecules). The resulting crystals usually congregate to larger spherical units with diameters in the range of 10 to 100 micrometers. These crystalline structures are called spherulites.^[134–136] In **Figure 20** the detailed morphology of a spherulite is schematically presented.^[135]

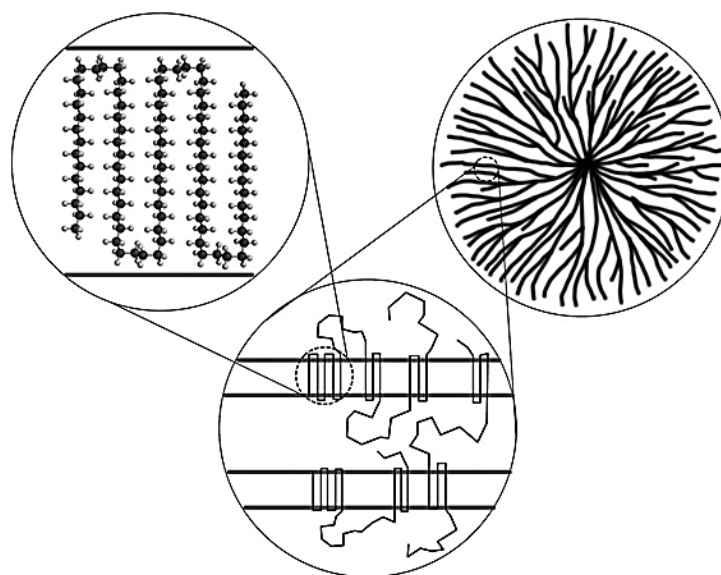


Figure 20: “Multiscale” schematic of semi-crystalline polymers according to Milner. Chain-folded crystalline lamellae (top left) lie adjacent to amorphous regions of comparable thickness (bottom). The lamellae are organized radially into micron-sized spherulites (top right).^[135]

In general, two types of nucleation, primary and secondary nucleation are distinguished. In the primary nucleation, the chain molecules combine to form a cylindrical nucleus. The cylinder axis points in the chain direction, and the height is much smaller than the length of the stretched molecule. This type of nucleation can be further divided into nucleation and crystal growth. The basic principle of secondary nucleation is identical to that of primary nucleation, except that crystallite nuclei grow on the surface of already full-grown crystallites. These usually form monomolecular layers of length l , width b and height a (**Figure 21**).^[136]

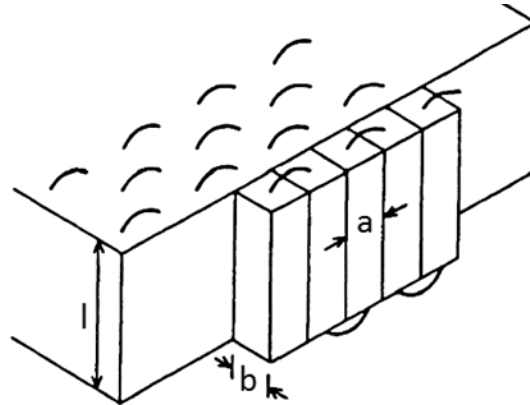


Figure 21: Schematically representation of a secondary nucleus grown on the surface of an already full-grown crystallite with the length l , the width b and the height a .^[136]

In the following, the physical principles of the nucleation and the crystal growth of semi-crystalline polymers are described in detail.

For the formation of a crystal nucleus out of a polymer melt, a driving force is required since the final state must be energetically favorable than the melt state (initial state). Thermodynamically, the free enthalpy ΔG of the system changes and a phase transition occurs only if ΔG is thereby reduced. At the melting point T_m the free enthalpies of melt (G_m) and crystal (G_c) are equivalent ($G_m = G_c$). Above T_m , the melt state is in thermodynamic equilibrium, since it has a lower free enthalpy than the crystal state. Upon cooling below T_m , the free enthalpy of the melt state increases and the crystal state is in thermodynamic equilibrium (**Figure 22**). The formation of a solid state below T_m is initiated with the formation of a nucleus based on a crystalline arrangement due to thermal fluctuations caused by thermal atomic motions. With nucleation, the system gains volume energy due to the lower free enthalpy of the volume of the nucleus.^[133]

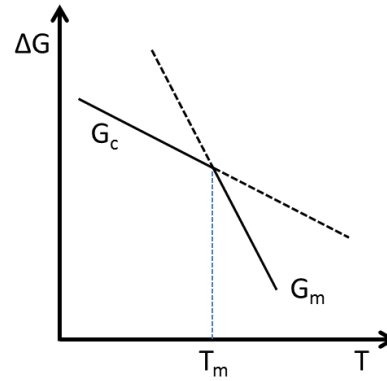


Figure 22: Schematic representation of the free enthalpies of the melt state (G_m) and of the solid state (G_c). At the melting point T_m the free enthalpies of melt and crystal are equivalent ($G_m = G_c$).

In contrast, the surface energy required to create an interface between the two different phases has to be raised. Consequently, the overall change of ΔG is composed of a volume fraction ΔG_{volume} , which releases energy, and a surface fraction $\Delta G_{surface}$, resulting in the following equation:^[133,137]

$$\Delta G = \Delta G_{volume} + \Delta G_{surface} \quad (1)$$

The required energy is proportional to the surface of the nuclei, whereas the released energy is proportional to its volume. For simplification, a nucleus can be considered as a spherical entity with radius r , resulting in **Equation 2**, with ΔG_{volume} as free volume enthalpy of the nuclei during the phase transition and σ as the surface tension of the nuclei.^[133,137]

$$\Delta G = -\frac{4}{3}\pi r^3 \cdot \Delta G_{volume} + 4\pi r^2 \sigma \quad (2)$$

ΔG :	free enthalpy
ΔG_{volume} :	free volume enthalpy of the nuclei
r :	radius of the nuclei
σ :	surface tension of the nuclei

Figure 23 shows schematically the free nucleation enthalpy ΔG and its surface and volume fraction as a function of the nucleus radius r below T_m of an ideal spherical nucleus. It is clear from the figure that first at a certain nucleus size, called the critical nucleation radius r_c , the nuclei have a positive energy balance compared to their environment. At the maximum of ΔG (ΔG_{rc}), the deviation of **Equation 2** is zero. This means that the system is in steady-state equilibrium. Consequently, below r_c more nuclei dissolve rather than they grow and above r_c more nuclei grow rather than they disappear. Thermodynamically stable nuclei are present at $\Delta G = 0$.^[133,137]

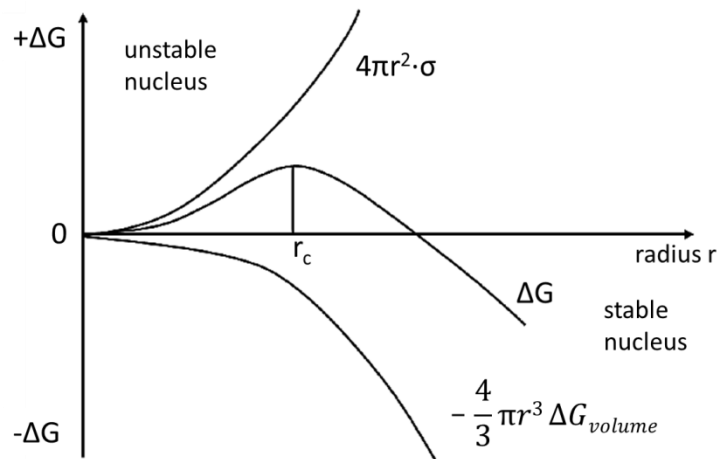


Figure 23: Schematically representation of the free nucleation enthalpy ΔG and its surface and volume fraction as a function of the nucleus radius r below T_m of an ideal spherical nucleus.^[137]

The phenomenon described above is called primary nucleation followed by crystal growth. Overall, three different nucleation mechanisms can be observed with respect to the primary nucleation of semi-crystalline polymers. These are the homogeneous nucleation, the orientation-induced nucleation and the heterogeneous nucleation.^[133] The homogeneous nucleation proceeds in the super-cooled melt without any further influences. Orientation-induced nucleation can often be observed in polymer processing techniques, such as extrusion or injection molding. The nucleation is caused by the orientation of polymer chains, due to flow and shear forces during processing.^[138] In heterogeneous nucleation, part of the nucleus surface is provided, for example, by a crucible wall, by suspended particles, or by intentionally added nucleating agents. These agents reduce the surface energy required for nucleation. Consequently, (referring to **Figure 23**) the ΔG required to reach ΔG_{rc} is smaller for heterogeneous nucleation. As a result the nucleation initiation shortens and the nuclei growth occurs at higher temperatures. Therefore, the crystallization temperature of the polymer increases, which is of fundamental importance for industrial processing and applications of semi-crystalline polymers.^[26,27,133] In addition, nucleating agents have enormous influence on the macroscopic properties of the polymer in the solid state. By adding these additives into the polymer melt the amount of nuclei as well as the nuclei density is enhanced. However, since the growth rate of the spherulites remains constant, the total size of all crystallites is reduced. This can have positive effects on the mechanical, such as elongation at break and the impact resistance, as well as the optical properties of the polymer.^[29,139–142] **Figure 24** shows the influence of the nucleating agent bis(3,4-dimethylbenzylidene)sorbitol (DMDBS) on the nucleation and morphology of isotactic

polypropylene (iPP). The addition of only 0.15 wt.-% DMDBS (**Figure 24b**) significantly reduces the spherulite size compared to the neat iPP (**Figure 24a**).^[143]

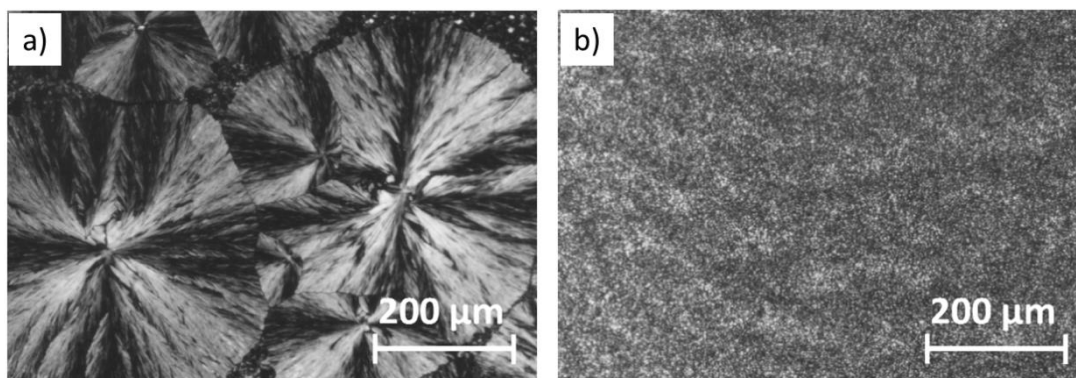


Figure 24: Polarized optical microscopy images of isotactic polypropylene without additive (a) and with 0.15 wt.-% of DMDBS (b) after cooling from the melt state to room temperature at a cooling rate of $10 \text{ K}\cdot\text{min}^{-1}$.^[143]

1.3.2 Supramolecular nucleating agents

The first nucleating agents for semi-crystalline polymers were inorganic salts such as titanium dioxide, potassium and sodium phosphates or small-particle sized minerals such as clay, talc and silica.^[144,145–149] Also polymers and oligomers, as well as organic pigments, were examined for their nucleation capability.^[26,150–153] Nowadays, about 20 chemical groups, both organic and inorganic, are involved in the production of nucleating agents. Among those supramolecular polymer additives gain more and more interest. Two important groups of these agents are organic acid derivatives^[27,29,139,154,155] and sorbitol derivatives.^[26,156,157] The special feature of these additives is that they can be completely dissolved in the polymer melt. Upon cooling from the melt these additives self-assemble prior to the polymer crystallization and therefore providing nuclei for heterogeneous nucleation. Due to their high surface to volume ratio, they provide a high density of nucleation.^[158] Yet, the supramolecular additives must accomplish several requirements. The additive should be completely dissolved in the polymer melt at the given processing conditions in order to ensure a homogeneous distribution of the additive in the polymer. This also requires a high thermal stability of the additives due to the high processing temperatures. Furthermore, it is imperative for the principle of heterogeneous nucleation that the nucleating agent has a higher crystallization temperature than the polymer to be nucleated.^[27] In addition, the additives should have structural units that allow supramolecular self-assembly by intermolecular forces. Moreover, the resulting self-assembled structure of the additive should feature an appropriate surface to allow epitaxial crystallization of the particular polymer.^[158] Due to the presence of heterogeneous nuclei, polymer crystallization growth is initiated at higher temperatures. This results in a shift of the peak crystallization temperature of the polymer towards higher

temperatures. A commonly used method for determining temperature transitions of polymers is non-isothermal differential scanning calorimetry (DSC).^[159] **Figure 25** shows the effect of different concentrations of a nucleating agent on the crystallization temperature of polyamide 6 (PA6) based on DSC thermograms^[160]. Neat PA6 crystallizes at about 185 °C whereas with the addition of the nucleating agent the crystallization temperature of PA6 is distinctly increased. Furthermore, it can be observed that the shift of the crystallization temperature towards higher temperatures is apparently concentration-dependent. Typically, there is an upper limit of nucleating agent addition, at which a too high nucleating agent concentration can cause phase separation between the additive and the polymer. This results in undissolved additive, which in turn cannot contribute in the nucleation of the polymer.^[29]

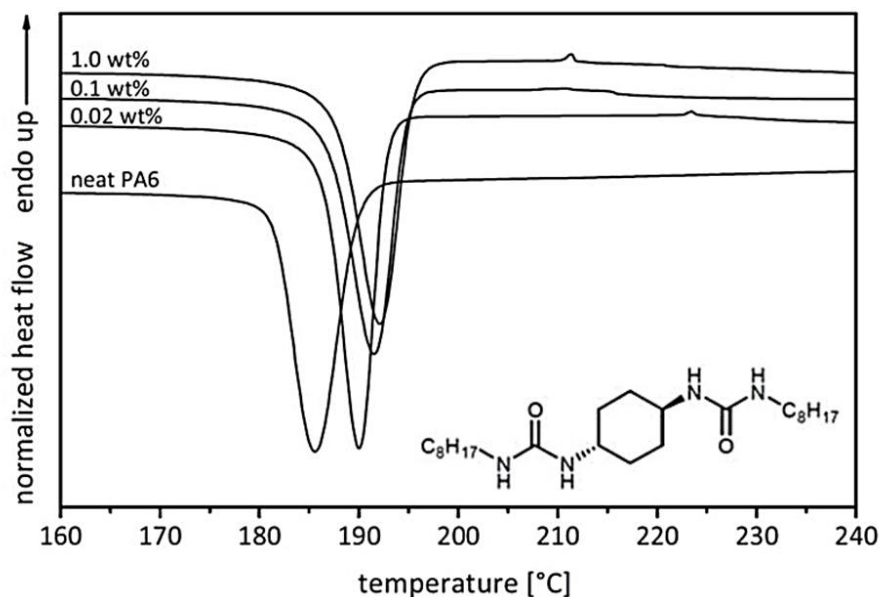


Figure 25: Differential scanning calorimetry thermographs of neat PA6 and PA6 comprising different amounts of a bisurea compound (inserted structure) at cooling rates of 10 K·min⁻¹ according to Richter et al.^[160]

Information about how efficient a nucleating agent for the corresponding polymer is, gives the nucleation efficiency (NE).^[161] This can be calculated according to the following equation:^[162]

$$NE(\%) = 100 \cdot \left(\frac{T_c^{nuc} - T_c^0}{T_c^{max} - T_c^0} \right) \quad (3)$$

where T_c^0 denotes the crystallization temperature of the neat polymer, T_c^{nuc} being the crystallization temperature of the polymer induced by a nucleating agent and T_c^{max} being the maximum crystallization temperature. The latter can be determined by so called self-seeding experiments, where the neat polymer is nucleated by its own crystal fragments. In general, this involves the partial melting of the polymer. The remaining unmolten crystal fragments can act as perfect nuclei for the crystallization of the polymer and thus increase the crystallization temperature.

2 Aim of the thesis

Poly(3-hexylthiophene) (P3HT) as highly used semiconducting polymer has been an integral part in the field of organic electronics for decades and has in this context earned itself a reputation as a model polymer for π -conjugated systems. Despite the intensive research, however, not all existing issues and open questions have been clarified till date. For example, controlling the solid-state morphology and order of semi-crystalline films still represents a challenge today. Several approaches have been conceived to manipulate the morphology of P3HT. For example, Smith et al. showed the formation of μm -long P3HT nanofibers from solution.^[115] P3HT nanofibers with a superstructure were obtained using 1,3,5-trichlorobenzene needles or carbon nanotubes as epitaxial surface.^[163,164] However, it is still unknown whether such P3HT nanostructures exhibit spatial variations of their structural and electronic properties along the fiber axis, which is important to understand charge and energy transport processes.^[165,166] A promising and straightforward approach to control the polymer solid-state morphology is nucleation. Supramolecular nucleating agents can significantly alter the solid state morphology of semi-crystalline polymers and, thus, enhance their properties. Nucleating agents are also able to increase the polymer crystallization temperature, to decrease the crystal size, and determine the crystal modification.^[24–31]

Therefore the goal of this thesis is the investigation and control of the solid-state morphology of P3HT with the help of tailored supramolecular polymer additives.

Design, synthesis and characterization of bis- and trisamides with pyridine substituents

To achieve the goal of this thesis, first, a novel class of supramolecular nucleating agents for P3HT must be designed. This nucleating agent must meet several requirements in order to be used as such: The additive must be soluble in the P3HT melt to ensure optimum dispersion in the system. Moreover, it must recrystallize upon cooling from the polymer melt above the crystallization temperature of neat P3HT. Finally, the additive should have a suitable epitaxially surface capable of crystallizing P3HT. The material class of bis- and trisamides can meet all these requirements and have already been proven their function as heterogeneous nucleating agents for semi-crystalline commodity polymers and engineering plastics, such as polypropylene or polyamide.

However, since there is a plethora of bis- and trisamides, in particular those compounds containing pyridine substituents in the periphery are considered in this work. These have

shown in preliminary investigations that their high thermal stability and surface functionality make them very promising candidates for nucleating P3HT. Therefore, a variety of different pyridine-containing bis- and trisamides, are to be synthesized, characterized and investigated regarding their ability to nucleate P3HT. All additives should have in common that the pyridine substituents are arranged symmetrically regarding the central core. However, the additives should differ among themselves with regard to their central core, their orientation of the amide groups and the type of pyridine substituent. In this way, chemically related but structurally different compounds with distinct properties and surfaces are to be generated, which allows one to establish structure-property relations.

The synthesis of the bis- and trisamides is based on an amidation reaction between corresponding acid chlorides and amine derivatives and will be characterized by common analytical methods, such as $^1\text{H-NMR}$ spectroscopy, mass spectrometry and Fourier-transform infrared spectroscopy. Subsequently, the additives are to be thermally investigated via thermogravimetric analyses (TGA), simultaneous differential thermal analyses (SDTA) and melting point measurements. Based on the results obtained, a preselection should be made which of these additives are thermally stable enough to nucleate P3HT in melted state, and correlations between the chemical structure and the resulting thermal properties of the additives should be detected.

Investigation of the self-assembly behavior of the synthesized supramolecular additives

A significant property of this class of additives is that their molecular building blocks are capable of forming supramolecular structures, such as nanofibers, via self-assembly. Therefore, self-assembly experiments in different organic solvents should be performed with all synthesized amide compounds. The solvents used for these investigations are the same as the most typically used solvents for dissolving P3HT. If supramolecular structures can be generated in this way, their enormous surface area can be used both for nucleating P3HT in bulk and in solution.

Selection and investigation of crystallization behavior of different P3HT grades

The different commercially available P3HT grades investigated in this work are to be subjected to a detailed thermal characterization before the nucleation tests with the various additives are carried out. The aim of these investigations is to determine the standard crystallization temperature T_c^0 and the maximum crystallization temperature T_c^{max} of the neat

P3HT grades. In order to reveal structure-property relations the grade with the largest ΔT_c is to be used in the further course of the nucleation investigations. Thereby T_c^{\max} is to be determined by so-called homogeneous self-nucleation. A further examination of the neat P3HT will be isothermal melt annealing. Using this method it is possible, as well as via self-seeding in solution, to generate highly-ordered P3HT spherulites.

Nucleation of P3HT with supramolecular nucleating agents

For the nucleation investigations of P3HT, all thermally suitable additives should be introduced into the P3HT-system in the same concentration. The additives, which prove to be nucleating agents for P3HT, will be used for concentration-dependent investigations. Furthermore, the nucleation efficiency must be determined for all successful additives. The P3HT spherulite sizes with and without nucleating agent are to be determined by polarization microscopic investigations on thin P3HT films. Furthermore, these investigations are intended to observe at which temperature the additives dissolve in the P3HT melt and at which temperature and in which form the additives crystallize upon cooling the melt. In order to confirm the nucleating effect of the additives, isothermal investigations will be performed.

Highly ordered shish-kebab superstructures

Finally, fibrous P3HT nanostructures are to be generated from solution. Such nanostructures have been known in literature for a long time; however, it is still unknown whether such P3HT nanostructures exhibit spatial variations of their structural and electronic properties along the fiber axis, which is important to understand charge and energy transport processes. In order to investigate the structural and electronic properties, long and oriented fibers with a parallel alignment are required. Therefore, the aim is to produce shish kebab like superstructures with a nucleating agent as shish and P3HT fibers as kebabs. Spatially resolved spectroscopy investigations along individual P3HT nanofibers will then be performed on these superstructures in order to preserve the photophysical properties.



3 Self-assembly of bis- and trisamides with pyridine substituents

Well-known classes of supramolecular building blocks are 1,3,5-substituted trisamides and 1,4-substituted bisamides. In particular, the former are well-known to self-assemble into one-dimensional aggregates and in the case of bisamides, also examples are known featuring one preferred crystallization growth. These building blocks are discussed in more detail in the following chapters.

3.1 Versatile building blocks in supramolecular chemistry

Prominent representatives of supramolecular building blocks, which are able to self-assemble into one-dimensional supramolecular structures, are symmetrically substituted bis- and trisamides.^[167–171] The general molecular structure of such compounds is schematically shown in **Figure 26**. The difference between these two supramolecular building blocks regarding their molecular structure is the number of their peripheral substituents. As can be deduced from the notations, trisamides are threefold substituted, while bisamides are twofold substituted.

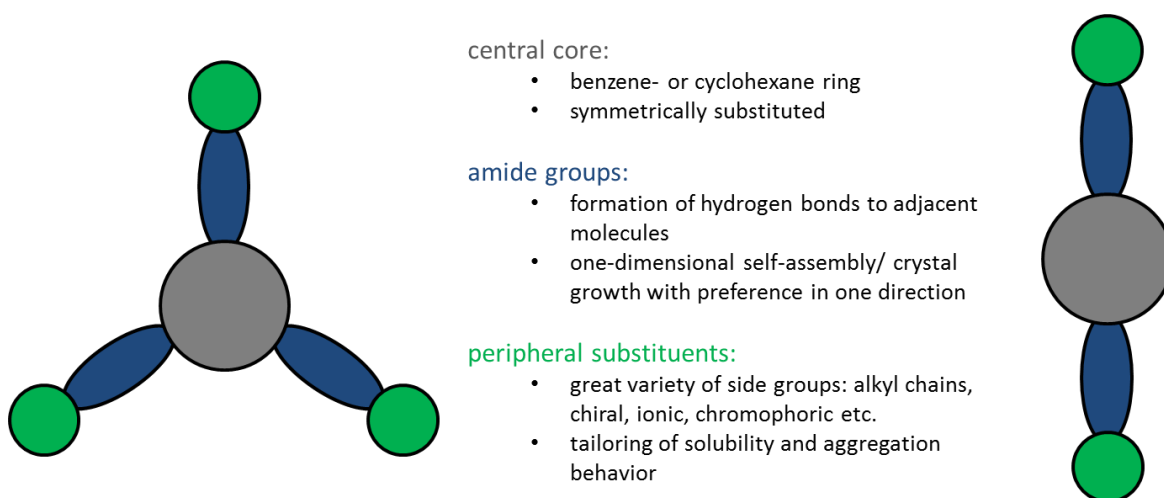


Figure 26: General molecular structure of 1,3,5-trisamides and 1,4-bisamides. The amid-groups (blue) are connected to the central core (grey) either by the carbon-atom of the C=O-bond or by the nitrogen-atom of the NH-bond. The peripheral substituents, which tailoring the solubility and aggregation behavior of the molecule are displayed in green.

The general structure of such compounds can be divided into three structural units: the central core, the symmetrically arranged amide bonds, and the peripheral substituents. The core is predominantly based on a benzene ring or a cyclohexane ring. At this core, the amide groups are attached either over the carbon atom of the C=O group or over the nitrogen atom. In a trisamide molecule, the amide groups are located at the positions 1, 3 and 5 of the central core. For a bisamide molecule, these are located at positions 1 and 4. Typically, the amide groups are capable of forming symmetrical twofold or threefold hydrogen bonds.

Accordingly, they are responsible for the strong complementary intermolecular interactions between adjacent molecules. The peripheral substituents may be simple alkyl chains or may also contain more sophisticated functional groups.^[170] Changes in the core-structure, the amide bond orientation or the periphery can directly influence the self-assembly behavior and the resulting aggregate properties. Replacing a cyclohexane ring with a benzene ring as core has a distinct effect on the thermal properties of the self-assembled structure. Variances in the periphery, on the other hand, have a significant influence on crystallographic order and on the dissolution behavior in polymer melts.^[29,168,169,172,173]

Bis- and trisamides are among the simplest and most versatile motifs of supramolecular chemistry to produce nano-objects. They are straightforward to synthesize and are well suited to investigate the self-assembly process as well as structure-property relationships.^[29,169,170,174] In particular for trisamides, parameters, such as temperature, concentration or pH-value, can lead to pronounced unidirectional growth of the molecules perpendicular to plane of the central core and result into supramolecular columns either in the solid-state, in the liquid crystalline state or in solution.^[169,171,175,176]

The first crystallographic studies on 1,3,5-benzenetrisamides were reported by Lightfoot *et al.*^[168] In their work, they examined the molecule *N,N',N''*-tris(2-methoxyethyl)benzene-1,3,5-tricarboxamide recrystallized from ethanol. This molecule self-assembles into columnar structures and crystallizes in the monoclinic space group $P2_1$. In addition to the strong, threefold hydrogen bonds between adjacent molecules, there are also π - π -interactions between the phenyl units which stabilize the formed aggregates (**Figure 27**).

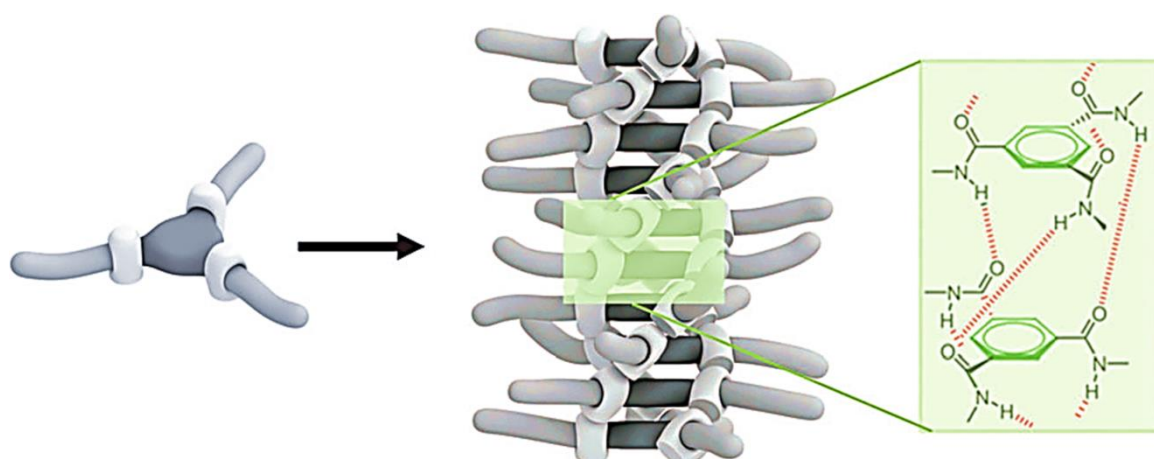


Figure 27: Schematic representation of C-centered benzene-1,3,5-tricarboxamide self-assembly into helical one-dimensional aggregates, which are stabilized by threefold intermolecular H-bonding and π - π -stacking of the phenyl rings.^[170]

During the self-assembly process, the amide groups rotate about 40° from the central plane of the benzene core and form three hydrogen bonds with both the overlying and the

underlying trisamide molecule. The cores of the adjacent disks are rotated relative to one another by 60°. On account of the resulting helical arrangement of the hydrogen bonds, these are strengthened and hold the aggregates together.^[168,177]

Benzene-1,3,5-tricarboxamides with tert-butyl substituents (BTAs) which are able to form columnar structures crystallize in the space group P6₃/m. Three helical bonding patterns can be observed along its columnar axis. Depending on the arrangement of the oxygen atoms in the column, two different configurations can be formed: the up- and the down configuration. In order to decrease the total energy within the supramolecular aggregate, adjacent columns arrange antiparallel in an antiparallel fashion.^[169]

3.1.2 Research fields and applications of bis- and trisamides

Due to the simple synthesis, the robustness of the self-assembly process and the large possibilities to vary the substituents in the periphery and thus to control the properties, bis- and trisamides are an integral part of numerous research and application areas.

It has thus been shown that bis- and trisamides, which bear substituents with appropriate polarity, can act as organo- or hydrogelator.^[176,178–180] Presence of benzoic acid in the periphery of BTAs, for example, yielded in pH-responsive hydrogelators after the self-assembly process. Self-assembled fibers with a very high aspect ratio exhibit bisamides with aliphatic substituents.^[175] Introduced in wide-meshed nonwovens, BTAs are used in filter technology, for example in fine dust filtration.^[181,182] Mechanical investigations via AFM bending experiments on such fibers show the high stability of these fibers (Young's modulus 3 GPa - 5 GPa).^[183,184] BTAs with azobenzene substituents exhibit photo-responsive properties and are therefore suitable for use in holographic data storage media.^[185–187] Furthermore, bis- and trisamides are frequently used as polymer additives. Benzene-1,3,5-tricarboxylic acid-(N-cyclohexyl)-trisamide, i. e. can improve the electret properties of polypropylene by acting as a trap for electrical charges. Therefore, it has potential to serve as an effective additive in electret materials.^[188,189] In addition, additives based on bis- and trisamides are excellent nucleating agents and clarifiers.^[27,29,190] Irgaclear XT 386 was the first commercially available BTA. It reduces the haze and significantly increases the crystallization temperature of isotactic polypropylene. The reason for this is the ideal surface structure of the self-assembled additive.^[169] The additive dissolves upon heating in the polymer melt and recrystallizes upon cooling before the polymer recrystallizes. As a result, epitaxial growth of the polymer is possible on the surface the supramolecular object. Among i-PP, polyvinyl fluoride (PVF),

polybutylene terephthalate (PBT), polylactide (PLA) and polyamides (PA) were successfully nucleated using these kinds or similar kinds of supramolecular additives.^[191,192] These supramolecular building blocks are also used in the field of biomedicine and sensor technology.^[193,194] They are also excellently suited for the coordination of metal ions and thus for catalytic purposes or for the deposition of silver or gold nanoparticles.^[195,196] Very often functionalized bis- and trisamides, especially pyridine-containing molecules are used for this purpose, which are discussed in more detail below.

3.1.3 Functional bis- and trisamides

As already described, the periphery of bisamides (BAs) and trisamides (TAs) has an enormous influence on the resulting crystal structure and properties of these structures. TAs with very short aliphatic substituents form sheet-like aggregates. However, TAs with longer alkyl chains tend to form columnar structures. The introduction of functional groups into the periphery can lead to several different crystalline structures simultaneously.^[169,197]

In the following, therefore, further details on BAs and TAs with functional periphery will be discussed. Very often BAs and TAs are found with amino acid-based substituents. Amino acids are the building blocks of proteins in living organisms. In nature, over 500 different amino acids can be found. However, a human's genetic code directly encodes only 20 of them. Twelve of these 20 amino acids can be found in the literature as substituents on BAs and TAs – predominantly alanine, glycine and cysteine were thereby investigated. For example, Maruyama et al. have extensively studied supramolecular gelators based on benzenetricarboxamides with amino acid methyl ester substituents for ionic liquids.^[178] In their work they deal with the amino acids glycine, L-alanine, L-valine, L-leucine, L-methionine and L-phenylalanine. Gel preparations were performed by preparing solutions consisting of a TA and an ionic liquid, which they then heated up to the temperature where the gelator has completely dissolved in the ionic liquid. Subsequently, the sample is cooled to room temperature, which leads to gel formation due to the fibrous self-assembly of the TA. **Figure 28** shows FE-SEM images of ionogels formed in the ionic liquids 1-butyl-3-methylimidazolium bis(trifluoromethylsulfonyl) amide [BuMelm][TFSA] and 1-butyl-3-methylimidazolium trifluoromethanesulfonate [BuMelm][CF₃SO₃]. As gelator benzene-1,3,5-tricarboxamide with L-valine methyl ester substituents was used in a concentration of 1 wt.-%. All the ionogels studied by Maruyama et al. have reversible thermal transition properties and

viscoelastic properties, which are typical for gels. Furthermore, the ionogels retained the high intrinsic conductivity of the ionic liquids even at high gelator concentrations.

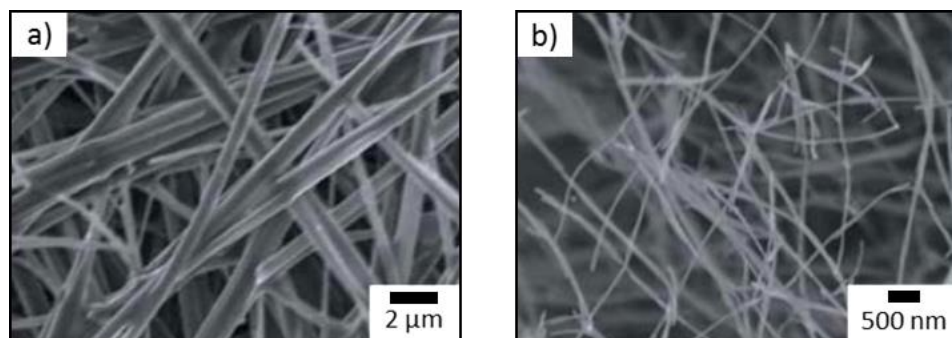


Figure 28: FE-SEM images of ionogels formed of benzene-1,3,5-tricarboxamide with L-valine methyl ester substituents in the ionic liquids (a) 1-butyl-3-methylimidazolium bis(trifluoromethylsulfonyl) amide [BuMelm][TFSA] and (b) 1-butyl-3-methylimidazolium trifluoromethanesulfonate [BuMelm][CF₃SO₃]. The concentration of the gelator in the ionic liquid was 1 wt.-%. For the FE-SEM analysis, the ionic liquid in the ionogel was first replaced with water followed by freeze-drying.^[178]

Haldar et al. studied BTAs with L-methionine and tyrosine substituents. They detected that the methionine derivative self-assembles by means of π - π -stacking and threefold amide-amide hydrogen bonds into one-dimensional nanorods. The tyrosine derivative, on the other hand, develops a porous structure due to lack of C₃-symmetry and triple amide-amide H-bonds. These structural differences entails that the N₂ sorption of the porous material is ten times higher than that of the columnar one.^[198]

Karmakar et al. investigated four functional 1,4-bisamides and one 1,3,5-trisamide, which feature amino acid derivatives in the periphery.^[199] These compounds were prepared by the reaction of terephthaloyl dichloride or benzene-1,3,5-tricarbonyl trichloride with the methyl ester protected amino acids. Alanine, isoleucine, leucine and valine were used as amino acids. All compounds - (2,2'-(terephthaloyl-bis(azanediyl))dipropanoic acid dihydrate (**K1**); 2,2'-(terephthaloylbis-(azanediyl))bis(3-methyl-pentanoic acid) monohydrate (**K2**); 2,2'-(terephthaloylbis-(azanediyl))bis(4-methylpentanoic acid) dihydrate (**K3**); 2,2'-(terephthaloylbis-(azanediyl))bis(3-methylbutanoic acid) dihydrate (**K4**); 2,2',2''-((benzene-1,3,5-tricarbonyl)-tris(azanediyl))-tripropionic acid hemihydrate (**K5**) - were successfully synthesized and characterized and the respective single crystal structures were solved. The compounds **K1** and **K2** form 3D hydrogen-bonded nets, which, however, differ in their final structure. **K1** forms chains via direct hydrogen bond of N-H \cdots O between the terephthalamide derivatives. In **K2**, the hydrogen bond is formed between the carboxylic COH-group and the ketone CO-group and lattice water links the chains together. The compounds **K3** (**Figure 29a**) and **K4** form 2D hydrogen bonded structures. Here all the chain connections between the terephthalamide derivatives are water mediated. **K5** forms hydrogen bonded dimers which

are connected to each other via hydrogen bonds and form a 3D primitive cubic lattice (**pcu**)-net (**Figure 29b**).^[199]

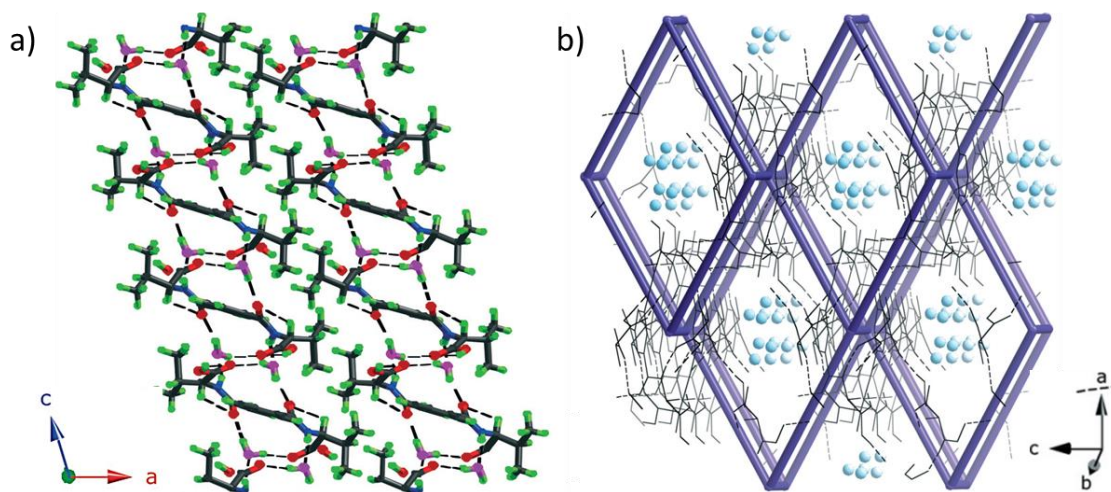


Figure 29: (a) Packing diagram of compound K3; note how the aliphatic groups assemble and are kept separate from the hydrogen bonding parts. (b) The hydrogen bonded pcu-net formed by the dimeric units of compound K5 with disordered water molecules (blue spheres) within the 3x3 Å wide channels.^[199]

Jung et al. reported on a customizable scheme of making use of modular hydrogel templates for controlling the helicity and formation of nanofibers over long distances.^[200] They described self-assembly of BTAs containing both amino acid-containing ligands and BTAs with pyridine-containing substituents. **Figure 30a** shows an overview of the hydrogel formation resulting from controlled assembly of nanofibers with tunable helicity by addition of two different chiral components (trimesoyltri (D-alanine) **Jung 2a**; trimesoyltri (L-alanine) **Jung 2b**) to a previously prepared gelator (benzene-1,3,5-tricarboxylic acid tris([3-([2,2';6',2'']-terpyridin-4'-ylamino)-propyl]-amide) **Jung 1**). A subsequent addition of Au (I) followed by UV exposure generates helically templated gold nanoparticle superstructures (**Figure 30b**) which are high quality, chiroptically active materials. Furthermore, the size of the gold nanoparticles, ranging from 2 nm up to 200 nm, could be easily controlled by the UV irradiation time.^[200]

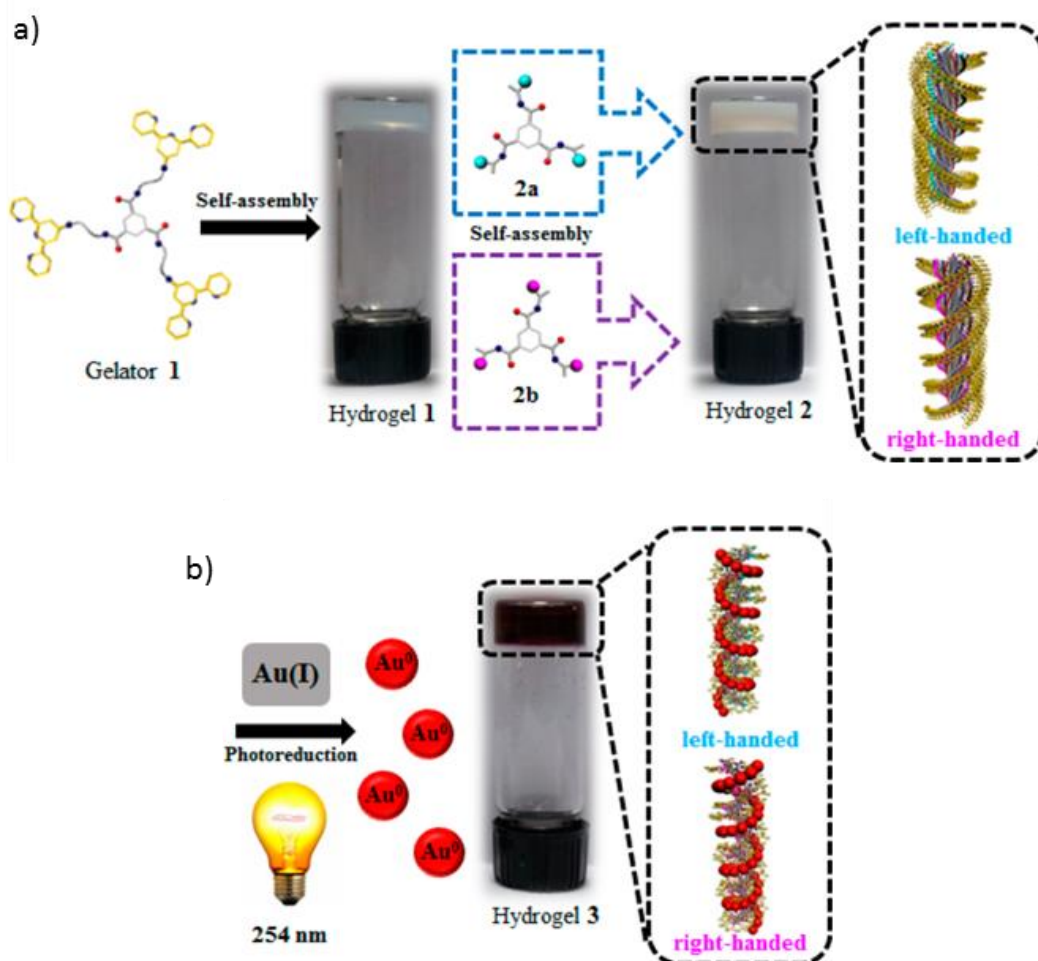


Figure 30: (a) Hydrogel formation resulting from controlled assembly of nanofibers with tunable helicity by addition of chiral Jung 2a or Jung 2b components to gelator Jung 1. (b) Subsequent addition of Au(I) followed by UV exposure to generate helically templated gold nanoparticle superstructures.^[200]

In the following, only the TAs and BAs with pyridine-containing substituents are considered, which were also investigated in this work.

The trisamide N^1, N^3, N^5 -tris(pyridine-4-yl)benzene-1,3,5-tricarboxamide (hereinafter **TA 1**) was first mentioned by Kumar et al. in 2004.^[201] Their studies showed that the trisamide, which is insoluble in water, is soluble in aqueous organic mixtures, such as DMSO, DMF, MeOH, EtOH, at higher temperatures. Upon cooling, the trisamide self assembles in fibrous structures resulting in hydrogelators. The single-crystal structure elucidation demonstrated a porous architecture with hydrophobic cavities, which is why this trisamide can also be used as a inclusion host.^[201] Biradha et al. could furthermore show that the single-crystal structure of **TA 1** depends on the solvent in which the trisamide is recrystallized.^[202] Luo et al. prepared with **TA 1** by self-assembly processes in $\text{CHCl}_3/\text{MeOH}$ hydrogen-bonded organic frameworks (HOFs). The trisamide forms thereby two-dimensional honeycomb structures by hydrogen bonding between the amide groups and the 4-pyridine rings. These honeycomb structures

superimpose and create π - π -interactions between the layers. These π - π -interactions hold the hierarchical structure together. The resulting pores have a size of about $6.8 \times 4.5 \text{ \AA}$ and showed are very good CO_2 adsorption.^[203] This trisamide is also used for the formation of porous metal organic frameworks (MOFs). The group of Lah was able to show that **TA 1** forms in combination with copper(II) ions, a unprecedented twofold interpenetrating (3,4)-connected 3D metal organic framework. Here the trisamide serves as a trigonal three-connection node and the copper ion as a square planar four-connection node.^[204] Tzeng et al. also used the C_3 -symmetry of **TA 1** to coordinate Cd(II), Zn(II) and Cu(II) ions. The tripyridinyl trisamide moieties are located inside the open channels. These channels have a diameter of about 7.5 \AA and are filled with chloride counter anions of the salts.^[205,206] Zhao et al. developed with **TA 1** positively charged metal organic frameworks (P-MOFs), which are able to selectively trap anions and therefore can be used in ion chromatography or drug delivery. Besides, these cationic networks showed a very high CO_2 and C_2H_2 uptake capacity.^[207] The work of Zhong et al. showed that not necessarily an organic co-solvent is needed to dissolve **TA 1** in water, but that the addition of Fe(III)/Fe(II) ions at elevated temperature is sufficient. However, the addition of other metal ions, such as Cu^{2+} , Co^{2+} , Ni^{2+} , K^+ , Na^+ and Mg^{2+} , did not alter the insolubility in water, even at elevated temperature. Upon cooling, **TA 1** self assembles and forms fibrous aggregates with the Fe ions through metal-ligand interactions and intermolecular hydrogen bonding (**Figure 31**). The resulting metallogels possesses good mechanical properties and thermoreversibility.^[208]

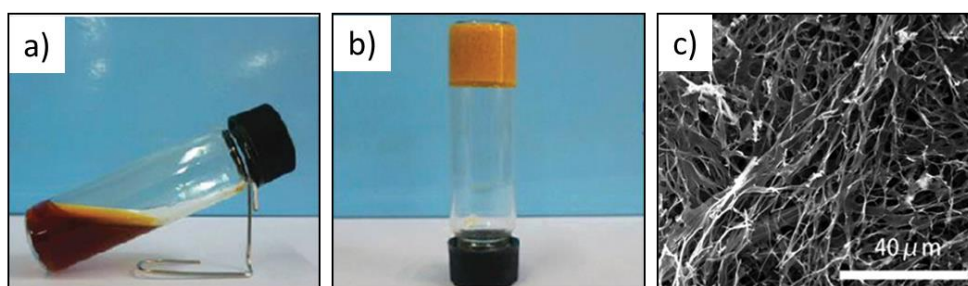


Figure 31: Photographs of **TA 1** with Fe(III) ions in water at elevated temperature (a) and at room temperature (b). SEM image of the xerogel from Fe(III)-**TA 1** metallogel(c).^[208]

The trisamide N^1, N^3, N^5 -tri(pyridin-4-yl)cyclohexane-1,3,5-tricarboxamide (hereinafter **TA 3**) was investigated by the Lee group for its ability to form metallogels.^[209] In their work they were able to show that the cyclohexane-based ligand **TA 3** forms in the presence of transition metal ions, particularly Cd^{2+} and Zn^{2+} supramolecular metallogels. The trisamide can also be gelled in the presence of cadmium counter ions such as SO_4^- , ClO_4^- and NO_3^- . **Figure 32a** shows photographs of the gelation experiments. No gel formation occurred upon the addition of Co^{2+} , Cu^{2+} , Ni^{2+} and Mn^{2+} (**Figure 32a 3-6**). In addition **TA 3** could also not gelate when the

cadmium counter ion was Cl^- , Br^- or I^- . X-ray analysis revealed that the trisamide ligand forms a coordination polymer structure based on the octahedral Cd^{2+} center. **Figure 32b** shows a TEM-image of such a Cd^{2+} -**TA 3** coordination polymer gel. The resulting fibrous structures have a diameter of 20-50 nm. Further investigations have shown that the rheological properties of the gel depend strongly on the concentration of Cd^{2+} ions. Furthermore, the xerogels can act as catalysts in the Knoevenagel condensation reaction.^[209]

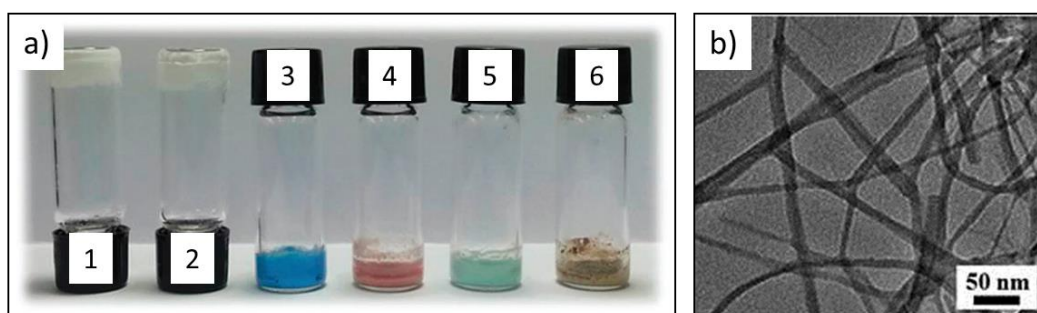


Figure 32: (a) Photographs of the trisamide **TA 3** with (1) CdSO_4 , (2) ZnSO_4 , (3) CuSO_4 , (4) CoSO_4 , (5) NiSO_4 and (6) MnSO_4 in H_2O . (b) TEM image of the coordination polymer gel Cd^{2+} -**TA 3**.^[209]

In the work of Jung et al. the trisamide **TA 3** was used to demonstrate that helical silica nanotubes can be encapsulated with reduced graphene oxide (rGO) to provide a hybrid material capable of the chiral transcription of organic components onto its surface.^[210]

Gong et al. used the trisamide $\text{N}^1, \text{N}^3, \text{N}^5$ -tri(pyridin-3-yl)cyclohexane-1,3,5-tricarboxamide (hereinafter **TA 6**) as a building block for the development of a tripodal fluorescent chemosensor. This chemosensor has amidepyridinium moieties as the key binding site and anthracene moieties as the sensing subunit and is thus able to bind H_2PO_4^- in polar organic solvents. The excellent binding of H_2PO_4^- is due to the synergy of several different interactions, such as electrostatic interactions, hydrogen bonding, as well as the dynamic conformational change via formation of unique binding-induced excimer.^[211]

The bisamide N^1, N^4 -di(pyridin-4-yl)terephthalamide (hereinafter **BA 1**) has been reported by Lin et al. concerning its co-assembly behavior with chiral compounds. Therefore, they selected phenylalanine-based enantiomers (right-handed **DPF** and lefthanded **LPF**) as basic units for constructing supramolecular chiral nanostructures and two achiral bis(pyridinyl) derivatives to regulate the chirality of the nanostructures. The handedness of the nanostructures could be inverted simply by exchanging the achiral molecule. **Figure 33a** schematically shows the helical inversion of the nanostructure based on the structural formulas of the enantiomeric gelators (**LPF**, **DPF**) and the achiral bis(pyridinyl) derivatives **BPy1** and **BA 1**. M and P denote left- and right-handed twisted nanofibers, respectively. The

measured SEM images of the xerogels of the right-handed (DPF-BPy1) and left-handed (DPF-BA 1) helical fibers are shown in **Figure 33b** and **c**.^[176]

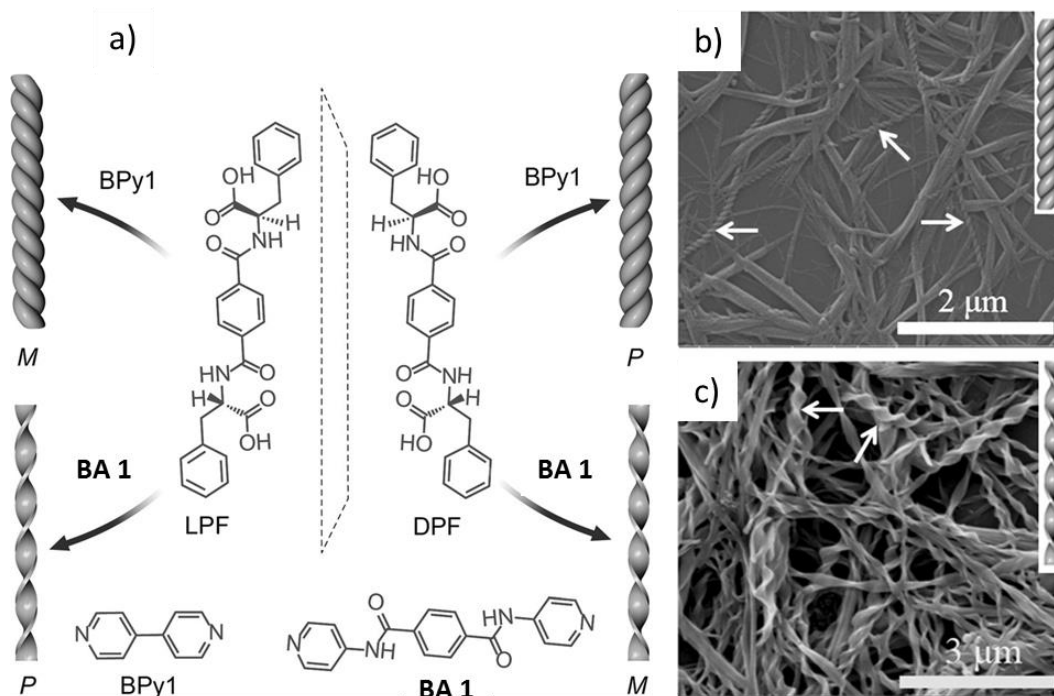


Figure 33: Scheme of the helical inversion of the nanofibers (a). SEM-images of the right-handed (DPF-BPy1) (b) and the left-handed (DPF-BA 1) (c) helical nanofibers.^[176]

Furthermore, a variety of current research reports on the use of **BA 1** in organometallic coordination polymers. Thereby a lot of different transition metal ions, such as Zn^{2+} , Co^{2+} , Cd^{2+} or Cu^{2+} , are used as the complex center and predominantly carboxylic acid derivatives as co-ligands. Depending on the metal ion and co-ligands used, a wide variety of complex structures can be observed. These structures vary from linear chains to 3D porous networks. For most of these compounds, high CO_2 adsorption can be measured, making them suitable for CO_2 capture and separation applications.^{212–218}

Biradha et al. attempted in their work to solve the crystal structure of both neat **BA 1** and the neat bisamide *N,N'*-(1,4-phenylene)diisonicotinamide (hereinafter **BA 2**). However, this was unsuccessful for both bisamides.^[219,220] The group of Safarifard also investigated in their work both bisamides **BA 1** and **BA 2** but as component of an organometallic frameworks. As transition metal ions, they used Zn^{2+} and 4,4-oxibisbenzoic acid (oba) as co-ligand. With these building blocks they synthesized the complexes $[Zn_2(oba)_2(BA\ 4a)] \cdot (DMF)_3$ (**Biradha 1**) and $[Zn_2(oba)_2(BA\ 4b)] \cdot (DMF)_5$ (**Biradha 2**). X-ray crystallography revealed that the complex **Biradha 1** crystallizes in the monoclinic space group $P2_1/n$ and **Biradha 2** in the space group $P2_1/c$. The neutral 3D MOFs are formed by threefold interpenetrated $\{Zn(oba)\}$ layers

connected through the N,N'-pillar bisamide ligands (**Figure 34**). Although both compounds are threefold interpenetrated, they still possess apparent 1D pore channels, which are filled with disordered guest solvent molecules. Furthermore, CO₂ adsorption studies revealed that **Biradha 1** has a significantly higher CO₂ uptake than **Biradha 2**.^[221]

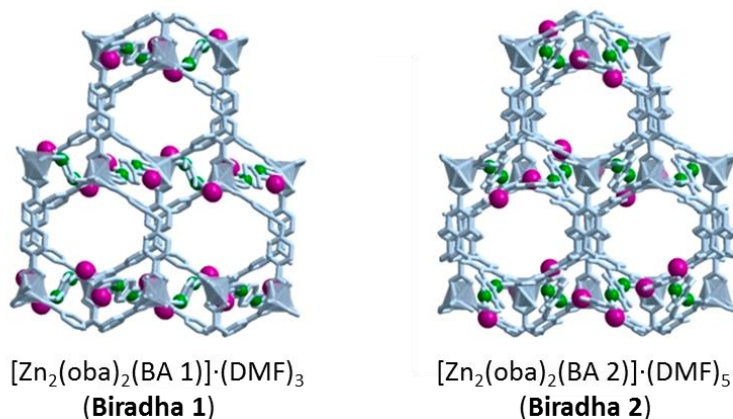


Figure 34: View of the pore channels of $[\text{Zn}_2(\text{oba})_2(\text{BA } 1)] \cdot (\text{DMF})_3$ (left) and $[\text{Zn}_2(\text{oba})_2(\text{BA } 2)] \cdot (\text{DMF})_5$ (right) highlighting the acylamide groups. Color code: N (green), O (purple).^[221]

Overall, a very large number of transition metal ions have been investigated in recent years in combination with the bisamide ligand **BA 2** in organometallic coordination polymers. The transition metal ions analyzed include Cd, Co and Ni^[222–224], Pd and Pt^[225], Cu^[223,226–229], Ag^[196,230,231], Hg^[232], Nd^[233] and Rh^[234,235].

The only scientific report about the bisamide N¹,N⁴-di(pyridin-4-yl)cyclohexane-1,4-dicarboxamide (hereinafter **BA 3**) was published by Wu et al. In their work, they describe the synthesis of **BA 3**, as well as its crystal structure and the photoluminescence properties. **BA 3** crystallizes in the monoclinic space group $P2_1/n$ and exhibits a *trans* conformation in which the pyridyl rings are parallel to each other. **Figure 35** shows the three-dimensional supramolecular structure. The emission spectrum of **BA 3**, measured in the solid state at room temperature, shows an emission peak at 461 nm upon an excitation of 360 nm. This emission peak may be attributed to the intra-ligand electron transitions.^[236]

Huang et al. report that the bisamide N¹,N⁴-di(pyridin-3-yl)cyclohexane-1,4-dicarboxamide (hereinafter **BA 6**) in combination with Cd²⁺ ions and 1,4-naphthalenedicarboxylic acid forms a 4-connected bimodal Moganite net with threefold interpenetration. Each Cd²⁺ ion is five-coordinated in a pyramidal geometry, three times with the oxygen atoms of two 1,4-naphthalenedicarboxylic acid ligands, once with the nitrogen atom of the pyridine ring of the **BA 6** and once with an oxygen atom of the amide bond of another **BA 6**. Accordingly, Cd²⁺ links with two bisamides and two 1,4-naphthalenedicarboxylic acid molecules.

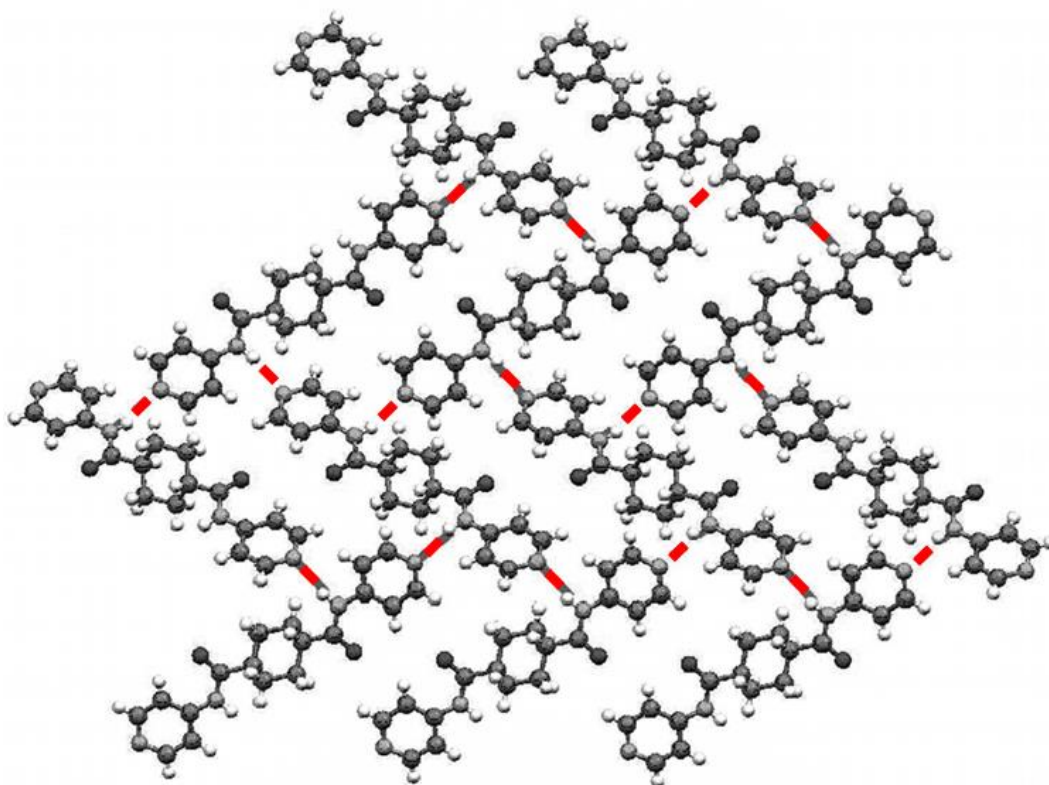


Figure 35: Crystal structure of BA 3. Strong intermolecular N-H...N hydrogen bonds indicated by red lines in the structure.^[236]

Each bisamide ligand links four Cd^{2+} ions. The fact that one bisamide molecule makes use of the nitrogen atoms of the pyridine rings to link the cadmium is common in literature. However, the fact that the two oxygen atoms of the amide groups are also used for the coordination has not been observed before. The schematic representation of the coordination mode of one, as well as between two bisamide ligands is shown in **Figure 36**.^[237]

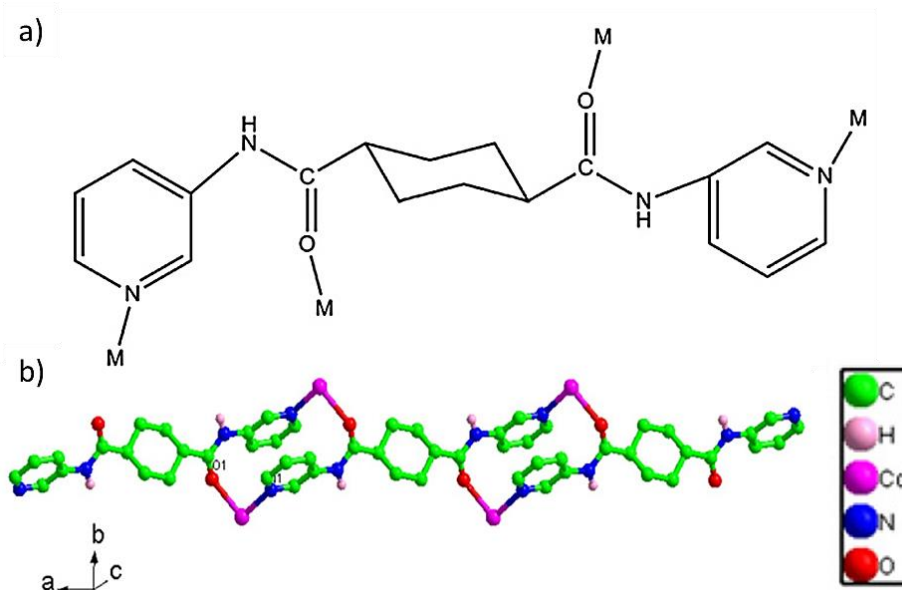


Figure 36: Schematic description of the fourfold connection mode of one bisamide ligand BA 6 (a) and between two bisamide ligands BA 6 and Cd^{2+} ions (b).^[237]

Wang et al. also investigated **BA 6** regarding the formation of coordination polymers with transition metals. In their work, they varied both the transition metals and the co-ligands and investigated the resulting structures. Cobalt and copper were used as ions, various aromatic polycarboxylic acids as co-ligands. The semi-rigid bis-pyridyl-bisamide ligand **BA 6** was always the major ligand in all compounds tested. They were able to show that the coordination polymers structure changes from 1D-chains to 3D-frameworks depending on the inserted carboxylic acid. Furthermore, fluorescence measurements and cyclic voltammetry studies have shown that these complexes are good candidates for potential applications in fluorescent and electrochemical fields.^[238] Further studies of transition metal coordination complexes with different transition metal ions, such as cadmium or zinc, and **BA 6** as ligands have been reported by Lin et al.^[239,240]

3.2 Selection, synthesis and self-assembly of pyridine-containing trisamides

In the following, the pyridine-containing trisamides investigated in this work are introduced, characterized as well as the results regarding their self-assembly behavior in organic solvents are described.

3.2.1 Trisamide selection and their structural variation

Figure 37 shows the six different pyridine-containing trisamides (TA) studied in this thesis. The TA can be divided into three groups. The first group includes benzene trisamides (BTAs) with 4-pyridine moieties. These include **TA 1** and **TA 2**. Both have a benzene core and differ only in the linkage of their amide bonds. Thus, the central core of **TA 1** is based on benzene-1,3,5-tricarboxylic acid, whereas **TA 2** is based on 1,3,5-triamino-benzene.

The second group includes cyclohexane trisamides (CTAs) with 4-pyridine moieties. These include **TA 3** and **TA 4**. Both have a cyclohexane core and differ only in the linkage of their amide bonds. The basic building blocks for these two trisamides are cyclohexane-1,3,5-tricarboxylic acid (**TA 3**) and cis, cis-cyclohexane-1,3,5-triamine (**TA 4**).

The third group includes cyclohexane trisamides (CTAs) with 2- and 3-pyridine moieties. These include **TA 5** and **TA 6**. Both trisamides are based on the same basic core, cyclohexane-1,3,5-tricarboxylic acid, as used for **TA 3**. Therefore, the difference is in the peripheral substituents. These are three symmetrically arranged 2-pyridine groups for **TA 5**, and three 3-pyridine groups at **TA 6**, respectively.

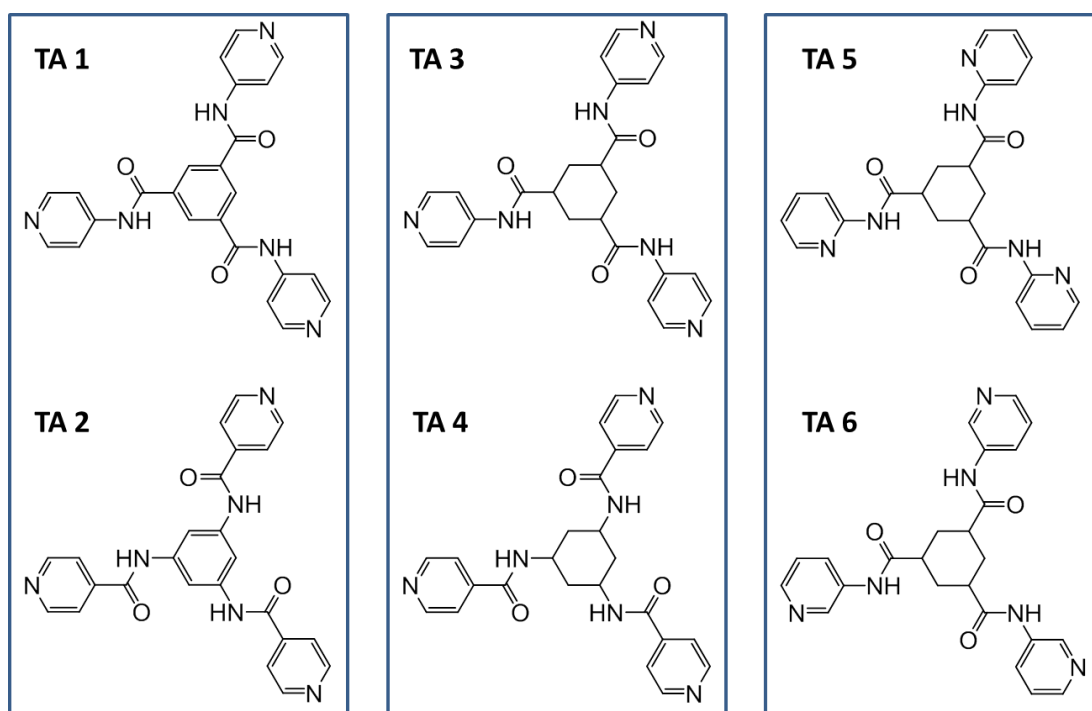


Figure 37: Chemical structures of the six investigated pyridine-containing trisamides in this work. The first group includes benzene trisamides with 4-pyridine moieties (left box), the second group includes cyclohexane trisamides with 4-pyridine moieties (central box) and the third group includes cyclohexane trisamides with 2- and 3-pyridine moieties (right box).

Solely three of these six pyridine-containing trisamides are already known in literature. These are **TA 1**, **TA 3** and **TA 6** (see **Chapter 3.1.3**).

3.2.2 Trisamide synthesis

The syntheses of the individual supramolecular molecules were carried out by the technicians J. Failner, S. Ganzleben, D. Hanft and R. Schneider under my guidance. The following thermal and analytical characterizations were accomplished by my self.

In general, the trisamides were obtained by an amidation reaction between an acid chloride and the respective amine derivative. For all syntheses, the component, which is to be attached to the central core, was present in slight excess during the reaction. This enables a complete threefold substitution at the core. Since both the core and the substituents vary, a generally valid, clear reaction scheme is hardly possible. Therefore, exemplarily the reaction scheme for the synthesis of **TA 1** is described below. All further syntheses of the selected trisamides are described in detail in the **Experimental 7.2**.

Figure 38 shows the reaction scheme of benzene-1,3,5-tricarbonyl trichloride with 4-aminopyridine yielding N^1, N^3, N^5 -tri(pyridin-4-yl)benzene-1,3,5-tricarboxamide (**TA 1**). Initially, 4-aminopyridine and TEA are mixed together with 80 mL of dried THF in a Schlenk flask. The acid chloride is then added under inert gas (N_2) and ice cooling. The reaction time amounts to

120 hours at reflux. After cooling the suspension to room temperature the white precipitate obtained is filtered off, washed in a mixture of THF/H₂O/Acetone and dried under high vacuum. The crude product was then recrystallized in DMF/Acetone; filtered off and dried to yield white crystals.

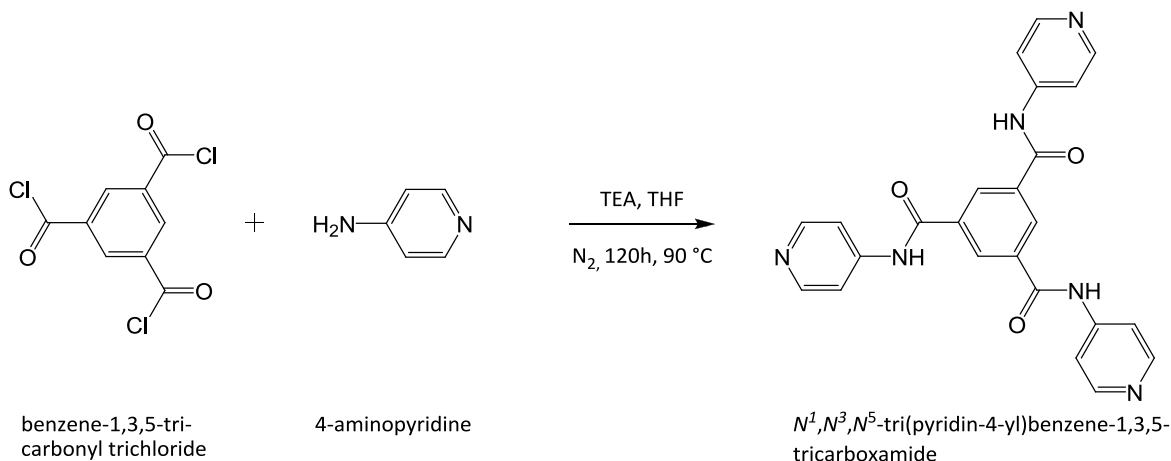


Figure 38: Synthesis of TA 1 via the reaction of benzene-1,3,5-tricarbonyl trichloride with 4-aminopyridine.

Table 1 lists the individual components for the respective trisamide syntheses of the trisamides, the solvent system for recrystallization as well as the yields after crystallization.

Table 1: Individual building blocks for the respective syntheses of the six different trisamides (TA 1-6), the solvent systems in which recrystallization occurs and the yields obtained after synthesis.

TA	Core	Substituent	Recrystallized from	Yield [%]
1	benzene-1,3,5-tricarbonyl trichloride	4-aminopyridine	DMF/acetone	29
2	benzene-1,3,5-triamine	isonicotinoyl chloride hydrochloride	DMF/H ₂ O	46
3	cyclohexane-1,3,5-tri-carbonyl trichloride	4-aminopyridine	DMF	24
4	cyclohexane-1,3,5-tri-amine hydrobromide	isonicotinoyl chloride hydrochloride	MeOH	73
5	cyclohexane-1,3,5-tri-carbonyl trichloride	2-aminopyridine	MeOH	10
6	cyclohexane-1,3,5-tri-carbonyl trichloride	3-aminopyridin	H ₂ O	51

The variation of the core and substituent building blocks can be seen from **Table 1**. Merely the trisamides **TA 1**, **TA 5** and **TA 6** have the same core, with different substituents. The solvents used for the recrystallization of the trisamides were predominantly DMF and methanol-containing systems. Only for **TA 6**, pure H₂O was used for the recrystallization of the trisamide after reaction. Solely with the trisamides **TA 2**, **TA 4** and **TA 6** relatively high yields could be achieved.

3.2.3 Analytical characterization

After synthesis, the individual compounds were analyzed by common methods such as $^1\text{H-NMR}$ spectroscopy, mass spectrometry and infrared spectroscopy to prove product formation and product purity.

Figure 39 shows exemplarily the $^1\text{H-NMR}$ spectrum of **TA 1**. All signals can be clearly assigned to the corresponding hydrogen atoms. The chemical shifts are considered in more detail below. The singlet at a shift of 8.76 ppm corresponds to the aromatic protons of the core (**1**). The location of the chemical shift as well as the formation of a singlet is common to this type of aromatic proton in a trisamide.

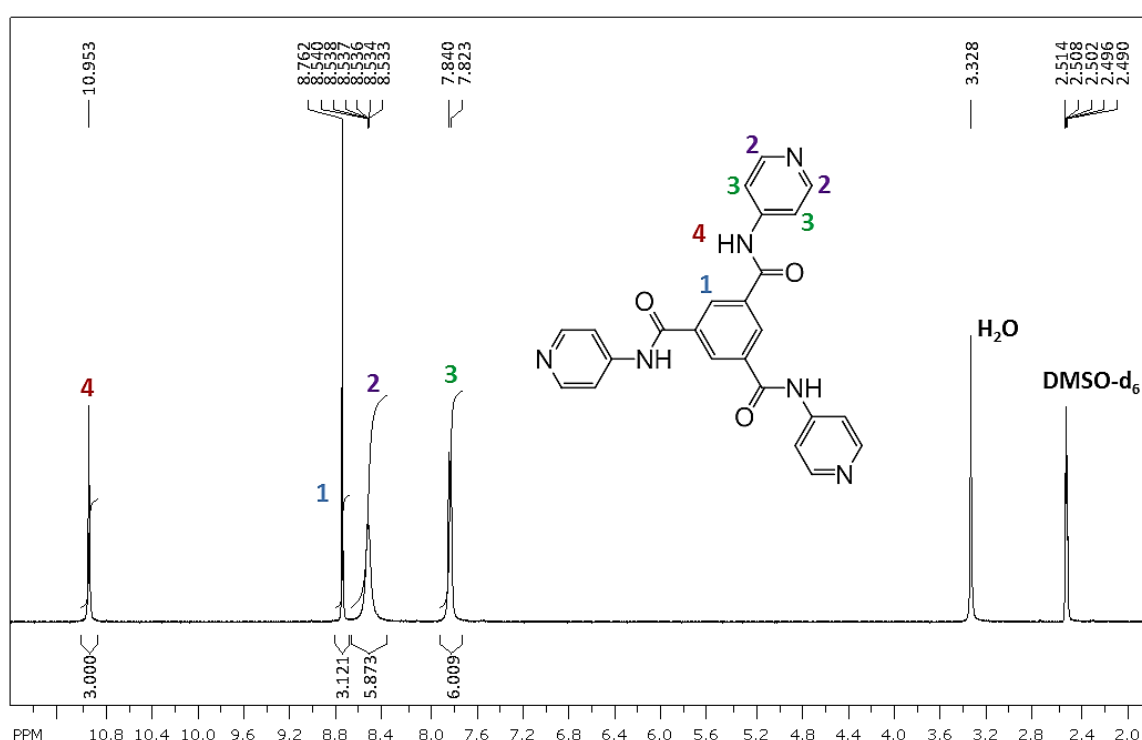


Figure 39: $^1\text{H-NMR}$ spectrum of **TA 1** in DMSO recorded with a 300 MHz NMR spectrometer (Bruker). The chemical structure of the expected trisamide is inserted into the spectrum and the signals obtained were assigned to the corresponding hydrogen atoms.

The four aromatic protons of the substituent show a doublet at 7.83 ppm (**3**) and a multiplet at a chemical shift of 8.53 ppm (**2**). The two protons in the immediate adjacency of the nitrogen atom of the substituent show a higher chemical shift than the two protons which are adjacent to the amide bond. The singlet at a chemical shift of 10.95 ppm can be attributed to the amide protons (**4**). The remaining two signals in the $^1\text{H-NMR}$ spectrum (2.50 ppm, 3.33 ppm) belong to the deuterated DMSO- d_6 , which served as solvent and water. If one considers the integrals of the individual signals, their ratio agrees well with the respective number of protons. By means of this analysis method it could be confirmed that this and all

the other desired trisamides were successfully synthesized. The $^1\text{H-NMR}$ spectra of the remaining trisamides are shown in **Appendix 8.1** along with the detailed assignment of the individual protons. No significant signals that indicate impurities were observed.

In addition, mass spectra were recorded on a FINNIGAN MAT 8500 spectrometer from Thermo Fisher Scientific using electron spray ionization (ESI) to characterize the trisamides. **Figure 40** shows exemplarily the mass spectrum of **TA 1**. First, the mass of the analyte has to be determined. Normally this is the mass of compound **TA 1**. In the case of electron ionization, a large fraction of ions are often cleaved. Therefore, the chemical structures of the fragments occurring during the measurement are additionally included in **Figure 40**. In the case of **TA 1**, a mass of 438 g mol^{-1} was detected, which conforms to the theoretical mass. The other signals represent fragments of the **TA 1**. In addition to a bare core, one- and two-armed molecules can also be observed which have been caused by the high electron energy used for the electron spray ionization.

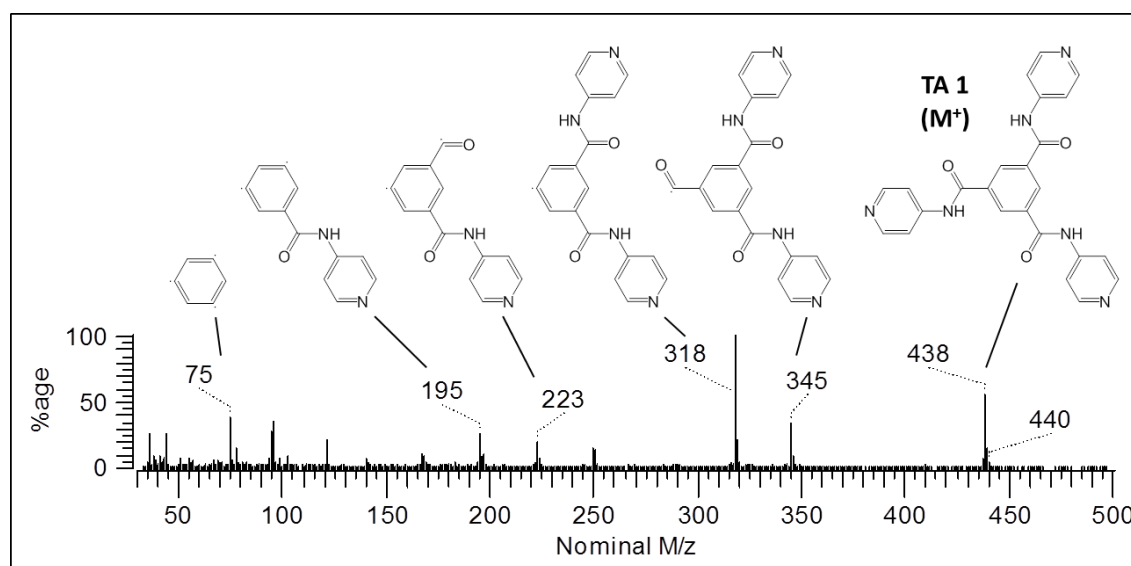


Figure 40: Determined mass spectrum of **TA 1**. The chemical structures of **TA 1** and the fragments, occurring during the measurement, are inserted to explain all main peaks.

The mass spectra of the remaining trisamides are shown in **Appendix 8.2**. For all compounds the theoretical masses could be confirmed by this method.

Fourier-transform infrared spectroscopy (FT-IR) was used as a third and last analytical method to characterize the trisamides. The IR spectra were recorded with a Perkin Elmer Spectrum 100 FT-IR spectrometer in a range of 4000 cm^{-1} to 650 cm^{-1} .

Figure 41 shows the recorded spectrum of **TA 1** and highlights the strongest vibrational signals. Of great importance are, in particular, the NH stretching vibration (Amid A), the CO

stretching vibration (Amide I) and the NH bending or CN stretching vibrations (Amide II). The CO stretching vibration at 1683 cm^{-1} suggests that the amidation reaction was successful. The Amide II vibration can be detected at 1589 cm^{-1} . An NH stretching vibration, which usually can be found at a wave number of about 3240 cm^{-1} , is not present for **TA 1**. Accordingly, it can be assumed that a structural supposition by FT-IR spectroscopy about pyridine-containing trisamides is not sufficient with regard to their self-assembly behavior. The FT-IR spectra of the remaining trisamides are shown in **Appendix 8.3**.

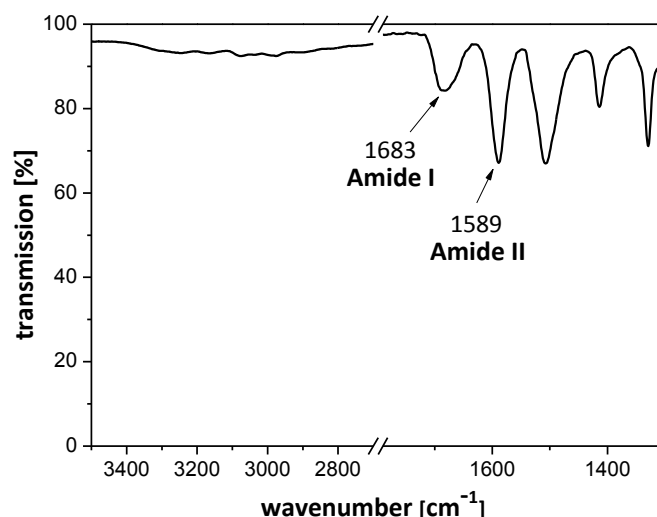


Figure 41: FT-IR spectrum of TA 1 recorded with a Perkin Elmer Spectrum 100 FT-IR spectrometer in the range of 3500 cm^{-1} to 1400 cm^{-1} .

3.2.4 Thermal characterization

The knowledge of the thermal properties of materials is always decisive, because it determines their use as additives at high temperatures, where solid nanostructures are required. Therefore the following section deals with the thermal characterization of the pyridine-containing trisamides. The investigations include thermogravimetric analyses (TGA), simultaneous differential thermal analyses (SDTA) and melting point measurements.

The TGA/SDTA measurements were performed on a Mettler Toledo TGA/SDTA 851e. Data were recorded with a heating rate of $10\text{ K}\cdot\text{min}^{-1}$ in a temperature range from 30 °C to 700 °C under nitrogen atmosphere. On the basis of the TGA measurements it is possible to determine up to which temperature the trisamides are thermally stable. In addition to the mass loss as a function of the temperature, the heat flow was also recorded by means of a simultaneous differential thermal analysis (SDTA). **Figure 42** shows exemplarily the recorded thermogram of **TA 1**. The remaining TGA/SDTA thermograms are shown in the **Appendix 8.4**.

The **Figure 42** reveals that **TA 1** is thermally stable up to almost 350 °C. A five percent mass loss occurs at a temperature of 379 °C. Subsequently, **TA 1** decomposes quickly. A residue content of 30 % at 700 °C indicates no or less pronounced sublimation. The simultaneously recorded heat flow shows a broad melting range with a local maximum at 379 °C. This indicates that **TA 1** decomposes directly during its melting.

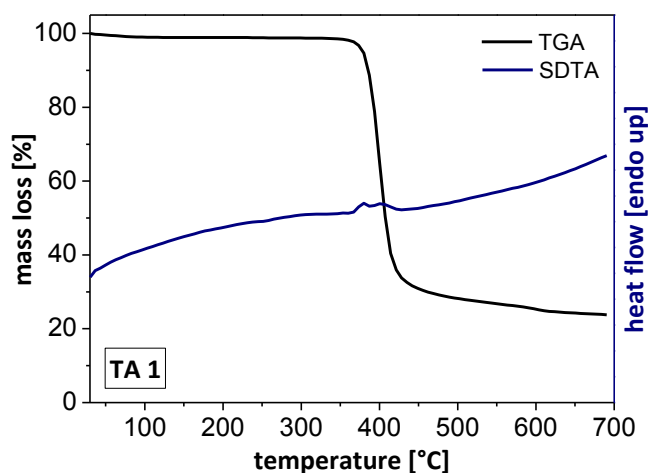


Figure 42: Thermograms of the thermogravimetric analysis (black line) and the SDTA (blue line) of N^1, N^3, N^5 tri(pyridin-4-yl)benzene-1,3,5-tricarboxamide (**TA 1**). Data were recorded with a heating rate of $10 \text{ K}\cdot\text{min}^{-1}$ in a temperature range from 30 °C to 700 °C under nitrogen atmosphere.

In **Table 2** the results of the TGA/SDTA measurements are summarized. The two additives **TA 2** and **TA 4**, which both have an amine-based core, are thermally most stable in comparison to the remaining trisamides with based on a carboxylic acid core. **TA 2** and **TA 4** show a five percent mass loss at a temperature of about 430 °C. However, the mass loss of **TA 4** is almost 100 % at 700 °C, while **TA 2** still has a residual residue content of 40 % at 700 °C. Accordingly, the benzene core is significantly more temperature-stable than the cyclohexane core. This assumption is confirmed by the results of the remaining trisamides.

Table 2: Summarized results of the TGA/SDTA measurements and the melting point determinations (MP90) of all six different trisamides.

TA	$T_{5\% \text{ mass loss}}$ [°C]	residue at 700 °C [%]	T_m (SDTA) [°C]	T_m (MP90) [°C]
TA 1	379	76	379	381.2
TA 2	432	62	448	> 400
TA 3	329	91	345	335.4
TA 4	426	99	421	> 400
TA 5	287	95	284	280.1
TA 6	377	92	393	380.2

Comparing **TA 1** and **TA 2** with each other, it can be seen that, as already mentioned, the trisamide based on 1,3,5-triamino benzene shows a higher melting temperature. This is also the case for the cyclohexane-based trisamides **TA 3** and **TA 4**. The lowest thermal stability shows **TA 5**, which already has a 5 % mass loss at 287 °C. The reason for this much lower thermal stability is most likely because the hydrogen atoms of the amide groups can interact with the lone pairs of the adjacent nitrogen atoms of the pyridine substituents, which significantly decreases the amide bond strength. Such intramolecular interactions are structurally not possible for the remaining trisamides.

The melting point measurements were performed on a melting point system MP 90 from Mettler Toledo. This system measures the turbidity of the material in the measuring tube. If haze is no longer present, this is an indication of a present isotropic melt of the material. Data were recorded with a heating rate of 10 K min⁻¹ in a temperature range from 30 °C to 400 °C. The results are given as an average value of three measurements and are summarized in **Table 2**. It can be seen that the two trisamides **TA 2** and **TA 4**, which are the only ones based on an amine core, have the highest melting temperatures. Since the temperature limit of the measuring device amounts to 400 °C, however, the values cannot exactly be determined and the two trisamides are therefore not comparable with one another. Comparing the trisamides **TA 1** and **TA 3**, which both have an acid-based nucleus and a 4-pyridine substituent with one another, it can be seen that **TA 1** (benzene-core) has a melting point 50 °C higher than **TA 3** (cyclohexane-core). Furthermore, the trisamides **TA 3**, **TA 5** and **TA 6** can also be compared with one another in terms of their melting temperatures. All of these TA's have acid-based cyclohexane cores and differ only in regard to their substituents. **TA 6**, with the 3-pyridine substituents, has the highest melting temperature at 380 °C. The lowest melting point is measured for **TA 5** (2-pyridin substituent). This has merely a value of 280 °C. Accordingly, a small difference in the structure of the substituent has a large effect on the thermal properties of these trisamides. The observed melting points determined with the MP90 system match well with the data from the previous SDTA measurements.

On the basis of the thermal results of the pyridine-containing trisamides, it can be seen that five of the six compounds are suitable for the subsequent P3HT nucleation studies in bulk. Only **TA 5** cannot be used for these investigations, since for these tests temperatures of 300 °C will be required. The **TA 5**, however, begins to decompose during melting at a temperature of 200 °C.

Before the P3HT nucleation experiments are detailed, a comprehensive characterization with regard to the self-assembly behavior of all six trisamides in organic solvents is described.

3.2.5 Self-assembly investigations of trisamides in organic solvents

A major goal of this work is the formation of supramolecular nanoobjects via self-assembly. As already mentioned in **Chapter 1.1.2**, both internal and external factors can initiate and control the self-assembly process. These include, for example, changes in molecular structure, temperature, concentration and pH-value. In addition, the used medium is also crucial. Owing to the importance of a high mobility of the building blocks, self-assembly processes often proceed conveniently in liquid media. The molecular structure, in particular of the periphery, can thereby have a significant influence on the solubility of the trisamide and therefore on the self-assembled structure.^[71–76]

In the following, the self-assembly investigations of the pyridine-containing trisamides (**TA 1-6**) in organic solvents, more precisely in chlorobenzene (CB) and ortho-dichlorobenzene (o-DCB), are described in detail. These halogenated aromatics were selected because they were also used to process P3HT from solution.

Self-assembly from solution was chosen to finally get an insight of the resulting nanoobject morphology via SEM. The underlying steps of the self-assembly process upon cooling can be schematically represented in a phase diagram of the additive concentration versus the temperature as shown in **Figure 43**. In such a phase diagram three regimes can be distinguished. At low to moderate concentrations the building blocks can be molecular dissolved at moderate to high temperatures (**I**). Upon cooling the self-assembly regime is entered (**II**). For high concentrations the building blocks cannot be completely dissolved till the boiling point of the solvent (**III**), however, upon cooling partial self-assembly may take place when entering regime **II**. The blue dots in **Figure 43** represent the solvent molecules; the red fibers as well as the red dots describe the trisamide in crystallized and dissolved state. In step **A**, the trisamide molecules are completely dissolved in the solvent at an elevated temperature. Here, a closed system is present so that an evaporation of the solvent is prevented. Thus the concentration of the system remains constant both during heating and cooling. Upon cooling of the sample (step **B**), the temperature change leads to a supersaturation of the system. As a result, the formation of supramolecular fibers or other supramolecular structures (e.g., sheets) occurs. After the cooling process is completed, the solvent is allowed to evaporate under ambient conditions (step **C**). In this way it is possible to

separate the generated trisamide structures from the solvent and to analyze the morphologies by means of microscopic investigations.

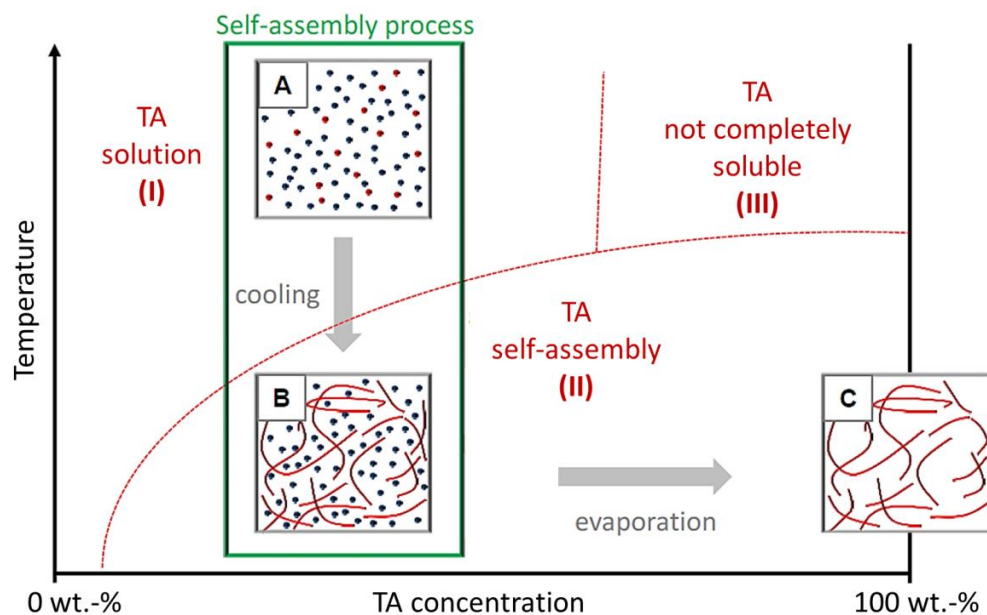


Figure 43: Schematic representation of the self-assembly process upon cooling (solvent: blue dots; dissolved benzene-1,3,5-tricarboxamide (BTA): red dots; supramolecular structures: red lines). At elevated temperature, a solution of entire dissolved BTA (A) is cooled to induce self-assembly, resulting in a suspension of supramolecular structures in the solvent (B). Complete solvent evaporation yields the supramolecular structures (C).

The experimental setup to perform the self-assembly tests can be compared to a simple batch cooling crystallizer. The self-assembly investigations in this work were performed in 4 mL glass vials. Initially, the respective trisamide is weighed in and then the appropriate amount of solvent is added to get a trisamide concentration of 0.03 % by weight in solution. The mixture is then placed in an ultrasonic bath for five minutes in order to obtain a homogeneous dispersion. In order to obtain lower concentrations, this stock solution (0.03 wt.-%) was diluted in each case with the appropriate amount of solvent after the ultrasonic treatment. Afterwards the vial is heated up to the boiling point of the respective solvent, under shaking. This corresponds to 131 °C for chlorobenzene and 179 °C for ortho-dichlorobenzene. During the heating process, the vial is closed. Therefore, no solvent can evaporate and, consequently, the concentration of trisamide in solution remains constant. After heating, the glass vial is cooled down to room temperature without active cooling.

In this way, the solubility behavior of the different trisamides in the various solvents was determined in a concentration range from 0.03 to 0.001 wt.-%. The results are summarized in **Table 3**. The abbreviations are defined as follows: **I** (insoluble), **P** (partially soluble), and **S** (soluble), at the corresponding temperatures.

Table 2 shows that the trisamides with 4-pyridine substituents (**TA 1** - **TA 4**), are almost completely insoluble in chlorobenzene. The two trisamides **TA 3**, **TA 4**, which are based on a cyclohexane core, show low solubility at low concentrations such as 0.001 wt.-%. **TA 5**, which carries 2-pyridine substituents in the periphery and is based on a cyclohexane core, is completely soluble in CB for all concentrations studied. **TA 6** (3-pyridine substituents) shows a partial solubility at a concentration of 0.01 wt.-%. For lower concentrations, it is finally completely soluble.

Table 3: Solubility behavior of the pyridine-containing trisamides in chlorobenzene (CB) and o-dichlorobenzene (o-DCB). For these investigations the solvents were heated to their boiling temperatures and different trisamide concentrations were tested. The abbreviations are defined as follows: I (insoluble), P (partially soluble), and S (soluble), at the corresponding temperatures.

	TA 1	TA 2	TA 3	TA 4	TA 5	TA 6
wt.-%	chlorobenzene (131 °C)					
0.03	I	I	I	I	P	I
0.01	I	I	I	I	S	P
0.005	I	I	I	P	S	S
0.001	I	I	P	S	S	S
wt.-%	ortho-dichlorobenzene (179 °C)					
0.03	U	U	P	P	S	S
0.01	U	U	P	S	S	S
0.005	U	U	S	S	S	S
0.001	P	P	S	S	S	S

Considering the solubilities of the trisamides in o-DCB, similar results are observed as in CB. The benzene-based trisamides (**TA 1**, **TA 2**) are almost completely insoluble. The two trisamides, which are based on a cyclohexane core and 4-pyridine substituents (**TA 3**, **TA 4**) are soluble at low concentrations such as 0.005 wt.-% and lower. The remaining two trisamides (**TA 5**, **TA 6**) are completely soluble within the investigated concentration range.

The solubility studies show that four out of six investigated trisamides can be dissolved in CB and o-DCB within the concentration range studied. Furthermore, it could be observed that all samples which were dissolved or partially dissolved at the boiling point of the solvent become turbid during the subsequent cooling. This is attributed to a self-assembly process upon cooling.

To determine which kind of morphology evolves after self-assembly, scanning electron micrographs of the samples were taken before and after the self-assembly experiment. **Figure 44** shows the SEM images of all six platinum sputtered trisamide powders directly as obtained after crystallization after their synthesis. It can be seen from the images that large crystals with undefined structure are present. Only **TA 6** still exhibits short needles, in addition to these crystals, but with a very low aspect ratio.

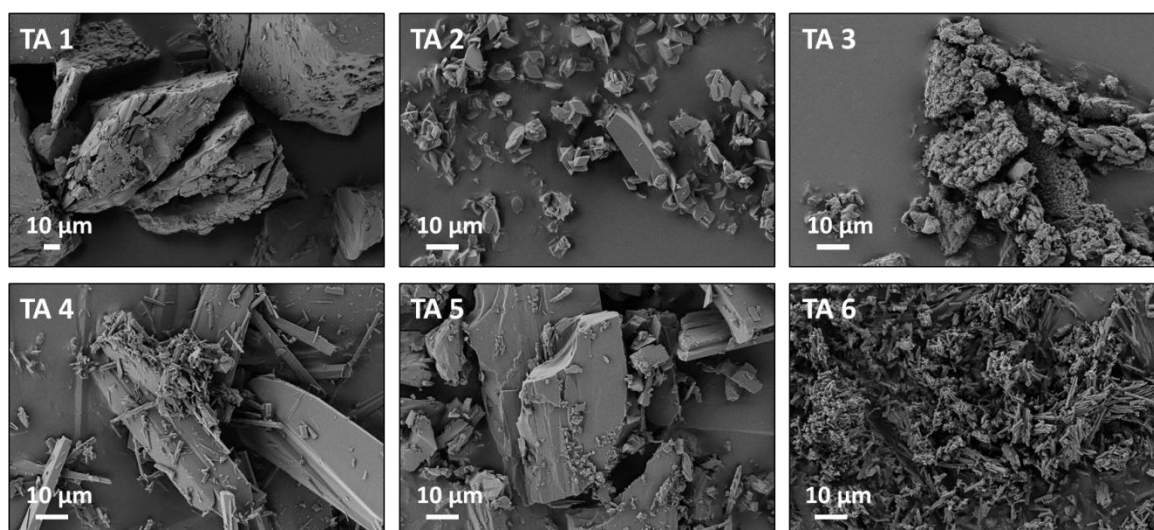


Figure 44: SEM images of the six trisamide powders after their synthesis. The samples were platinum sputtered before SEM investigations.

For the preparation of the SEM samples of the self-assembled trisamides, 30 μl of the respective sample were placed on a DSC-cover. The solvent was then evaporated at room temperature for several hours. The dried sample was then sputtered with platinum and examined via SEM.

For the morphological comparison by means of SEM images, only the samples which were at least partial soluble in the used solvents are studied, since these samples lead to self-assembled structures. The trisamide **TA 3** showed partial solubility at higher concentrations (300-100 ppm) within the solubility studies in ortho-dichlorobenzene. Below a concentration of 100 ppm, the trisamide was completely soluble at elevated temperature. Before the SEM images were taken the solvent was removed. **Figures 45a-d** show SEM images of **TA 3** after the self-assembly process in o-DCB as a function of the trisamide concentration in solution. For all concentrations supramolecular fibers can be observed. In addition to the fibers, larger structures are visible which are very similar to the **TA 3** after its synthesis. Therefore, it can be concluded that the trisamide has incompletely dissolved in o-DCB in any concentration.

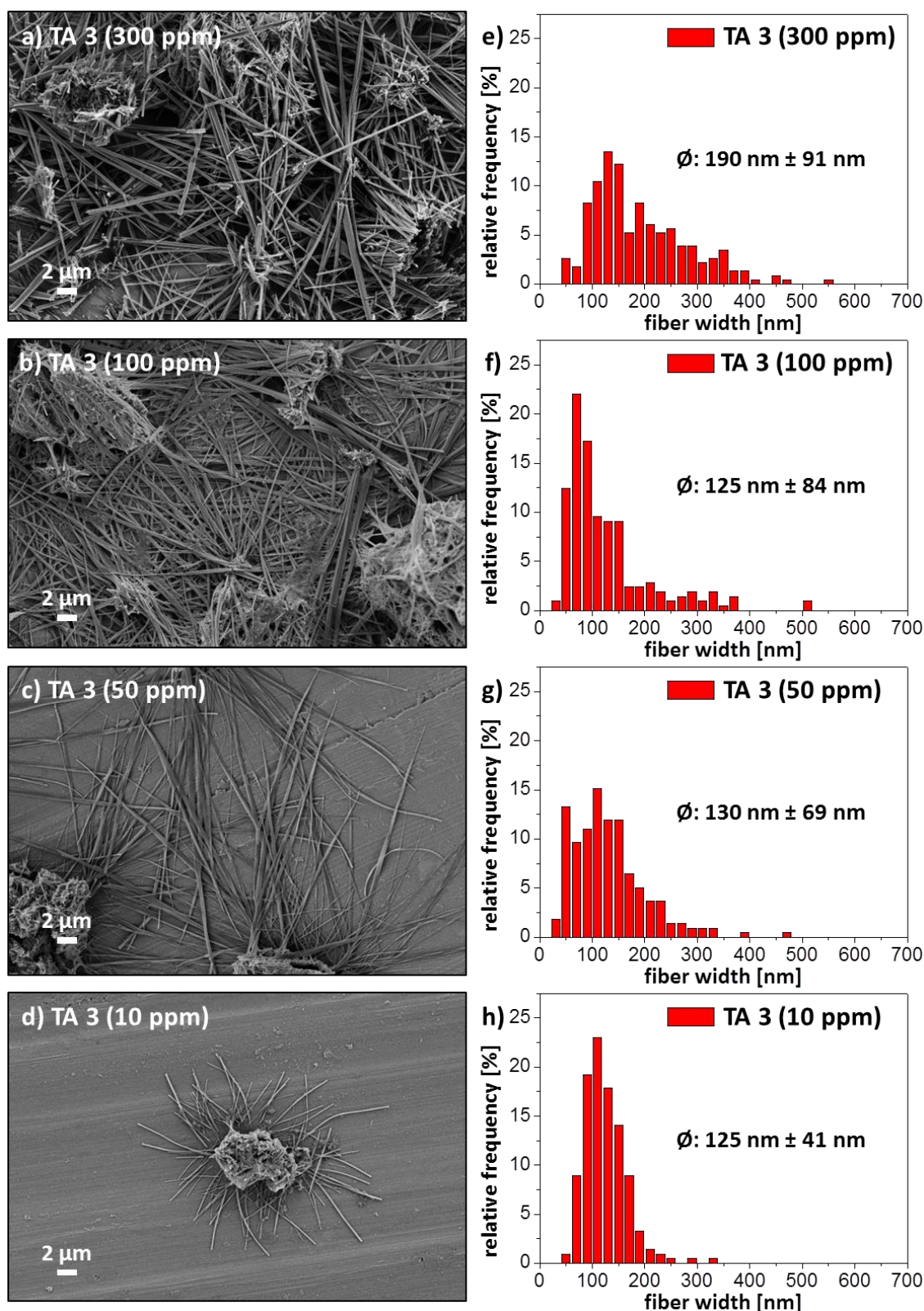


Figure 45: (a-d) SEM micrographs of supramolecular nanofibers of TA 3 prepared by self-assembly upon cooling in *o*-DCB at various trisamide concentrations: (a) 300 ppm, (b) 100 ppm, (c) 50 ppm, (d) 10 ppm. (e-h) Corresponding fiber widths histograms, based on at least 200 sized fibers.

Furthermore, fiber width determinations were performed for all different concentrations. For this purpose, images of each sample were made at different positions with always the same magnification. Typically, a magnification factor of 5000 were selected. The obtained images

were then evaluated with the software "ImageJ". After the pixel-to-length ratio was set, at least 200 fiber widths were measured from each sample and corresponding fiber width histograms were made (**Figures 45e-h**). The histograms show that the distribution width of the fiber widths reduces slightly with decreasing concentration. For the highest concentration, the determined mean fiber width is 190 nm (see **Figure 45e**). However, a very large number of fibers are also observed, which are more than two-times as large as the mean fiber width. For a concentration of 100 ppm, the mean fiber width is reduced to 125 nm, which remains virtually constant by further decreasing the concentration. Only the distribution width becomes narrower, so that at the lowest concentration (10 ppm **Figure 45h**), almost all the measured fibers are smaller than 300 nm.

In conclusion, supramolecular self-assembly of **TA 3** was successfully observed in o-DCB, even if the trisamide could not be completely dissolved in this solvent.

Another trisamide which showed complete or partial solubility only in o-DCB is **TA 4**. The cyclohexane-based trisamide which carry 4-pyridine substituents differs from the previously discussed **TA 3** only with regard to the orientation of the amide linkage, since **TA 4** is based on cis, cis-cyclohexane-1,3,5-triamine. The **Figures 46a-d** show the SEM images of **TA 4** after the self-assembly process in o-DCB. It can be observed, that for all concentrations studied supramolecular fibers are present. Considering the sample with the highest concentration of trisamide in solution (300 ppm; **Figure 46a**), supramolecular band-like structures can be observed in addition to the fibers. It can be assumed that this is initial **TA 4** since a complete dissolution of the trisamide was not observed at this concentration. For the samples with lower concentrations, such band-like structures, at least to this large extent, are not observed. Comparison of the SEM images shows that the supramolecular fibers become narrower depending on their concentration in solution. Furthermore, a very high aspect ratio of the fibers is present for all samples since the fibers are only a few hundred nanometers thick but at least 1000 times as long.

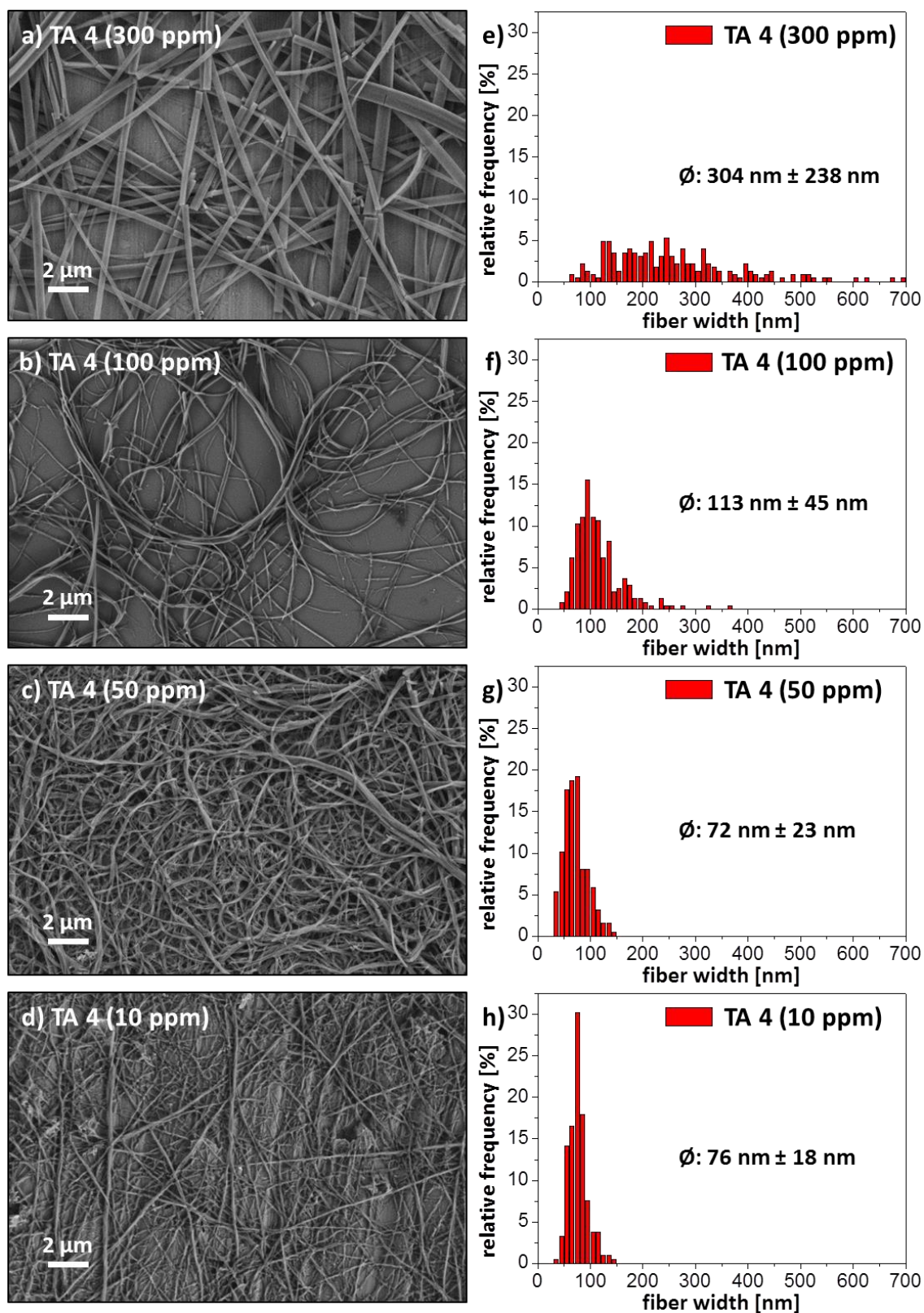


Figure 46: (a-d) SEM micrographs of supramolecular nanofibers of TA 4 prepared by self-assembly upon cooling in *o*-DCB at various trisamide concentrations: (a) 300 ppm, (b) 100 ppm, (c) 50 ppm, (d) 10 ppm. (e-h) Corresponding fiber widths histograms, based on at least 200 sized fibers.

The resulting fiber widths histograms are shown in **Figures 46e-h** next to the corresponding SEM images. With the exception of the sample at 300 ppm all fiber widths were below 500 nm. In case of the 300 ppm sample, 95 % of the fiber widths were within 700 nm (**Figure 46e**). The

remaining five percent of the fibers have widths between 700 and 1500 nm (not shown). If the concentration of the trisamide in solution decreases, the fiber width distribution becomes narrower. From a concentration of 100 ppm, only a few fibers are wider than 200 nm. For smaller concentrations, the histogram shifts to even smaller values. Considering the determined mean fiber width (**Figure 47**), it can be seen that these decrease with reducing concentration. For a trisamide concentration in solution of about 300 ppm, the mean fiber width is approximately 300 nm. For a concentration of 100 ppm, this is reduced to 113 nm and from a concentration of 50 ppm, a minimum fiber width of approximately 70 nm is established.

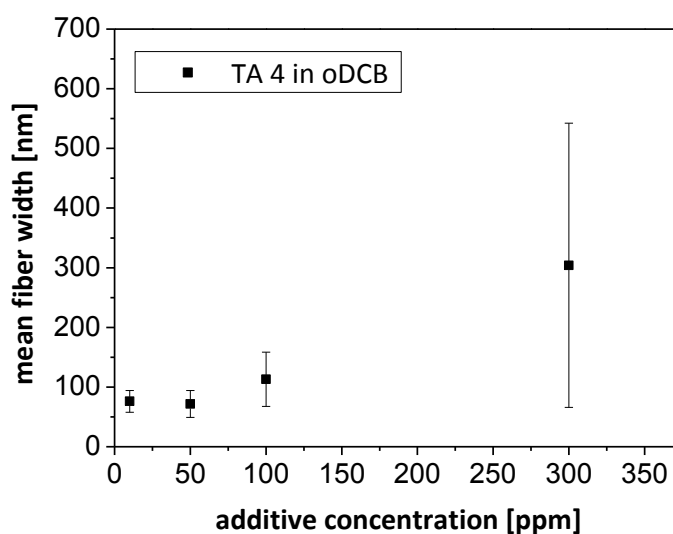


Figure 47: Influence of the trisamide concentration in o-DCB on the resulting mean fiber width of the supramolecular fibers of TA 4. Each mean fiber width takes into account at least 200 sized fibers.

In the following, the self-assembly experiments of the two cyclohexane-based trisamides **TA 5** and **TA 6** are described in detail. The two trisamides, which either was very soluble in both CB and o-DCB, differ only by their substituents (**TA 5**: 2-pyridine; **TA 6**: 3-pyridine). **Figure 48** shows the SEM images of **TA 5** taken after the self-assembly process as a function of the concentration in solution both for the investigations in CB (**Figures 48a-d**) as well as in o-DCB (**Figures 48e-h**). Comparing the SEM images after the self-assembly experiment with the neat **TA 5** powder, one can see that the self-assembly process was successful. The **TA 5** shows supramolecular structures in both investigated solvents. In this case, the nanofibers are mainly composed of broad bundles.

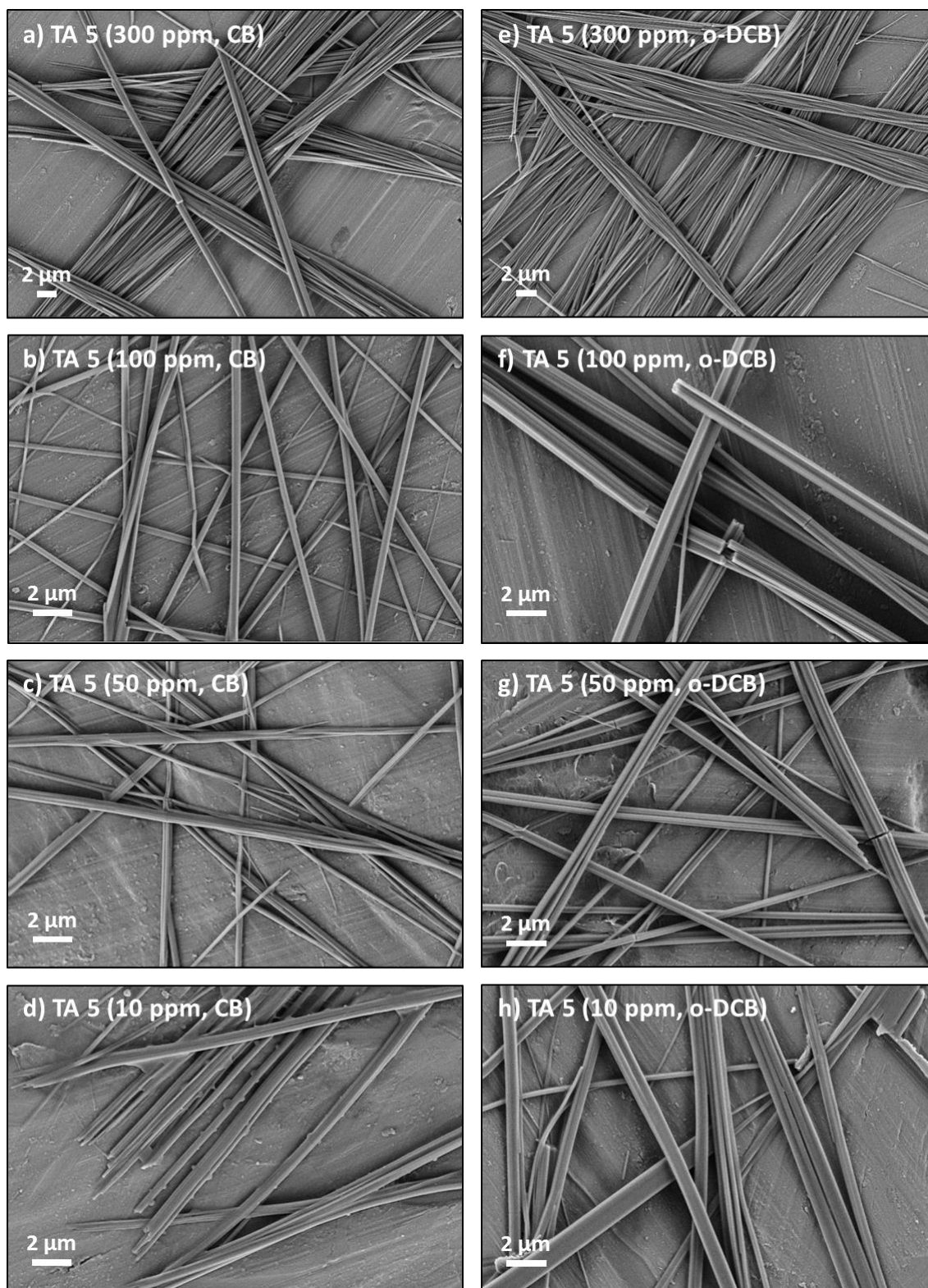


Figure 48: SEM micrographs of supramolecular nanofibers of TA 5 prepared by self-assembly upon cooling in CB (a-d) and in o-DCB (e-h) at various trisamide concentrations: (a,e) 300 ppm, (b,f) 100 ppm, (c,g) 50 ppm, (d,h) 10 ppm.

Figure 49 shows such a previously mentioned bundle in an enlarged SEM-image. On the basis of this fiber bundle formation, the measurement of the individual fibers is relatively difficult since the fibers cannot always be clearly separated from each other.

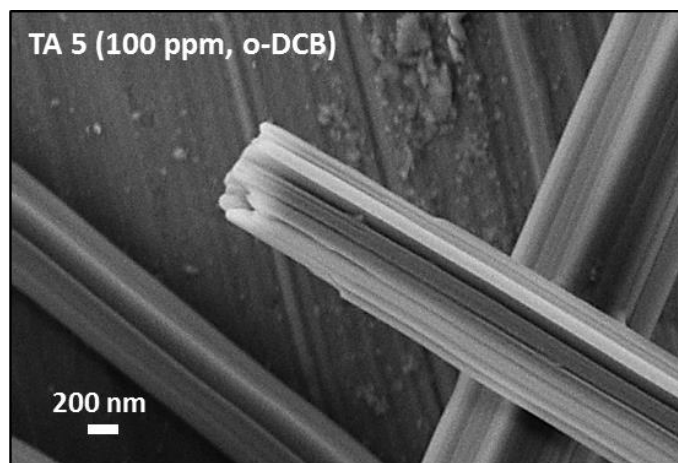


Figure 49: SEM-image of a nanofiber bundle of TA 5 self-assembled in o-DCB at a trisamide concentration of about 100 ppm. The individual nanofibers have a width of approximately 100 nm, the formed bundle of approximately 800 nm.

For the determination of the mean fiber width, 200 fibers per concentration and solvent were measured. The resulting fiber width histograms are summarized in **Figure 50**. The distribution width of the measured fiber widths remains virtually constant for almost all samples. Only the 300 ppm sample in CB has a higher distribution width, which is probably due to the incomplete solubility in this case. Furthermore, the maximum distribution shifts to smaller fiber widths values with decreasing concentration of trisamide.

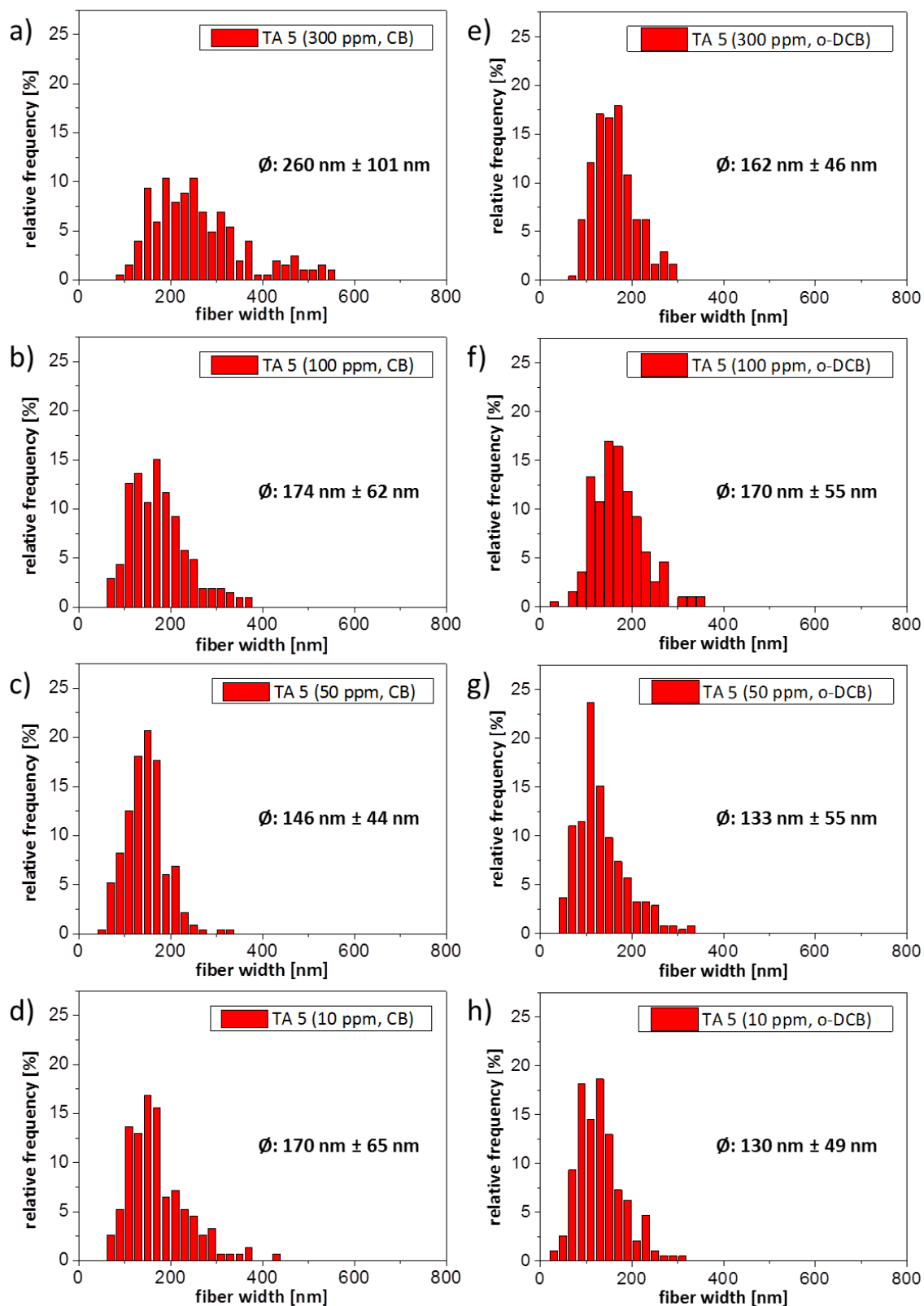


Figure 50: Fiber width histograms of TA 5 self-assembled in CB (a-d) and o-DCB (e-h) at various concentrations: (a,e) 300 ppm, (b,f) 100 ppm, (c,g) 50 ppm, (d,h) 10 ppm. The histograms are based on at least 200 sized fibers.

The mean fiber widths determined are plotted in Figure 51 as a function of the trisamide concentration. With the exception of the 300 ppm sample, all mean fiber widths are in the range of 150 nm. Accordingly, a significant reduction in the fiber width relative to the

concentration is not observed. A further reduction in the concentration could possibly result in such a fiber width reduction.

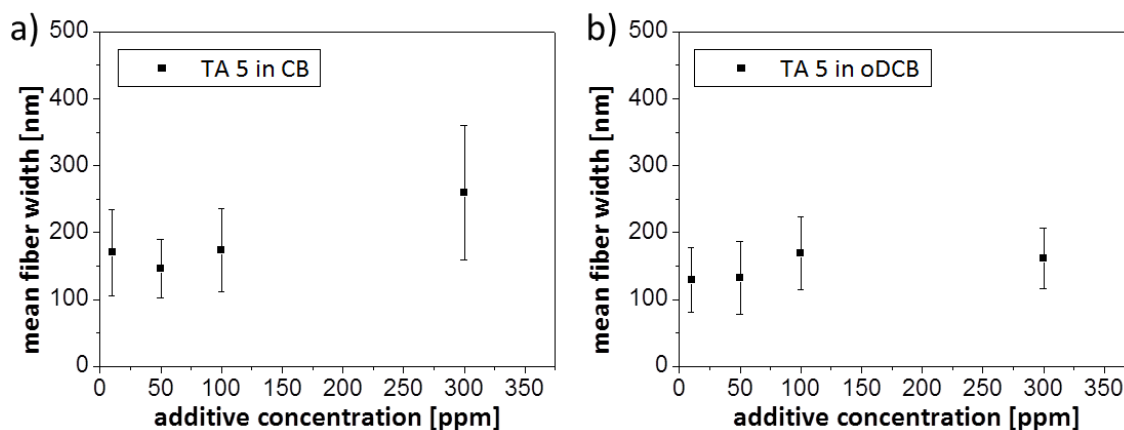


Figure 51: Influence of the trisamide concentration on the resulting mean fiber width of supramolecular fibers of TA 5 in CB (a) and o-DCB (b). Each mean fiber width takes into account at least 200 sized fibers.

Ultimately, the trisamide TA 6 exhibits good solubility in CB and o-DCB. The SEM images after the SA experiment are shown in Figure 52. Nanofibers are observed in both solvents for all concentrations studied. However, for the highest concentration (300 ppm) in CB, the presence of initial morphology of the trisamide predominates. Therefore, this sample is not used for fiber width determination. It can be clearly seen from the SEM images that the fibers become narrower and longer as the concentration reduces. Furthermore, the quantity of fibers for studies in o-DCB extremely increases with lower concentrations. This is also a clear indication that the overall fiber width has decreased.

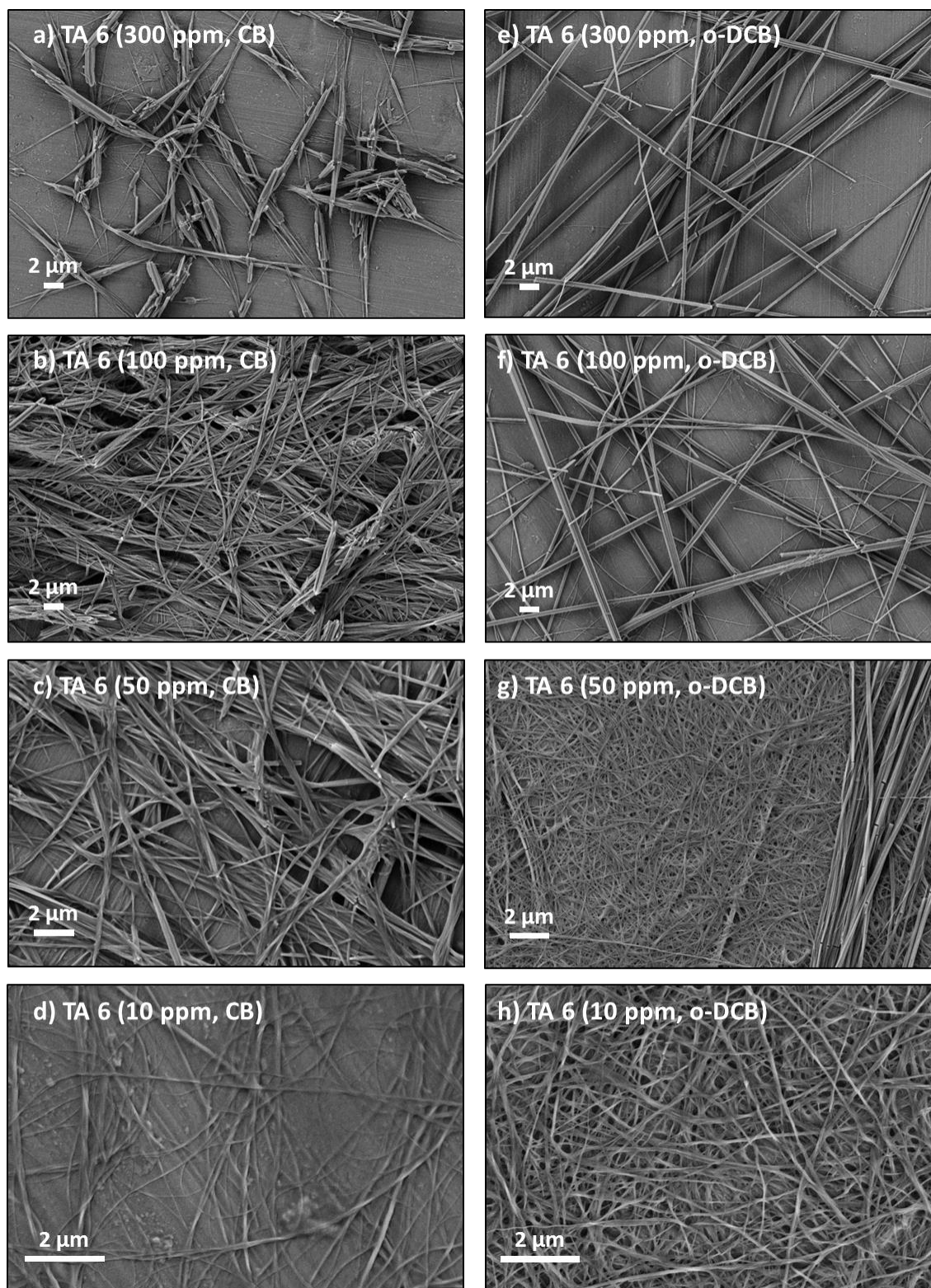


Figure 52: SEM micrographs of supramolecular nanofibers of TA 6 prepared by self-assembly upon cooling in CB (a-d) and in o-DCB (e-h) at various trisamide concentrations: (a,e) 300 ppm, (b,f) 100 ppm, (c,g) 50 ppm, (d,h) 10 ppm.

Figure 53 shows the histograms that have resulted from the measurement of more than 200 fibers per sample in dependency of concentration and solvent. It can be seen that the fiber width distribution becomes narrower with decreasing concentration of TA 6 and shifts to

smaller values. Particularly for the samples with the lowest concentration of additive, very narrow distributions can be observed.

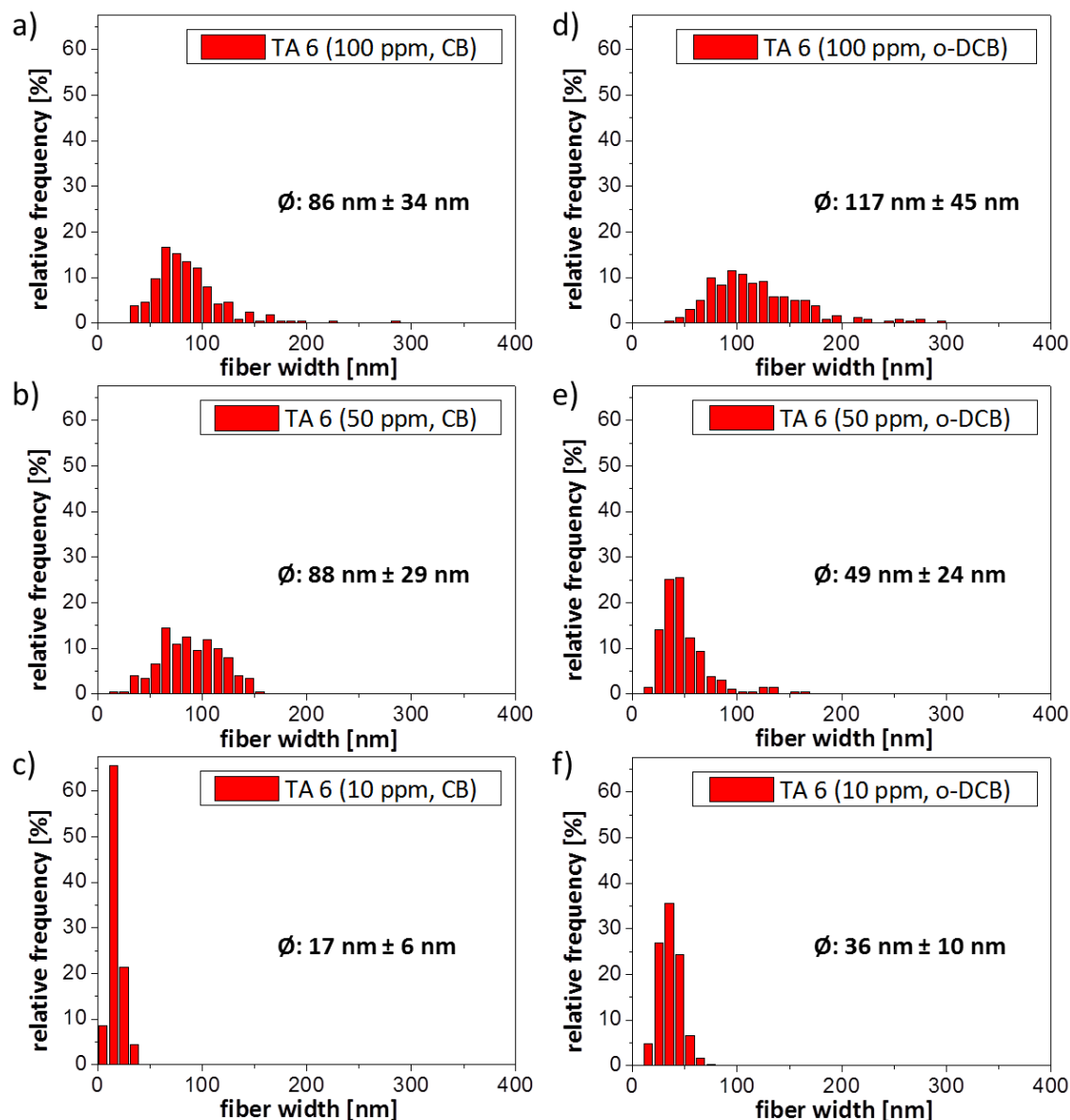


Figure 53: Fiber width histograms of TA 6 self-assembled in CB (a-d) and o-DCB (e-h) at various concentrations: (a,e) 300 ppm, (b,f) 100 ppm, (c,g) 50 ppm, (d,h) 10 ppm. The histograms are based on at least 200 sized fibers.

The significant dependence of the mean fiber width on the concentration is shown in **Figure 54**. At a concentration of 100 ppm, this amounts to approximately 100 nm for both samples. For one tenth of the concentration, this is drastically reduced and is only about 20 nm for the sample from CB and 35 nm for the sample from o-DCB. On the basis of these very small fiber width values, it can be assumed that no fiber bundles have formed, but instead only individual fibers are present.

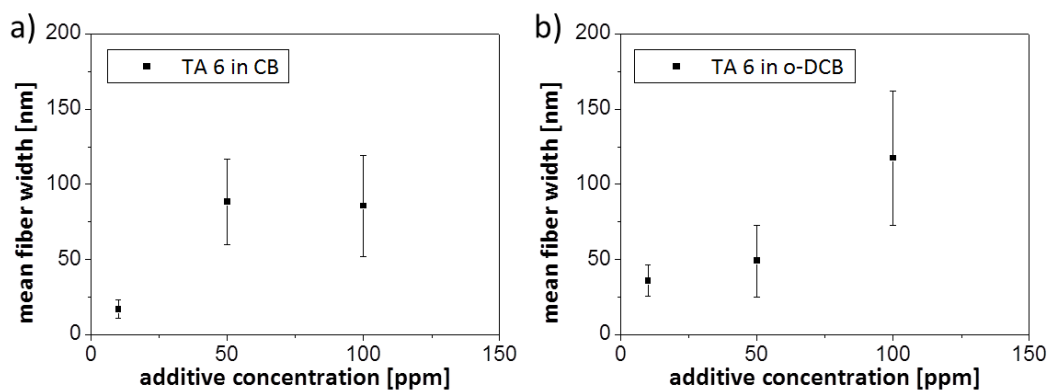


Figure 54: Influence of the trisamide concentration on the resulting mean fiber width of supramolecular fibers of TA 6 in CB (a) and o-DCB (b). Each mean fiber width takes into account at least 200 sized fibers.

In **Table 4** the mean fiber widths of all trisamides, which were at least partial soluble in o-DCB, are recorded as a function of the trisamide concentration in solution. There, the influence of the modification of only one structural parameter in the trisamide molecule on the fiber formation and the resulting fiber width can be seen. The star-marked data indicate a partial solubility of the corresponding trisamide at the respective concentration in solution. Comparing the two trisamides **TA 3** and **TA 4**, which differ only in the orientation of their amide linkage, one can see that both trisamides show self-assembly in o-DCB. Considering the mean fiber widths at small concentrations, it is observed that they are for **TA 4** (based on cyclohexane-1,3,5-triamine) only half as wide as for **TA 3** (based on cyclo-hexane-1,3,5-tricarboxyl acid). A further comparison can be made between the trisamides **TA 3** (4-pyridine), **TA 5** (2-pyridine) and **TA 6** (3-pyridine), since these differ only in terms of their substituents. For the 100 ppm samples the determined fiber width of all three TAs are in the same order of magnitude. The reduction of the sample concentration results in a significant reduction in the mean fiber width of **TA 6**, whereas the mean fiber width of the other two trisamides remains unchanged. For a concentration of 10 ppm, the resulting fibers of **TA 6** are only a quarter as thick as for **TA 3** and **TA 5** at the same concentration.

Table 4: Summarized results of the calculated mean fiber widths of the pyridin-containing trisamides in dependency of the trisamide concentration in o-DCB. The star-marked data indicate a partial solubility of the corresponding trisamide at the respective concentration in solution.

	TA 3	TA 4	TA 5	TA 6
concentration [ppm]	mean fiber width [nm]			
300	190*	304*	162	289*
100	125*	113	170	117
50	130*	72	133	49
10	125*	76	130	36

In summary, the self-assembly to nanofibers in CB were successful performed for two of the six trisamides. In *o*-DCB, fiber-like structures could be realized for four trisamides. The thinnest fibers, both in CB and *o*-DCB, could be observed for **TA 6**, the thickest fibers for **TA 3** and **TA 5**. Accordingly, there is a significant influence of the substituent on the resulting supramolecular fibers. Furthermore, a dependence of the fiber width on the linkage of the amide bond could be detected. The trisamide based on the triamine core (**TA 4**) shows significant thinner fibers than the respective trisamide based on the tricarbonyl acid core (**TA 3**).

3.2.6 Self-assembly investigations of trisamides in aqueous solutions

The trisamides **TA 1** and **TA 2** are the two pyridine-containing trisamides in this work, which showed no self-assembly behavior in the organic solvents due to lack of solubility. However, it is known from literature that **TA 1** forms hydrogels via hydrophobic interactions in water with the addition of small amounts of organic solvents such as DMSO, EtOH, MeOH and DMF.^[201] Hydrogels illustrate an interesting research field and can be found in various applications, for example in the production of filter media.^[181,182] Accordingly, self-assembly experiments were performed in aqueous solutions with the two trisamides **TA 1** and **TA 2**. In addition to water, the organic solvents ethanol (EtOH), isopropyl alcohol (IPA), acetone (Ac) and tetrahydrofuran (THF) were used for these investigations. Although both trisamides are insoluble in water, in the presence of the used polar solvents, both the trisamides are soluble in selected solvent mixtures. The role of the organic solvents seems to be helping the trisamides to be soluble in the aqueous solvent mixture since both the trisamides are unable to form gels with these organic solvents alone. It may be noted here that often hydrogelators are water-insoluble and a suitable co-solvent is required to solubilize the gelator molecules in the aqueous medium.^[201]

The self-assembly experiments in the aqueous solutions were performed similar as described for the investigations in the chlorinated solvents. In the following the results for the **TA 1** are described in more detail. **Figure 55** shows an overview of the investigated systems. All solvent mixtures feature a ratio of organic solvent to water of four to one. The figure also shows the temperatures which were necessary to completely dissolve the respective concentration of trisamide. The maximum concentration of trisamide which could be solubilized is also shown in the figure. The inserted figures show the samples at their maximum temperature (left) and after cooling to room temperature (right).

<u>EtOH/H₂O:</u> solvent ratio: 4:1 solvent temp.: 70°C TA-concentration: 5000 ppm		<u>IPA/H₂O:</u> solvent ratio: 4:1 solvent temp.: 75°C TA-concentration: 2500 ppm	
<u>Ac/H₂O:</u> solvent ratio: 4:1 solvent temp.: 60°C TA-concentration: 2500 ppm		<u>THF/H₂O:</u> solvent ratio: 4:1 solvent temp.: 60°C TA-concentration: 2000 ppm	

Figure 55: Overview of the aqueous solvent systems used for self-assembly studies of TA 1. Indicated are the individual solvent ratios, the solvent temperature at which the trisamide completely dissolved and the maximum trisamide concentration which could be dissolved. Ethanol (EtOH), isopropyl alcohol (IPA), acetone (Ac) and tetrahydrofuran (THF).

It can be seen that gel formation has taken place for all systems after cooling down the samples to room temperature. To analyze the hydrogel formation and to analyze the supramolecular structures, SEM investigations were conducted. **Figure 56** shows the SEM images of the xerogels of TA 1 prepared in various aqueous solvent systems. Very dense fiber networks can be observed for all the systems. The thickest fibers as well as the widest network meshes can be found for the system EtOH/H₂O. The two systems IPA/H₂O and THF/H₂O visually show the thinnest fibers as well as the highly dense fiber networks.

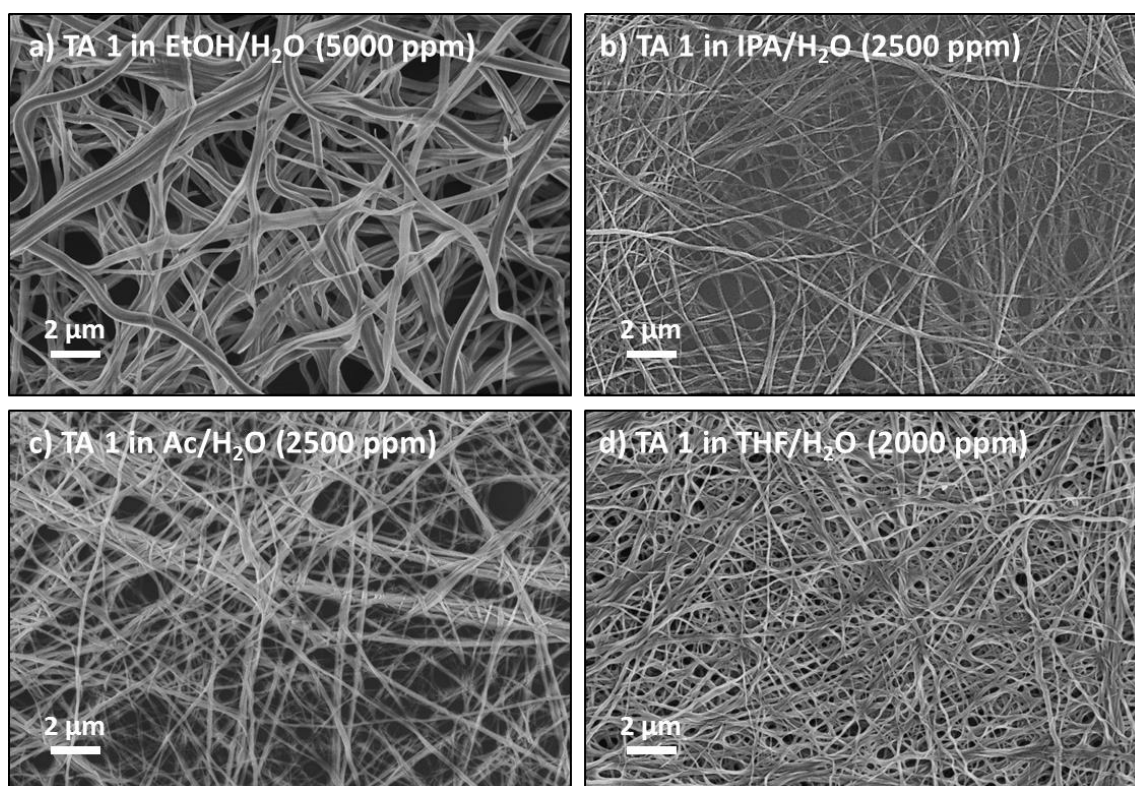


Figure 56: SEM micrographs of supramolecular nanofibers of TA 1 prepared by self-assembly upon cooling in (a) EtOH/H₂O (4:1), (b) IPA/H₂O (4:1), (c) Ac/H₂O (4:1) and (d) THF/H₂O (4:1). The concentration of TA 1 in the respective solvent systems varied and is displayed the SEM-Images.

The results of the fiber width studies are shown in the histograms in **Figure 57**. The average fiber width of **TA 1** in EtOH/H₂O is about 200 nm and is therefore twice as large as the fibers resulted for the system Ac/H₂O. The smallest fiber widths are found for the systems IPA/H₂O and THF/H₂O. Here, the nanofibers have on average only a width of about 60 nm. Furthermore, the fiber width distributions are the closest for these two systems.

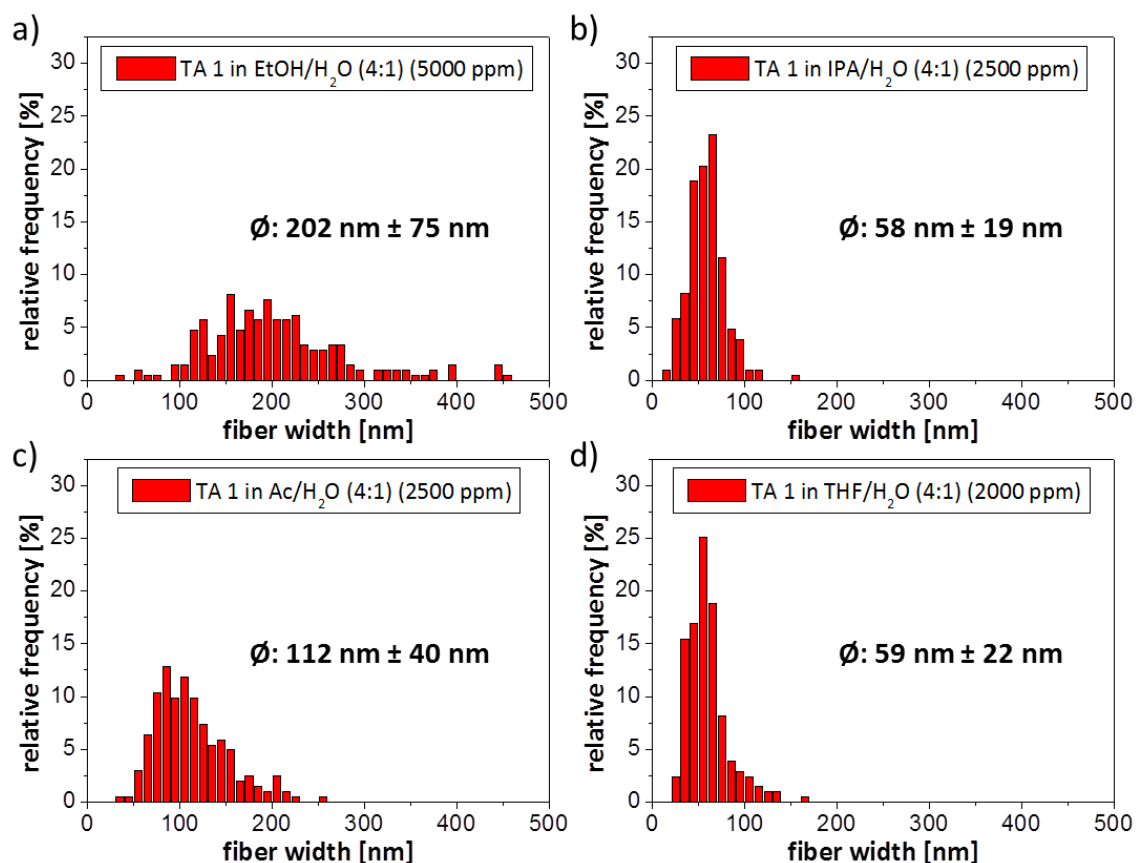


Figure 57: Fiber widths histograms and mean fiber widths of **TA 1** self-assembled in (a) EtOH/H₂O (4:1), (b) IPA/H₂O (4:1), (c) Ac/H₂O (4:1) and (d) THF/H₂O (4:1). The concentration of **TA 1** in the respective solvent systems varied and is displayed the histogram legends. For the calculation of the mean fiber widths at least 200 fibers were sized for each system.

The last remaining trisamide with which no self-assembly in fibrous structures was observed in the previous non-polar solvents is trisamide **TA 2**. This trisamide has also not been noted in the literature. Due to the structural similarities to **TA 1**, self-assembly studies were also performed with **TA 2** in the various aqueous solvent systems as described above. However, it was not rudimentarily possible to solubilize the **TA 2** at these high concentrations. A drastic reduction of the concentration by a factor of about 100 finally brought success for the system THF/H₂O. **Figure 58a** shows the SEM image of **TA 2** after the self-assembly experiment in THF/H₂O. The ratio of THF to H₂O was three to one. The concentration of trisamide in solution was only 55 ppm. The Figure shows that fibrous self-assembly occurred. However, the fibers predominantly exist in twisted fiber bundles. This makes the determination of the average

fiber width difficult. The result of this determination is shown in **Figure 58b** in the form of a histogram. It results in a mean fiber width of 114 nm with a relatively broad distribution.

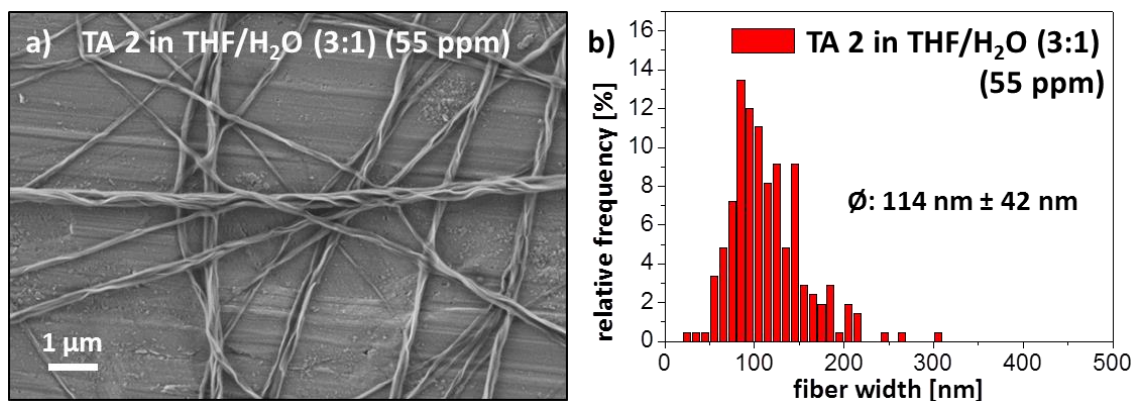


Figure 58: (a) SEM micrograph of supramolecular nanofibers of TA 2 prepared by self-assembly upon cooling in THF/H₂O (3:1). The concentration of TA 2 in the solvent systems was 55 ppm. (b) Fiber width histogram and mean fiber width of TA 2 self-assembled in THF/H₂O (3:1). For the calculation of the mean fiber width at least 200 fibers were sized.

In summary, for the self-assembly studies of the pyridine-containing trisamides in the various organic solvents and in the aqueous solvent mixtures, self-assembly to fibrous nanostructures could be successfully observed for all six trisamides. The resulting fiber widths were dependent on both the molecular structure of the trisamide and the concentration of the trisamide in solution and the selected solvent.

3.3 Selection, synthesis and self-assembly of pyridine-containing bisamides

In the following, the pyridine-containing bisamides investigated in this work are introduced, characterized and the results regarding their self-assembly behavior in organic solvents are described.

3.3.1 Bisamide selection and their structural variation

Figure 59 shows the different pyridine-containing bisamides (BA) studied in this work. The here investigated BAs can be divided into three groups. The first group includes BAs based on a symmetrical benzene core with 4-pyridine moieties. **BA 1** and **BA 2** both feature a benzene core and differ only in the attachment of their amide bonds. Thus, they are based on terephthalic acid (**BA 1**) and 1,4-phenylenediamine (**BA 2**) as core. The second group includes cyclohexane BAs with 4-pyridine moieties. These include **BA 3** and **BA 4**. Both have a cyclohexane core and differ only in the linkage of their amide bonds. Here, the basic building blocks are cyclohexane-1,4-dicarboxylic acid (**BA 3**) and cyclohexane-1,4-diamine (**BA 4**).

The third group includes cyclohexane bisamides with 2- and 3-pyridine moieties. These include **BA 5** and **BA 6**. Both bisamides are based on the same basic core, trans-cyclohexane-1,4-dicarbonyl dichloride. Therefore, they differ in the peripheral substituents, such as two symmetrically arranged 2-pyridine groups (**BA 5**) and two symmetrically arranged 3-pyridine groups (**BA 6**).

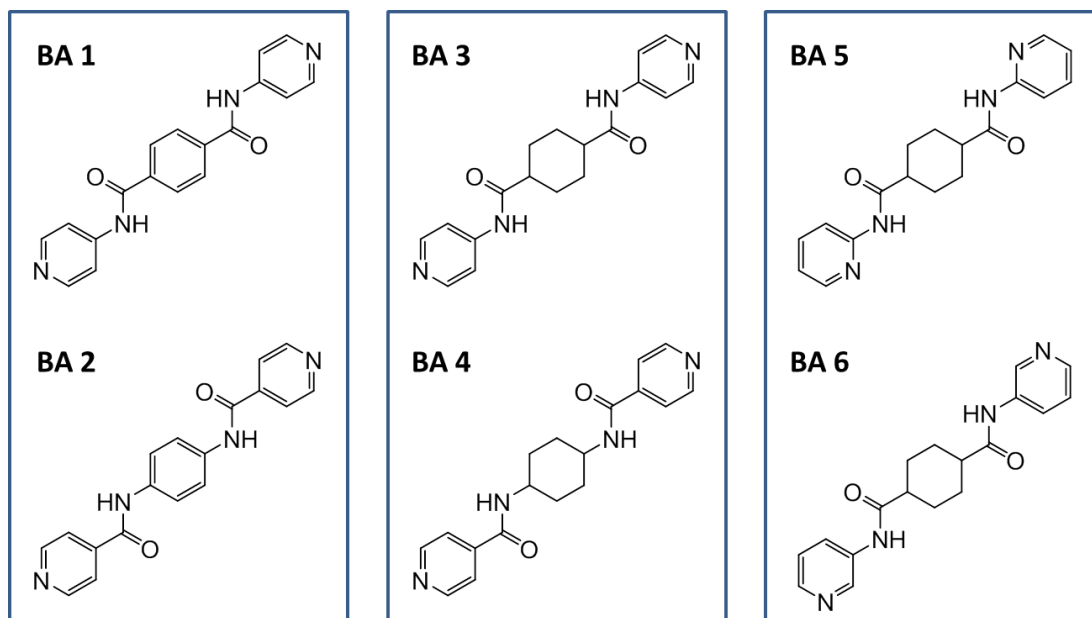


Figure 59: Chemical structures of the six investigated pyridine-containing bisamides in this work. The first group includes benzene bisamides with 4-pyridine moieties (left box), the second group includes cyclohexane bisamides with 4-pyridine moieties (central box) and the third group includes cyclohexane bisamides with 2- and 3-pyridine moieties (right box).

Four of these six pyridine-containing bisamides are already known in literature. These are **BA 1-3** and **BA 6** (see **Chapter 3.1.3**).

3.3.2 Bisamide synthesis

The syntheses of the individual molecules were carried out by the technicians J. Failner, S. Ganzleben, D. Hanft and R. Schneider under my guidance. The following thermal and analytical characterizations were accomplished by my self.

In general, the bisamides were obtained by an amidation reaction between an acid chloride and an amine derivative. For all syntheses, the component, which is to be attached to the central core, was present in the excess during the reaction, to guarantee a complete substitution of the core. Since both the core and the substituents vary, no general valid reaction scheme can be shown. Therefore, the reaction scheme for the synthesis of **BA 1** is exemplarily shown below. All further syntheses of the bisamides studied in this thesis are shown in detail in the **Experimental 7.3**.

Figure 60 shows the reaction scheme of terephthaloyl dichloride with 4-aminopyridine to obtain N^1,N^4 -di(pyridin-4-yl)terephthalamide (**BA 1**). Initially, 4-aminopyridine, triethylamine (TEA) and LiCl are mixed together with 50 ml of NMP in a Schlenk flask. Terephthaloyl dichloride is then added under inert gas (N_2) and ice cooling. The reaction time amounts to 48 hours at a temperature of 80 °C. The resulting reaction mixture is precipitated in ice water; the solid is filtered off and dried. The crude product obtained is subsequently dissolved in DMSO and precipitated again in 500 ml of water. The final product is dried at 60 °C under high vacuum to get a greyish powder in a yield of 54 %.

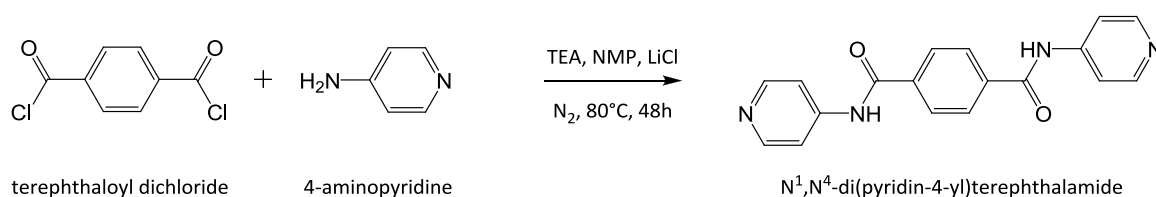


Figure 60: Synthesis of **BA 1** via the reaction of terephthaloyl dichloride with 4-aminopyridine.

Table 5 lists the reactants for the respective bisamide syntheses of the bisamides, the solvent or solvent mixture for recrystallization as well as the yields obtained.

Table 5: List of the individual reactants for the respective syntheses of the seven different bisamides, the solvent systems in which recrystallization occurs and the yields obtained after synthesis.

BA	Core	Substituent	Recrystallization	Yield [%]
1	terephthaloyl dichloride	4-aminopyridine	DMSO/H ₂ O	54
2	1,4-phenylenediamine	isonicotinoyl chloride hydrochloride	DMF/H ₂ O	33
3	trans-cyclohexane-1,4-dicarbonyl dichloride	4-aminopyridine	DMSO	64
4	trans-cyclohexane-1,4-diamine	isonicotinoyl chloride hydrochloride	DMSO	27
5	trans-cyclohexane-1,4-dicarbonyl dichloride	2-aminopyridine	MeOH	20
6	trans-cyclohexane-1,4-dicarbonyl dichloride	3-aminopyridin	MeOH	64

The solvents used for the recrystallization of the bisamides were predominantly DMSO and MeOH. Only for **BA 2**, a mixture of DMF/H₂O was used for the recrystallization after the extraction of the bisamide in MeOH. With the bisamides **BA 1**, **BA 3** and **BA 6** yields over 50 % could be achieved.

3.3.3 Analytical characterization

All individual compounds were analyzed by common methods such as $^1\text{H-NMR}$ spectroscopy, mass spectrometry and infrared spectroscopy to prove product formation and product purity.

Figure 61 shows exemplarily the $^1\text{H-NMR}$ spectrum of **BA 1**. All signals could be clearly assigned to the corresponding hydrogen atoms. The singlet at a chemical shift of 8.13 ppm corresponds to the aromatic protons of the core (**1**). The location of the chemical shift as well as the formation of a singlet is expected for this type of aromatic protons in a bisamide.

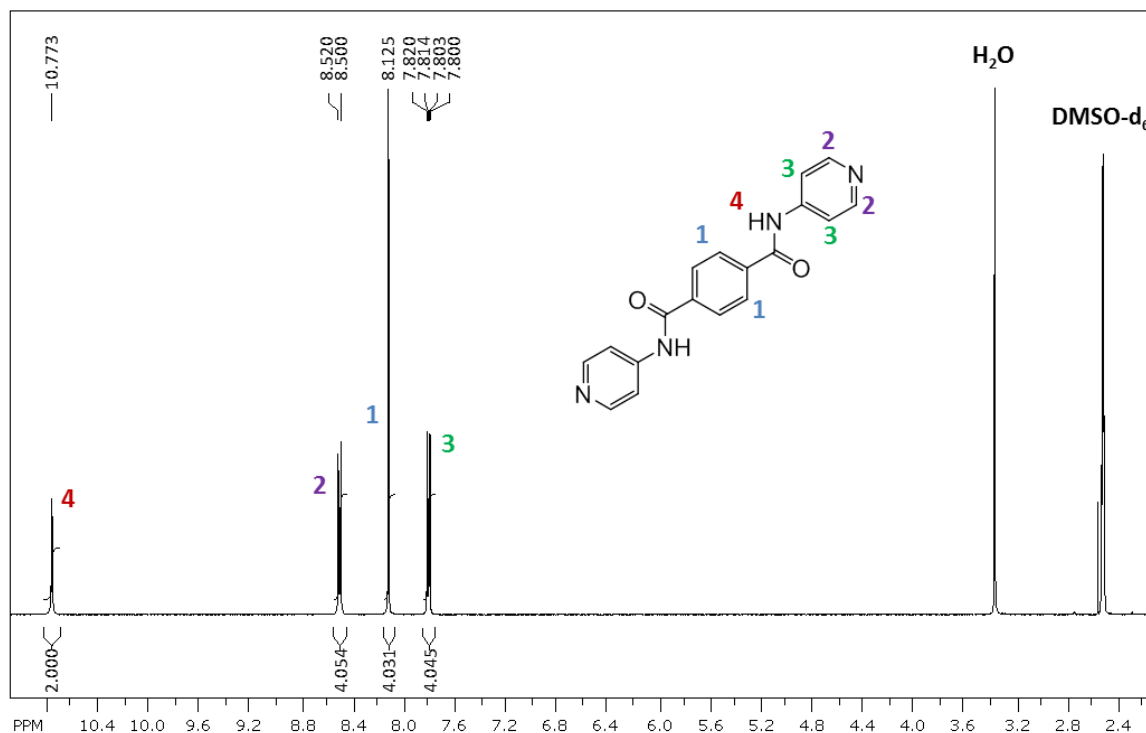


Figure 61: $^1\text{H-NMR}$ spectrum of **BA 1** in DMSO-d_6 recorded with a 300 MHz NMR spectrometer (Bruker). The chemical structure of the expected bisamide is inserted into the spectrum and the signals obtained were assigned to the corresponding hydrogen atoms.

The aromatic protons of the substituent show multiplets at a chemical shift of 7.81 ppm (**3**) and 8.51 ppm (**2**). Thus the two protons attached to the electron-poorer carbon atoms in the immediate adjacency of the nitrogen atom of the pyridine substituent show a higher chemical shift than the two protons which are adjacent to the amide bond. The singlet at a chemical shift of 10.77 ppm can be attributed to the amide protons (**4**). The remaining two signals in the $^1\text{H-NMR}$ spectrum (2.50 ppm, 3.33 ppm) belong to the deuterated DMSO-D_6 , which served as solvent and water. If one considers the integrals of the individual signals, their ratio agrees well with the respective number of protons. Thus, the formation of **BA 1** could be clearly confirmed. The $^1\text{H-NMR}$ spectra of the remaining bisamides are shown in **Appendix 8.1.** along with the detailed assignment of the individual protons. No significant signals that indicate impurities were observed.

In addition, mass spectra were recorded on a FINNIGAN MAT 8500 spectrometer from Thermo Fisher Scientific using electron spray ionization (ESI) to characterize the bisamides. **Figure 62** shows exemplarily the mass spectrum of **BA 1**. First, the mass of the analyte has to be determined. The molecular ion peak belongs to the heaviest ion and can be found at 318 m/z. This is the mass of compound **BA 1**. However, in the case of electron ionization, a large fraction of ions are often cleaved. Therefore, the chemical structures of the fragments occurring during the measurement are additionally included in **Figure 62**. Therefore, the other signals can be assigned to fragments of **BA 1**.

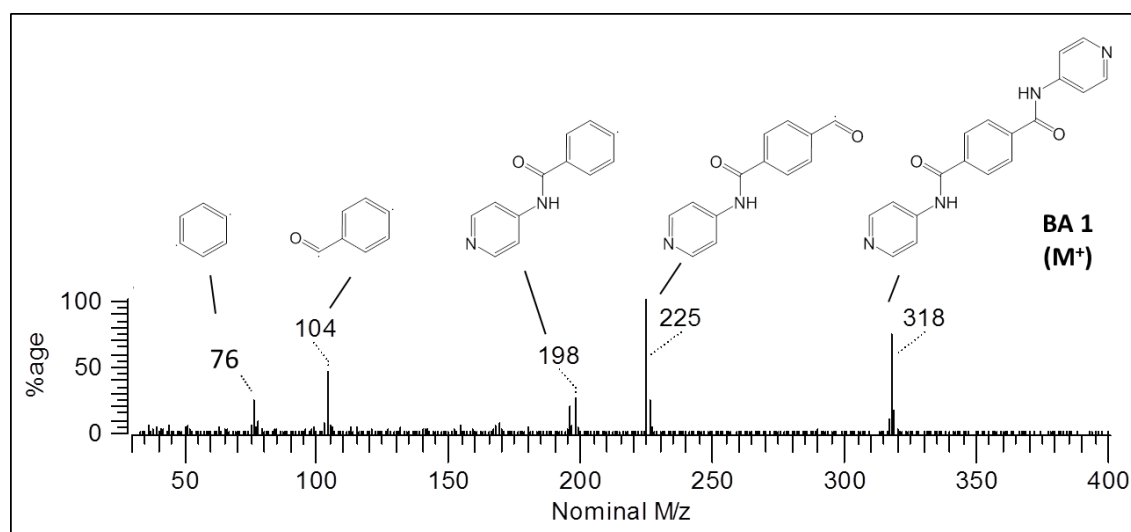


Figure 62: Determined mass spectrum of **BA 1**. The chemical structures of **BA 1** and the fragments, occurring during the measurement, are inserted to complete all main peaks.

The mass spectra of the remaining bisamides are shown in **Appendix 8.2**. For all compounds the expected molar masses could be confirmed by this method.

Fourier-transform infrared spectroscopy (FT-IR) was used as a third analytical method to characterize the bisamides. The IR spectra were recorded with a PerkinElmer Spectrum 100 FT-IR spectrometer in a range from 4000 cm^{-1} to 650 cm^{-1} .

Figure 63 shows the recorded spectrum of **BA 1** and highlights the most important vibrational signals. Of great importance are, in particular, the CO stretching vibration (Amid I) and the NH bending or CN stretching vibrations (Amid II). The CO stretching vibration at 1689 cm^{-1} suggests that the amidation reaction was successful. The Amide II vibration can be detected at 1593 cm^{-1} . The FT-IR spectra of the remaining bisamides are shown together with their most important vibration numbers in **Appendix 8.3**.

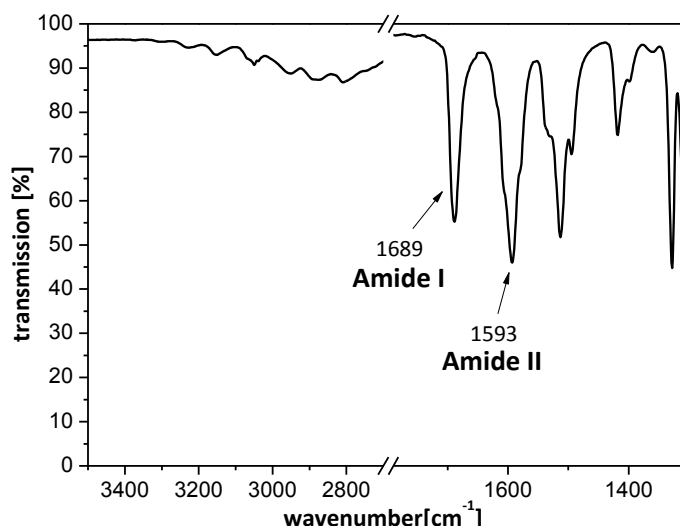


Figure 63: FT-IR spectrum of BA 1 recorded with a Perkin Elmer Spectrum 100 FT-IR spectrometer in a range of 3500 cm^{-1} to 1400 cm^{-1} .

3.3.4 Thermal characterization

The following section deals with the thermal characterization of the pyridine-containing bisamides. The investigations include thermogravimetric analyses (TGA), simultaneous differential thermal analyses (SDTA) and melting point measurements.

The TGA/SDTA measurements were performed on a Mettler Toledo TGA/SDTA 851e. Data were recorded with a heating rate of 10 $\text{K}\cdot\text{min}^{-1}$ in a temperature range from 30 $^{\circ}\text{C}$ to 700 $^{\circ}\text{C}$ under nitrogen atmosphere. On the basis of the TGA measurements it is possible to determine up to which temperature the bisamides are thermally stable. In addition to the mass loss as a function of the temperature, the heat flow was also recorded by means of a simultaneous differential thermal analysis (SDTA). **Figure 64** shows exemplarily the recorded thermogram of **BA 1**. All other TGA/SDTA thermograms are shown in **Appendix 8.4**.

The **Figure 64** reveals that **BA 1** is thermally stable at least up to 330 $^{\circ}\text{C}$. A five percent mass loss can be determined at a temperature of 384 $^{\circ}\text{C}$. Subsequently, the **BA 1** mass loss occurs very quickly. A residue content of 13 % at 700 $^{\circ}\text{C}$ indicates that **BA 1** decomposes and no or less pronounced sublimation is taking place. The simultaneously recorded heat flow shows a broad melting range with a local maximum at 378 $^{\circ}\text{C}$. This indicates that **BA 1** decomposes directly upon melting.

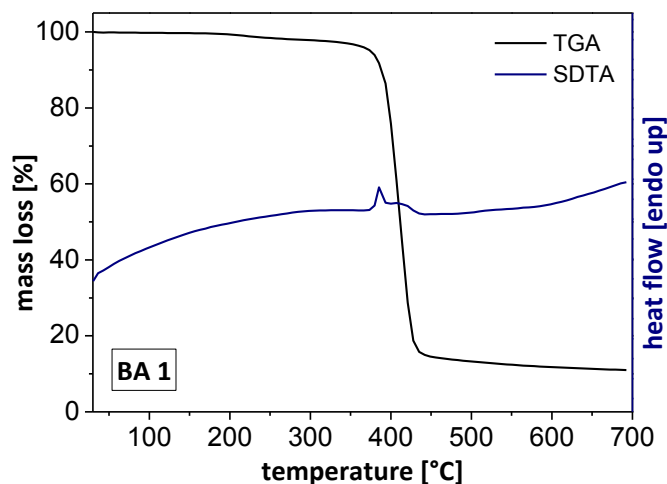


Figure 64: Thermograms of the thermogravimetric analysis (black) and the SDTA (blue) of N^1,N^4 -di(pyridin-4-yl)terephthalamide (BA 1). Data were recorded with a heating rate of $10 \text{ K}\cdot\text{min}^{-1}$ in a temperature range from $30 \text{ }^\circ\text{C}$ to $700 \text{ }^\circ\text{C}$ under nitrogen atmosphere.

In **Table 6** the results of the TGA/SDTA measurements are summarized. It shows that all bisamides with 4-pyridine substituents (**BA 1 – BA 4**), whether benzene or cyclohexane based core, are thermally very stable and decomposition take place well above $330 \text{ }^\circ\text{C}$. The bisamides with the 2- (**BA 5**) and 3-pyridine substituents (**BA 6**) are thermally much more susceptible and begin to decompose at $240 \text{ }^\circ\text{C}$. Furthermore, it is observed that the residue content at T_{end} ($700 \text{ }^\circ\text{C}$) of the benzene-based bisamides is higher than that of the cyclohexane-based compounds.

Table 6: Summarized results of the TGA/SDTA measurements and the melting point determinations (MP90) of all six different bisamides.

BA	$T_{5\% \text{ mass loss}} [^\circ\text{C}]$	residue at $700 \text{ }^\circ\text{C} [\%]$	$T_m (\text{SDTA}) [^\circ\text{C}]$	$T_m (\text{MP90}) [^\circ\text{C}]$
BA 1	384	89	378	378
BA 2	372	87	331	330
BA 3	386	99	406	> 400
BA 4	350	99	364	361
BA 5	307	99	318	315
BA 6	307	97	324	293

The melting point determinations were performed on a melting point analyzer MP 90 from Mettler Toledo. Data were recorded with a heating rate of $10 \text{ K}\cdot\text{min}^{-1}$ in a temperature range from $30 \text{ }^\circ\text{C}$ to $400 \text{ }^\circ\text{C}$. The results are given as an average value of three measurements and are also summarized in **Table 6**.

The observed melting points determined with the MP90 system match very well with the data obtained from the previous SDTA measurements. In a similar manner, the bisamides

BA 1 and **BA 3** show the highest melting temperatures. Both bisamides feature the carboxylic acid groups at the core and have 4-pyridine substituents. Comparing **BA 1** and **BA 2** with one another, it can be seen that, as already mentioned, the bisamide based on terephthalic acid (**BA 1**) shows a higher melting temperature than that based on 1,4-phenylenediamine (**BA 2**). This is also the case for the cyclohexane-based bisamides **BA 3** and **BA 4**. Furthermore, the bisamides **BA 3**, **BA 5** and **BA 6** can also be compared with one another in terms of their melting temperatures. All of these bisamides have carboxylic acid-based cyclohexane cores and differ only in regard to their substituents. **BA 3**, with the 4-pyridine substituents, shows the highest melting temperature beyond 400 °C. The lowest melting temperature with a value of 293 °C is measured for **BA 6** (3-pyridin substituent). Accordingly, a small difference in the structure of the substituent has a large effect on the thermal properties of these bisamides.

On the basis of these thermal results of the pyridine-containing bisamides, it can be seen that four out of the six compounds are suitable for the subsequent P3HT nucleation studies since a thermal stability as well as a melting point of more than 300 °C is required for these studies. Only **BA 5** and **BA 6** cannot be used for these investigations since these compounds begin to decompose at a temperature of 240 °C.

3.3.5 Self-assembly investigations of bisamides in organic solvents

In the following, the self-assembly investigations of the pyridine-containing bisamides in chlorinated solvents, more precisely in chlorobenzene and ortho-dichlorobenzene, are described. These halogenated aromatics were selected because they were also used to process P3HT from solution. Similarly as described above, self-assembly upon cooling was investigated. Thus the experimental setup corresponds to the setup of the self-assembly studies of the pyridine-containing trisamides in chlorinated solvents. The self-assembly investigations were performed in 4 mL glass vials. Initially, the respective bisamide is weighed in and then the respective amount of solvent is added to obtain a bisamide concentration of 0.03 wt.-% in solution. The mixture is then placed in an ultrasonic bath for five minutes in order to obtain a homogeneous dispersion. To achieve lower concentrations, this stock solution (0.03 wt.-%) was diluted with a respective amount of the same solvent after the ultrasonic treatment. Afterwards the vial is heated up to the boiling point of the solvent, under shaking. This amounts to 131 °C for chlorobenzene and 179 °C for ortho-dichlorobenzene. During the heating process the glass is closed to keep the concentration constant.

The observations on the solubility behavior of the different bisamides in the various solvents at different concentrations are summarized in **Table 7**. The abbreviations are defined as follows: **I** (insoluble), **P** (partially soluble), and **S** (soluble), at the boiling temperatures of the selected solvent.

The table shows that all investigated bisamides are soluble in both CB and o-DCB, at almost all investigated concentrations at the respective boiling points of the solvents. **BA 3**, which is based on a cyclohexane core and two 4-pyridine substituents, shows the lowest solubility in CB. In this solvent, it is completely soluble only at a maximum concentration of 10 ppm. The bisamides **BA 5** and **BA 6**, which have the same core and the same amide centering as **BA 3** and differ only in their substituents, show the best solubility over the entire concentration range investigated for both CB and o-DCB. The table further shows that in general the solubility of the bisamides in o-DCB is higher than in CB.

Table 7: Solubility behavior of the pyridine-containing bisamides in chlorobenzene (CB) and o-dichlorobenzene (o-DCB). For these investigations the solvents were heated to their boiling temperatures and different bisamide concentrations were tested. The abbreviations are defined as follows: I (insoluble), P (partially soluble), and S (soluble), at the corresponding temperatures.

	BA 1	BA 2	BA3	BA 4	BA 5	BA 6
wt.-%	chlorobenzene (131 °C)					
0.03	I	P	I	P	S	S
0.01	P	S	I	S	S	S
0.005	S	S	P	S	S	S
0.001	S	S	S	S	S	S
wt.-%	ortho-dichlorobenzene (179 °C)					
0.03	P	P	P	P	S	S
0.01	S	S	S	S	S	S
0.005	S	S	S	S	S	S
0.001	S	S	S	S	S	S

The solubility studies show that self-assembly upon cooling is in principle for all bisamides possible in the investigated concentration range, with the exception of **BA 3** in CB, which is only completely soluble at very low concentrations.

After heating process, the glass vials were cooled down to room temperature without active cooling. Thereby it could be observed that all samples which were dissolved or partially

dissolved at the boiling point of the used solvents showed a precipitation of the bisamide during the subsequent cooling, indicating self-assembly upon cooling.

Prior to the SEM investigations of the morphology of the self-assembled structures the powders directly after the synthesis was investigated first. **Figure 65** shows the SEM images of all six bisamide powders directly after their synthesis and purification via crystallization from polar solvents. It can be seen from the images that no bisamide features fibrous structures. Instead, large crystals or undefined structures are observed for most of them. Furthermore, sheet-like structures can be observed as for example for **BA 3**. It should be noted that sheet-like structures are not uncommon for bisamides and bisureas.

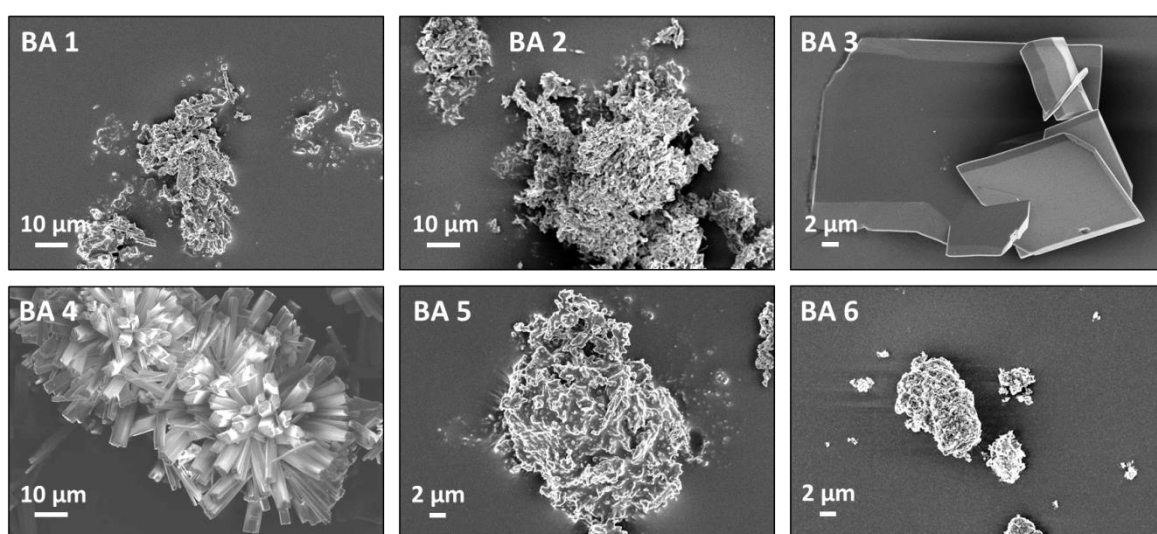


Figure 65: SEM images of the bisamides BA 1-6 after their synthesis and recrystallization. The samples were platinum sputtered before SEM investigations.

To determine the morphology of self-assembled structures, scanning electron micrographs of the samples were made after the self-assembly experiments and compared with the products after synthesis as described before. For the preparation of the SEM samples, 30 μl of the respective sample were placed on a DSC-lid after the end of the self-assembly process. The solvent was then evaporated at room temperature for several hours. The dried sample was then sputtered with platinum and examined via SEM.

The bisamide **BA 1**, which comprises a terephthalic acid core and two 4-pyridine substituents, showed partial solubility at a concentration of 100 ppm in CB. Below this concentration, the bisamide was completely soluble. This is reflected in SEM. **Figure 66** shows the SEM images of **BA 1** after the self-assembly process in CB as a function of the bisamide concentration in solution. Supramolecular fibers can not be observed for any of the samples, but partially less defined thin plate-like structures are observed. For the sample with the highest bisamide

concentration in CB, no self-assembled structures are observed, only the initial **BA 1** powder (**Figure 66a**). As the bisamide concentration decreases, the initial bisamide powder content decreases and the proportion of self-assembled plate-like structures increases. For the lowest concentration investigated, only self-assembled sheets of **BA 1** can be observed (**Figure 66d**).

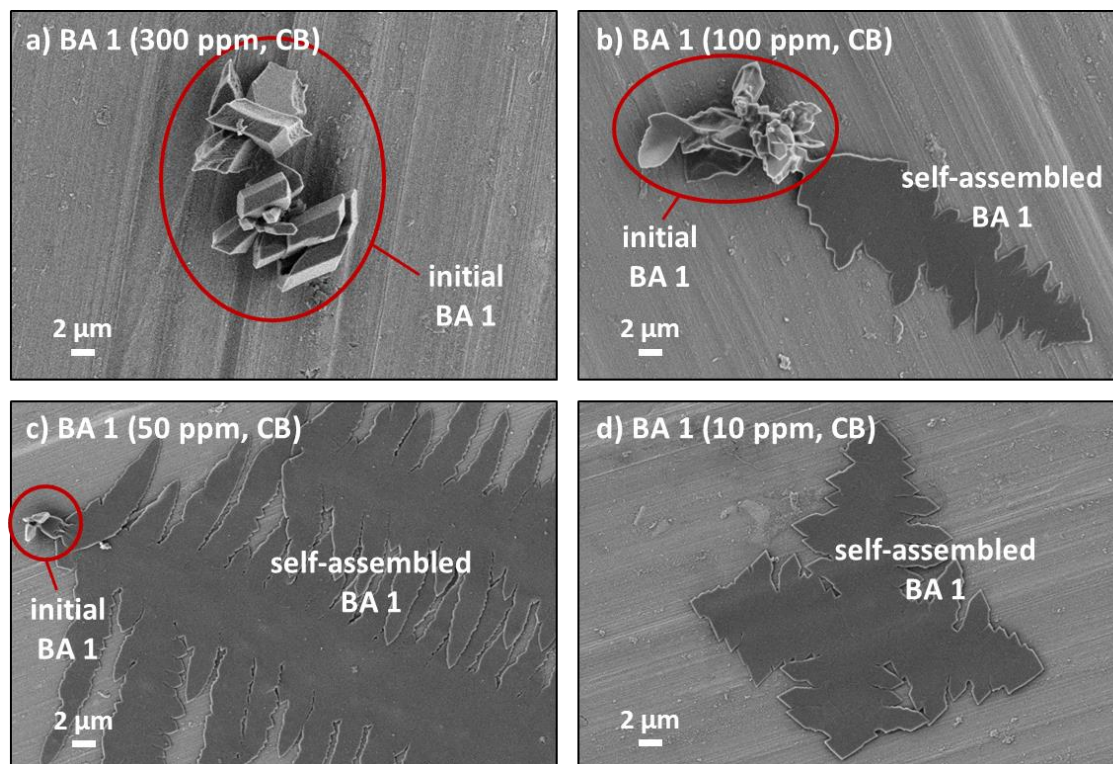


Figure 66: SEM images of initial **BA 1** and self-assembled sheet-like structures of **BA 1** subject to the bisamides concentration in CB: a) 300 ppm, b) 100 ppm, c) 50 ppm, d) 10 ppm.

A similar morphology can be observed after the self-assembly process of **BA 1** in o-DCB (see **Figures 67a-d**). Due to the higher solubility of **BA 1** in o-DCB, these structures can also be found for the highest concentration of this bisamide in solution. Furthermore, Initial **BA 1** powder cannot be observed after the self-assembly processes in o-DCB for the concentration ranges studied.

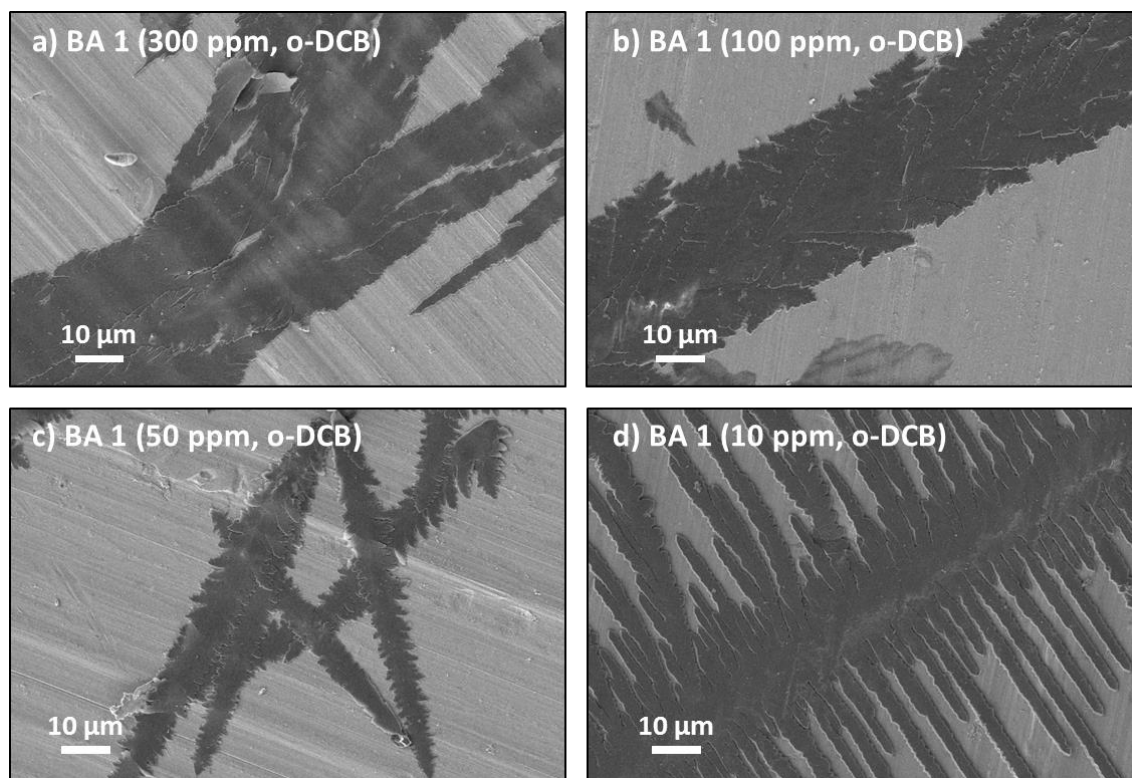


Figure 67: SEM images of self-assembled sheet-like structures of BA 1 subject to the bisamides concentration in o-DCB: a) 300 ppm, b) 100 ppm, c) 50 ppm, d) 10 ppm.

The bisamide **BA 2**, which molecular structure differs only in the orientation of the amide group from the previously described **BA 1**, is soluble in both CB and o-DCB at almost all concentrations investigated. Only for the highest concentration of 300 ppm **BA 2** is only partial soluble. **Figure 68** shows the SEM images of **BA 2** taken after the self-assembly process as a function of the concentration in solution both for the investigations in CB (**Figures 68a-d**) as well as in o-DCB (**Figures 68e-h**). Comparing the SEM images after the SA-experiment with the neat **BA 2** powder (**Figure 65**), a clear morphology change from undefined structure to a fibrous morphology can be observed.

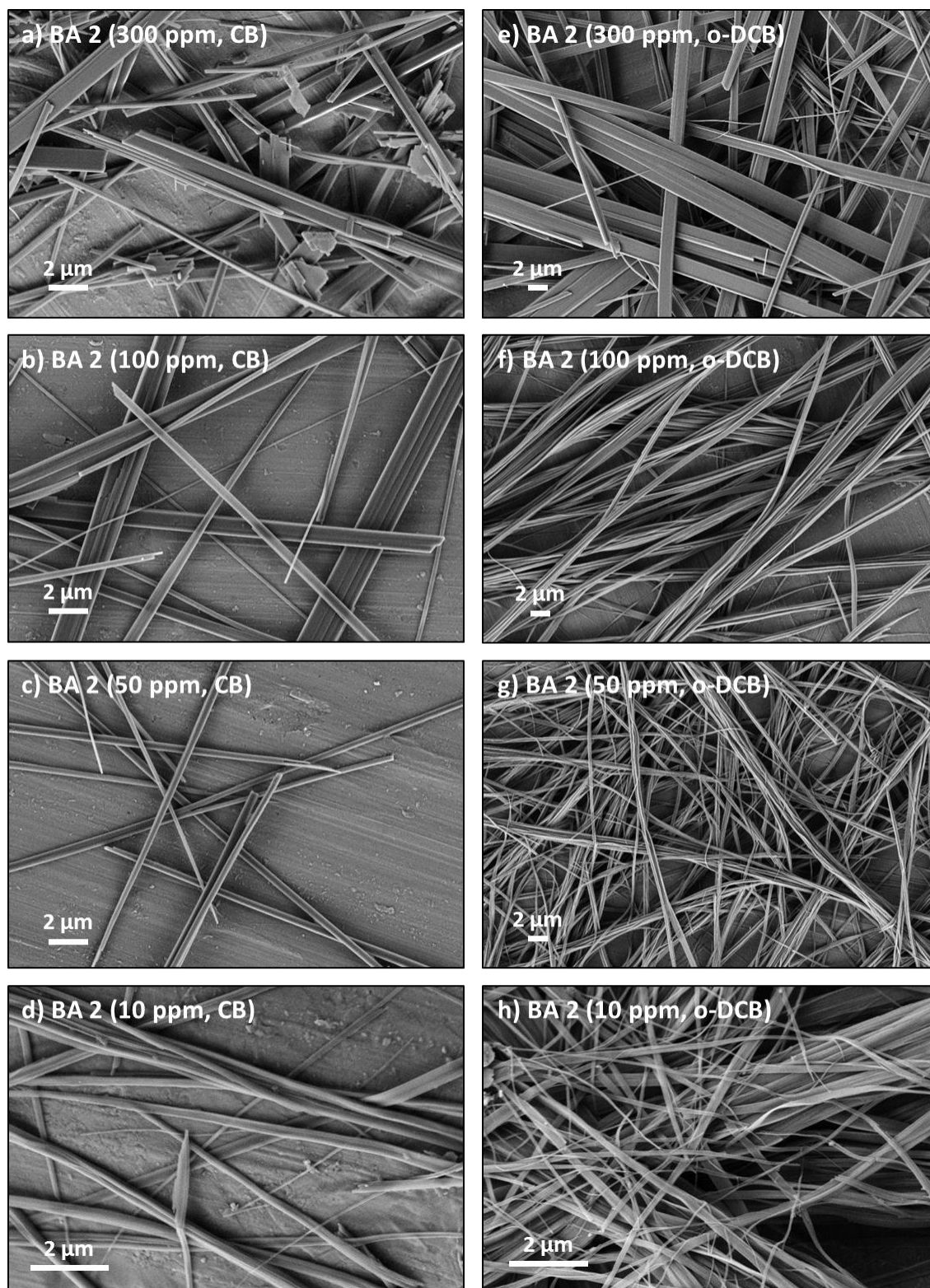


Figure 68: SEM micrographs of supramolecular nanofibers of BA 2 prepared by self-assembly upon cooling in CB (a-d) and in o-DCB (e-h) at various bisamide concentrations: (a,e) 300 ppm, (b,f) 100 ppm, (c,g) 50 ppm, (d,h) 10 ppm.

In this case, the nanorods are mainly bands together and form a ribbon-like morphology. This is clearly shown in **Figure 69**, which shows enlarged SEM images of **BA 2** after the self-assembly process in CB for a concentration of 100 ppm in solution. Accordingly, a large

number of nanorods assemble into a several micrometer wide band. The individual width of the nanorods is determined to approximately 200 nm.

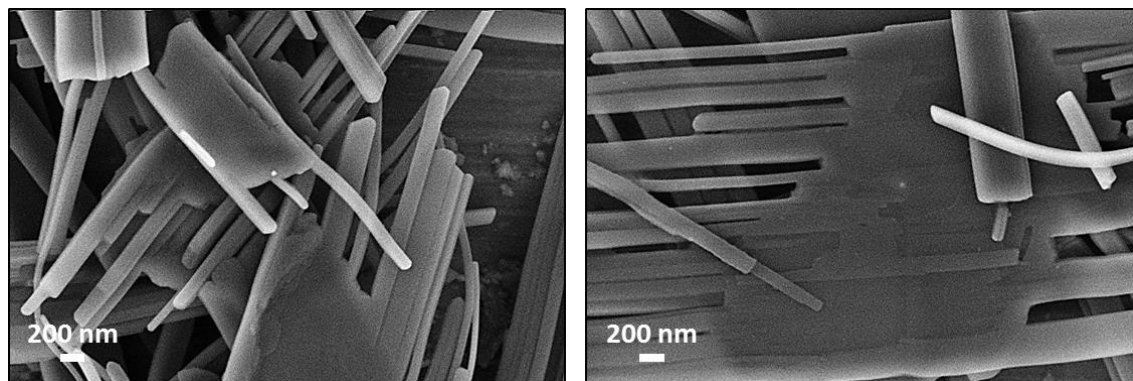


Figure 69: SEM micrographs of supramolecular nanorods of BA 2 prepared by self-assembly upon cooling in CB with a bisamide concentration of about 100 ppm. A large number of nanorods bands together into a several micrometers wide ribbon. The individual nanorods have a width of approximately 200 nm, the formed ribbons between 1-3 μm .

In order to make more precise statements with regard to the nanorods width as a function of the concentration of the bisamide and of the solvent, in turn fiber width determinations are carried out. For this purpose, at least 200 nanorods were measured for each sample in order to obtain a statistical reasonable mean value. The resulting histograms are summarized in **Figure 70**. For the highest concentration of BA 2 in solution, very large distribution widths result for both solvent systems. This may be due to the fact that ribbons were wrongly measured as single nanorods. Since the distribution width for the lower concentrations becomes significantly narrower, the rods width axes of the histograms are each provided with a break in order to visualize the fiber distribution. For both solvent systems it can be observed that as the concentration decreases, the distribution width becomes narrower and shifts towards lower fiber width values. This concentration dependence is more pronounced for the samples in o-DCB than for the samples in CB.

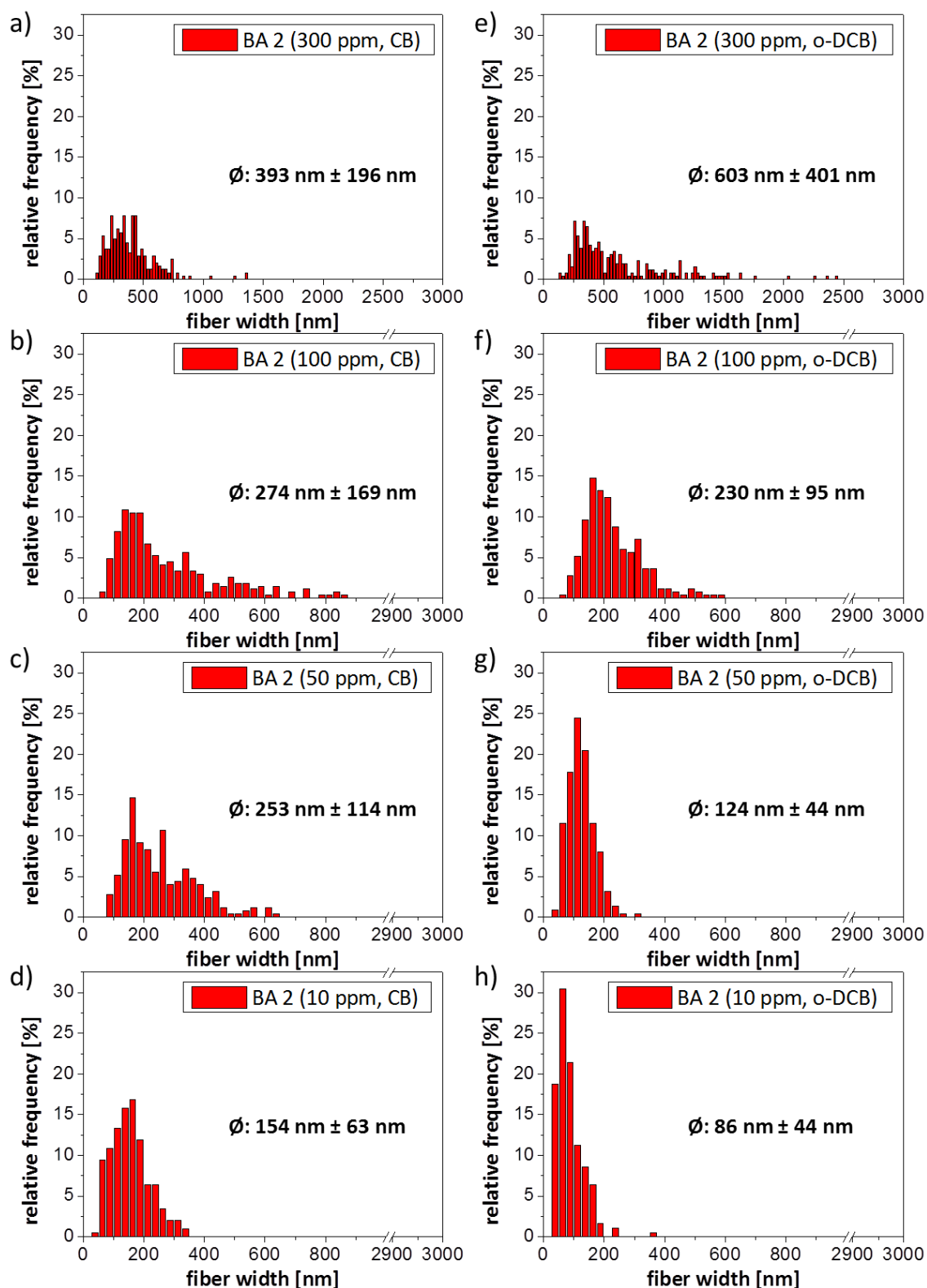


Figure 70: Fiber widths histograms of BA 2 self-assembled in CB (a-d) and o-DCB (e-h) at various concentrations: (a,e) 300 ppm, (b,f) 100 ppm, (c,g) 50 ppm, (d,h) 10 ppm. The histograms are based on at least 200 sized fibers.

The significant dependence of the mean fiber width on the bisamide concentration is plotted in **Figure 71**. The high fiber width value determined for the 300 ppm sample in o-DCB should be treated with caution, since the distribution width was immense. Nevertheless, for both systems a continuous decrease of the fiber width with decreasing concentration can be

observed. At a **BA 2** concentration of 100 ppm, the mean fiber width determined for both systems is approximately of the same order of magnitude (about 250 nm). However, as the concentration is lowered further, significantly thinner fibers are obtained in *o*-DCB than in CB. Here it was found that for the lowest concentration of 10 ppm, the average fiber width in *o*-DCB was determined to 86 nm, which is only half of that in CB (154 nm).

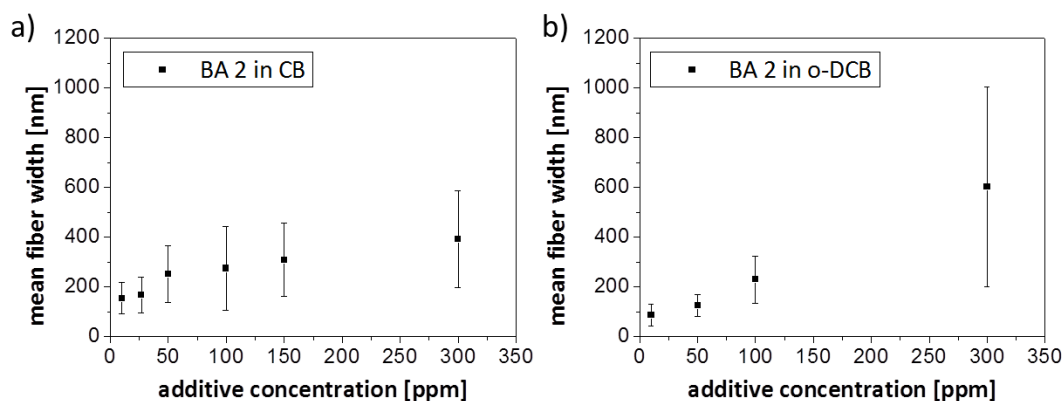


Figure 71: Influence of the bisamide concentration on the resulting mean fiber width of supramolecular fibers of BA 2 in CB (a) and *o*-DCB (b). Each mean fiber width takes into account at least 200 sized fibers.

The bisamide **BA 3** comprising a cyclohexane dicarboxylic acid core and two 4-pyridine moieties can hardly be dissolved in CB. Therefore, no morphology changes were found in this solvent. The corresponding concentration-dependent SEM images are shown in **Figure 72**.

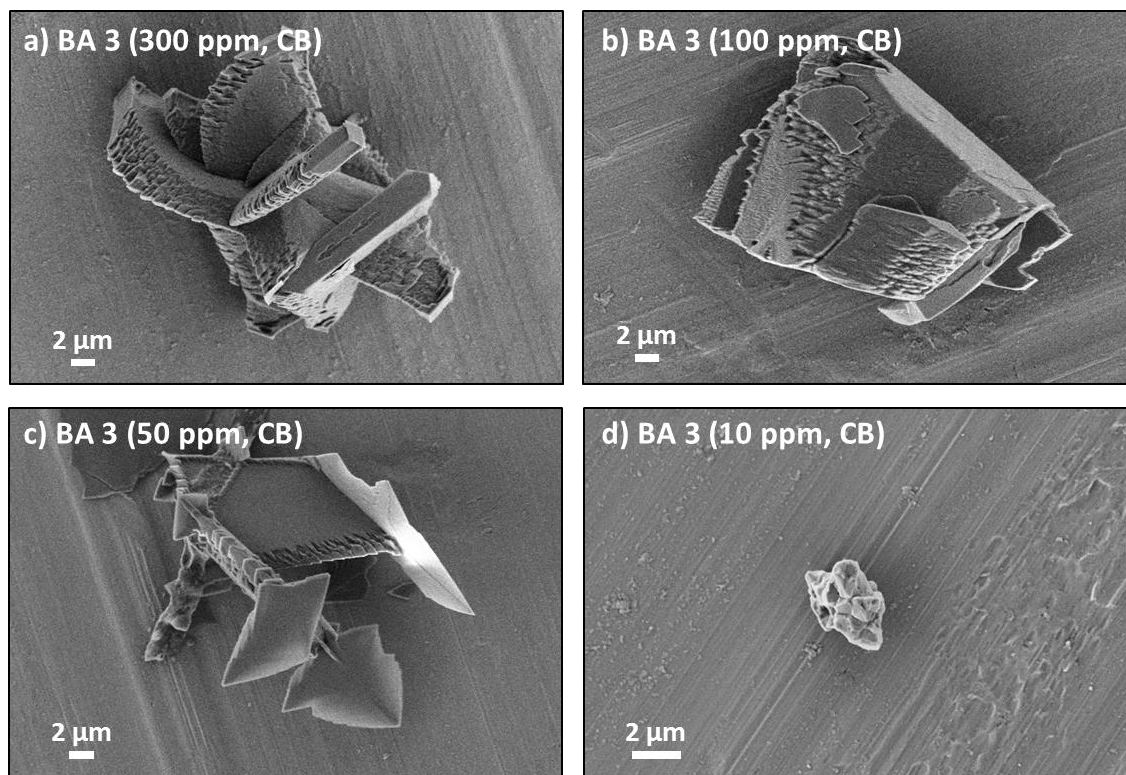


Figure 72: SEM images of BA 3 after the self-assembly experiments in CB subject to the bisamides concentration in solution: a) 300 ppm, b) 100 ppm, c) 50 ppm, d) 10 ppm. For all samples only the initial BA 3 morphology can be observed.

In *o*-DCB the solubility of **BA 3** was more pronounced. **Figure 73** shows the recorded SEM images. From these it can be seen that the morphology changes for all investigated concentrations compared to the initial powder. However, there are no supramolecular fibers, but sheet-like structures that are superimposed in several layers. For the 300 ppm sample also initial **BA 3** powder can be found as well.

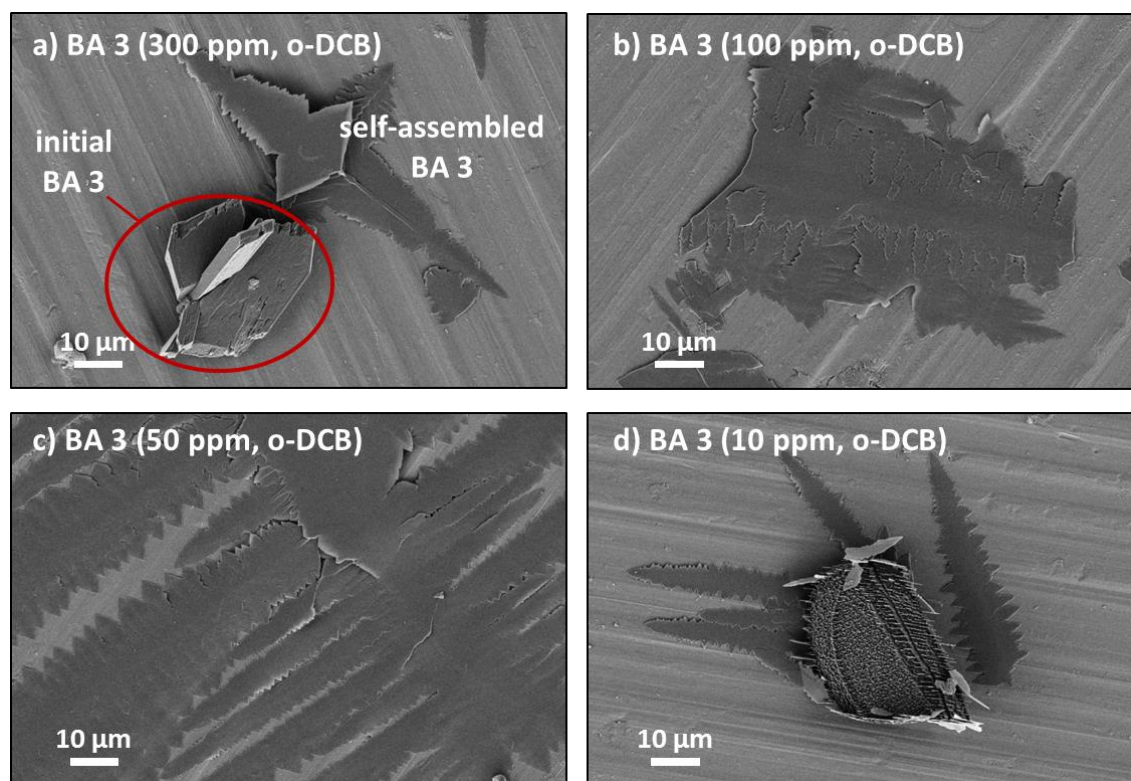


Figure 73: SEM images of self-assembled sheet-like structures of BA 3 subject to the bisamides concentration in *o*-DCB: a) 300 ppm, b) 100 ppm, c) 50 ppm, d) 10 ppm. Only for the sample with the highest concentration of bisamide in *o*-DCB the initial BA 3 morphology can be observed next to the self-assembled BA 3 sheets.

The bisamide **BA 4**, which differs only in the orientation of the amide group to the cyclohexane core from the previous discussed **BA 3**, showed good solubility in both chlorinated solvents. **Figure 74** shows the recorded SEM images after the SA-experiments. The figure shows that **BA 4** forms supramolecular nanorods in both CB and *o*-DCB. These rods can be observed in CB up to a maximum concentration of 100 ppm. For the investigations in *o*-DCB, rod-like structures can be found over the entire concentration range studied. At the minimum BA concentration (10 ppm) these rods are very short and merge into each other.

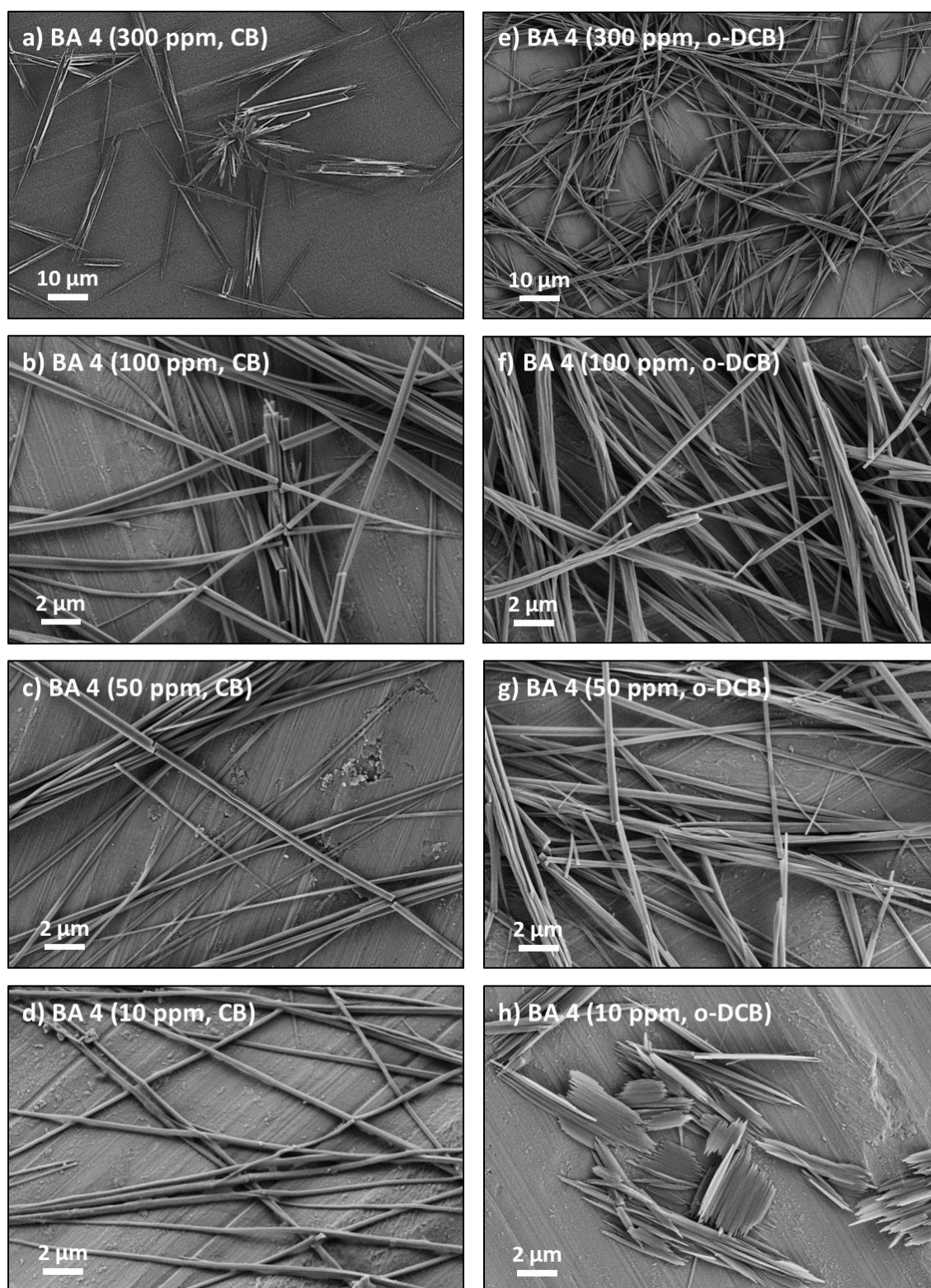


Figure 74: SEM micrographs of supramolecular nanofibers of BA 4 prepared by self-assembly upon cooling in CB (a-d) and in o-DCB (e-h) at various bisamide concentrations: (a,e) 300 ppm, (b,f) 100 ppm, (c,g) 50 ppm, (d,h) 10 ppm.

On the basis of the recorded SEM images, the individual concentration-dependent “fiber” (rods) widths were measured. The resulting histograms are summarized in the in **Figure 75**. It can be seen from the figure that the fiber width distributions continuously narrow with

decreasing **BA 4** concentration and shift to smaller values, except for the short nanorods in **Figure 74h**.

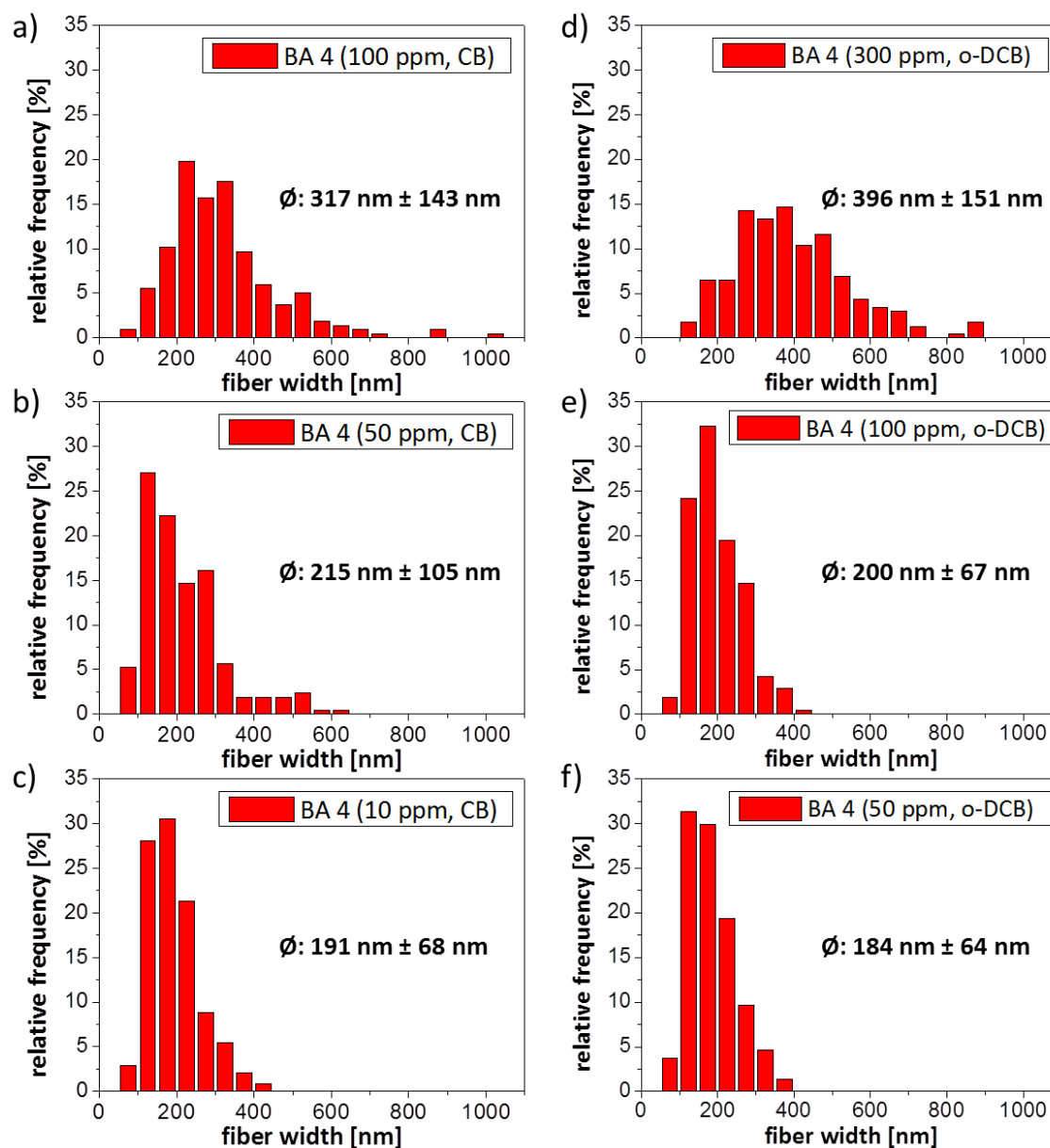


Figure 75: Fiber widths histograms of **BA 4** self-assembled in **CB** (a-c) and **o-DCB** (d-f) at various concentrations: (d) 300 ppm, (a,e) 100 ppm, (b,f) 50 ppm, (c) 10 ppm. The histograms are based on at least 200 sized fibers.

The calculated average fiber widths are plotted in **Figure 76** as a function of the **BA 4** concentration. The figure shows that the average fiber widths in both systems decrease slightly with the decrease in concentration and settle to a value of about 200 nm. Also, a further reduction in concentration would probably not lead to thinner fibers.

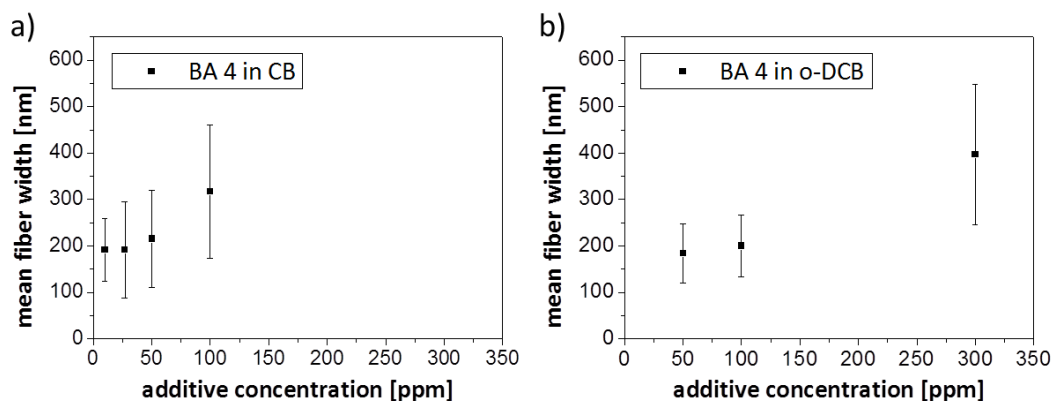


Figure 76: Influence of the bisamide concentration on the resulting mean fiber width of supramolecular fibers of BA 4 in CB (a) and o-DCB (b). Each mean fiber width takes into account at least 200 sized fibers.

In the following, the self-assembly experiments of the two cyclohexane-based bisamides **BA 5** and **BA 6** are described. The two bisamides, which both were very soluble in CB and o-DCB, differ only by their substituents. **BA 5** has two 2-pyridine substituents, whereas **BA 6** has two 3-pyridine substituents. **Figure 77** shows the SEM images of **BA 5** taken after the self-assembly process for different concentrations in solution in CB. Comparing the SEM images after the self-assembly experiment with the neat **BA 5** powder, one can see that a morphology change has taken place. The resulting structures feature leaf-like building blocks, which partially appear in a star shape. For the lowest concentration investigated, a defined morphology could not be found. Presumably **BA 5** is in that low concentration already completely soluble in CB at room temperature, so that no self-assembly upon cooling can take place. **Figure 78** shows the SEM images of **BA 5** after the self-assembly experiments in o-DCB. As in CB, this bisamide also shows no supramolecular fibers in o-DCB. Instead, double arrow-shaped layers are formed, are apparently growing away from a common center. These double-headed crystals are over 100 μm long and have their largest expansion, both in height and in width, in their center. Comparing the structures obtained after the self-assembly experiments in CB and o-DCB with one another, it becomes clear that the solvent has an enormous influence on the self-assembly behavior of one and the same molecule.

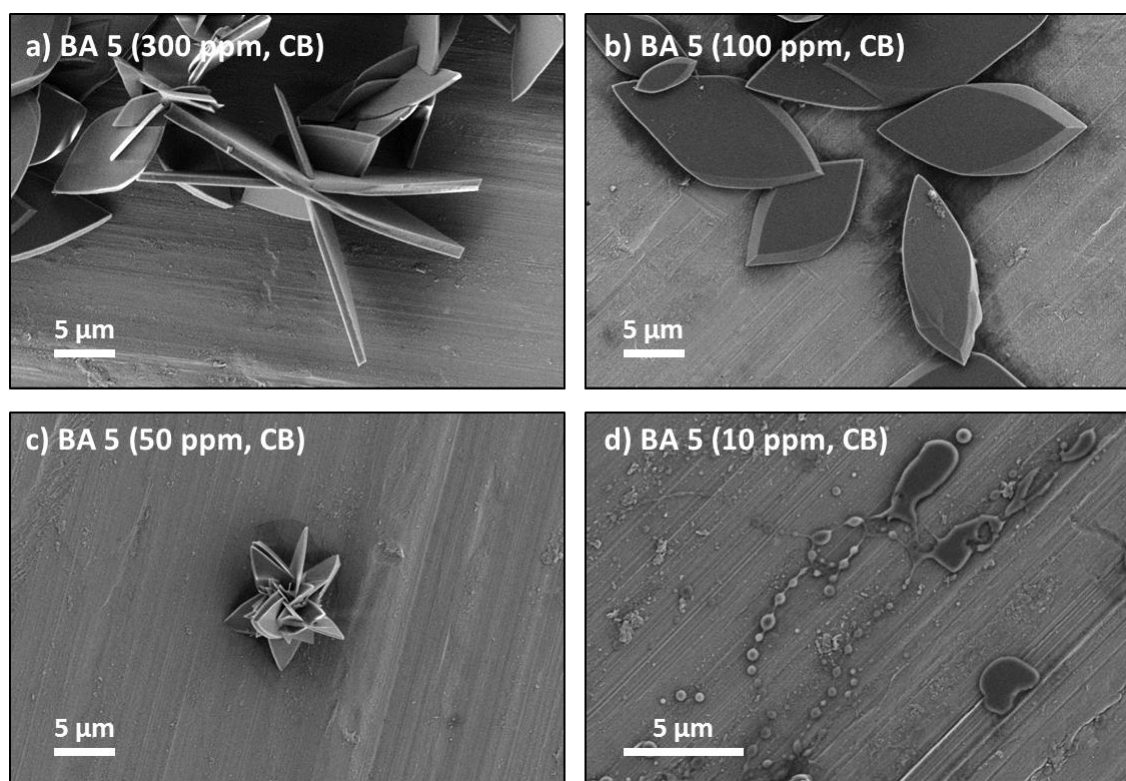


Figure 77: SEM micrographs of supramolecular leaf-like structures of BA 5 prepared by self-assembly upon cooling in CB at various bisamide concentrations: (a) 300 ppm, (b) 100 ppm, (c) 50 ppm, (d) 10 ppm.

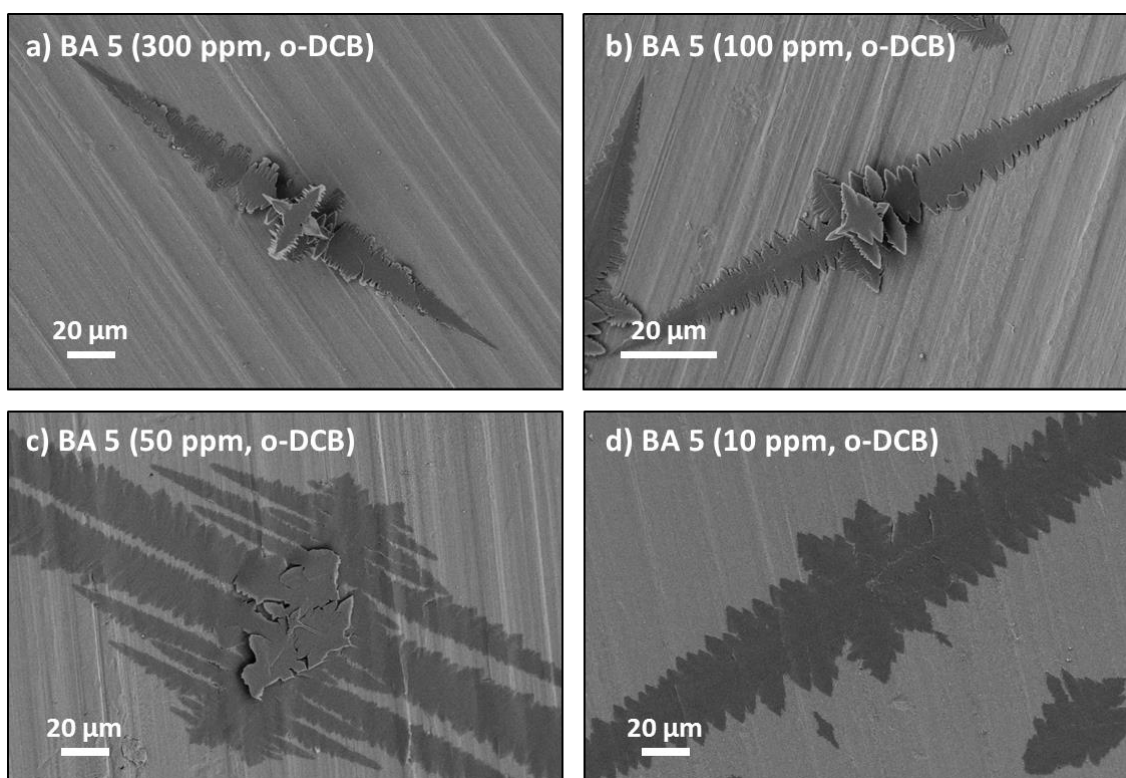


Figure 78: SEM micrographs of supramolecular layer-like structures of BA 5 prepared by self-assembly upon cooling in o-DCB at various bisamide concentrations: (a) 300 ppm, (b) 100 ppm, (c) 50 ppm, (d) 10 ppm.

Finally the **Figures 79** and **80** show the SEM images after the self-assembly experiments of **BA 6** in CB and o-DCB as a function of the bisamide concentration in solution. Self-assembly to nanostructures was successful performed in both solvent systems. In CB (**Figure 79**)

individual plates of about 2 μm in width and 20 μm in length can be observed. With reduced concentration, the quantity of these structures decreases significantly and, moreover, they become more transparent, which is an indication that the plate thickness also decreases.

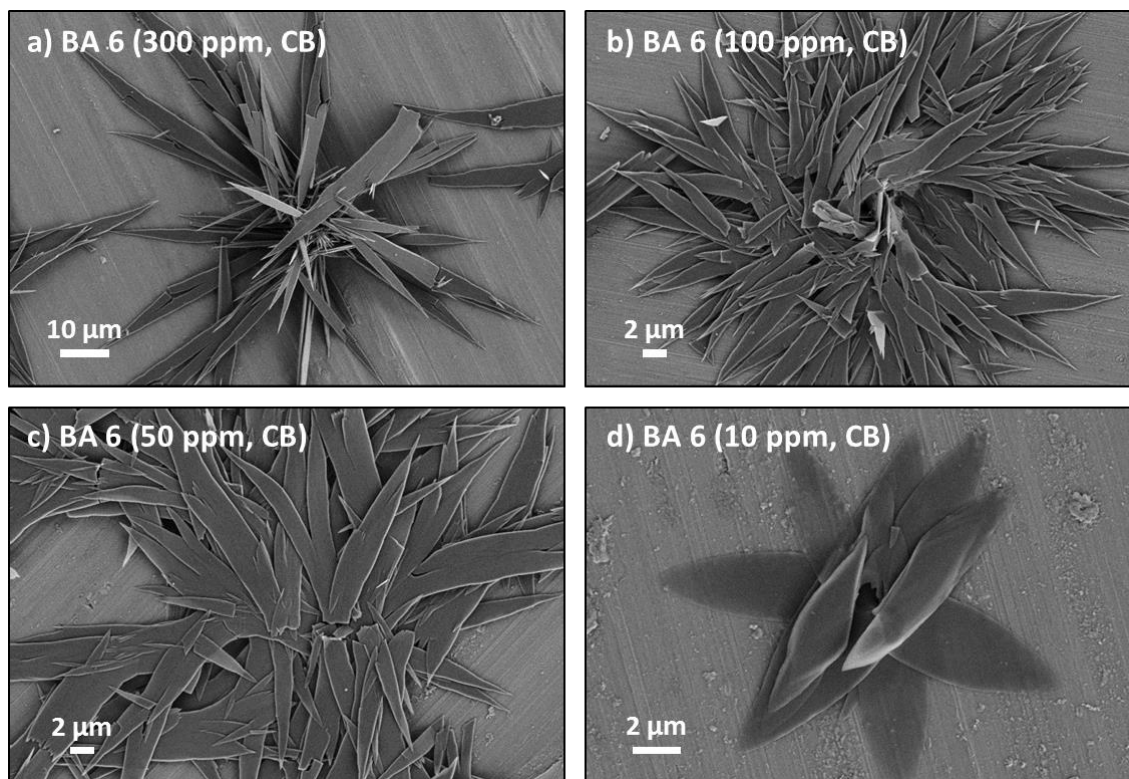


Figure 79: SEM micrographs of supramolecular flower-like structures of BA 6 prepared by self-assembly upon cooling in CB at various bisamide concentrations: (a) 300 ppm, (b) 100 ppm, (c) 50 ppm, (d) 10 ppm.

In *o*-DCB (**Figure 80**) completely different structures are formed after the self-assembly experiments. These are less-defined large crystals, with a length of about 20 μm and a width of 10 μm . For the lowest BA 6 concentration star-shaped crystals can also be found.

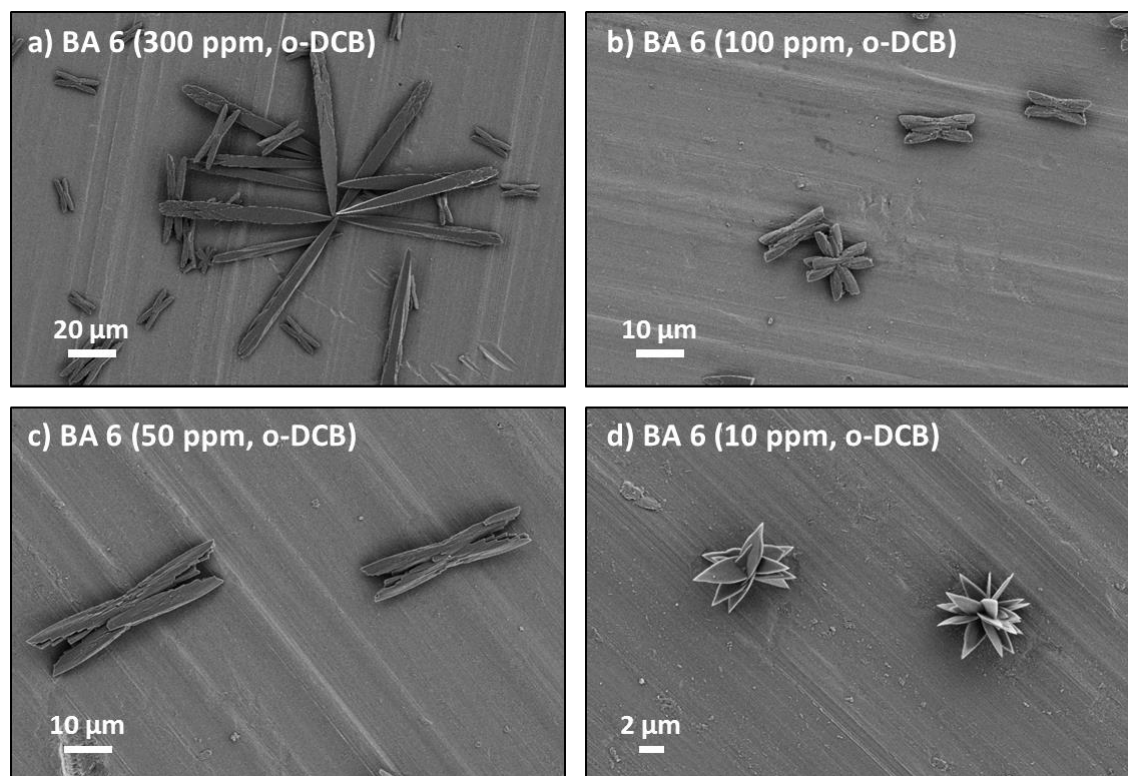


Figure 80: SEM micrographs of supramolecular undefined structures of BA 6 prepared by self-assembly upon cooling in o-DCB at various bisamide concentrations: (a) 300 ppm, (b) 100 ppm, (c) 50 ppm, (d) 10 ppm.

3.3.6 Summary of the determined nanostructures

With all six pyridine-containing bisamides investigated in this work, supramolecular self-assembly could be observed in the chlorinated solvents. For the most of them defined morphologies could be found. Four bisamides (**BA 1**, **BA 3**, **BA 5** and **BA 6**) showed layer-like structures. Compared with each other, these structures, however, are completely different. Thus not only sheet-like structures but also double-arrow-shaped building blocks and leaf-like forms could be detected on the basis of the SEM images. These bisamides have in common that they all have a “C-centering” of the amide group, but differ in core and substituents. Furthermore, it has been shown that the solvent has significant influence on the structure formation of these BA molecules after the self-assembly experiments. The remaining two bisamides (**BA 2** and **BA 4**) showed supramolecular fiber-like structures in both CB and o-DCB after the self-assembly experiments. **Table 8** summarizes the calculated mean “fiber” widths of these bisamides as a function of the particular concentration and the solvent. The marked data indicate a partial solubility of the corresponding BA at the respective concentration in solution and, thus, takes into account that initial powder morphology is also present. The two bisamides **BA 2** and **BA 4** are the only two bisamides in this work which have “N-centering” of the amide group and differ only in their central core. **BA 2** has a benzene core, whereas **BA 4**

has a cyclohexane core. Comparing the determined fiber widths of both BA's shows that they are similar in both CB and o-DCB. However, it can also be observed that the resulting fiber widths in o-DCB are somewhat lower on average than in CB. The thinnest fibers, with a mean width of 86 nm, can be shown for **BA 2** for the lowest concentration in o-DCB.

Table 8: Summarized results of the calculated mean fiber widths of the pyridin-containing bisamides in dependency of the used solvents and the bisamide concentration. The marked data indicate a partial solubility of the corresponding bisamide at the respective concentration in solution.

	BA 2	BA 4
chlorobenzene		
concentration [ppm]	mean fiber width [nm]	mean fiber width [nm]
300	393*	
100	274	317
50	253	215
10	154	191
ortho-dichlorobenzene		
concentration [ppm]	mean fiber width [nm]	mean fiber width [nm]
300	603*	396*
100	230	200
50	124	184
10	86	

4 Nucleation of poly(3-hexylthiophene) with supramolecular additives

This chapter focuses on the nucleation of poly(3-hexylthiophene) (P3HT) in bulk using supramolecular nucleating agents. To evaluate the nucleation efficiency of individual additives with respect to nucleation capability of P3HT, neat bulk P3HT must be characterized in detail first. For this purpose, three different P3HT grades were selected and thermally and analytically characterized.

4.1 Characterization of different P3HT grades

4.1.1 Analytical characterization of different P3HT grades

Three commercial available P3HT grades were selected and analyzed to study the influence of molecular weight (M_w), regioregularity (RR) and polydispersity (PDI) on the thermal behavior of P3HT. These P3HT grades had the trade names *RMI_001_EE1* (hereinafter **P3HT-1**), *RMI_001_EE2* (hereinafter **P3HT-2**) and *Sepiolid P200* (hereinafter **P3HT-3**) from *Rieke Metals Incorporation*. To determine molecular weight and polydispersity, gel permeation chromatography (GPC) measurements in THF were performed. The manufacturer's specifications regarding the regioregularity have been adopted. The results of the analytical investigations are listed in **Table 9**. The table shows that the data provided by the supplier differ to some extent from the data determined. Thus, in the following the more accurate data obtained from the analytical characterizations are used. The P3HT-Grade **P3HT-2** shows the largest molecular weight ($62 \text{ kg}\cdot\text{mol}^{-1}$) and the highest PDI (2.1). The P3HT-Grade **P3HT-3** has the lowest M_w ($20 \text{ kg}\cdot\text{mol}^{-1}$) and the smallest PDI (1.6). The values of both M_w and PDI of **P3HT-1** (M_w : $31 \text{ kg}\cdot\text{mol}^{-1}$, PDI: 1.8) are between the data of the other two P3HT grades. Regarding regioregularity, **P3HT-1** shows the highest value, **P3HT-3** the lowest one.

Table 9: Analytical data of three commercial available P3HT grades provided by the supplier (*Rieke Metals Incorporation*) and remeasured at the department MC I (University of Bayreuth).

	P3HT-1		P3HT-2		P3HT-3	
	Supplier	MC I	Supplier	MC I	Supplier	MC I
M_w [$\text{kg}\cdot\text{mol}^{-1}$]	30	31	60-75	62	20-40	20
PDI	1.8	1.8	1.7-1.9	2.1		1.6
RR [%]	97	n.d.	≥ 96	n.d.	≥ 95	n.d.

4.1.2 Thermal characterization of the different P3HT grades

In order to determine decomposition and phase transitions, a detailed thermal characterization by means of thermogravimetric analysis (TGA) and dynamic differential calorimetry (DSC) measurements was performed.

Thermogravimetric analysis

Thermogravimetric analysis can be used to determine the temperature range of a material in which it is thermally stable. Furthermore, this method provides information on decomposition temperatures and the type of decomposition.

Since P3HT decomposes thermo-oxidative at approximately 285 °C in an oxygen atmosphere, all samples were measured under inert gas (N₂).^[241] TGA data were recorded with a heating rate of 10 K·min⁻¹ in a temperature range from 30 °C to 700 °C. All P3HT grades feature almost identical thermograms. **Figure 81** shows, exemplarily, the TGA thermogram of **P3HT-2**, the TGA thermograms for **P3HT-1** and **P3HT-3** are shown in **Appendix 8.4**. **Figure 81** shows that **P3HT-2** is thermally stable under N₂ atmosphere up to 400 °C. A five percent mass loss can be observed 447 °C (dashed blue line). Subsequently, a step-like mass loss of about 70 % up to 550 °C can be observed. These results are also consistent with data described in literature.^[241]

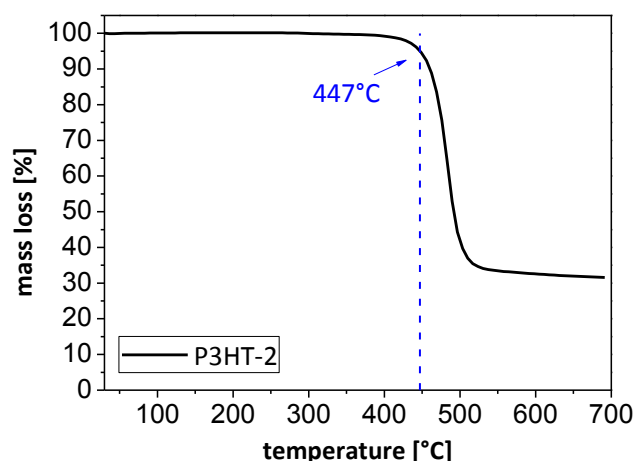


Figure 81: Thermogravimetric analysis thermogram of P3HT-2. TGA data were recorded with a heating rate of 10 K·min⁻¹ in a temperature range from 30 °C to 700 °C under nitrogen atmosphere. The inserted dashed blue line indicate 5 % mass loss up to the current temperature.

Dynamic differential calorimetry (DSC) measurements

DSC measurements provide information on melting, crystallization and recrystallization temperatures as well as a possible glass transition temperature. Based on the previous TGA measurements, a high temperature stability of all P3HT grades is determined. According to literature, P3HT with a M_w of about 30 kg·mol⁻¹ has a melting point of about 240 °C. However,

previous studies at our department have shown that a temperature of about 300 °C is necessary to completely melt all P3HT crystallites. If the sample is not heated up to this temperature, self-nucleation takes place and the resulted crystallization temperature is falsified. For this reason, a maximum heating temperature of 300 °C, with an isothermal holding step for five minutes, was selected for the following DSC measurements. In total, this heating and cooling cycle is performed three times for every grade with a heating and cooling rate of 10 K·min⁻¹, respectively. A detailed description of sample preparation and temperature profiles can be found in **Experimental 7.1**.

Figure 82 shows the recorded DSC thermograms of the different P3HT grades. It can be clearly observed that the first melting and crystallization peaks of all grades differ significantly from their respective second and third peaks. This is frequently observed with polymers due to the thermal history which must be erased first. Therefore, the first heating and cooling curve within the DSC thermograms is not taken into account for the evaluation of the data.

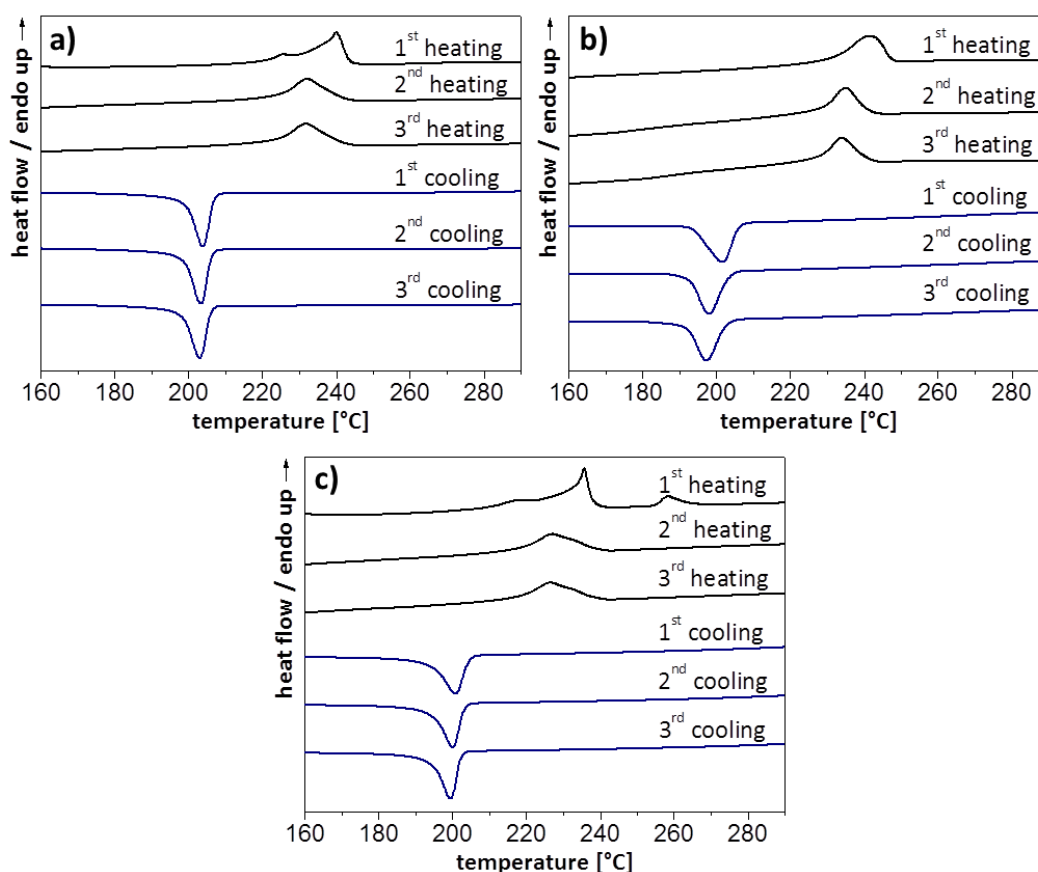


Figure 82: DSC thermograms of neat (a) P3HT-1, (b) P3HT-2 and (c) P3HT-3. Data were recorded with heating and cooling rates of 10 K·min⁻¹.

The averaged results from several DSC measurements of the different P3HT grades are listed in **Table 10**. Only the values of the second heating and cooling curves were used for the calculation of the mean values.

Table 10: Thermal characteristics of different P3HT grades obtained via DSC studies: Melting temperature T_m , melting enthalpy ΔH_m , standard crystallization temperature T_c^0 and crystallization enthalpy ΔH_c .

	T_m [°C]	ΔH_m [J/g]	T_c^0 [°C]	ΔH_c [J/g]
P3HT-1 (RR = 97 %; $M_w = 31 \text{ kg}\cdot\text{mol}^{-1}$)	232.1	21.0	203.0	-20.7
P3HT-2 (RR \geq 96 %; $M_w = 62 \text{ kg}\cdot\text{mol}^{-1}$)	235.4	18.9	198.6	-19.3
P3HT-3 (RR \geq 95 %; $M_w = 20 \text{ kg}\cdot\text{mol}^{-1}$)	226.8	16.8	199.3	-18.3

Table 10 shows that the mean values regarding melting temperature (T_m) and crystallization temperature (T_c^0) of the different P3HT grades differ. For **P3HT-2**, which has the largest M_w , the highest melting temperature of about 235 °C was determined. The lowest melting temperature shows **P3HT-3** (227 °C), which has the lowest M_w . The melting temperature of **P3HT-1** amounts to 232 °C and is thus between the values of the other two grades. On the basis of these results, a tendency of the melting temperature of P3HT as a function of the molecular weight can be observed. Here, the higher the M_w , the higher the observed T_m . This tendency does not apply to the determined T_c^0 , since both **P3HT-2** (198.6 °C) and **P3HT-3** (199.3 °C) have approximately the same crystallization temperature. The highest T_c^0 , however, shows **P3HT-1** with approximately 203 °C. Considering the enthalpies a clear tendency can be observed and is attributed to the regioregularity. The higher RR, the higher are the resulting enthalpies. This applies to both ΔH_m and ΔH_c . The reason for that is, that a higher RR leads to more ordered crystallites and thus to a higher enthalpy.

Long-term stability measurements of the different P3HT grades

Since the P3HT samples are subjected to prolonged thermal stress for the subsequent self-nucleation tests, the thermal long-term stability of the different grades must be investigated. Therefore, the different P3HT grades are examined by means of DSC measurements with respect to their long-term stability. For these measurements, the same temperature profile as in the previous DSC measurements is used; however, the heating and cooling cycle is repeated ten times.

Figure 83 shows the recorded heating and cooling curves of the stability measurement of **P3HT-1**. In this case, the second heating curve shows a melting peak T_m of approximately 232 °C. This peak decreases after ten heating and cooling cycles only by 1.5 °C. The second cooling curve has a crystallization temperature of 203 °C and also shifts only insignificantly after heating and cooling the sample ten times, so that the crystallization temperature of **P3HT-1** amounts to 202 °C after the 10th cooling. For both ΔH_m and ΔH_c , slight decreases in

the values can be observed. After ten times of applied thermal stress, the enthalpy values decrease by approximately 10 %.

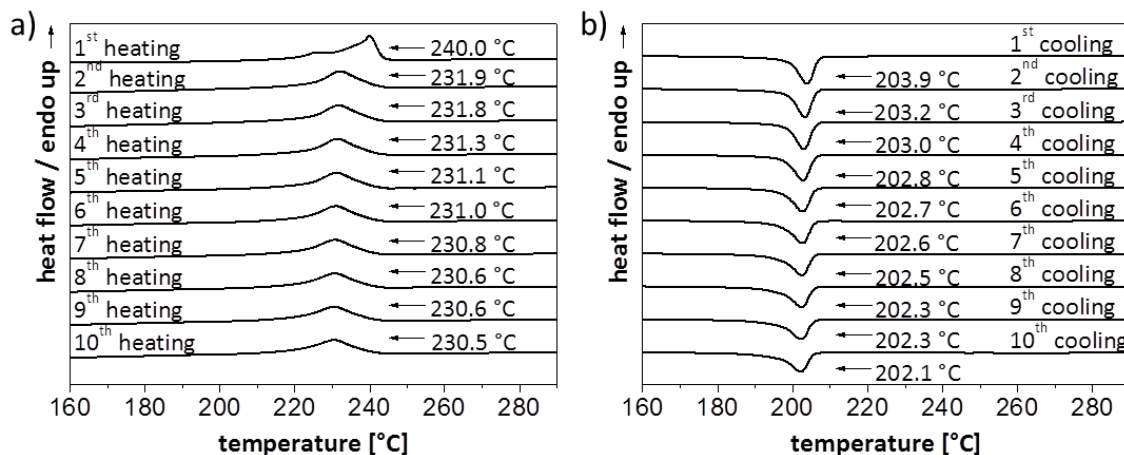


Figure 83: DSC thermographs of the long-term stability measurements of neat P3HT-1; (a) heating curves, (b) cooling curves. Data were recorded with heating and cooling rates of $10 \text{ K}\cdot\text{min}^{-1}$. The crystallization temperature slightly decreases with increasing cycle number.

Figure 84 shows the heating and cooling curves of the long-term stability measurement of P3HT-2. The maximum of T_m amounts to $235 \text{ }^\circ\text{C}$. After ten heating and cooling cycles, this decreases by about $2 \text{ }^\circ\text{C}$. The second cooling curve has a T_c of about $198 \text{ }^\circ\text{C}$. After ten times of thermal stress, this is shifted to $195 \text{ }^\circ\text{C}$. The values of the enthalpies also show a slight decrease. For ΔH_m , the value at the end of the period was reduced by 15 %, ΔH_c even by 20 %. However, it must be noted that for the self-nucleation tests, the maximum heating temperature is significantly reduced after the third heating cycle and therefore the P3HT-2 is no longer exposed to these extreme stresses. Furthermore, the stability measurements show that the enthalpies have remained virtually unchanged up to the fourth process cycle, which is why the self-nucleation tests can be performed without any concerns.

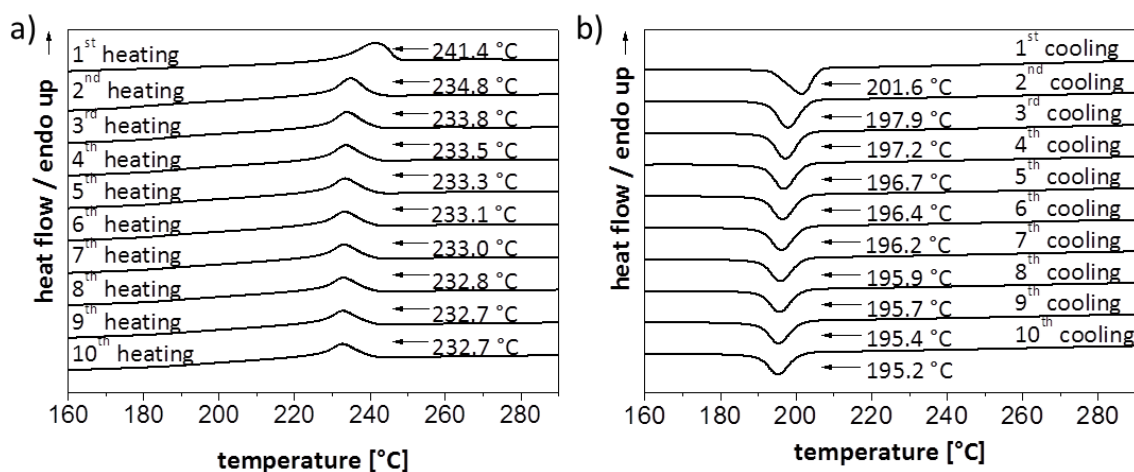


Figure 84: Differential scanning thermographs of the stability measurements of neat P3HT-2: (a) heating curves, (b) cooling curves. Data were recorded with heating and cooling rates of $10 \text{ K}\cdot\text{min}^{-1}$. The crystallization temperature slightly decreases with increasing cycle number.

Figure 85 shows the heating and cooling curves of the stability measurement of P3HT-3. On the basis of the second heating curve, a T_m at approximately 227 °C can be observed, which decreases after 10 times of heating and cooling by about 2 °C. The crystallization temperature shifts from 200 °C to 198 °C, also by 2 °C, after this prolonged thermal stress. For both ΔH_m and ΔH_c , only a slight drop in the enthalpy value (-5 %) can be observed after ten times of applied thermal stress.

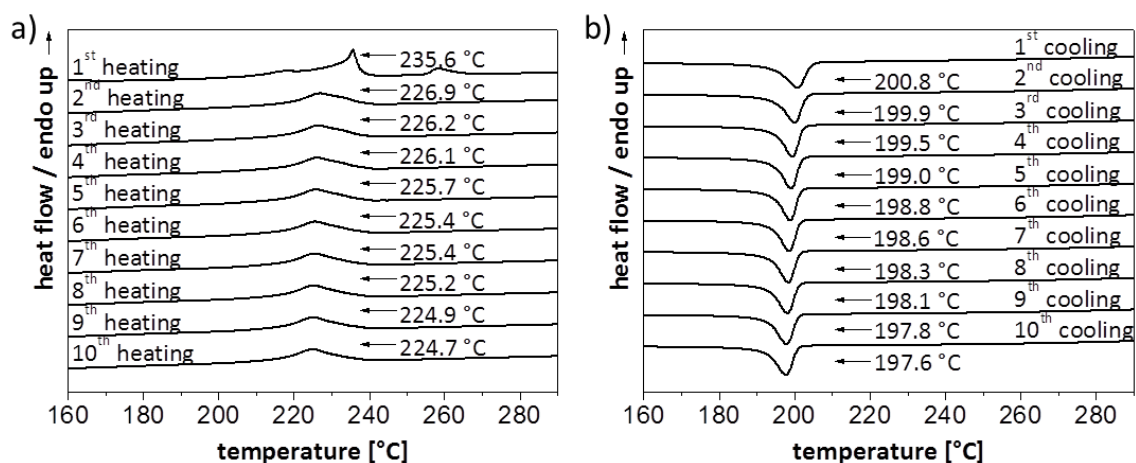


Figure 85: Differential scanning thermographs of the stability measurements of neat P3HT-3: (a) heating curves, (b) cooling curves. Data were recorded with heating and cooling rates of 10 K·min⁻¹. The crystallization temperature slightly decreases with increasing cycle number.

In summary, it can be seen from the stability measurements that all three P3HT grades are thermally stable when a thermal stress is applied and only minimal decomposition processes occur under these extreme temperature conditions. Accordingly, the self-nucleation studies can be performed without thermal concerns.

Self-nucleation measurements of the different P3HT grades

Via self-nucleation experiments it is possible to determine the maximum crystallization temperature of a neat polymer. Therefore self-nucleation experiments were performed adopting the method by Lotz et al.^[161] for polypropylene and Richter et al.^[160] for polyamides and polybutylene terephthalate to determine the respective T_c^{\max} of the three different P3HT grades. To create a temperature profile, four steps are required for self-nucleation. These are shown in **Figure 86**. In the first step (A), the sample is completely molten to erase the thermal history of the polymer. Subsequently, in the second step (B), a crystalline "standard" phase (T_c^0) is produced via crystallization upon cooling.

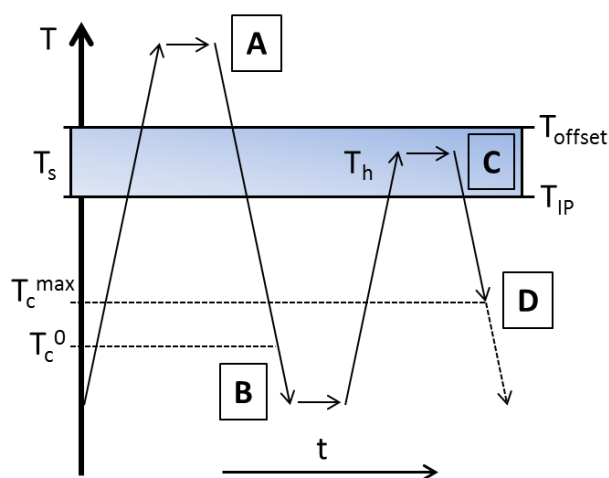


Figure 86: Schematic representation of the temperature profile as a function of the time during a self-nucleation experiment. (A) Erasure of the thermal history of the polymer, (B) determination of the standard crystallization temperature T_c^0 , (C) partially melting of the polymer at the holding temperature T_h in the area of T_s (melting area) between the inflection point (T_{IP}) of the second derivation of the melting peak and its offset (T_{offset}), (D) determination of the maximum crystallization temperature T_c^{\max} .

Then, the real step of self-nucleation takes place. The polymer is partially molten (C) at a temperature T_h (holding temperature). This temperature is located in the area of T_s (partially melting area) between the inflection point (T_{IP}) of the second derivation of the melting peak and its offset (T_{offset}) (shaded region in **Figure 87**). Since the polymer is only partially molten, unmolten crystal fragments remain. These fragments can act as perfect nuclei for the crystallization of the polymer upon cooling (D). As a result, the crystallization temperature of the polymer shifts towards higher values. By lowering the holding temperature in the area of T_s , the maximum crystallization temperature T_c^{\max} of the polymer can be determined.

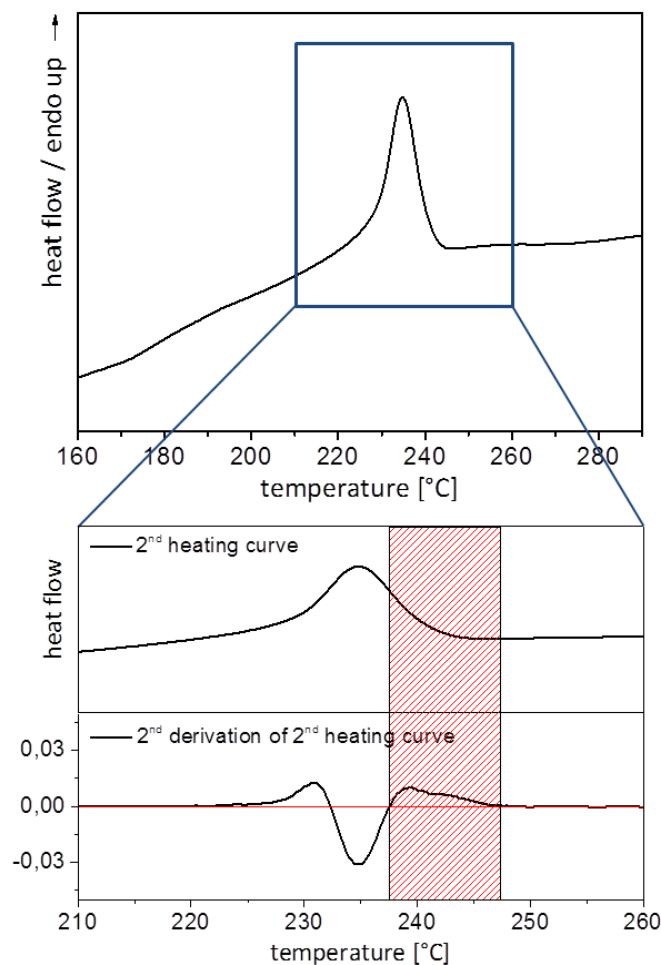


Figure 87: Melting endotherm of P3HT-2 (top) and indication of the partial melting range (shaded region) used for self-nucleation experiments (bottom).

On the basis of the previous DSC results, an individual temperature profile for the self-nucleation tests was determined for each grade. **Figure 88** shows the heating and cooling curves of the self-nucleation experiments of **P3HT-1**. After two standard cycles (150 °C - 300 °C), the maximum heating temperature was reduced to 248 °C and then reduced by a further two Kelvin for each additional cycle. From **Figure 88a** it can be seen that the maximum melting temperature of **P3HT-1** increases with decreasing maximum heating temperature by about 3 °C. This is due to the fact that only the smaller P3HT crystallites can melt at the present heating temperature, whereas the larger crystallites do not completely melt. On cooling, these unmelted crystallites then nucleate the molten P3HT and thus become larger than in the cycle before. These larger crystallites require a longer residence time at a certain temperature in the next step until they are molten and so the melting range shifts to larger values. **Figure 88b** shows that the crystallization temperatures also increase with decreasing maximum heating temperature. The reason for that is that the crystallization of molten P3HT can still occur on as yet unmelted P3HT crystallites. Thus, the higher the

maximum heating temperature is chosen, the less nuclei, which initiate crystallization, are present.^[161] The highest crystallization temperature T_c^{\max} is observed for a maximum heating temperature T_h^{\max} of 244 °C and amounts to 205.3 °C. Comparing T_c^{\max} with T_c^0 of **P3HT-1**, a ΔT_c ($T_c^{\max} - T_c^0$) of 2.3 °C can be determined.

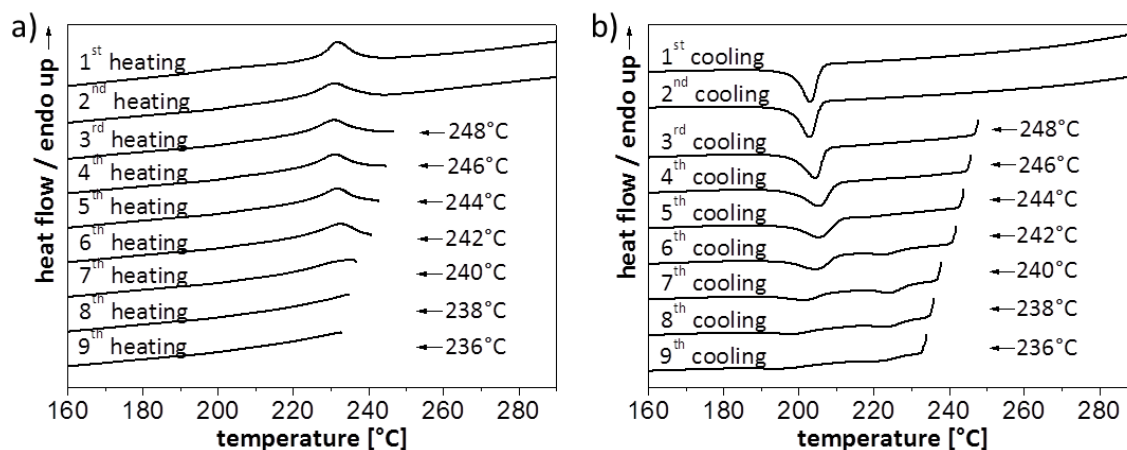


Figure 88: Crystallization exotherms of neat P3HT-1 for different self-nucleation temperatures; (a) heating curves, (b) cooling curves. A maximum polymer crystallization temperature T_c^{\max} of 205.3 °C was determined at a maximum heating temperature T_h^{\max} of 244 °C. DSC heating and cooling rate: 10 K·min⁻¹.

Figure 89 shows the recorded heating and cooling curves of the self-nucleation experiments of **P3HT-2**. It can be observed that T_m shifts to larger values with decreasing maximum heating temperature due to the fact that under these conditions predominantly large P3HT crystallites are present (Figure 89a). The shift of the T_c to higher values appears very clearly within this series (Figure 89b). Determined T_c^{\max} amounts to 207.7 °C and belongs to a T_h^{\max} of 244 °C. Accordingly, a ΔT_c of almost 10 °C could be achieved for **P3HT-2** by self-nucleation.

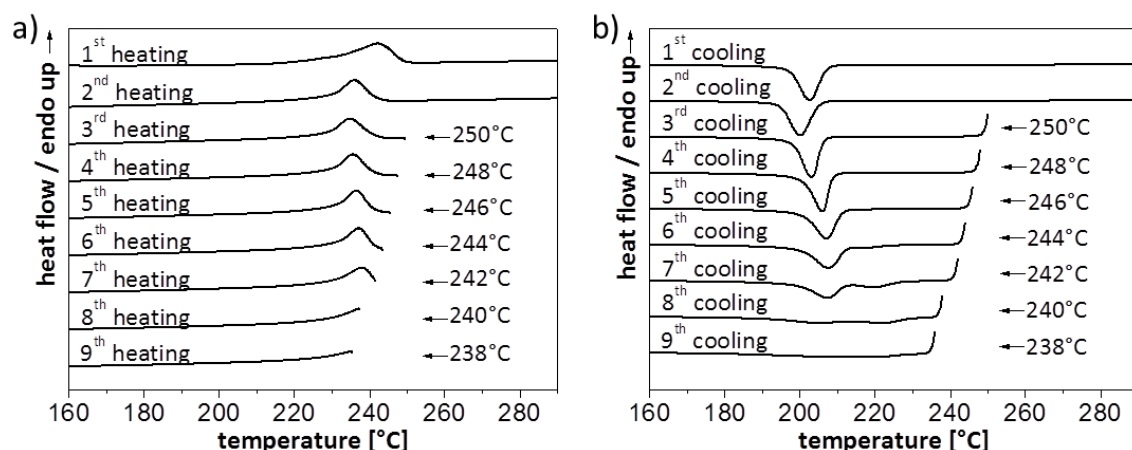


Figure 89: Crystallization exotherms of neat P3HT-2 for different self-nucleation temperatures; (a) heating curves, (b) cooling curves. A maximum polymer crystallization temperature T_c^{\max} of 207.7 °C was determined at a maximum heating temperature T_h^{\max} of 244 °C. DSC heating and cooling rate: 10 K·min⁻¹.

Figure 90 shows the heating and cooling curves of the self-nucleation experiments of **P3HT-3**. Considering the values of the melting points of the first five heating curves, excluding the first heating curve, they are nearly constant (226 °C). For the remaining three heating cycles T_m is

increased by 5.5 °C up to 231.5 °C. T_c also increases with decreasing T_h^{\max} , as it could be seen for the previous two P3HT grades. T_c^{\max} determined by self-nucleation can be observed for a T_h^{\max} of 242 °C and amounts to 199.9 °C. This corresponds to an increase of only about 0.6 °C compared to T_c^0 of **P3HT-3**.

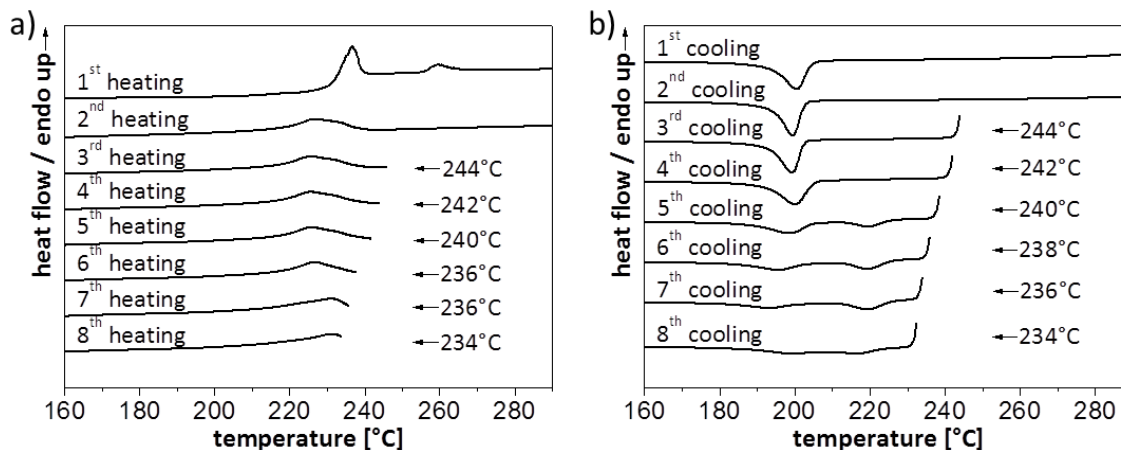


Figure 90: Crystallization exotherms of neat P3HT-3 for different self-nucleation temperatures; (a) heating curves, (b) cooling curves. A maximum polymer crystallization temperature T_c^{\max} of 199.9 °C was determined at a maximum heating temperature T_h^{\max} of 242 °C. DSC heating and cooling rate: 10 K·min⁻¹.

Comparison of the self-nucleation measurements of the different P3HT grades

Hereinafter, the results of the self-nucleation experiments of the three different P3HT grades are compared. For this purpose, the measured minimum and maximum crystallization temperatures, as well as the maximum heating temperatures T_c^{\max} , which are necessary to reach T_c^{\max} , and ΔT_c are listed in **Table 11**.

Table 11: Determined data of T_c^0 , T_c^{\max} , T_h^{\max} and ΔT_c from the self-nucleation measurements.

Grade	T_c^0 [°C]	T_c^{\max} [°C]	T_h^{\max} [°C]	ΔT_c [°C]
P3HT-1	203.0	205.3	244.0	2.3
P3HT-2	198.6	207.7	244.0	9.1
P3HT-3	199.3	199.9	242.0	0.6

On the basis of the results of the initial DSC investigations it has already been shown that the different P3HT grades differ in their thermal characteristics. This is also the case for the ascertained maximum crystallization temperatures from the self-nucleation investigations. **Table 11** shows that **P3HT-2** has the highest T_c^{\max} with about 207.7 °C. The lowest T_c^{\max} shows **P3HT-3** with a value of 199.9 °C. This value is only about 0.6 °C above its standard crystallization temperature. Taking possible DSC measurement errors and the presence of a ΔT_c of less than one degree Celsius into account, nucleation studies on this P3HT grade are unrewarding, and are therefore not performed later on. The same applies for **P3HT-1**. Here an increase in crystallization temperature by 2.3 °C was observed by self-nucleation. The

highest difference between T_c^0 and T_c^{\max} is shown for **P3HT-2**. Here, ΔT_c amounts to 9.1 °C. Based on these results, all following nucleation studies were performed with this P3HT grade.

4.2 Preparation of P3HT spherulites via melt annealing

An approach to create thin P3HT films with increased order can be achieved by controlled homogeneous nucleation and self-seeding, respectively. Thereby, spherulite growth occurs due to very low or controlled nucleation densities. To obtain a low nucleation density, mainly solvent vapor annealing is used. With this method, Yang et al. were able to produce large spherulites from poly(3-butylthiophene) (P3BT). Furthermore, it could be observed that a transition from *Form I* to *Form II* occurs as soon as the sample has been treated with CS₂ vapor.^[242,243] Crossland et al. have shown that this method is also suitable to produce defined P3HT spherulites. Their studies showed that controlled swelling and subsequent deswelling in CS₂ vapor allow precise control of the nucleation density and thus of the size of the resulting spherulites. These exhibit a highly ordered edge-on orientation and can grow up to 100 μm in diameter (**Figure 91a**).^[244] Charge transport measurements along the *b-c*-plane have shown that macroscopic charge carrier mobility is anisotropic and perpendicular to the direction of growth of the spherulitic structures is three times higher than along the π -stacking direction. The higher mobility is explained by the presence of so-called tie-molecules. These tie-molecules lie between lamellae and provide fast intrachain transport bridges through the amorphous zone.^[245] In addition to the solvent vapor annealing method, the crystallizable solvent technique can also be used to produce highly anisotropic films directly from solution. Müller et al. used in their studies the crystallizable solvent 1,3,5-trichlorobenzene (TCB) in combination with CB. During spin-coating a solution of P3HT in CB/TCB, with a TCB concentration above 4 vol.-%, TCB already starts to solidify in spherulitic structures while P3HT is still dissolved. In the following epitaxial crystallization of the P3HT onto the TCB crystals leads to a spherulite-like arrangement of the P3HT. The epitaxial crystallization occurs due to the close match between the repeating distance of TCB and the thiophene units of the P3HT. After subsequently sublimation of the TCB the generated P3HT structures remain and thus leave behind a replica of the original TCB spherulites (**Figure 91b**).^[246]

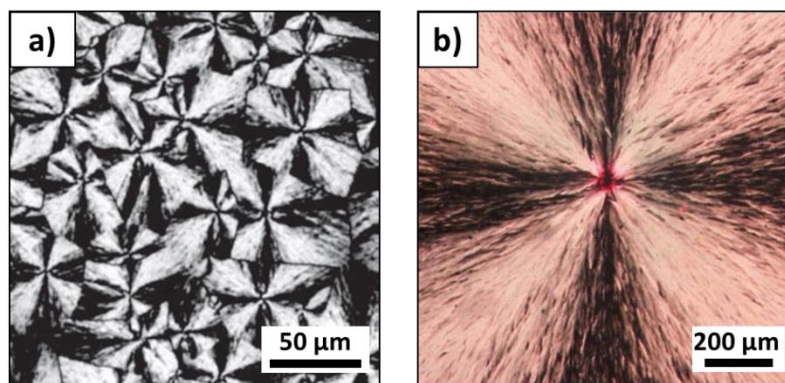


Figure 91: (a) Polarized optical microscopy (POM) image of a 40 nm thick P3HT film crystallized for 1800 seconds at constant CS_2 vapor pressure of 79 % after initial swelling (P^{initial} 91.0 % for 600 seconds).^[244] (b) Cross-polarized optical micrograph of a P3HT thin film, spin-coated from TCB/CB (7.5 vol.-% TCB).^[246]

Qiu et al. studied the electrohydrodynamic instabilities in P3HT films by applying strong electric fields to the film and compared the results with thermally annealed P3HT samples. They were able to show that by using this method large-scale highly ordered columnar P3HT structures on the film surface can be generated (**Figure 92**). Thereby all P3HT columns exhibit a typical Maltese cross pattern, indicating the formation of highly ordered P3HT spherulites. Furthermore, by increasing the electric field strength, the spherulite size can be controlled. The thermally annealed samples, however, did not show any Maltese cross pattern. The results indicate that the applied electric field reduces the nucleation density in the P3HT film.^[247]

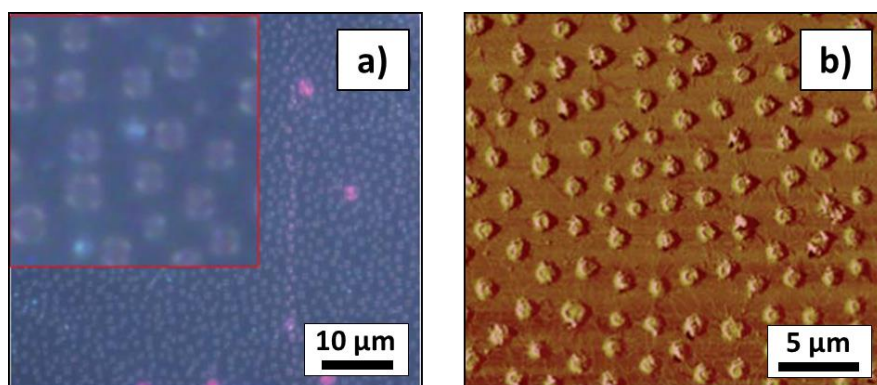


Figure 92: (a) POM image of P3HT crystalline columns created by electrohydrodynamic instabilities. The P3HT films were treated by the electric field of $60 \text{ V}\cdot\mu\text{m}^{-1}$. The inset shows an enlarged image where the Maltese cross patterns are visible. (b) AFM phase image of a P3HT film treated by the electric field of $60 \text{ V}\cdot\mu\text{m}^{-1}$ for 30 min.^[247]

Spherulitic structures of classic semi-crystalline polymers such as polyethylene are mainly generated via melt annealing. For this purpose, the polymer film is heated above the respective melting temperature of the polymer and then annealed isothermally at temperatures between the melting temperature and the crystallization temperature of the polymer. The higher the annealing temperature is chosen, the lower the nucleation density and the higher the resulting spherulites size. Due to the high melting temperatures of conjugated polymers and the possible thermal degradation, melt annealing is problematic for

such polymers. In this context, no spherulites for P3ATs after spin-coating and subsequent melt annealing have been reported so far. Only Hüttner et al. investigated the structure formation of P3HT-F8TBT (poly[(9,9-dioctyluorene)-2,7-diyl-alt-(4,7-bis(3-hexylthien-5-yl)-2,1,3-benzo-thiadiazole)-2',2''-diyl]) blends via both melt annealing and solvent vapor annealing experiments. They were able to show that the lamellar crystallization of regioregular P3HT is not disturbed by the presence of F8TBT. For the melt annealing tests, the blend films were annealed at a temperature of 230 °C and then slowly cooled to room temperature (5 K min⁻¹). Both methods resulted in the formation of P3HT spherulites within the blend film.^[248] However, there are no reports on neat P3HT spherulites produced by this method yet.

In this work, melt annealing investigations on neat P3HT films were performed. For this purpose, **P3HT-2** films of different thicknesses are produced by spin-coating of **P3HT-2** in solutions of CB. Thereby, the thickness of the films can be controlled by the concentration of **P3HT-2** in solution; the higher the P3HT concentration in solution, the thicker the resulting polymer film. The spin-coated films are then heated up to 300 °C under a N₂ atmosphere, kept isothermal at this temperature for three minutes and then cooled down to 150 °C. The heating and cooling rate was 10 K·min⁻¹ each. **Figure 93** shows optical microscope images of a thermally treated **P3HT-2** film with a thickness of ca. 350 nm, spin-coated from a 4 wt.-% solution in CB. The images were taken at selected temperatures of the first heating process (**a-c**) and the second heating process (**d-f**). **Figure 93a** shows the **P3HT-2** microstructure, which is present directly after spin-coating from solution. At a temperature of 260 °C the **P3HT-2** is completely molten. No crystallites are apparent (**Figure 93b**). After the film has been cooled down to 150 °C and then heated up again to 200 °C (**Figure 93d**), the film morphology has changed significantly compared to the morphology after spin-coating. If this film is then heated up to 260 °C, a spherulitic structure can be obtained. These spherulites melt at approximately 270 °C.

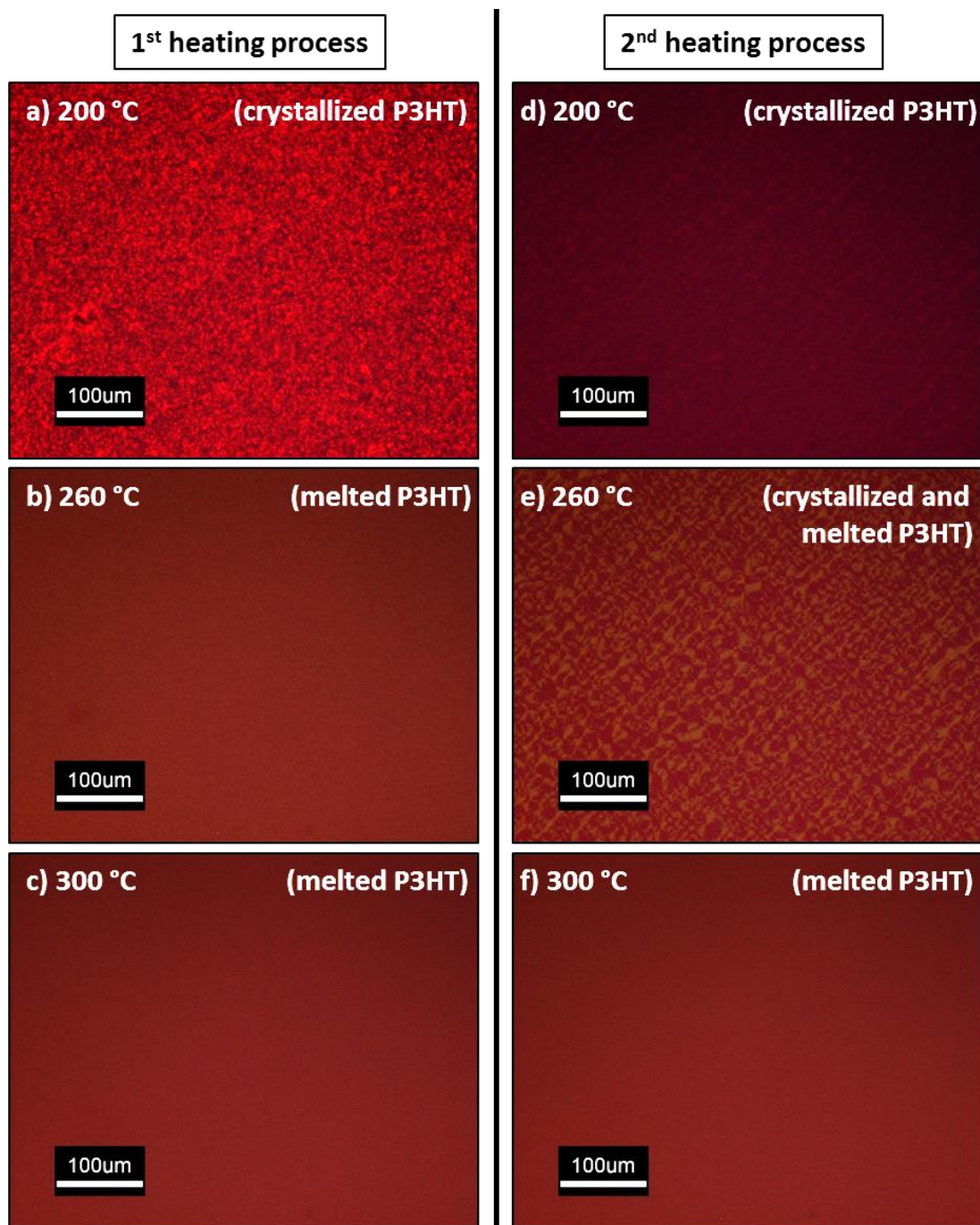


Figure 93: Polarized optical microscopy images of a neat P3HT-2 film spin-coated from a 4 wt.-% CB solution on a clean glass substrate: (a-c) micrographs taken at the stated temperatures during the first heating process; (d-f) micrographs taken at the stated temperatures during the second heating process. The experiments were performed under nitrogen atmosphere with heating and cooling rates of $10 \text{ K}\cdot\text{min}^{-1}$.

In order to gain insights into the spherulitic growth microscopic images between crossed polarizers were recorded during the first cooling cycle and analyzed (Figure 94). Figure 94a shows the micrograph of the P3HT-2 film at a temperature of 243 °C. It can be seen that even at this temperature the P3HT spherulites arise. These spherulites have fully covered the film at 240 °C (Figure 94b). Note that this temperature is above the respective melting temperature for P3HT-2 (235 °C). Upon further cooling, the film morphology does not change

significantly till 215 °C. At this temperature, at which **P3HT-2** typically crystallizes, a darkening of the film can be observed (**Figure 94d**). However, the spherulitic P3HT structure can still be noticed.

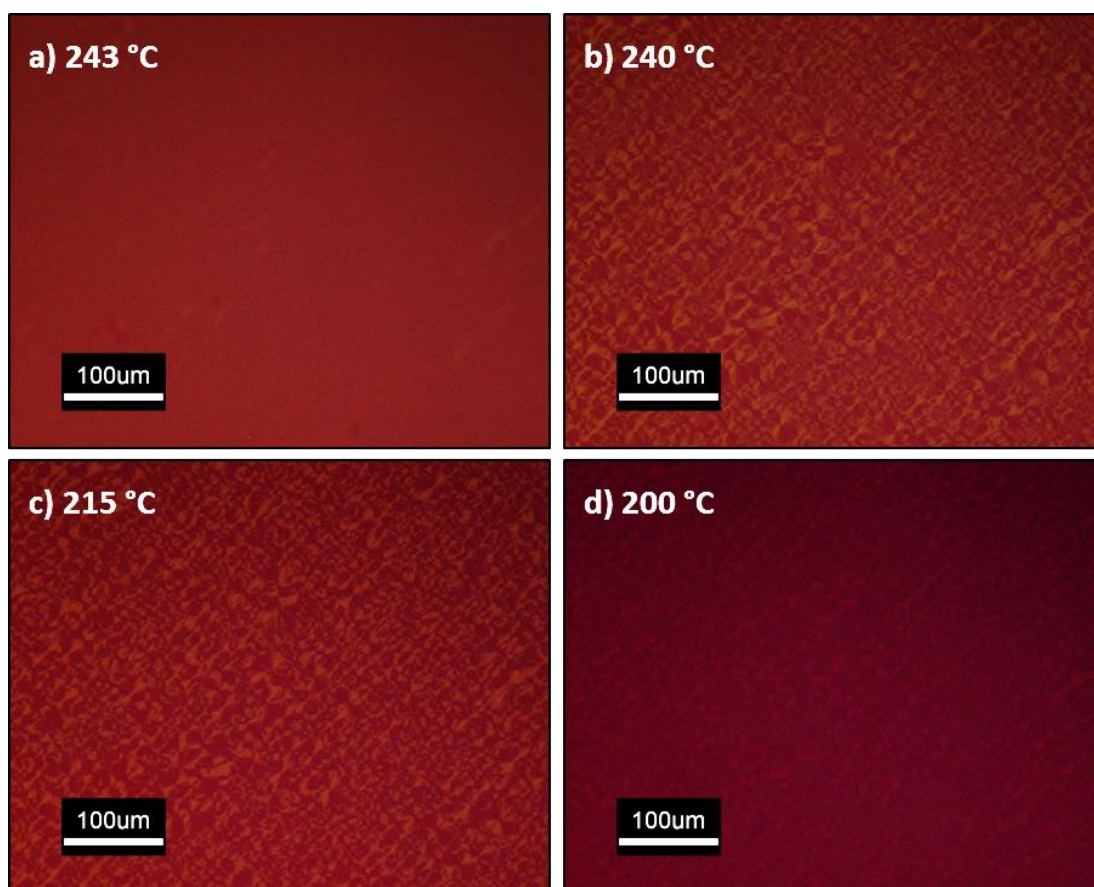


Figure 94: Polarized optical microscopy images of a neat **P3HT-2** film spin-coated from a 4 wt.-% CB solution on a clean glass substrate: The micrographs (a-d) were taken at the stated temperatures upon cooling from 300 °C. The experiments were performed under nitrogen atmosphere with heating and cooling rates of 10 K·min⁻¹.

In a second experiment a **P3HT-2** film was prepared by spin-coating a 4 wt. % **P3HT-CB** solution. After that a heating and cooling step as described above is performed to erase the thermal history. After subsequent heating to 300 °C, the film was cooled down (10 K·min⁻¹) and kept isothermal at a temperature of 250 °C. The microscopic images taken at different annealing times are shown in **Figure 95**. As it can be seen from **Figure 95a** the **P3HT-2** film is at the beginning of the annealing process completely featureless. After five minutes of thermal annealing, however, the first spherulites have formed (**Figure 95b**). Upon further melt annealing the amount of spherulites does not increase, but a significant growth of the spherulite can be observed (**Figure 95c-f**). This growth continues with the annealing time. After 30 minutes of thermal treatment another part of the film was focused to observe a separated spherulite more closely (**Figure 95g-i**). This spherulite has reached a total size of about 300 μm in diameter after 120 minutes at 250 °C. The micrographs indicate that the **P3HT** nucleation density is extremely low and constant at 250 °C, as evidenced by the few

existing spherulites and no new ones emerge. Besides the spherulites, a homogeneous P3HT melt is presumably still present.



Figure 95: Polarized optical microscopy images of a neat P3HT-2 film spin-coated from a 4 wt.-% CB solution on a clean glass substrate: The micrographs were taken at 250 °C at the stated isothermal annealing times. Before the images were taken, the P3HT film was heated up to 300 °C and subsequently cooled down to the isothermal annealing temperature of about 250 °C. The experiments were performed under nitrogen atmosphere with heating and cooling rates of 10 K·min⁻¹ (before the isothermal annealing).

The spherulite size can be controlled not only by the annealing time but also by the annealing temperature. The higher the annealing temperature is chosen, the lower the nucleation density and the higher the resulting spherulites size. However, since the nucleation density is already very low in this experiment, an increase of the annealing temperature would lead to an extreme increase of the annealing time in order to observe larger spherulites. Therefore, the influence of the film thickness on the spherulite size was investigated instead. For this purpose, a film of **P3HT-2** is spin-coated from a 5 wt.-% chlorobenzene solution, which results in an approximately 150 nm thicker film than the previously investigated film (450 nm) of a 4 wt.-% solution. Afterwards, the identical melt annealing experiment is performed with this film. The microscopic images taken at different annealing times are shown in **Figure 96**. At the beginning of the annealing experiment the P3HT film is completely featureless. After five minutes at 250 °C the first spherulites emerge (**Figure 96b**). Upon further thermal treatment

the amount and the size of the spherulites increase. After 60 minutes the whole film is covered with spherulites, indicating the end of the spherulite growth (**Figure 96e**). If the film is further cooled down, the morphology of the film does not change. However, there is again a darkening of the film, at the standard crystallization temperature of **P3HT-2** (**Figure 96h-i**). These results suggest that there are apparently two different crystallization mechanisms for P3HT and therefore, in addition to the two polymorphic forms (*Form I* and *Form II*, see **Figure 19**) known, another polymorph in the range of the melting temperature of P3HT exists.



Figure 96: Polarized optical microscopy images of a neat P3HT-2 film spin-coated from a 5 wt.-% CB solution on a clean glass substrate: The micrographs (a-e) were taken at 250 °C at the stated isothermal annealing times. Before the images were taken, the P3HT film was heated up to 300 °C and subsequently cooled down to the isothermal annealing temperature of about 250 °C. The micrographs (f-h) were taken at the stated temperatures upon cooling from 250 °C after 60 minutes of isothermal annealing. The experiments were performed under nitrogen atmosphere with heating and cooling rates of $10 \text{ K}\cdot\text{min}^{-1}$ (before and after the isothermal annealing).

Finally, a third **P3HT-2** film with a thickness of $1.2 \mu\text{m}$ was spin-coated from a 10 wt.-% solution in chlorobenzene on which melt annealing experiments were performed. Here, isothermal annealing was performed at 245 °C, since the annealing temperature of 250 °C did not lead to spherulitic crystal formation. At this temperature, only very few nuclei emerged, which indicates an extremely low nucleation density. Since the growth of the separate spherulites was not limited by adjacent spherulites, they were able to grow up to more than $500 \mu\text{m}$ in diameter (**Figure 97a**). The figure also shows that the spherulites are

still surrounded by a homogeneous P3HT melt. Upon cooling of the sample, however, smaller spherulites are formed immediately in the melt and finally covering the entire film at a temperature of 220 °C (**Figure 97b**). Further cooling, in the range of the standard crystallization temperature of P3HT, leads to the already observed darkening of the total film, so that both types of spherulites, can only be seen vaguely (**Figure 97c-d**).

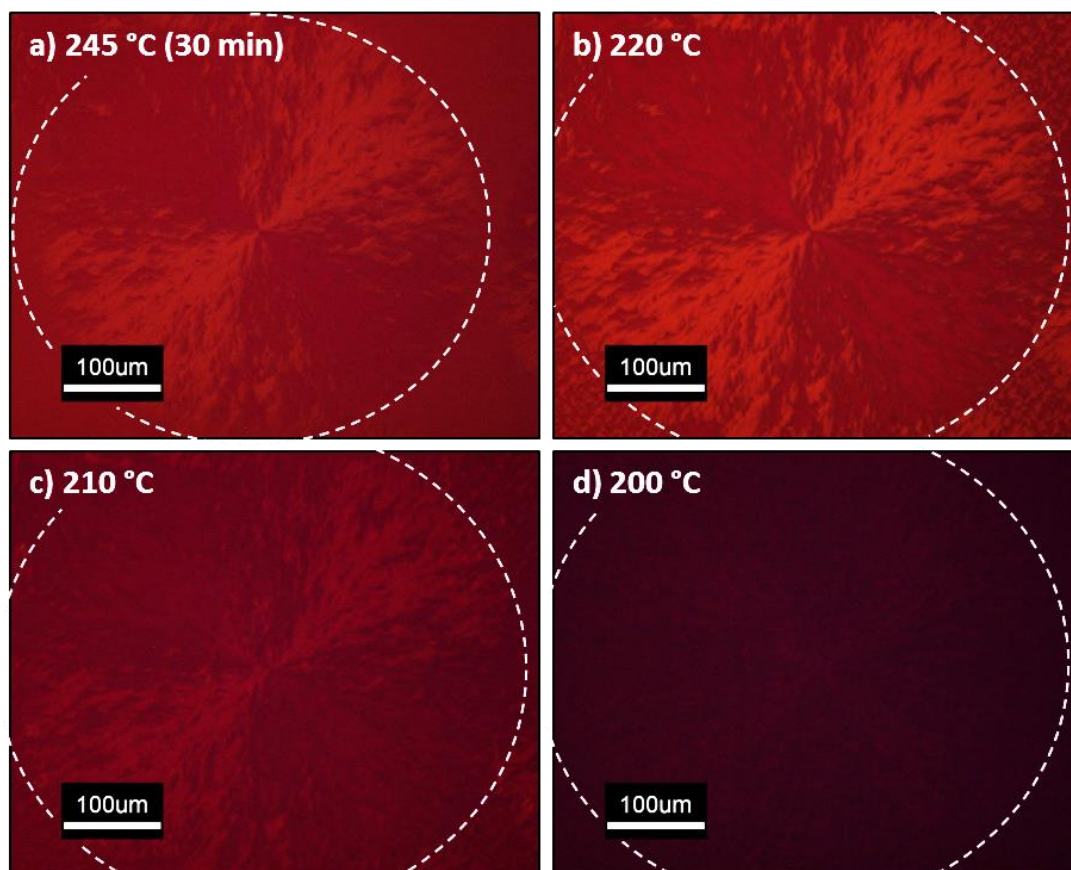


Figure 97: Polarized optical microscopy images of a neat P3HT-2 film spin-coated from a 10 wt.-% CB solution on a clean glass substrate: The micrograph (a) was taken after 30 minutes of isothermal annealing at 245 °C. Before this image was taken, the P3HT film was heated up to 300 °C and subsequently cooled down to the isothermal annealing temperature of about 245 °C. The micrographs (b-d) were taken at the stated temperatures upon cooling from 245 °C after 30 minutes of isothermal annealing. The experiments were performed under nitrogen atmosphere with heating and cooling rates of 10 K·min⁻¹ (before and after the isothermal annealing).

Subsequently heating of the film (**Figure 98a**) above the standard melting temperature of P3HT (240 °C) the portion of the film which crystallized at 200 °C melts, the large type of spherulite however remain unchanged. Further heating causes the small spherulites to melt first. The larger spherulites begin to melt only at a temperature of 265 °C (**Figure 98c**). Above 270 °C the entire film is homogeneously molten (**Figure 98d**). The different melting temperatures, as well as the different crystallization temperatures indicate that dissimilar P3HT polymorphs are present.

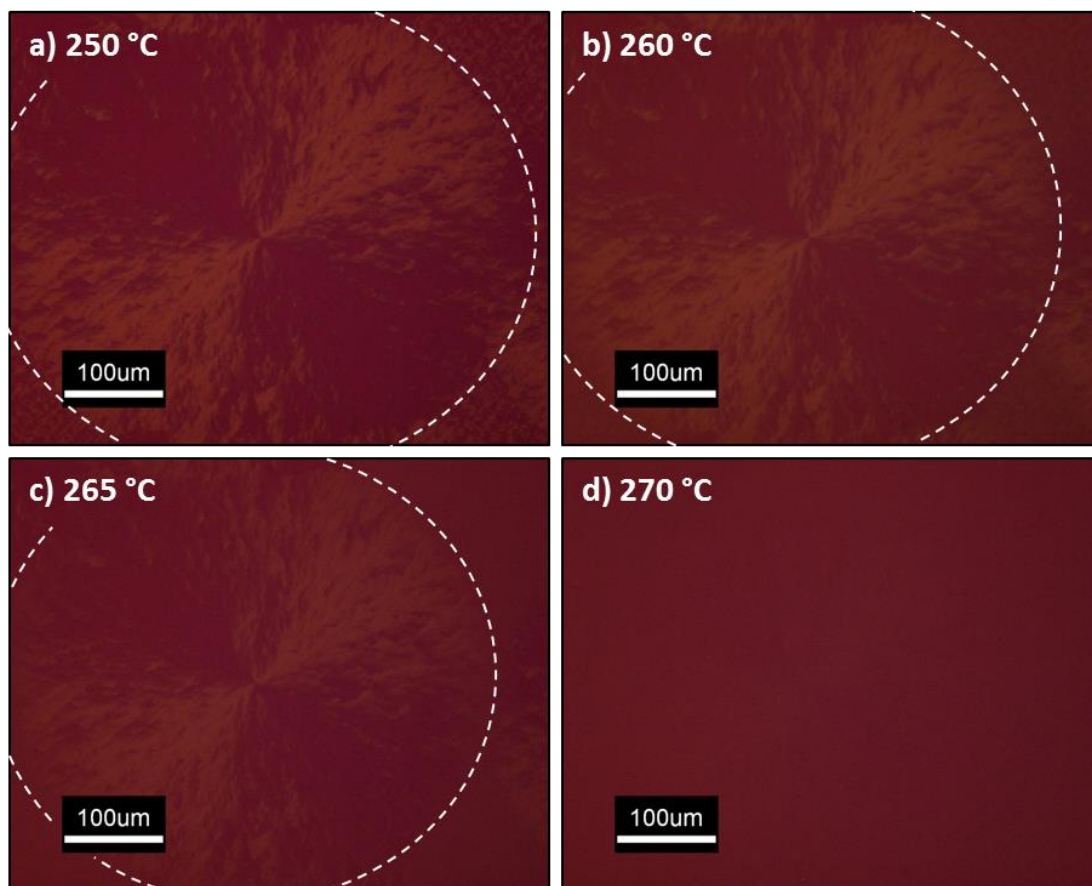


Figure 98: Polarized optical microscopy images of a neat P3HT-2 film spin-coated from a 10 wt.-% CB solution on a clean glass substrate: The micrographs (a-d) were taken at the stated temperatures. Before the images were taken, the present P3HT film was heated up to 300 °C, then cooled down to 245 °C. After an annealing time of 30 minutes at 245 °C the film was subsequently cooled down to 200 °C and the heated up again to take the shown images. The experiments were performed under nitrogen atmosphere with heating and cooling rates of 10 K·min⁻¹ (before and after the isothermal annealing).

4.3 Nucleating agents for P3HT

The blend system consisting of P3HT:PCBM represents the most frequently used blend system for the active layer of organic solar cells.^[125] The nanomorphology of this layer strongly determines the device performance. P3HT, as a semi-crystalline polymer, can self-assemble in a crystalline structure and thereby provide adequate hole mobility. To increase this mobility, several approaches have been reported. For instance it is presumed, that an improvement in hole mobility can be generated by increasing the overall crystallinity of P3HT or the P3HT crystallite size.^[249] However, it is in general difficult to significantly increase the degree of crystallinity of the same polymer which may also be attributed to the chain entanglements preventing molecular diffusion. In addition, complicated conformational transitions of the flexible side chains and the semi-flexible backbone are necessary for crystallization.^[250] Therefore, despite all efforts, researcher have not been able yet to show the full potential of P3HT and, thus, P3HT is lagging behind in comparison to highly crystalline

conjugated small molecules.^[249] Recent reports have shown that the connectivity between ordered P3HT domains, via the so-called tie molecules, has also an impact on P3HT hole mobility. An increased connectivity can be achieved, for example, by increasing the molecular weight of P3HT.^[249] Gomez et al. showed that even accelerated crystallization kinetics leads to more tie molecules in polythiophenes.^[251] In the case of P3HT the crystallization kinetics can also be changed by the use of nucleating agents. Therefore, the development of new and suitable nucleating agents for organic semiconducting polymers is a highly topical field of research.^[23]

Hadziioannou et al. reported that the statistical copolymer thieno[3,2-*b*]thiophene-*alt*-pentathiophene is a nucleating agent for P3HT, which improves the degree of crystallinity and the hole mobility.^[252] The same group were able to show that the block copolymer poly(3-hexylthiophene)-*b*-polyisoprene (P3HT-*b*-PI) is also an effective nucleating agent for P3HT. By addition of 7 wt.-% P3HT-*b*-PI to pristine P3HT, the crystallization temperature increased by nearly 2 °C (**Figure 99**). A nucleation efficiency of about 31 % was found. Furthermore, an increase in the P3HT crystal density was observed within the films, resulting in an overall increase of crystallinity.

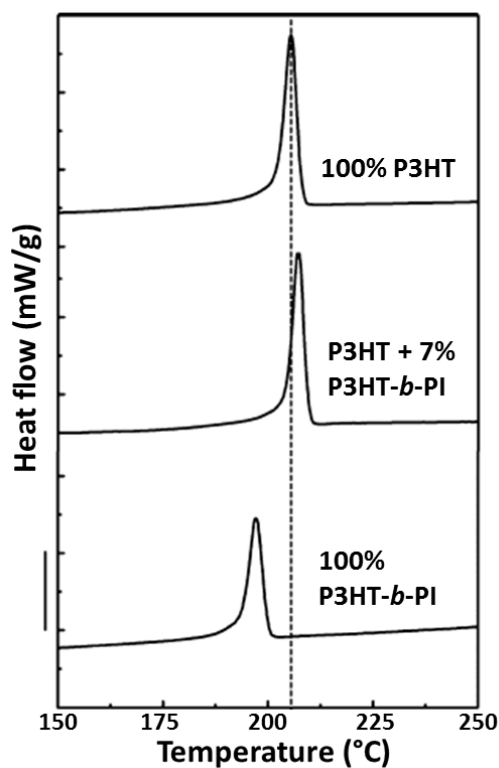


Figure 99: DSC cooling scans of pristine P3HT (top), P3HT:P3HT-*b*-PI blend (middle), and pristine P3HT-*b*-PI (bottom). The segmented vertical line indicates the standard peak crystallization temperature T_c^0 (205.4 °C) of P3HT.^[253]

Yang and Lu investigated via several kinetic crystallization models, a non-isothermal crystallization behavior of P3HT in the presence of reduced graphene oxide (*rGO*). They were able to show that the crystallization peak temperature and the crystallinity of P3HT dramatically increase dependent on the content of the added *rGO* (**Figure 100**). Since the modified Avrami and Ozawa models failed to effectively describe the crystallization behavior, they applied the combined Avrami-Ozawa model proposed by Mo and coworkers. The results show, that at low *rGO* concentrations in the P3HT/*rGO* nanocomposite the crystallization rate is higher than for pristine P3HT. However, a large amount of *rGO* lowers the crystallization rate, because *rGO* significantly suppresses the chain diffusion of P3HT due to the strong π - π interaction between P3HT and *rGO*.^[254]

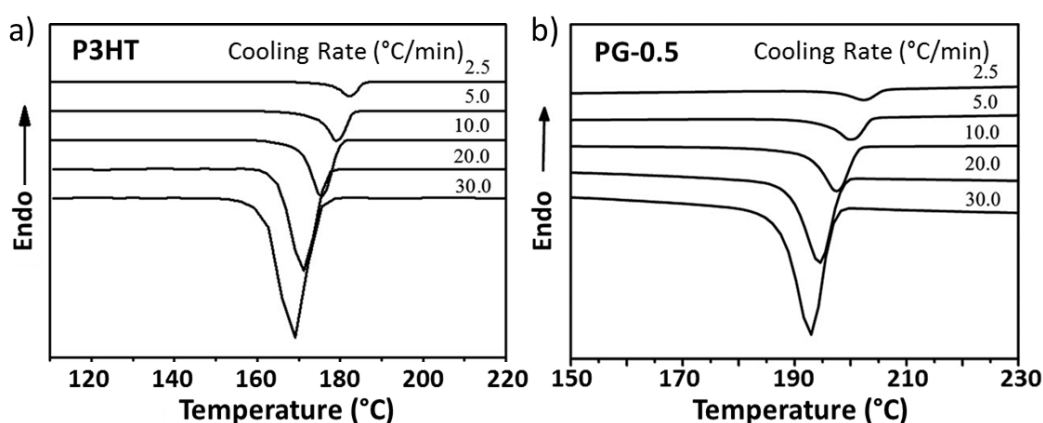


Figure 100: DSC cooling curves of (a) pristine P3HT and (b) P3HT/*rGO* nanocomposites (PG-0.5) recorded at different cooling rates. The *rGO* concentration in the composite amounts to 0.5 wt.-% with respect to the P3HT.^[254]

The Chabinyk group investigated the influence of the commercially available nucleating agents 1,3:2,4-bis(3,4-dimethylbenzylidene)sorbitol (DMDBS; Millad 3988) and tris-*tert*-butyl-1,3,5-benzenetrisamide (BTA; Irgaclear XT 386), which were originally designed as nucleating agent for isotactic polypropylene, on the microstructure formation of the polymeric semiconductors poly(3-dodecylthiophene) (P3DDT) and P3HT.^[23,131] The two nucleating agents are able to fully dissolve at the molecular level in the molten or dissolved polymer and, on cooling or solvent removal, form well-dispersed supramolecular structures. The results regarding the solidification behavior of P3HT showed that the addition of 1 wt.-% BTA increased the onset crystallization temperature of P3HT in solution (6 wt.-% in xylene) by about 7 °C (**Figure 101a**), the addition of 20 wt.-% DMDBS by about 2 °C. They also reported that the nucleation of the P3HT do not alter its charge transport properties (**Figure 101b**).^[23]

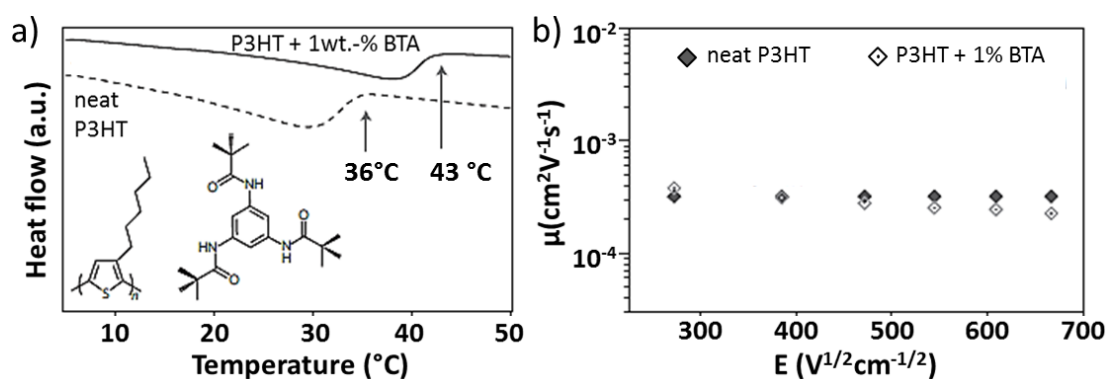


Figure 101: (a) DSC cooling thermograms of P3HT, solidified from solution (6 wt.-% xylene) with and without the nucleating agent Irgaclear XT 386. The onset crystallization temperature is raised (indicated by the arrows) by 7 °C. The insets show the chemical structures of P3HT and Irgaclear XT 386. (b) Time-of-flight photoconductivity hole mobility for neat P3HT (solid diamonds) and P3HT with 1 wt.-% Irgaclear XT 386 (open diamonds).^[23]

Yuan and Huo analyzed the nucleating effect of 1,2,3,4-bis(p-methylbenzylidenesorbitol) (MDBS), another sorbitol derivative whose structure is similar to DMDBS, on P3HT.^[249] They demonstrate that MDBS is an effective heterogeneous nucleating agent for P3HT and verified this by studies of the isothermal crystallization kinetics of P3HT with and without MDBS. The plots of relative crystallinity X_t versus the crystallization time t show the typical sigmoidal characteristic that reflects the three steps of crystallization: initial nucleation, primary nucleation and secondary nucleation (Figure 102). The figure shows that the crystallization half-time $t_{1/2}$ increases with increasing isothermal holding temperature for both pure P3HT and P3HT with MDBS. However, at the same isothermal holding temperature, $t_{1/2}$ is always lower for the P3HT samples with MDBS than without MDBS.^[249]

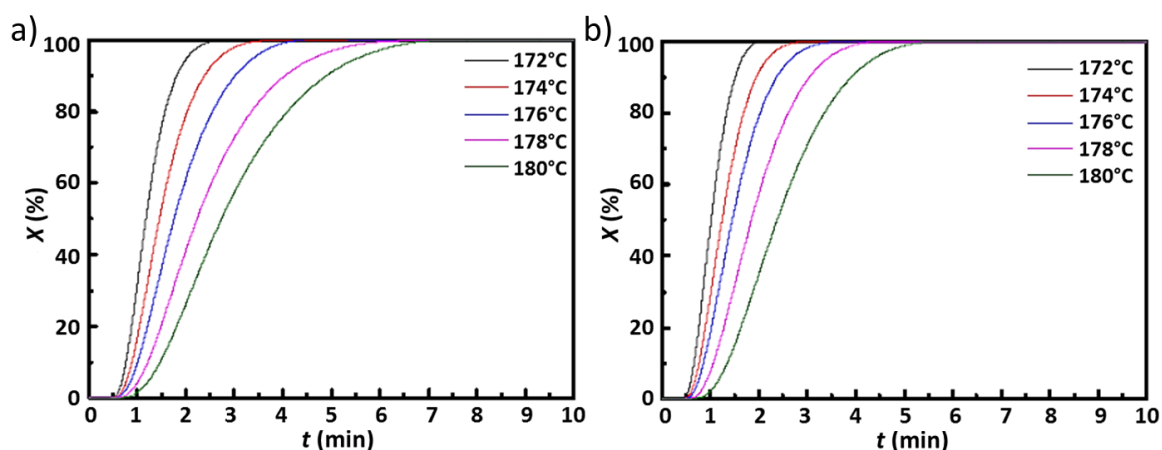


Figure 102: Plots of relative crystallinity X_t of neat P3HT (a) and P3HT with 2 wt.-% MDBS (b) as a function of crystallization time t for various isothermal holding temperatures.

Using the Avrami model, they determined the nucleation mechanism and the crystallization rates of P3HT. Yuan and Huo found that n varies from 2.02 to 2.21 for pure P3HT and from 2.08 to 2.48 for P3HT with MDBS, which indicate that the addition of MDBS has little effect on the nucleation mechanism of P3HT (Figure 103). Furthermore they showed in their work, that the hole mobility of a P3HT:PCBM device significantly increases (30 times the value of a

pristine P3HT:PCBM device) after the addition of MDBS. They attribute this to the enhanced connectivity between ordered P3HT regions, due to the formation of more tie molecules.^[249]

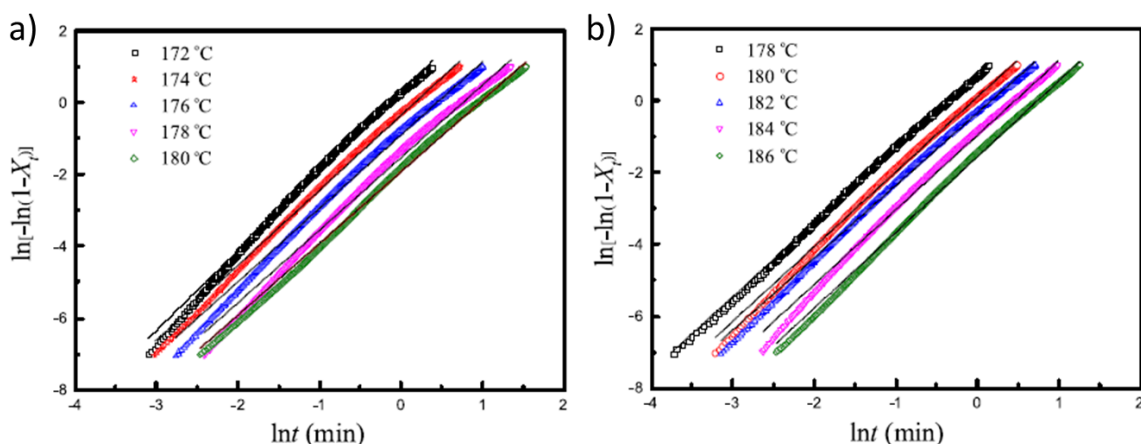


Figure 103: Plots of $\ln[-\ln(1-X_t)]$ versus $\ln t$ for isothermal crystallization of neat P3HT (a) and P3HT with 2 wt.-% MDBS (b) for various isothermal holding temperatures.

The results of these studies suggest that nucleating agents may not only have influence on the optical and mechanical properties of industrial polymers, but can also have a positive influence on semiconducting polymers or small molecules. Therefore, the most important implication of the previous work mentioned is that there is a need for new, specifically designed nucleating agents.^[23]

4.4 Nucleation investigations of P3HT with pyridine-containing bis- and trisamides

As shown in the previous thermal investigations of neat P3HT, a temperature profile with a maximum heating temperature T_h^{\max} of 300 °C and a five-minute isothermal holding time is necessary for nucleation experiments by means of DSC, in order to completely erase the thermal history. Accordingly, additives which are intended to act as nucleating agents must be thermally stable up to this temperature. Furthermore, in order to provide the necessary nuclei for the heterogeneous crystallization of P3HT, the additives must crystallize upon cooling before P3HT crystallization takes place. An overview of the thermal characteristics of the additives tested in this work is presented in the **Chapters 3.2.4** and **3.3.4**. On the basis of these results, nine pyridine-containing compounds accomplish this requirement and are subsequently investigated as potential nucleating agents for **P3HT-2**.

4.4.1 Evaluation of suitable and highly efficient nucleating agents for P3HT

In order to get overviews which of the various additives are able to act as nucleating agent for **P3HT-2**, nucleation measurements are performed with all additives at the same concentration ratio. For these measurements the concentration of the additive relative to

P3HT-2 was set to 1 wt.-%. The trisamides **TA 1-4** and **TA 6** and the bisamides **BA 1-4** were investigated. Except for the **TA 6**, which carries 3-pyridine moieties, all other additives have 4-pyridine substituents in the periphery. The sample preparation and the conduction of the measurements is described in **Experimental 7.1** in detail.

Figure 104a shows the second cooling curves of the nucleation measurements, both of neat **P3HT-2** (red) and of **P3HT-2** with nucleating agents (black). The molecular structures of the additives which are capable of nucleating P3HT are shown in **Figure 104b**.

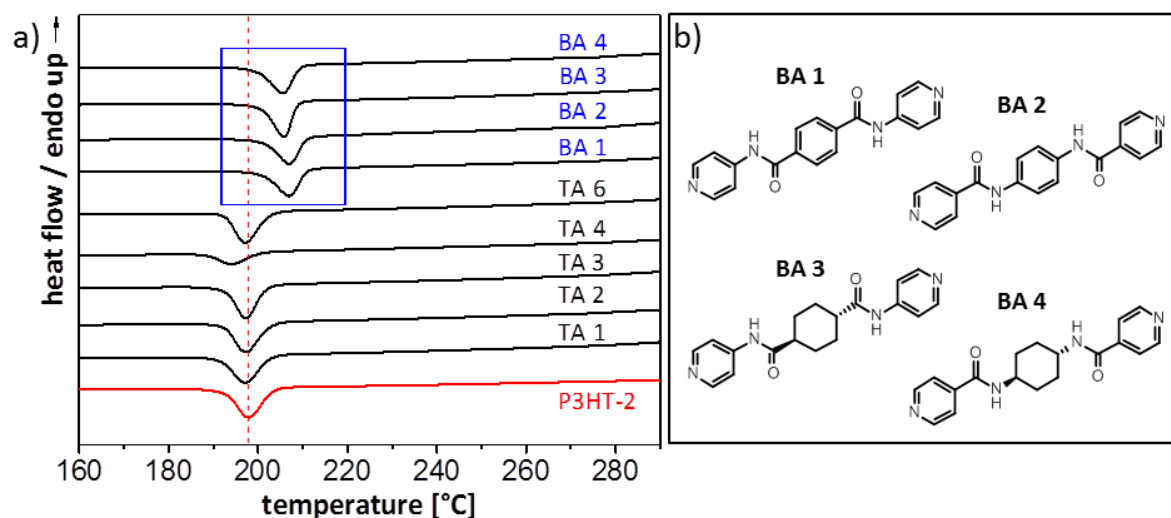


Figure 104: (a) DSC exotherms of neat **P3HT-2** (red curve) and **P3HT-2** comprising 1.0 wt.-% of pyridine containing bis- and trisamides (black curves). Of the nine additives tested, a total of four are able to nucleate **P3HT-2**. The inserted blue box shows the increase in T_c^{nuc} of **P3HT-2** by these four nucleating agents. DSC heating and cooling rate: $10 \text{ K}\cdot\text{min}^{-1}$. (b) Molecular structures of the four pyridine-containing bisamides capable of nucleating **P3HT-2**.

The **Figure 104** clearly shows that only the four bisamides **BA 1-4** are capable of nucleating **P3HT-2**. Furthermore, it can be observed that the nucleation effect is largely independent of the central core and the orientation of the amide linkage of these bisamides (see molecular structures in **Figure 104b**). The crystallization temperature of **P3HT-2** increases by almost 9°C after the addition of 1 wt.-% for each of these bisamide additives. Considering the crystallization temperature T_c^{nuc} of **P3HT-2** with compound **TA 4**, it can be observed that this temperature decreases by 4°C compared to the standard crystallization temperature T_c^0 of **P3HT-2**. Accordingly, **TA 4** hampers the crystallization of **P3HT-2**. No shift in T_c^{nuc} is observed for the remaining trisamide additives studied.

Based on these results, it can be concluded that only the *bisamides* with the 4-pyridine substituents can act as highly efficient nucleating agents for P3HT. Therefore, concentration-dependent nucleation experiments were performed only with these additives.

4.4.2 Nucleation of P3HT with BA 1-4 in dependency of the additive concentrations

Since the additives **BA 1-4** have already been proven being effective nucleating agents for **P3HT-2**, concentration dependent nucleation experiments were performed to evaluate the optimal bisamide concentration regarding the nucleation efficiency. Comparing the crystallization temperatures of nucleated **P3HT-2** (**Figure 104a**) with the maximum crystallization temperature for neat **P3HT-2** (207.7 °C) it is found that an additive concentration of 1 wt.-% results in an almost 100 % nucleation efficiency. In order to get insight into the nucleation behavior of P3HT with the nucleating agents, the concentration of the bisamides for the concentration-dependent investigations were performed in the range of 0.0025 to 1 wt.-%.

4.4.2.1 Nucleation of P3HT with BA 1 (*N*¹, *N*⁴-di(pyridine-4-yl)terephthalamide)

Figure 105 outlines the results of the concentration dependent nucleation experiments of **P3HT-2** with the additive **BA 1**. This bisamide comprises a terephthalic acid core and two 4-pyridine substituents. The highest additive concentration was 1 wt.-%, the lowest 0.0025 wt.-%, with respect to **P3HT-2**.

The determined **P3HT-2** melting temperatures after the addition of the bisamide **BA 1** slightly fluctuate above the standard melting temperature of **P3HT-2**. Thus, no concentration-dependency of T_m of **P3HT-2** by the addition of the additive can be observed (**Figure 105a**).

More importantly, a concentration-dependent increase in the crystallization temperature can be observed (**Figure 105b**). In order to show this concentration-dependent increase in more detail, the determined crystallization temperatures are plotted in dependency of the additive concentration in **Figure 105c**. By adding 1 wt.-% of **BA 1**, a T_c^{nuc} of 206.8 °C was determined. If the concentration of additive is reduced to 0.025 wt.-% the measured T_c^{nuc} changes only insignificantly. If the error of measurement is considered, it can be assumed that the T_c^{nuc} of P3HT remains constant by addition of an additive concentration of 0.025 wt.-% or higher. For lower additive concentrations, a concentration-dependent decrease of T_c^{nuc} can be observed. The lowest concentration used within this series (0.0025 wt.-%) still shows an increase of T_c^{nuc} of about 2 °C. These results show that *N*¹,*N*⁴-di(pyridine-4-yl)terephthalamide is an highly efficient nucleating agent for **P3HT-2**, since very low concentrations are sufficient to already increase the T_c^{nuc} markedly.

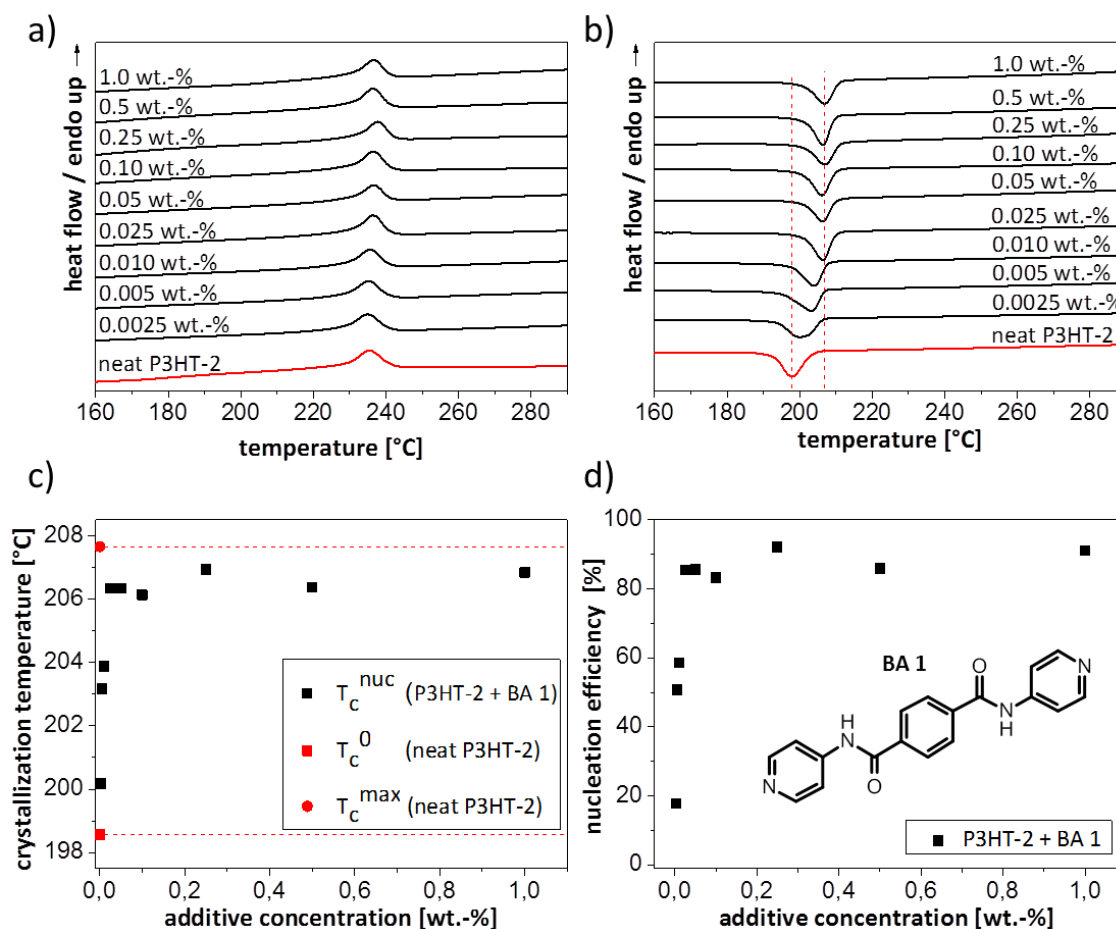


Figure 105: (a) Second heating curves and (b) second cooling curves of neat P3HT-2 (red curve) and P3HT-2 comprising different amounts of BA 1 (black curves). DSC heating and cooling rate: $10 \text{ K}\cdot\text{min}^{-1}$. (c) Polymer crystallization temperatures of P3HT-2 comprising BA 1 as function of the additive concentration. (d) Calculated nucleation efficiencies of BA 1 on P3HT-2 as function of the additive concentration. Insert shows the molecular structure of BA 1.

Figure 105d shows the calculated values of the nucleation efficiency as a function of the BA 1 concentration. To calculate the nucleation efficiency Equation 3 (Chapter 1.3.2) was used, where T_c^0 denotes the standard crystallization temperature of the neat P3HT-2, T_c^{nuc} being the crystallization temperature of P3HT-2 induced by the nucleating agent BA 1 and T_c^{max} being the maximum crystallization temperature of P3HT-2.

A continuous increase in NE can be observed up to an addition of 0.025 wt.-% of additive BA 1. At this concentration an inflection point is present and the NE reaches a plateau. As a consequence, the NE cannot be improved by further increasing the additive concentration. Here, the maximum efficiency which could be achieved for the additive BA 1 is 92 %.

4.4.2.2 Nucleation of P3HT with BA 2 (*N,N'*-(1,4-phenylene)diisonicotinamide)

Figure 106 summarizes the results of the concentration dependent nucleation experiments of P3HT-2 with the additive BA 2. This bisamide differs only in the orientation of the amide groups from the previously described BA 1.

Figure 106a shows the second heating and Figure 106b the second cooling curves of P3HT-2 with different concentrations of BA 2. Similarly as described above the bisamide concentration was investigated in the range of 0.0025 to 1 wt.-%, with respect to P3HT-2.

The determined P3HT-2 melting temperatures after the addition of the bisamide BA 2 show the same behavior as observed with BA 1 (Figure 105a).

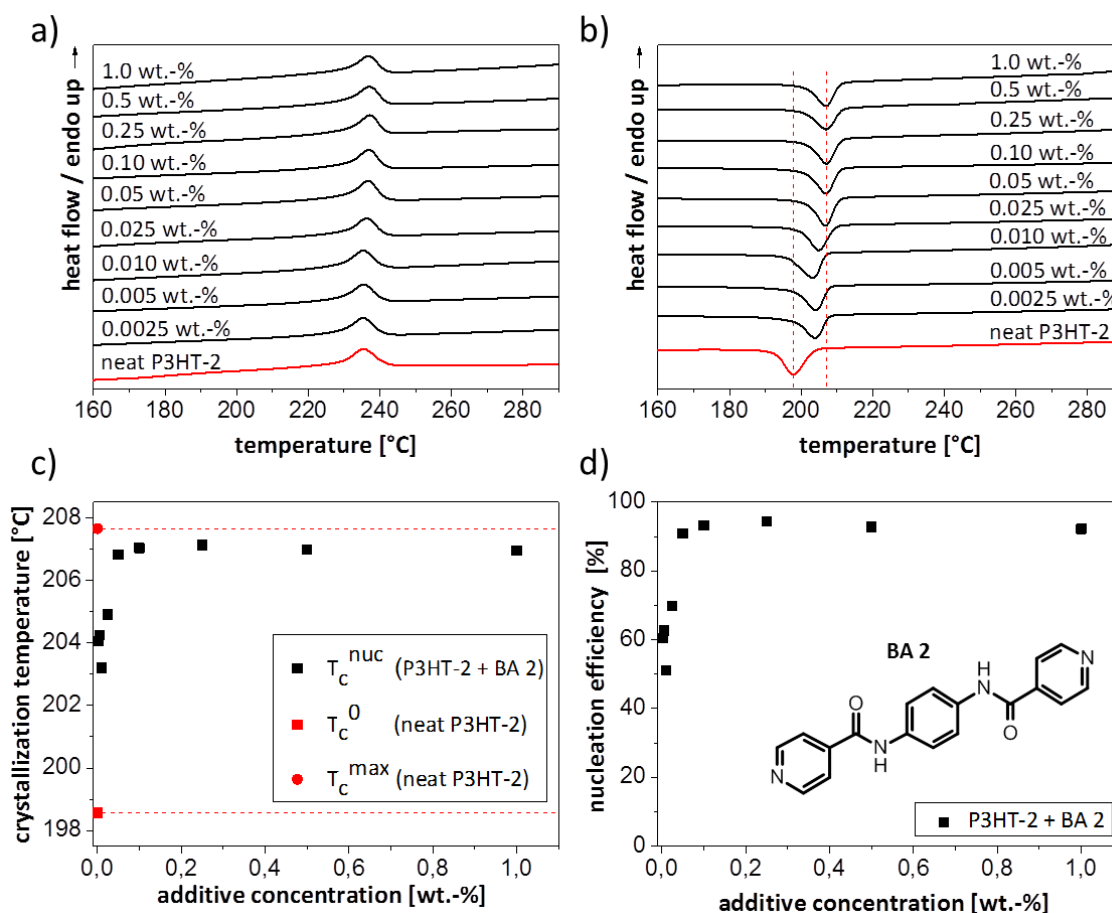


Figure 106: (a) Second heating curves and (b) second cooling curves of neat P3HT-2 (red curve) and P3HT-2 comprising different amounts of BA 2 (black curves). DSC heating and cooling rate: 10 K·min⁻¹. (c) Polymer crystallization temperatures of P3HT-2 comprising BA 2 as function of the additive concentration. (d) Calculated nucleation efficiencies of BA 2 on P3HT-2 as function of the additive concentration. Insert shows the molecular structure of BA 2.

For the highest BA 2 concentration (1 wt.-%), the determined T_c^{nuc} for P3HT-2 amounts to 206.9 °C. This value is more than 8 °C above T_c^0 of neat P3HT-2. Considering all cooling curves (Figure 106b), it can be observed that the T_c^{nuc} of P3HT-2 remains constant with decreasing additive concentration down to a value of 0.05 wt.-%. Afterwards, a concentration-dependent reduction of T_c^{nuc} can be observed. Figure 106c illustrates this concentration dependency

more detailed. Even at the lowest additive concentration, T_c^{nuc} amounts to approximately 204 °C and thus 5 °C above T_c^0 . This indicates that the bisamide forms nanostructures at low concentrations in P3HT which act as nucleation sites. Therefore it is apparent that even very small amounts of **BA 2** are sufficient to significantly increase the crystallization temperature of **P3HT-2**. To illustrate that additive **BA 2** is also a highly effective nucleating agent for P3HT the calculated nucleation efficiencies are plotted against the additive concentration in **Figure 106d**. A continuous increase in nucleation efficiency can be observed up to an additive concentration of about 0.05 wt.-%. Hereafter, the nucleation efficiency reaches a plateau and remained constant despite further increasing of the additive concentration. Thus, the maximum efficiency, which could be achieved for the additive **BA 2** is 94 %. Even with the lowest additive concentration (0.0025 wt.-%), which was investigated in this work, an already high nucleation efficiency of 60 % can be observed.

4.4.2.3 Nucleation of P3HT with **BA 3** (*N¹,N⁴-di(pyridin-4-yl)cyclohexane-1,4-dicarbox-amide*)

Figure 107 outlines the results of the concentration dependent nucleation experiments of **P3HT-2** with the additive **BA 3**. This bisamide comprises a trans-cyclohexane-1,4-dicarboxylic acid core and two 4-pyridine substituents.

Figures 107a and **b** show the DSC thermograms of the second heating and second cooling curves of **P3HT-2** with different amounts of **BA 3**. Related to P3HT, the highest **BA 3** concentration investigated was 1 wt.-%, the lowest 0.01 wt.-%. **Figure 107a** shows that the T_m of **P3HT-2** also remains unchanged after the addition of the bisamide. For the measured T_c^{nuc} the situation is here different. In dependency of the additive concentration in P3HT the T_c^{nuc} increase more gradually compared to **BA 1** and **BA 2** (**Figure 107b**). The highest crystallization temperature can be detected upon an addition of 1 wt.-% of **BA 3** and amounts to 205.8 °C. This is an increase of almost 8 °C compared to T_c^0 of neat **P3HT-2**. However, very small amounts of the bisamide are already sufficient to significantly increase T_c^{nuc} of **P3HT-2** by 3 °C.

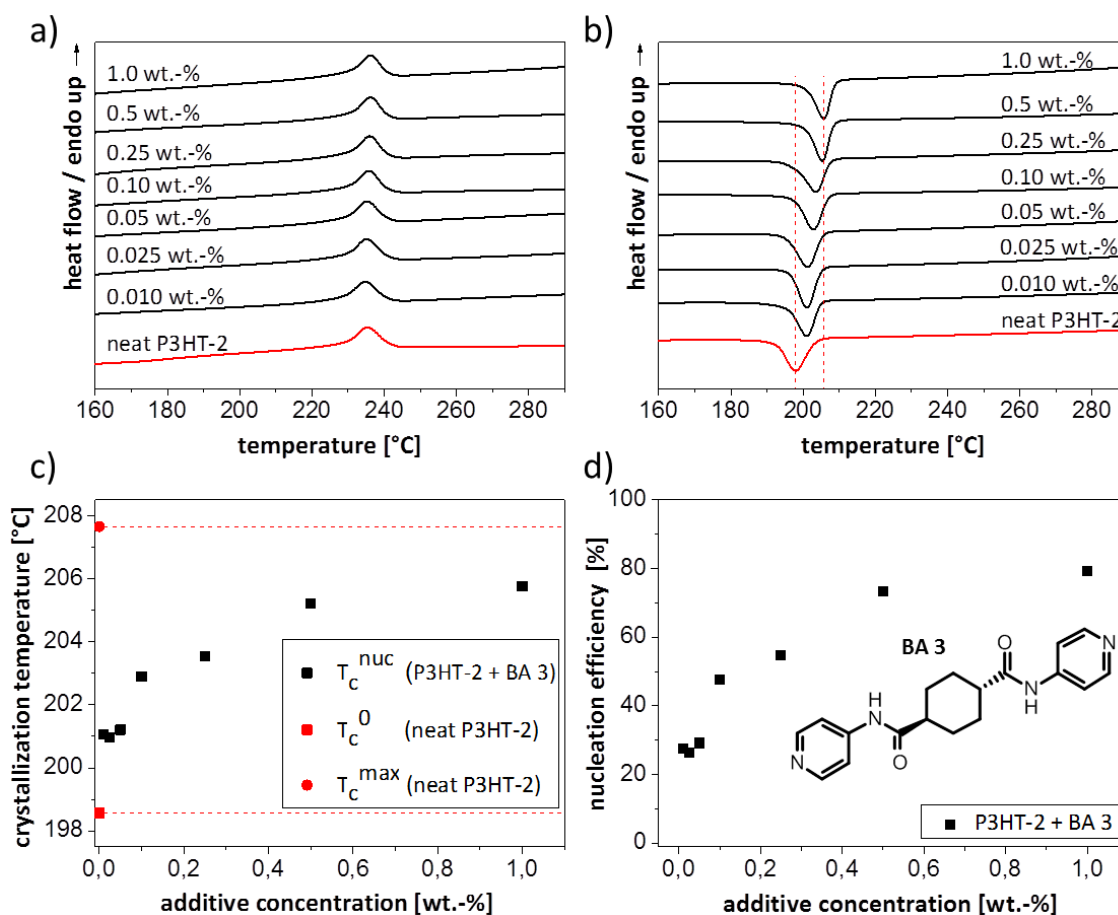


Figure 107: (a) Second heating curves and (b) second cooling curves of neat P3HT-2 (red curve) and P3HT-2 comprising different amounts of BA 3 (black curves). DSC heating and cooling rate: $10 \text{ K}\cdot\text{min}^{-1}$. (c) Polymer crystallization temperatures of P3HT-2 comprising BA 3 as function of the additive concentration. (d) Calculated nucleation efficiencies of BA 3 on P3HT-2 as function of the additive concentration. Insert shows the molecular structure of BA-3.

Figure 107c provides clearer visualization that the T_c^{nuc} increases continuously with the additive concentration. This increase flattens at high additive concentrations but a clear plateau can not be observed. However, it can be expected that a further increase of the BA 3 concentration above the value of 1 wt. % does not lead to a significant higher T_c^{nuc} of P3HT-2. This is also reflected by the plot of the calculated nucleation efficiencies (Figure 107d). A continuous increase in efficiency can be observed up to the additive concentration of 1 wt.-%. The highest determined NE, which could be achieved with the nucleating agent BA 3, amounts to approximately 80 %.

4.4.2.4 Nucleation of P3HT with BA 4 (*N,N'*-((1*r*,4*r*)-cyclohexan-1,4-diyl)diisonicotinamide)

Finally, the results of the bisimide BA 4 with regard to the nucleation of P3HT-2 are discussed. As BA 3, BA 4 is based on a cyclohexane core but differs in the linking of the amide groups. Figure 108 shows the summary of the DSC experiments of all investigated concentrations of

BA 4. Figure 108a shows that the T_m of **P3HT-2** does not increase due to the addition of the additive. Instead, T_c^{nuc} shifts significantly to higher values upon the addition of **BA 4** (Figure 108b). This shift is continuously increasing up to an additive concentration of 0.25 wt.-%. For higher concentrations, the T_c^{nuc} does not change and remains constant. Furthermore, it seems that after the addition of **BA 4**, in the concentration area of 0.01-0.05 wt.-%, two crystallization peaks are formed. It is assumed that the higher one indicates nucleated **P3HT-2**, the lower one neat non-nucleated **P3HT-2**. The reason for this is attributed to an inhomogeneous distribution of the additive in the P3HT melt, or probably to a too low additive concentration, which provides insufficiently heterogeneous nuclei. For the determination of T_c^{nuc} in this concentration range, always the higher peak value was selected.

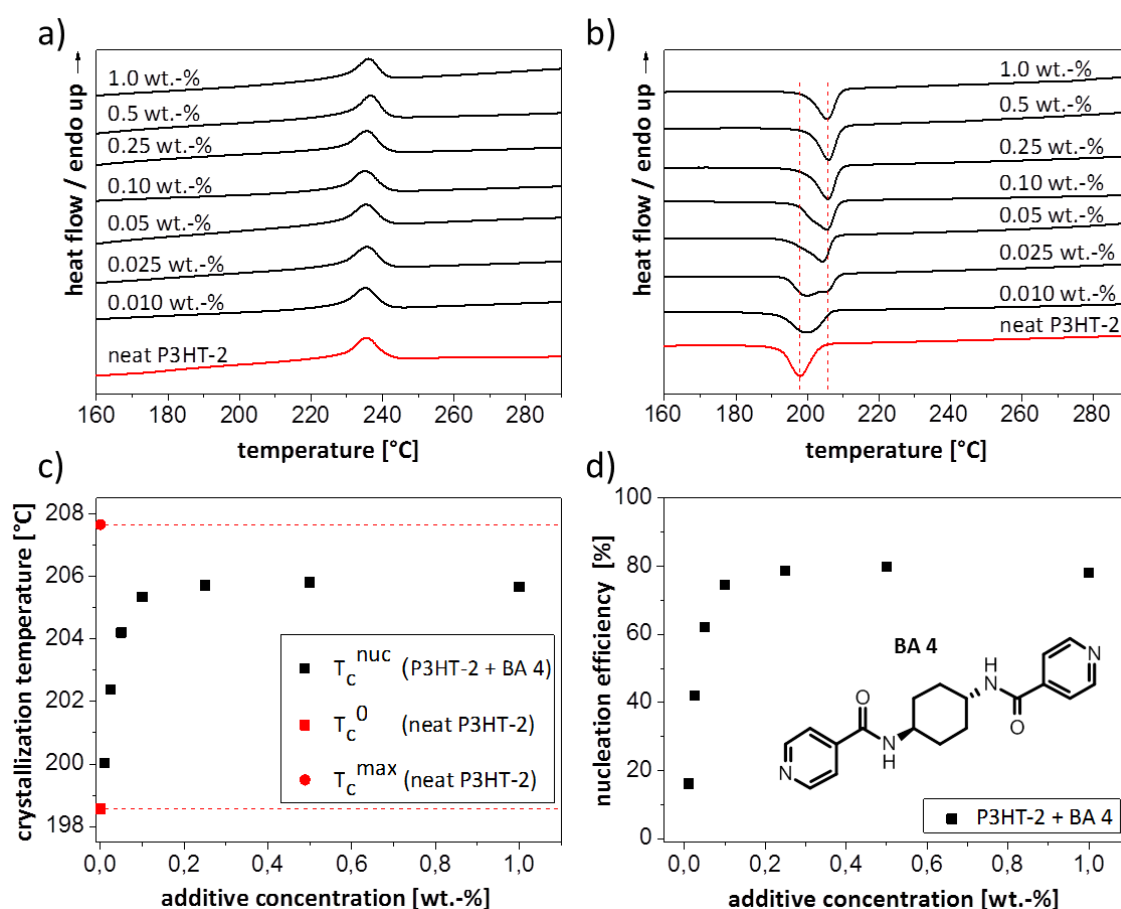


Figure 108: (a) Second heating curves and (b) second cooling curves of neat P3HT-2 (red curve) and P3HT-2 comprising different amounts of BA 4 (black curves). DSC heating and cooling rate: $10 \text{ K}\cdot\text{min}^{-1}$. (c) Polymer crystallization temperatures of P3HT-2 comprising BA 4 as function of the additive concentration. (d) Calculated nucleation efficiencies of BA 4 on P3HT-2 as function of the additive concentration. Insert shows the molecular structure of BA 4.

Figure 108c shows the measured T_c^{nuc} of **P3HT-2** comprising **BA 4** as a function of the additive concentration. A degressive pattern of the T_c^{nuc} with increasing additive concentration can be observed, which eventually reaches a plateau. The maximum crystallization temperature amounts to 205.8°C and can be achieved with an additive concentration of 0.5 wt.-%. This

value is almost 8 °C above T_c^0 of **P3HT-2**. **Figure 108d** shows the corresponding values for the nucleation efficiencies of **BA 4** as nucleating agent for P3HT. Even the addition of small amounts of **BA 4** shows an efficiency of over 50 %. The maximum NE amounts to 80 % and can be observed for an additive concentration of 0.5 wt.-%. According to this N,N'-(cyclohexan-1,4-diyl)diisonicotinamide can be regarded as an efficient nucleating agent for **P3HT -2**.

4.4.4.5 Comparison of the different nucleating agents for P3HT

In the previous chapter, the results of the nucleating agents **BA 1-4** were presented in detail. Here the different additives are compared and evaluated with each other. **Figure 109** shows the calculated nucleation efficiencies of all successfully used nucleating agents as function of their respective concentrations. Thereby, the two pyridine-containing bisamides **BA 1** and **BA 2** based on benzene cores show the highest efficiencies with over 90 % in value. They differ only in the orientation of the amide groups. Obviously, this has little impact on their ability to nucleate P3HT efficiently. Instead, it becomes clear that the bisamide core has a significant influence on the nucleation of P3HT, compared to the other two bisamides **BA 3** and **BA 4**, which are based on a cyclohexane core and feature obvious lower efficiencies.

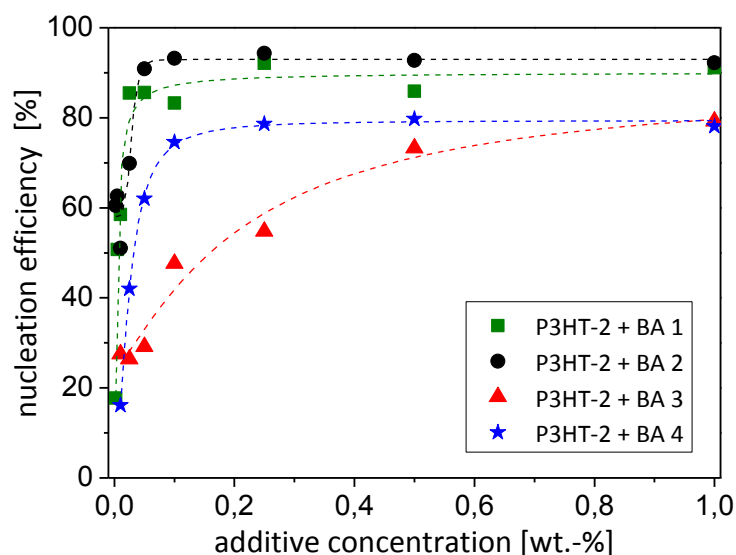


Figure 109: Calculated nucleation efficiencies of **BA 1** (green squares), **BA 2** (black circles), **BA 3** (red triangles) and **BA 4** (blue stars) on **P3HT-2** as a function of the additive concentrations.

The nucleation efficiencies of the nucleating agents **BA 1**, **BA 2** and **BA 4** reach a plateau even at low additive concentrations (0.1-0.25 wt.-%). In contrast, bisamide **BA 3** shows a steady increase in efficiency over the complete concentration range investigated. This increase flattens at high additive concentrations. Thus, it can be assumed that a further

increase of the **BA 3** concentration above the value of 1 wt. % does not lead to a significant higher efficiency. To conclude, all these bisamides are excellent nucleating agents for **P3HT-2**.

4.4.3 Isothermal crystallization behaviors of P3HT-bisamide compounds

A further possibility to investigate polymer crystallization at higher temperatures next to the addition of nucleating agents can be performed by isothermal crystallization at temperatures slightly above the standard onset crystallization temperature of the polymer. Such isothermal investigations can also be used to verify the nucleating effect of an additive, because the isothermal crystallization investigation is often regarded as more sensitive compared to the dynamic DSC investigation. In this case, the nucleation mechanism and crystallization rates can also be described with the Avrami model. The Avrami equation specifically describes the kinetics of crystallization. It's expressed as.^[255]

$$1 - X_t = \exp(-kt^n) \quad (4)$$

or

$$\ln[-\ln(1 - X_t)] = \ln k + n \ln t \quad (5)$$

where k denotes the temperature-dependent crystallization rate constant and n is the Avrami exponent, which depends on the nucleation geometry.^[249,255] In order to determine the parameters of the Avrami equation, the relative crystallinity X_t must first be plotted against the isothermal holding time (**Figure 110a**).

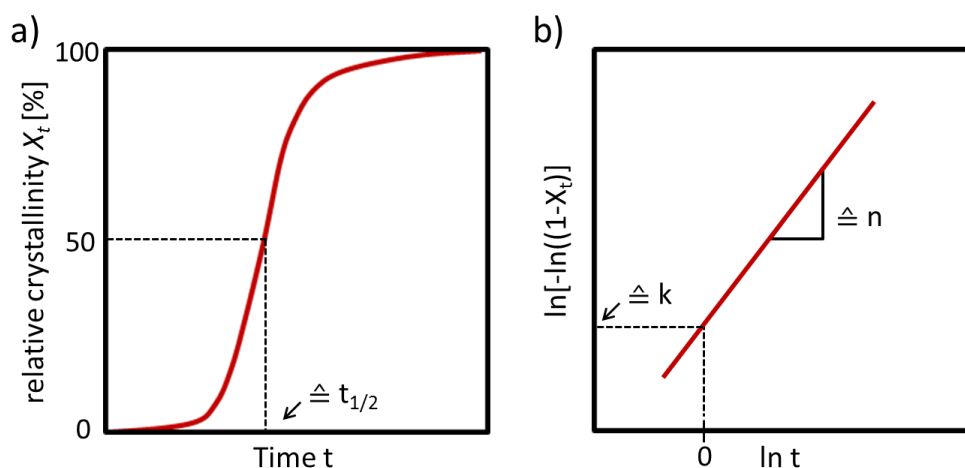


Figure 110: (a) Typical isothermal transformation plot of the relative crystallinity in dependency of the isothermal holding time. The crystallization half-time $t_{1/2}$ corresponds to the time where 50 % of the polymer is crystallized during the isothermal holding. (b) Plot of the avrami equation to determine the avrami exponent n (corresponds to the slope of the linear fit) and the crystallization rate k (corresponds to the intercept of the fit with the Y-axis).

The relative crystallinity corresponds to the integration of the crystalline region of the isothermal DSC curve. On the basis of this plot the crystallization half-time $t_{1/2}$ can also be determined, which is located at 50 % of X_t . After plotting $\ln[-\ln(1-X_t)]$ versus $\ln t$ and fitting the

linear regime of the data, the avrami exponent n corresponds to the slope of the linear fit and the crystallization rate k corresponds to the intercept of the linear fit with the Y-axis (Figure 110b). In order to verify the nucleating effect of the pyridine-containing bisamides on the P3HT crystallization, isothermal crystallization kinetics of **P3HT-2** with and without nucleating agent were studied via DSC, plotted and evaluated as described before. The sample preparation for the isothermal DSC experiments was identical to that of the nucleation tests in the previous chapter for the dynamic DSC experiments. The corresponding temperature profile is shown in the experimental part. The investigated isothermal holding temperatures (T_{iso}) were 214 °C and 216 °C. The concentration of additive with respect to **P3HT-2** was 1 wt.-%. In addition, concentration-dependent isothermal crystallization studies were also performed with the bisamide **BA 1** for both T_{iso} at 214 °C and 216 °C.

Figure 111 shows the isothermal DSC thermographs of **P3HT-2** with and without different nucleating agents for isothermal annealing temperatures of 214 °C and 216 °C.

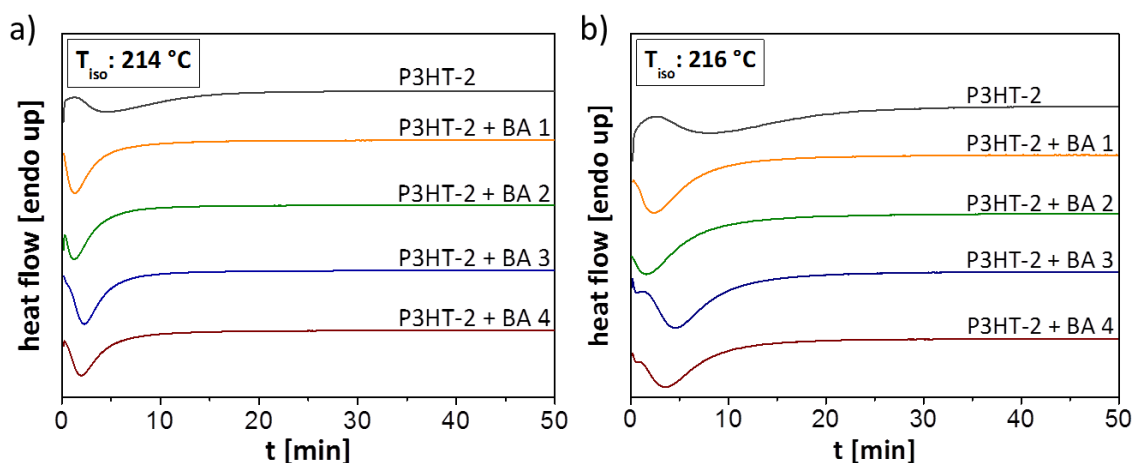


Figure 111: Isothermal DSC thermographs of **P3HT-2** with and without different nucleating agents for an isothermal holding temperature of 214 °C (a) and 216 °C (b). The concentration of the additives with respect to **P3HT-2** was 1 wt.-% each.

For both temperatures it can be observed that the neat **P3HT-2** begins to crystallize much later than the **P3HT-2** samples with the different bisamide additives. In some cases, the additivated samples are almost completely crystallized before the neat P3HT even starts to crystallize. After that, the additives can initiate the P3HT crystallization at much higher temperatures. Furthermore, it can be seen that the crystallization of **P3HT-2** starts with the additives **BA 1** and **BA 2** fastest. These samples are also completely crystallized first. The samples with the additives **BA 3** and **BA 4** require slightly longer time to complete crystallization of the P3HT than the previously mentioned samples, however, are also readily crystallized well before the neat **P3HT-2**.

Figure 112a shows the change in relative crystallinity X_t as a function of crystallization time t for neat **P3HT-2** and **P3HT-2** with different pyridine-containing nucleating agents for the investigated T_{iso} of 214 °C and T_{iso} of 216 °C (**Figure 112c**). The DSC thermograms on which both figures are based on are shown in previous **Figure 111**. The curves in the **Figures 112a** and **c** have the typical sigmoidal shape as mentioned in **Figure 110a**, which reflects the initial nucleation step, radial crystal growth (primary crystallization step) and finally the lamellae thickening step (secondary crystallization).^[249] The dashed line within the graph serves as guidance for the eye and describes 50 % of the P3HT crystallization. The points of intercept of this straight line with the sigmoidal curves finally indicate the crystallization half-time $t_{1/2}$ as X-values.

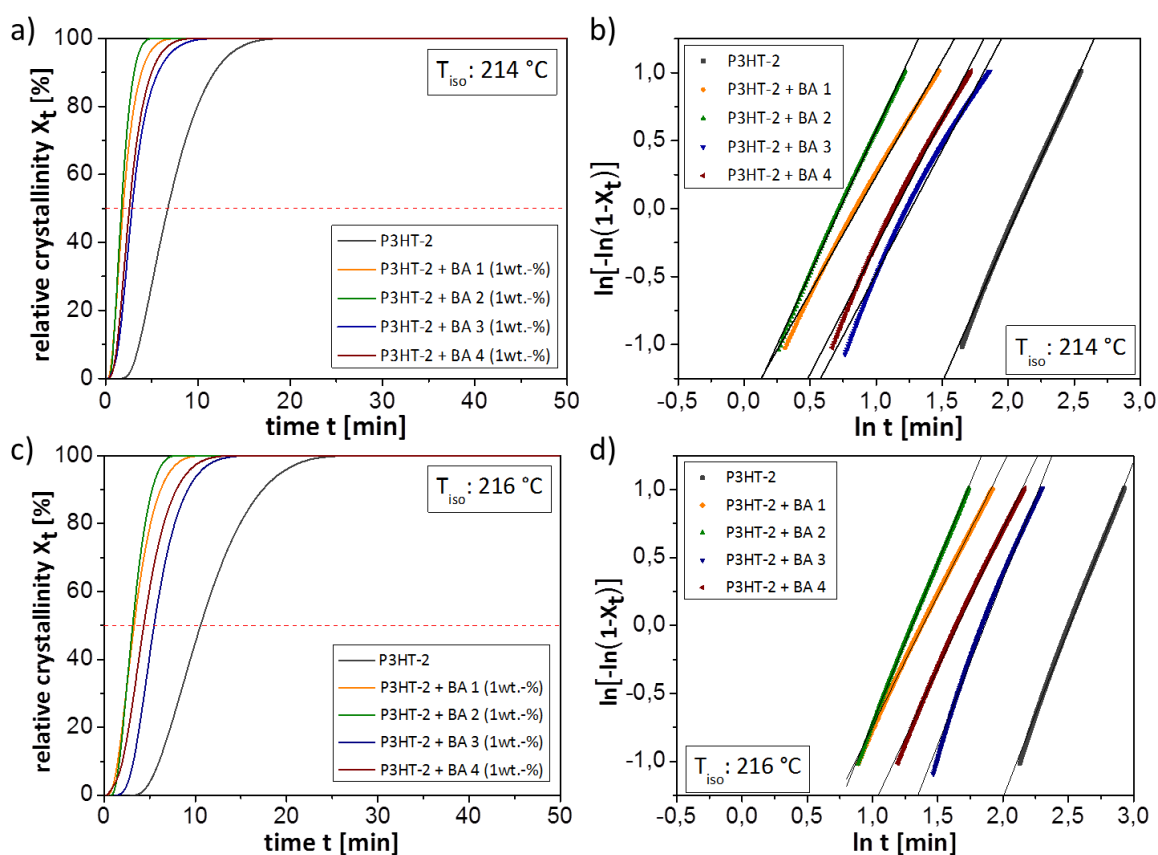


Figure 112: (a,c) Plot of relative crystallinity X_t of P3HT-2 with and without with several pyridine-containing bisamides as a function of crystallization time t for an isothermal annealing temperature of 214 °C (a) and 216 °C (c). The red dashed line represents 50 % of relative crystallinity. (b,d) Plot of $\ln[-\ln(1-X_t)]$ as a function of $\ln t$ for isothermal crystallization of P3HT-2 with and without with several pyridine-containing bisamides as nucleating agents. The isothermal crystallization temperatures were 214 °C (b) and 216 °C (d). The concentration of the nucleating agents was 1 wt.-% each in respect to P3HT-2.

The determined values of $t_{1/2}$ of all samples for the two different T_{iso} are listed in **Table 12**. Based on this data, it can be shown that neat **P3HT-2** takes more than three times as long to reach $t_{1/2}$ as the two **P3HT-2** samples comprising the nucleating agents **BA 1** and **BA 2**. Compared to the samples with the bisamides **BA 3** and **BA 4**, $t_{1/2}$ is about twice as long. These results can be observed for both isothermal crystallization temperatures (214 °C and 216 °C).

The **Figures 112a** and **c** also show that all curves of the nucleated **P3HT-2** samples are very close to each other and show a slightly higher slope than the curve of the neat **P3HT-2**. This indicates a higher crystallization rate of the nucleated P3HT samples compared to the neat **P3HT-2** crystallization rate. To provide more detailed information on the rate of crystallization and the nucleation mechanism the Avrami model with its equation (**Equation 5**) is used, where the parameter X_t describes the relative crystallinity, k denotes the temperature-dependent crystallization rate constant and n is the Avrami exponent. **Figure 112b** shows the plots of $\ln[-\ln(1-X_t)]$ versus $\ln t$ of neat **P3HT-2** and **P3HT-2** with different nucleating agents for T_{iso} of 214 °C and **Figure 112d** the results for T_{iso} of 216 °C. As mentioned above, the values of the rate constant k and the Avrami exponent n can be obtained from the intercept of the linear region and the slope, respectively. The determined values for the two different investigated T_{iso} are summarized in **Table 12**. It can be seen that the values for the Avrami exponent n of the nucleated samples are all slightly lower than those of the corresponding neat **P3HT-2** samples. However, the values are very close together, indicating that the addition of the nucleating agents may have little effect on the nucleation mechanism.

Table 12: Crystallization kinetics data obtained from the Avrami model for P3HT-2 with several nucleating agents at two different isothermal crystallization temperatures (214 °C and 216 °C).

T_{iso}	Sample	n	k [min^{-1}]	$t_{1/2}$ [min]
214 °C	P3HT-2	2.20	0.010	6.76
	P3HT-2 + BA 1 (1 wt.-%)	1.70	0.231	1.90
	P3HT-2 + BA 2 (1 wt.-%)	2.10	0.217	1.72
	P3HT-2 + BA 3 (1 wt.-%)	1.82	0.100	2.87
	P3HT-2 + BA 4 (1 wt.-%)	1.87	0.116	2.58
216 °C	P3HT-2	2.47	0.002	10.57
	P3HT-2 + BA 1 (1 wt.-%)	1.93	0.069	3.29
	P3HT-2 + BA 2 (1 wt.-%)	2.35	0.047	3.13
	P3HT-2 + BA 3 (1 wt.-%)	2.43	0.011	5.48
	P3HT-2 + BA 4 (1 wt.-%)	2.05	0.034	4.36

In contrast to the Avrami exponents, the differences in the determined k values are significant. It can be shown that the k values of the nucleated samples are distinctly higher than for neat **P3HT2**, both at T_{iso} of 214 °C and T_{iso} of 216 °C. The highest differences can be observed between neat **P3HT-2** and **P3HT-2** with the nucleating agent **BA 1** at T_{iso} of 216 °C.

Therefore, additional concentration-dependent isothermal crystallization investigations were performed with this bisamide. The concentration of **BA 1** with respect to **P3HT-2** was reduced within these experiments from 1 wt.-% to 0.1 wt.-% and 0.025 wt.-%.

Figure 113a shows the change in relative crystallinity X_t as a function of crystallization time t for neat **P3HT-2** and **P3HT-2** with different concentrations of the pyridine-containing nucleating agent **BA 1** for a T_{iso} of 214 °C. The results for the investigations for a T_{iso} of 216 °C are shown in **Figure 113c**. The curves show once more the typical sigmoidal progression, which has already been discussed above. Furthermore it can be seen, that the curves of the nucleated samples are almost superimposed, whereas the curve of the neat **P3HT-2** sample is shifted at higher isothermal crystallization times.

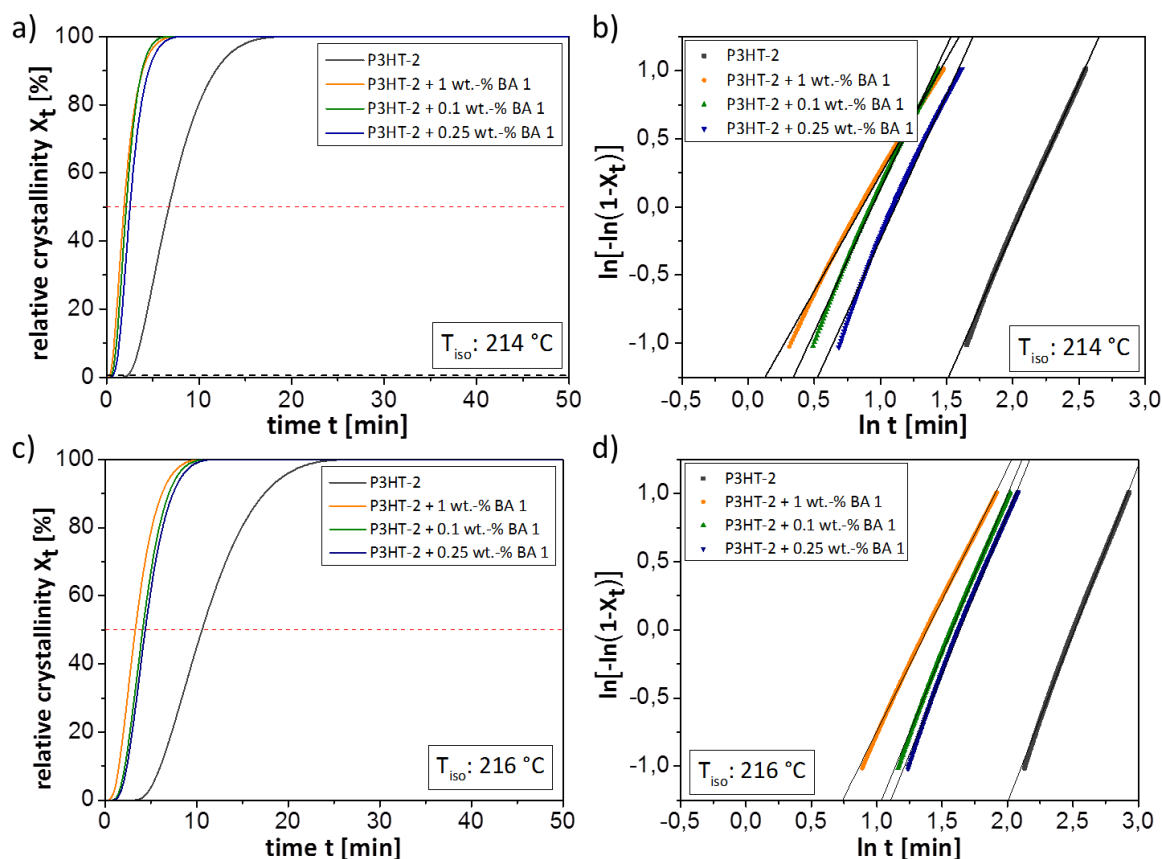


Figure 113: (a,c) Plot of relative crystallinity X_t of P3HT-2 with different concentrations of the nucleating agent **BA 1** as a function of crystallization time t for an isothermal annealing temperature of 214 °C (a) and 216 °C (c). The red dashed line represents 50 % of relative crystallinity. (b,d) Plot of $\ln[-\ln(1-X_t)]$ as a function of $\ln t$ for isothermal crystallization of P3HT-2 with different amounts of **BA 1**. The isothermal crystallization temperatures were 214 °C (b) and 216 °C (d).

The intersection points of the dotted straight line, which indicates 50 % P3HT crystallinity, with the sigmoidal curves reflect the $t_{1/2}$ values. These are listed in **Table 13** for the two different T_{iso} . Based on these data, it can be shown that there is a dependency of $t_{1/2}$ on the additive concentration used; the higher the amount of **BA 1**, the lower the $t_{1/2}$. Comparing $t_{1/2}$

of neat **P3HT-2** with $t_{1/2}$ of **P3HT-2** comprising the lowest **BA 1** concentration (0.025 wt.-%), investigated within this series of experiments, one recognizes that even this small amount of additive is sufficient to reduce $t_{1/2}$ by a factor of 2.5. These results can once more be observed for both isothermal crystallization temperatures (214 °C and 216 °C). **Figure 113b** shows the plots of $\ln[-\ln(1-X_t)]$ versus $\ln t$ of neat **P3HT-2** and **P3HT-2** with different concentrations of **BA 1** for an isothermal crystallization temperature of 214 °C, **Figure 113d** the results for a T_{iso} of 216 °C. The determined parameters of the Avrami model are summarized in **Table 13**. The Avrami exponent n and the temperature-dependent crystallization rate constant k also show a dependence on the bisamide concentration. The higher the concentration is, the lower the slope of the straight line and thus the exponent n and the higher the rate constant k . With decreasing **BA 1** concentration, the Avrami parameters approach the values of neat **P3HT-2**. This trend is confirmed for both isothermal temperatures.

Table 13: Crystallization kinetics data obtained from the Avrami model for P3HT-2 with several concentrations of BA 1 and at two different isothermal crystallization temperatures.

T_{iso}	Sample	n	k [min^{-1}]	$t_{1/2}$ [min]
214 °C	P3HT-2	2.20	0.010	6.76
	P3HT-2 + BA 1 (0.025 wt.-%)	2.13	0.094	2.53
	P3HT-2 + BA 1 (0.1 wt.-%)	2.10	0.140	2.14
	P3HT-2 + BA 1 (1 wt.-%)	1.70	0.231	1.90
216 °C	P3HT-2	2.47	0.002	10.57
	P3HT-2 + BA 1 (0.025 wt.-%)	2.35	0.021	4.38
	P3HT-2 + BA 1 (0.1 wt.-%)	2.33	0.026	4.11
	P3HT-2 + BA 1 (1 wt.-%)	1.93	0.069	3.29

The previous DSC studies have shown that the four bisamides **BA 1-4** are excellent nucleating agents for **P3HT-2**. The subsequent studies of the isothermal crystallization kinetics of **P3HT-2** with and without these bisamides confirmed their nucleating effect.

4.4.4 Polarized optical microscopy investigations on P3HT-bisamide films

In the previous chapter it could be shown that the four bisamides **BA 1**, **BA 2**, **BA 3** and **BA 4** are excellent supramolecular nucleating agents for P3HT. These nucleating agents ensure that the number of nuclei in the polymer melt is tremendously increased, and thus the nucleation density. However, since the growth rate of the P3HT spherulites is expected to remain constant, the total size of all crystallites is reduced. In order to examine the extent to which

the insertion of the bisamides influenced the P3HT crystallite sizes, optical microscope images were taken on P3HT-bisamide films.

The procedure of the optical microscopy investigations is shown schematically in **Figure 114**. Initially, 3 wt.-% solutions of **P3HT-2** in CB were prepared for the preparation of the thin films. These solutions were then heated up to 50 °C to homogeneously dissolve the P3HT and then spin coated onto glass slides yielding films with thickness of approximately 300 nm. The individual bisamides were self-assembled separately in CB (standard procedure see **Chapter 3.3.5**). After the self-assembly process the solvent was evaporated. The remaining self-assembled bisamide were then added onto the prepared P3HT films (**A**). Via this procedure, sharp boundaries could be generated which allow to distinguish clearly between P3HT and the additive. The prepared P3HT-bisamide films were then heated up to 300 °C within a hot stage under nitrogen atmosphere. During this heating process, the P3HT melted first (**B**). Further heating led to a dissolving of the bisamide in the P3HT melt (**C**).

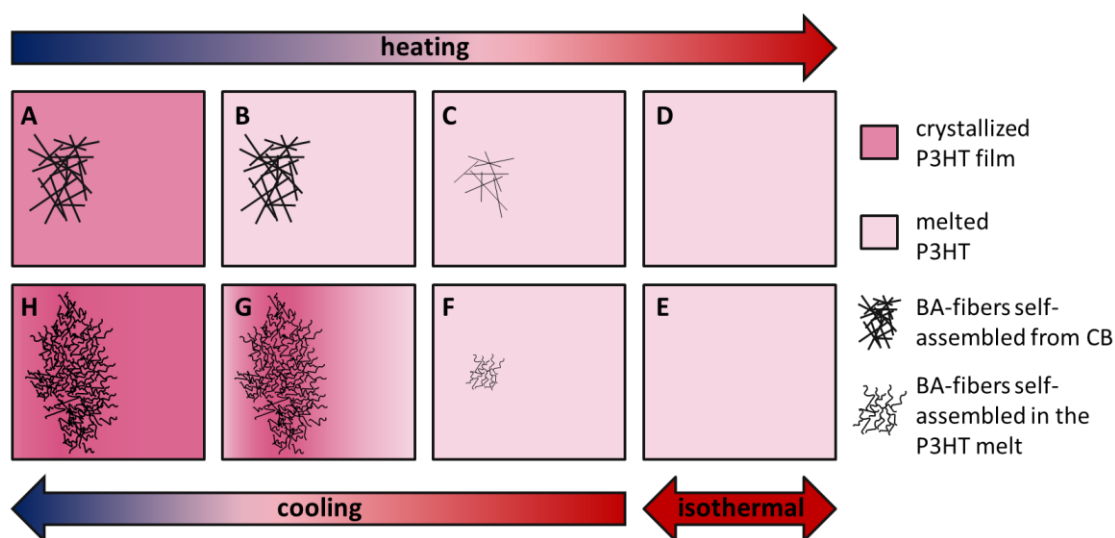


Figure 114: Schematic illustration of the procedure of the optical microscopy investigations. Shown are the heating steps (A-D), the isothermal holding at 300 °C (E) and the cooling steps (F-H). The heating and cooling rates were 10 K·min⁻¹ each.

Subsequently, at 300 °C when all the bisamide is dissolved (**D**) the samples were kept isothermal for five minutes, to ensure complete P3HT melting and bisamide dissolving (**E**). The samples were then cooled down to 150 °C. During the cooling process, the bisamide crystallized prior to the P3HT (**F**). Thus, providing appropriate nucleation sites for the later on crystallization of the P3HT. Further cooling led to the crystallization of the P3HT at the bisamide crystals first (**G**). Finally, at temperatures of the standard crystallization temperature of P3HT the remaining melted P3HT crystallized (**H**). The heating and cooling rates during these investigations were 10 K·min⁻¹ each.

Figure 115 shows a micrograph of a neat **P3HT-2** film after cooling from its melt at 150 °C. The image shows that the neat P3HT spherulites are already too small to be observable by the optical microscopy. Consequently, the P3HT spherulites of the nucleated samples could not be observed as well, since they are expected to be even smaller. A comparison of the crystallite sizes of neat and nucleated P3HT is therefore not possible using polarized optical microscopy images. However, this technique can be used to investigate whether the bisamide additive dissolves in the polymer melt upon heating and at which temperature the additive recrystallizes upon cooling.

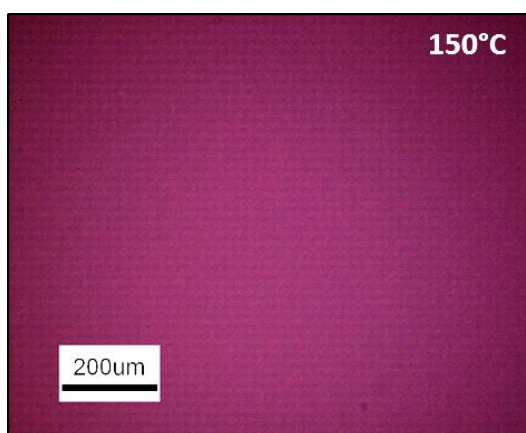


Figure 115: Polarized optical microscopy image of a neat **P3HT-2** film. The micrograph was taken at the end of the cooling process at 150 °C. The experiment was performed under nitrogen atmosphere at heating and cooling rates of 10 K·min⁻¹, respectively. Purple color indicates P3HT crystallization at this temperature. P3HT-2 spherulites can not be detected.

Figure 116 shows a series of recorded micrographs taken during the heating and cooling process, as well as during the isothermal annealing period of a **P3HT-2** film comprising self-assembled bisamide **BA 2**. Thereby, the **P3HT-2** film represents the violet background of the micrograph on which the **BA 2** fibers (orange) rest. At 240 °C the violet P3HT film starts to become brighter, indicating that the P3HT is melting. At about 250 °C, the **BA 2** domain starts to decrease, signifying that the bisamide dissolves in the P3HT melt. **Figure 116f** shows, that after five minutes at 300 °C the bisamide has been completely dissolved in the polymer melt. During the subsequent cooling process, the bisamide starts to crystallize at approximately 260 °C, which is fairly far above the standard crystallization temperature T_c^0 (198 °C) of **P3HT-2**. Upon further cooling a fibrous network was formed in the polymer melt. At about 230 °C, the **BA 2** is fully recrystallized and thus can act as a heterogeneous nucleating agent for the molten P3HT. Between 210 °C and 200 °C a change in color of the background from light violet to dark violet can be observed. This indicates the crystallization of the **P3HT-2** film which correlates very well with the observed phase transition from the previous DSC investigations.

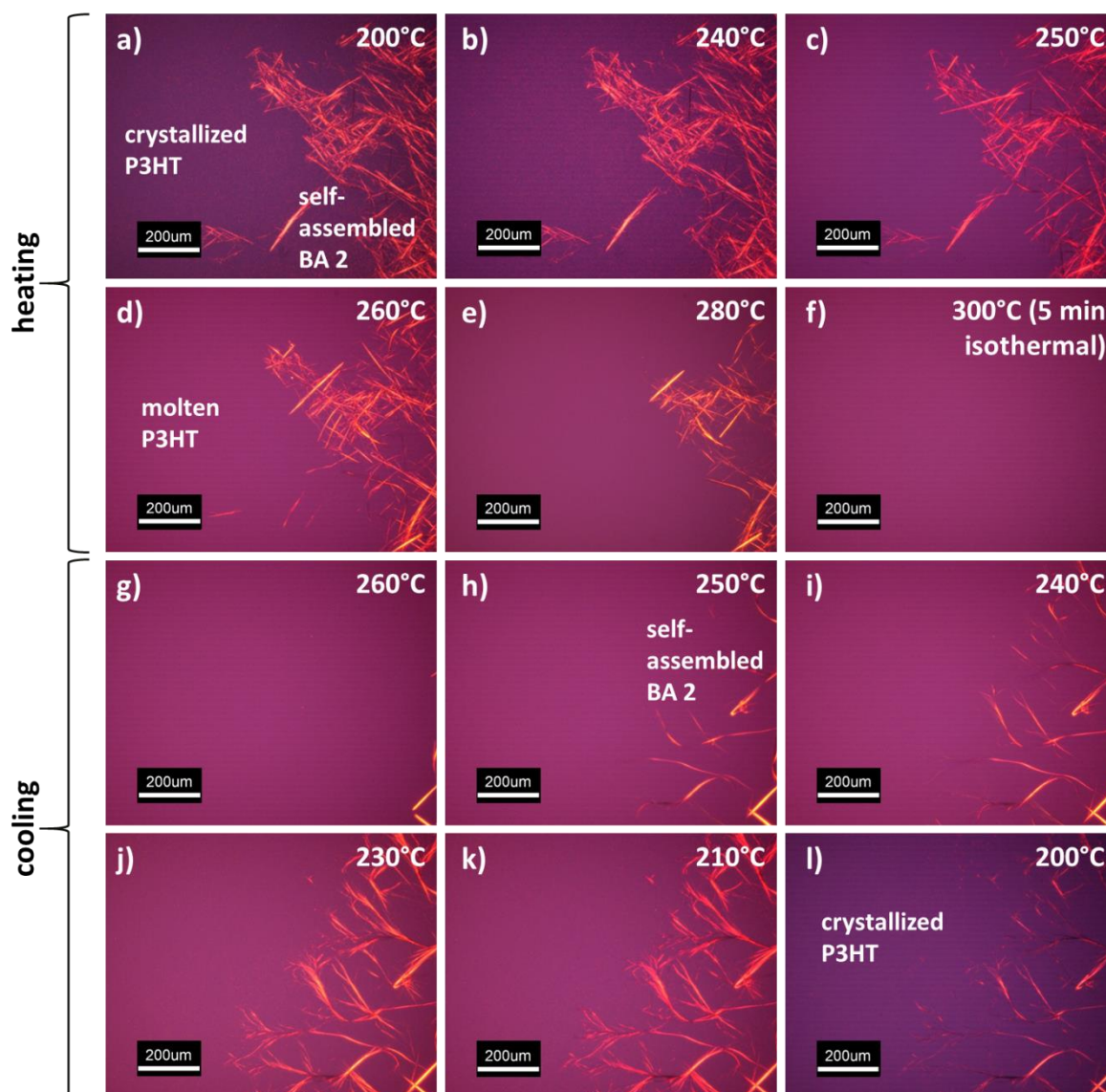


Figure 116: Polarized optical microscopy images of a P3HT-2 film with self-assembled BA 2 nanofibers on the top of the P3HT film: (a-e) micrographs taken during the heating process; (f) micrograph taken at the end of the isothermal annealing period at 300 °C; (g-l) micrographs taken during the cooling process. The experiments were performed under nitrogen atmosphere at heating and cooling rates of 10 K·min⁻¹. The immediate color change upon cooling from 210 °C (k) to 200 °C (l) indicates the P3HT crystallization.

The bisamide **BA 4**, which has been successfully proven to be an efficient nucleating agent for **P3HT-2**, shows, like **BA 2**, a fibrous morphology after the self-assembly process in chlorobenzene. The polarization microscope examinations on these P3HT-bisamide films are shown in **Figure 117**. As described above, the purple background is attributed to the neat crystalline P3HT film and the orange needles are assigned the bisamide. The micrographs show that **BA 4** starts to dissolve in the P3HT melt at a temperature of 250 °C. At approximately 260 °C it is almost completely dissolved. During the subsequent cooling process, it starts to crystallize at 240 °C and thus far above T_c^0 of **P3HT-2**. During this crystallization process, the bisamide forms a fiber network in the P3HT melt. **BA 4** is completely self-assembled at a temperature of approximately 220 °C and thus providing

heterogeneous nucleating sites for P3HT. Upon further cooling, a darkening can be observed near to the **BA 4** fibers, which indicate the crystallization of **P3HT-2**. However, compared to the DSC studies of P3HT comprising this bisamide, this temperature is still well above the onset crystallization temperature of this polymer additive combination. Therefore, it is more likely that this is not the crystallizing **P3HT-2**, but rather the focus of the measurement has been lost due to differences in the height of the film. Between 210 °C and 200 °C a significant change in color of the background from light violet to dark violet can be observed. This indicates the crystallization of the **P3HT-2**.

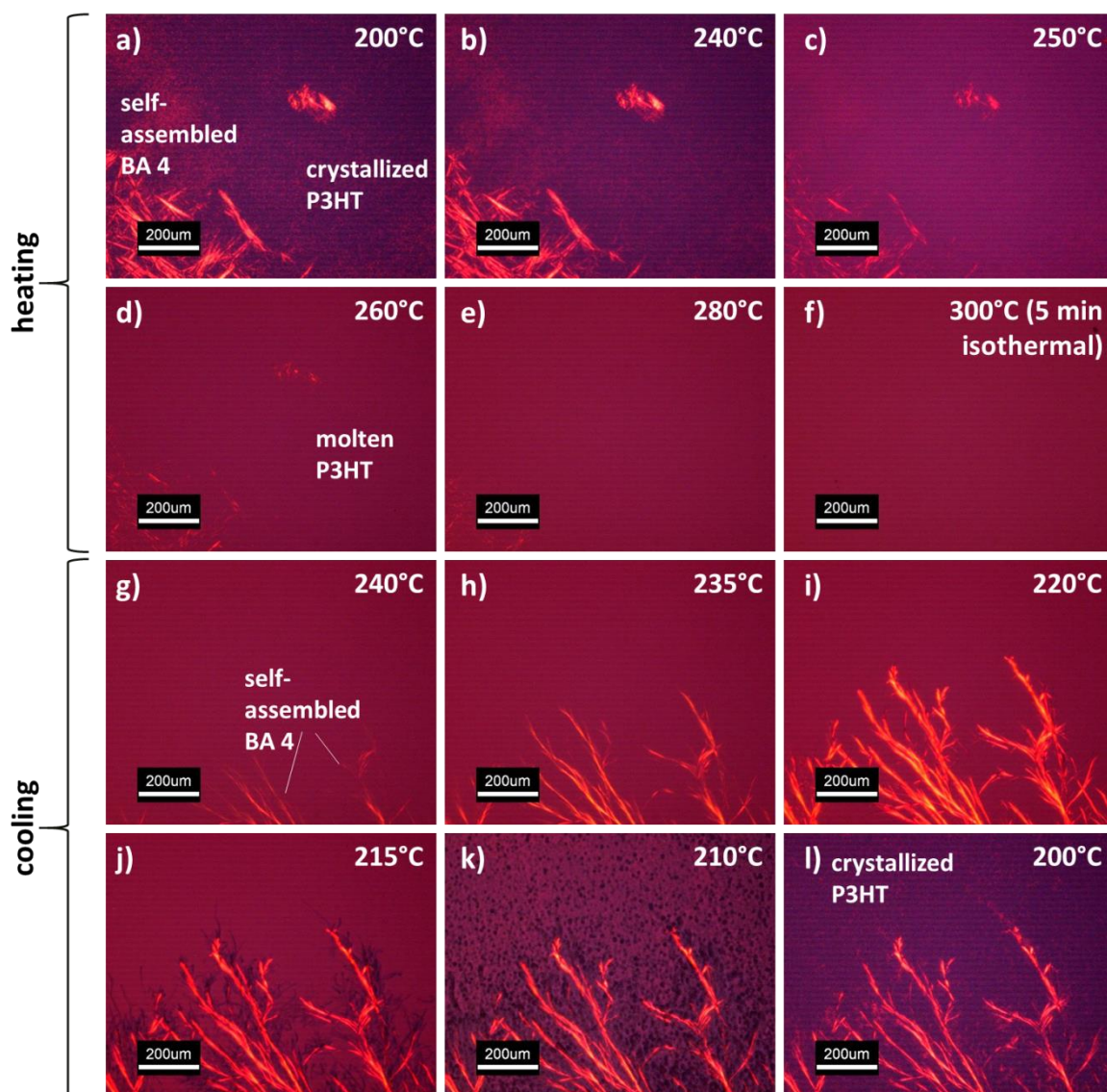


Figure 117: Polarized optical microscopy images of a P3HT-2 film comprising self-assembled BA 4 nanofibers on the top of the P3HT film: (a-e) micrographs taken during the heating process; (f) micrograph taken at the end of the isothermal holding period at 300 °C; (g-l) micrographs taken during the cooling process. The experiments were performed under nitrogen atmosphere with heating and cooling rates of $10 \text{ K}\cdot\text{min}^{-1}$. The immediate color change upon cooling from 210 °C (k) to 200 °C (l) indicates the P3HT crystallization.

The remaining two bisamides **BA 1** and **BA 3**, which are also able to efficiently nucleate P3HT, did not show any fibrous structures after the self-assembly experiments in CB (see Chapter

3.3.5). **BA 1** is based on a terephthalic acid core and **BA 3** on a trans-cyclohexane-1,4-dicarboxylic acid core. Thus, they differ from the two preceding bisamides (**BA 2**, **BA 4**) in their orientation of the amide groups to the central core. Both bisamides are much more thermally stable than their diamino based equivalents. The micrographs of the polarization microscopy examinations are shown in the **Figures 118** and **119**. Up to a temperature of 300 °C, both bisamides hardly show any solubility in the P3HT melt. Therefore, the maximum heating temperature has been increased up to 340 °C for these experiments.

The polarization microscope studies of the **P3HT-2** films with the bisamide **BA 1** are shown in **Figure 118**.

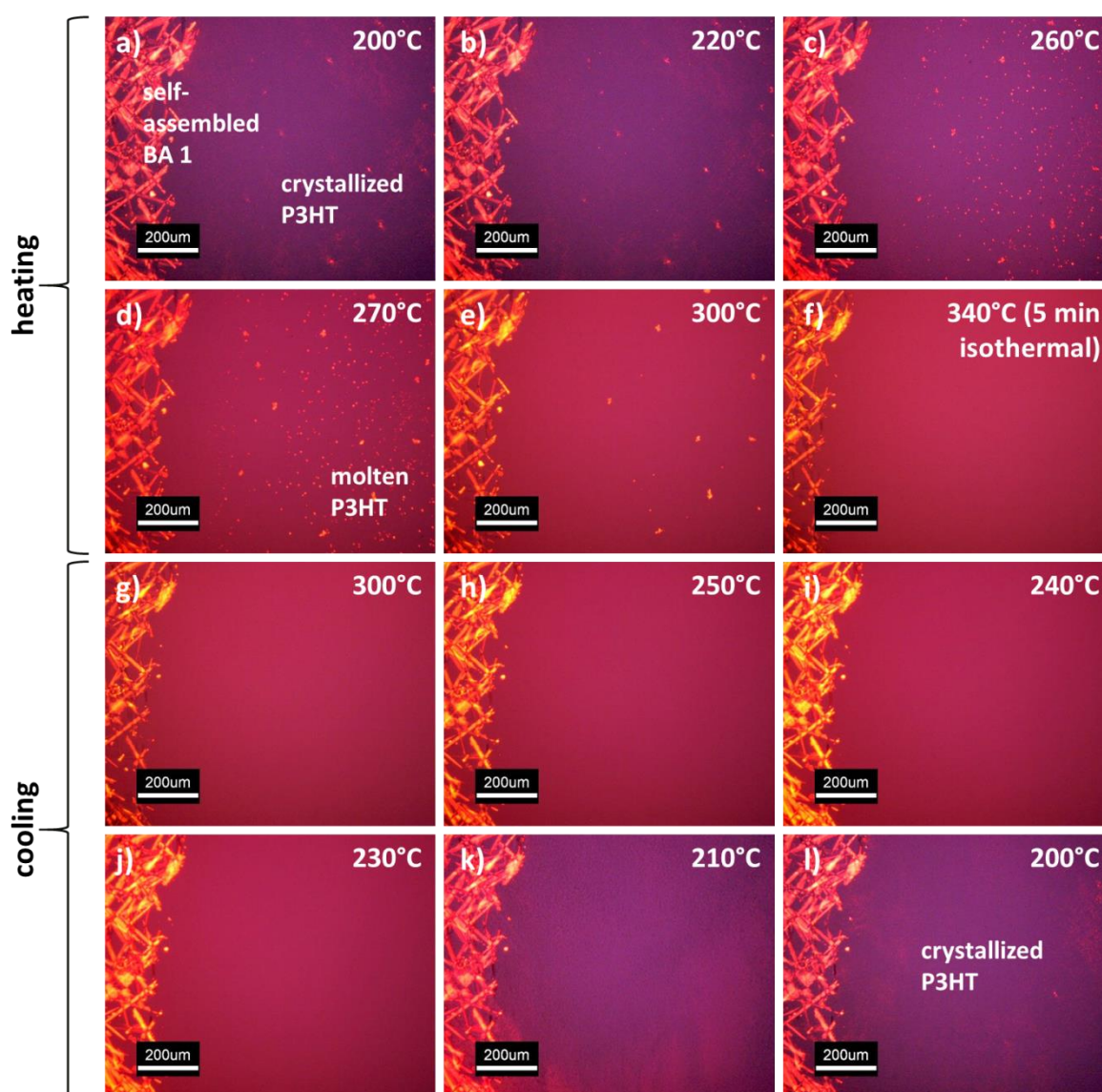


Figure 118: Polarized optical microscopy images of a P3HT-2 film comprising self-assembled BA 1 nanofibers on the top of the P3HT film: (a-e) micrographs taken during the heating process; (f) micrograph taken at the end of the isothermal holding period at 340 °C; (g-l) micrographs taken during the cooling process. The experiments were performed under nitrogen atmosphere with heating and cooling rates of 10 K·min⁻¹.

The purple background describes the neat P3HT film and the orange needles the bisamide **BA 1**. The micrographs show that **BA 1** dissolved only marginally in the P3HT melt up to a temperature of 340 °C (**Figure 118f**), thus, no defined temperature can be determined at which **BA 1** is completely dissolved in the P3HT melt and at which temperature **BA 1** has crystallized upon cooling. Furthermore, comparing **Figures 118g** to **118l**, it can be assumed that **BA 1** does not form macroscopically visible crystals upon cooling in the P3HT melt. The crystallization of the P3HT film, which is indicated by the color change from light to dark violet, can be observed at 210 °C for this sample. This is within the range of the onset crystallization temperature for P3HT with this nucleating agent (see **Figure 105**).

Figure 119 shows the polarization microscope examinations of **P3HT-2** with the bisamide **BA 3**. The purple background describes the neat P3HT film and the orange needles the bisamide.

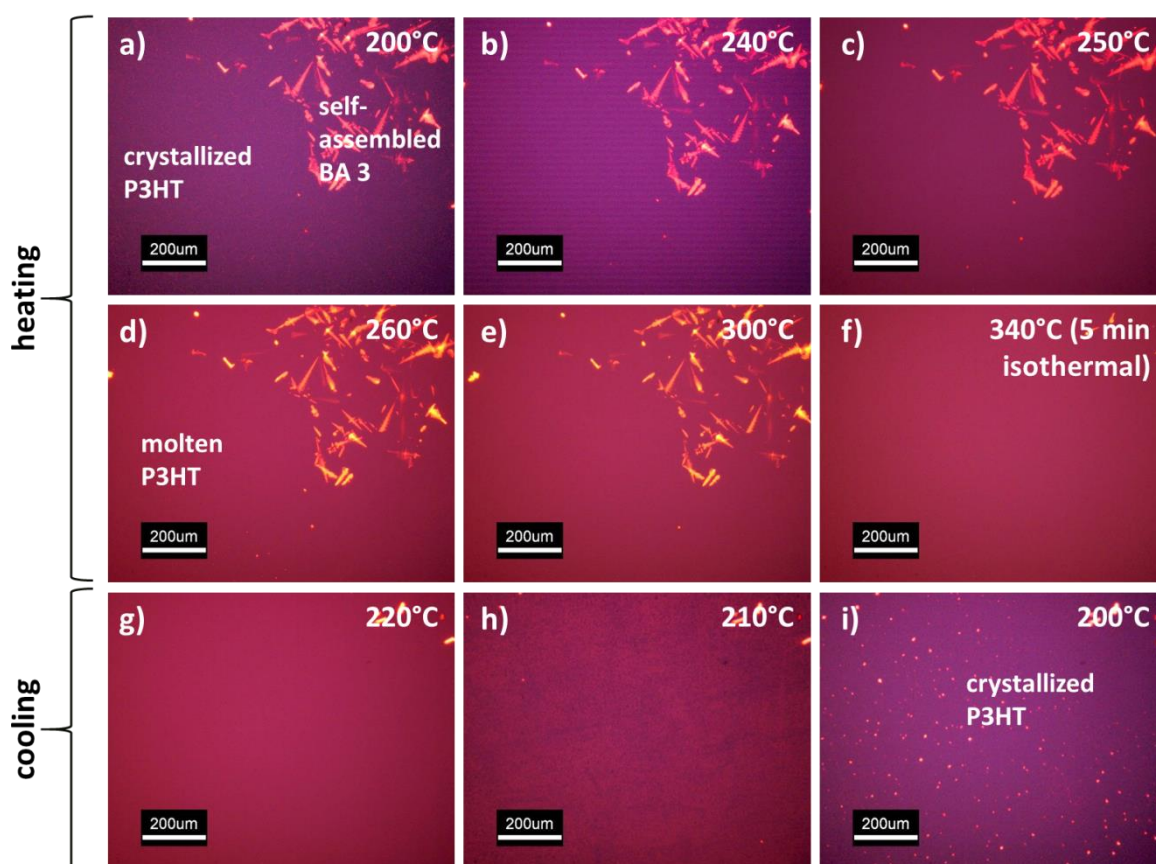


Figure 119: Polarized optical microscopy images of a P3HT-2 film comprising self-assembled **BA 3** nanofibers on the top of the P3HT film: (a-e) micrographs taken during the heating process; (f) micrograph taken at the end of the isothermal holding period at 340 °C; (g-i) micrographs taken during the cooling process. The experiments were performed under nitrogen atmosphere with heating and cooling rates of 10 K·min⁻¹.

The micrographs show that **BA 3** first dissolves in the P3HT melt for temperatures above 300 °C. At a temperature of 340 °C **BA 3** is almost completely dissolved in the P3HT melt

(**Figure 119f**). As described for experiments with **BA 1**, upon cooling of the film, however, it is not possible to specify an explicit temperature at which the bisamide crystallizes. It can be assumed that the dissolved bisamide diffuses very quickly through the P3HT melt and does not form macroscopic visible crystals during its crystallization. Only at the end of the experiment at 200 °C (**Figure 119i**), after the **P3HT-2** has also been crystallized, 10 µm large crystals can be observed, which may be attributed to crystallized **BA 3**.

To conclude, an optical visualization of the nucleation of P3HT could not be directly demonstrated with the polarized optical microscopy investigations in terms of a transcrystallization of the P3HT on the nucleating agents, since already the neat **P3HT-2** crystallites are too small to visualize them with the microscope. However, it could be shown for **BA 2** and **BA 4** that these additives completely dissolve in the P3HT melt at temperatures below 300 °C and crystallize upon cooling well before the **P3HT-2** crystallizes. **BA 1** and **BA 3** can be at least partially dissolved and provide nucleation sites for P3HT crystallization as these findings are in good agreement with the observations made by DSC.

5 Highly ordered shish-kebab superstructures

5.1 Nanofiber formation of P3HT in solution

Π -conjugated polymers such as P3HT may self-assemble into one-dimensional aggregates with a high aspect ratio. In literature these are often referred to as nanowhiskers, nanofibrils, nanofibers and nanorods. Thereby the aggregation is driven by strong perpendicular π - π -interactions of the conjugated backbone and by hydrophobic interactions of the side chains of P3HT.^[114]

Ihn et al. reported for the first time of P3HT nanowhiskers in 1993.^[115] In their investigations they used cyclohexanone as solvent for P3HT. Since cyclohexanone is a poor solvent for P3HT, the mixture must be heated up to 50 °C to completely dissolve P3HT at a concentration of 0.05 wt.-% (with respect to cyclohexanone). By slowly cooling the sample with a cooling rate of 25 °C·h⁻¹, the dissolved P3HT crystallizes. The resulting nanofibrils showed a width of 15 nm, a height of 5 nm and a length of more than 10 μ m (**Figure 120a**). Crystal structure studies proved that there was an edge-on orientation present. Furthermore, the results showed, with regard to the height of the nanofibers, that they are built up of only two or three layers of polymer chains. The enormous aspect ratio illustrates the strong packaging tendency along the π -stacking direction. Since the P3HT grade used for this investigations had a molecular weight of about 29 kg·mol⁻¹, the average contour length of the chains is calculated at approximately 65 nm. However, the fact that the resulting nanowhiskers have only a width of around 15 nm clearly shows that chain folding has taken place.^[115]

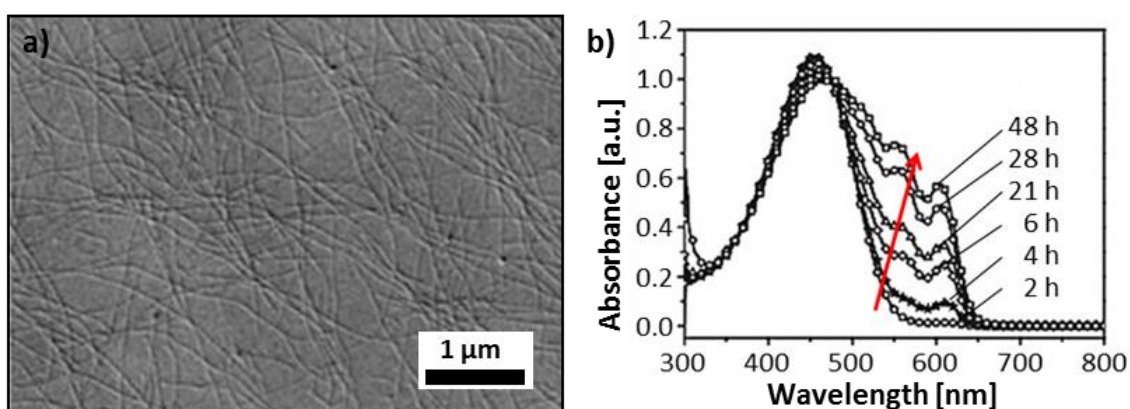


Figure 120: (a) Transmission electron micrograph of poly(3-hexylthiophene) whiskers grown from a 0.05 wt.-% cyclohexanone solution.^[115] (b) Absorption spectra of a 1 wt.-% solution of P3HT in p-xylene heated at 80 °C to ensure complete dissolution of the polymeric material and then allowed to evolve after cooling to room temperature for different periods of time.^[256]

After this report of Ihn et al., several groups investigated the formation and characterization of such self-assembled P3HT nanostructures. Thereby two processing methods have

established: the so-called “whisker method” and the so-called “mixed solvent method”. Both approaches rely on the growth of the fibers is driven by strong π - π -interactions and undesirable interactions between the solvent and the polymer backbone due to a limited solubility.^[257]

The “whisker method” make use of a poor solvent to form P3HT nanowhiskers. Guillerez et al. used in their studies p-xylene as a poor solvent for P3HT. After dissolving P3HT at 80 °C the mixture is slowly cooled to room temperature (20 °C·h⁻¹).The resulting dispersions remain stable over a period of several weeks. For a concentration of P3HT of more than 2 wt.-% with respect to p-xylene, a gel formation can be observed. By "in situ" linear absorption spectroscopy the aggregation in solution can be monitored (**Figure 120b**). It could be observed that additional vibronic structures are formed at 525, 555, and 610 nm, indicating the formation of highly ordered structures. The resulting nanofibers are up to 5 μ m long, 5 to 15 nm high, and 30 to 50 nm wide.^[256] Samitsu et al. used anisole for effective nanofiber production according to the “whisker method”. They investigated the influence of cooling rate, polymer concentration, and regioregularity of various poly-3-alkylthiophenes on the resulting nanofiber morphologies. They were able to show that the width of the nanofibers increases slowly as the alkyl chain length increases. AFM studies showed that the height of the nanofibers (3-4 nm) corresponds to about 2 to 3 laminated layers of the polymer backbones separated by alkyl side chains and that the nanofiber long axis consists of more than 10⁴ parallel stacks of extended polymer backbones.^[258] Han et al. reported that subsequent ultrasonic oscillation of P3HT nanowhiskers prepared in p-xylene increases the coverage degree of homogeneously distributed nanofibrils and the crystallinity of the film.^[259]

The second method, the “mixed-solvent method” combines several solvents for nanofiber production. Usually, the P3HT is initially dissolved in a good solvent at elevated temperature. Subsequently, a poor solvent is added which induces self-assembly and agglomeration of the polymer due to the increasingly unfavorable interactions between the polymer backbone and the molecules of the poor solvent.^[257] First investigations using this method were reports from Kiriy et al. Initially, P3HT is dissolved in CHCl₃ as a good solvent. After that hexane, as poor solvent, for the polythiophene backbone is added. This results in highly aggregated one-dimensional nanostructures of P3HT with a helical conformation of the backbone.^[260] Yang et al. also used the “mixed-solvent method” for their investigations. Besides to CHCl₃ they also studied o-DCB as good solvent for P3HT. They were able to show that this approach is a

simple “annealing-free” method to significantly increase the degree of crystallinity of P3HT in a composite film.^[261] Investigations with acetonitrile (AN) as poor solvent have shown that, depending on the concentration of AN, an increased edge-on orientation of the P3HT crystallites, related to the substrate, occurs.^[262] Fast and multiple cycles of ultrasonic treatment of P3HT in the dipolar system of CB and AN result in alternating aggregation and deaggregation processes of the polymer chains. Thereby highly ordered P3HT aggregates emerge.^[263] Zhai et al. have shown that P3HT nanofibrils can grow into highly ordered two-dimensional nanoribbons (**Figure 121a**). However, this can only be observed for P3HT with a very low molecular weight ($<10 \text{ kg}\cdot\text{mol}^{-1}$), since exclusively elongated chains are present and no chain folding takes place. For P3HT with higher molecular weight ($>10 \text{ kg}\cdot\text{mol}^{-1}$) chain folding (U-turn of the polymer includes 6-7 alkylthiophene rings) leads to more defective nanofibrils. These poorly defined surfaces inhibit the further growth of the nanowhiskers into nanoribbons.^[116]

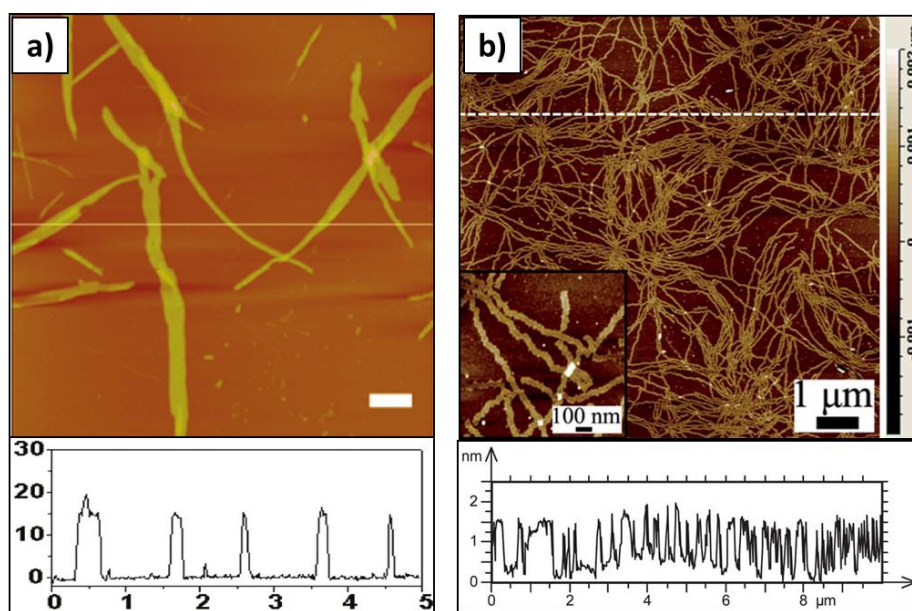


Figure 121: (a) Tapping-mode AFM height images (top) and the cross section of the line trace (bottom) of P3HT nanoribbons (10.2 kDa, $5.0 \times 5.0 \mu\text{m}$) on silicon wafers (SiO_2/Si substrates) by spinning-coating. Scale bar: 500 nm. (b) Topography image (top) of P3HT monolayer nanowhiskers on Si wafer (inset is an enlarged view) and the cross section profile (bottom) at the position marked by the white dashed line.^[116,264]

Su et al. have shown, however, that “chain folding” is not mandatory for P3HT with a higher molecular weight. Self-assembly investigations of P3HT ($16.000 \text{ kg}\cdot\text{mol}^{-1}$) in CHCl_3 over a period of one week have led to monolayer of nanowhiskers (**Figure 121b**). These whiskers are tens of micrometers in length and remarkable roughly 30 nm in width, which is much broader than the common literature values. The height amounts to 1.6 nm, which corresponds to the height of P3HT in the side-chain direction. Two factors are decisive for the suppression of chain folding: On the one hand, the strong π -conjugation in the longitudinal direction and on

the other hand, the side chain molecules, whose interactions with the solvent inhibits crystal growth in the side chain direction.^[264] An innovative and quicker approach to generate such highly ordered P3HT structures in a few minutes involves the addition of concentrated sulfuric acid to a dilute P3HT chloroform solution. The acid causes a slight oxidation of the P3HT, which led to an immediate growth of the nanowhiskers.^[265]

In almost all reports described above the good solvent was, in terms of the quantity, the major component. The investigations of Lam et al. however, have shown that even with the poor solvent as the major component, it is possible to generate P3HT nanofibers. Thereby, the poor solvent ensures chain organization and self-assembly of the polymer, whereas the good solvent controls the nanomorphology.^[257] A similar approach was followed by Lobov et al. In their studies, they initially dissolved P3HT in a poor solvent before adding the same volume of the good solvent. After subsequent ultrasonic treatment and a storage time of 72 hours in the dark under N₂, P3HT nanofibers of different lengths, depending on the P3HT concentration in the solution mixture, were formed. Using the alternating current poling method, they were also able to align at least the long nanofibers (>2 μm) along the external alternating electrical field.^[266]

5.2 Shish-kebab-superstructures with P3HT

Using the methods described above, it is possible to produce P3HT nanofibers, however, the resulting nanofibers do not show any kind of orientation on a given substrate; instead the nanofibers are randomly distributed on the respective substrate. Different approaches were established to produce highly oriented anisotropic films. These approaches mainly include the control of nucleation and crystal growth.^[113]

One approach to create orientation in thin P3HT films can be achieved by controlled homogeneous nucleation and self-seeding as previously described in **Chapter 4.2**. Another approach to create orientation in a polymer film can be induced by mechanical rubbing.^[267–270] Brinkmann et al. report that with implied shear forces the polymer backbone orient along the rubbing direction and thereby a transition from an edge-on orientation to a face-on orientation takes place. However, this method is highly molecular weight dependent, as chain entanglement and chain folding impede reorientation of the chains and alignment of pre-aggregated π-stacks.^[269] An advantage of this method is the independence from the applied substrate, which may allows a large-scale processing.^[113]

A third promising approach to induce order in thin films can be realized by epitaxial growth. In general epitaxy describes the direct growth of a crystalline or semi-crystalline material on a substrate.^[113] In contrast to organic epitaxy, which is controlled by weak non-covalent interactions, the epitaxy of inorganic materials is characterized by covalent bonds.^[271] Single crystals of aromatic salts such as potassium acid phthalate (KAP) or potassium-4-bromobenzoate (K-BrBz) are very well suited to serve as substrates for epitaxial crystallization of P3HT, as they are very temperature stable. This is extremely important because the epitaxial crystallization often takes place over several hours of isothermal annealing. Through this annealing process, the P3HT crystallites copy the morphology of the substrate material. With this method it is possible to produce large-area order of conductive P3HT films.^[113]

The first reports of efficient organic epitaxy of P3HT by Brinkmann describe the directed epitaxial crystallization of P3HT on long 1,3,5-trichlorobenzene (TCB) crystals. The resulting crystalline nanostructures show a “shish-kebab”-like nanomorphology. Thereby the TCB needles form the so-called “shish”, which act as heterogeneous nucleation sites for P3HT. Upon solvent evaporation the P3HT crystallize onto the shish and forming the lateral crystalline fibrous “kebabs”.^[113,163]

Brinkmann et al. also prepared such shish-kebab structures by drop-casting a P3HT film from a 1 wt.-% solution in CB onto a glass substrate. Subsequently, TCB powder was deposit onto the P3HT film surface and the substrate was heated up to 80 °C. At this temperature, TCB ($T_m = 63$ °C) is in a liquid state and acts as a solvent for P3HT. After adding approximately 30 μ l of pyridine and a cover slide on top of the film, the substrate is cooled down to room temperature. Upon cooling the TCB crystallizes in fibrous structures, whereas the P3HT is still dissolved in pyridine. During evaporation of the pyridine at room temperature over several hours the P3HT crystallizes epitaxially on the surface of the TCB needles. The TCB trunks can then be removed by evaporation in a vacuum oven (10^{-2} mbar for 1 hour). A schematic structure together with a bright-field TEM image of such a shish-kebab structure is shown in **Figure 122**. This method leads to highly anisotropic layers of P3HT with fibrous morphology and a high in-plane orientation of the chains. The periodically arranged P3HT chains show a periodicity of 18-30 nm and are up to 400 nm long.^[272] With this approach Jimison et al. produced highly anisotropic layers of fibrous P3HT with a predominant face-on orientation of the chains. Thereby the P3HT backbone aligns parallel to the longitudinal axis of the TCB crystals.^[273]

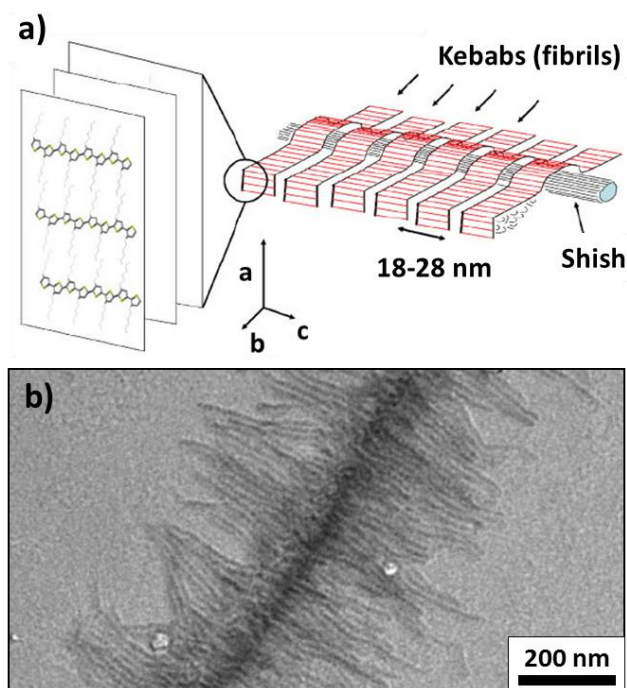


Figure 122: (a) Schematic structure of a shish-kebab fiber. The axis directions for the unit cell are depicted by arrows. (b) Bright-field TEM images of oriented shish-kebab fibers made of regioregular poly(3-hexylthiophene). The TEM images show the periodic branching of lateral crystalline lamellae (kebabs) on the thread-like core (shish).^[272]

Zhai et al. showed that via a bottom-up approach, self-assembly process led to hierarchical P3HT-carbon nanotube (CNT) superstructures. By means of the “mixed solvent method” using CHCl_3 and anisole P3HT nanowires crystallized perpendicular from the CNT surface (Figure 123).

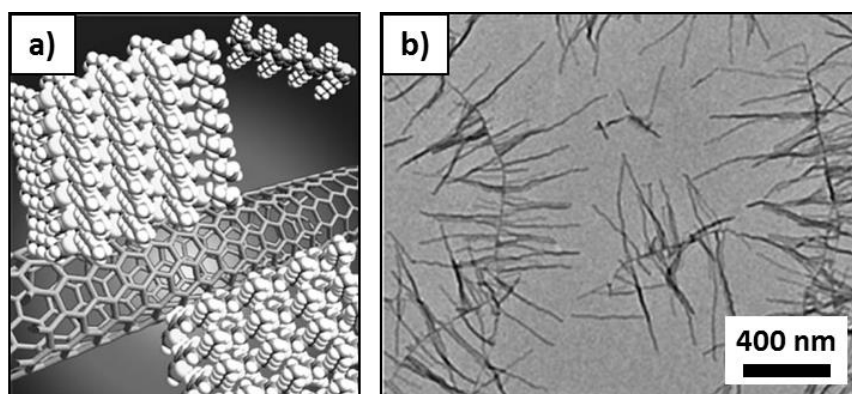


Figure 123: (a) Schematic illustration of hierarchical poly(3-hexylthiophene)/carbon nanotube (CNT) supramolecular structures. P3HT nanowires growing perpendicular from CNT surface with a uniform width and height (b) Transmission electron microscopy image of P3HT supramolecular structures formed on carbon nanotubes. The sample was fabricated through a bottom-up CNT induced P3HT crystallization strategy with a P3HT/SWCNT mass ratio of 40.^[164]

The resulting kebab nanofibers have a uniform height and width (12-15 nm). The fiber length and density can be adjusted and varied by the weight ratio of P3HT to CNTs - the higher the P3HT concentration, the longer the kebabs and the higher the density. For example, a P3HT mass fraction of 40 wt.-% referred to the CNTs resulted in an average fiber length of approximately 400 nm. If the P3HT content amounts only to 5 wt.-%, the resulting fibers were

as little as around 40 nm long.^[164,274] Misra et al. also produced P3HT-CNT shish-kebab nanostructures and investigated the influence of the molecular weight of P3HT on the resulting morphology and photophysical properties of the nanostructures. They showed that an increase in molecular weight from 14 kDa to 60 kDa significantly affects the shish-kebab dimensions, although nucleation and growth remains a consistent epitaxial process. P3HT with a high molecular weight showed shorter kebab fibers than P3HT with a low molecular weight, but an increase in the graft density. Therefore, it is assumed that the connectivity between successive fibrils is due to very small tie molecules. These molecules, on the other hand, are very large for the low molecular weight samples, resulting in the observed low graft density.^[275,276]

Wei et al. showed that shish kebab structures can also be formed by non hybrid systems. They report on branched and hyperbranched P3HT nanostructures, whereby both the shish and the kebabs are made of P3HT. The linear trunks (kebabs) are first produced by dissolving P3HT in o-DCB followed by a slow evaporation process of the solvent in a sealed vial. By addition of triethylamine (TEA) into the system, branched P3HT nanostructures (shish-kebabs) can be observed. Thus, two different nucleation processes can be noticed during the formation of these branched structures: First, homogeneous nucleation takes place by the production of the shishes. In the second step, for the growth of kebabs, heterogeneous nucleation is present. Furthermore, it could be shown that by increasing the TEA content, the kebab fibers lengthen significantly. This is due to the fact that the heterogeneous nucleation process becomes dominant with a high content of TEA. Thus, more P3HT is used for the growth of kebabs than for the nucleation of shishes. However, a maximum fiber length was observed with a TEA addition of 60 μm . Further increase of the amine content leads to a rapid decrease in kebab length and results in the formation of bundles of nanowires. Furthermore, this work has shown that, upon a ternary nucleation process, it is also possible to create hyperbranched P3HT nanostructures with this system.^[277]

Hayward et al. report about the production of tunable P3HT-perylene tetracarboxydiimide donor/acceptor shish kebab nanostructures. Thereby the perylene tetracarboxydiimide as an electron acceptor forms the Shishes and the P3HT (e-donor) the kebabs. During the process the P3HT molecules stabilize the perylene tetracarboxydiimide in supersaturated solutions and thus enable the formation of linear perylene tetracarboxydiimide nanowires. Their surfaces serve as heterogeneous nucleation sites for the crystallization of the P3HT kebabs.

The fiber dimensions of both the shishs and kebabs can be adjusted by varying the mass ratio of the individual components, the solvent system used and the alkyl substituent at the perylene tetracarboxydiimide.^[278,279]

Huo et al. produced P3HT-MDBS hybrid-shish-kebab nanostructures by spin-coating from hot o-DCB solutions. Thereby the sorbitol derivative MDBS, which act as a supramolecular nucleating agent for P3HT, forms the shish.^[249] The P3HT nanofibrils, which grow perpendicular on the MDBS surfaces, exhibit a uniform width and height. The length of the kebabs can be influenced by various parameters. These include solvent evaporation rate, spin-coating temperatures, spin-coating rates, P3HT concentration in solution, solvent quality and substrate used.^[280]

5.3 Preparation of P3HT nanofibers with shish-kebab-like superstructures

A straightforward way to induce orientation in P3HT thin films can be realized by shish-kebab-like superstructures. Therefore, the following chapter is devoted to the production and characterization of such structures.

5.3.1 Material selection

Two different P3HT grades were used for the production and investigation of the shish-kebab superstructures. On the one hand the commercially available **P3HT-2**, which has already been extensively investigated for the nucleation experiments, and on the other hand a P3HT grade synthesized by Ruth Lohwasser in the group *Applied functional Polymers (AFuPo)* of Prof. Mukundan Thelakkat. This grade is referred in the following as **P3HT-4**. It has a molecular weight of $24 \text{ kg}\cdot\text{mol}^{-1}$, which is about half the size of the previously discussed **P3HT-2**, a very narrow PDI of 1.15 and a very high regioregularity (>98%). This allows one to compare shish-kebab superstructures with a highly defined polymer and a commercial grade.

Since a hybrid shish-kebab system is to be created by forming the kebabs of P3HT, another material must form the shishs. For this purpose, three different supramolecular compounds were selected. These included the two bisamides **BA 2** and **BA 4** and the trisamide **Irgaclear XT 386**. All of these were investigated individually in combination with P3HT.

BA 2 is based on 1,4-phenylenediamine and features two 4-pyridine substituents. As previously determined this bisamide self-assembles in chlorobenzene in fibrillar structures and is moreover a very effective nucleating agent for P3HT. The second investigated bisamide

within these studies is **BA 4**. It also features two 4-pyridine substituents, however, is based on trans-cyclohexane-1,4-diamine. This bisamide also forms nanofibers upon self-assembly in CB and is a good nucleating agent for P3HT. The last compound studied for the shish-kebab production is the trisamide **Irgaclear XT 386**, which is a specially designed nucleating agent for melt solidification of i-polypropylene. This trisamide is based on a triaminobenzene core and features three tert-butyl substituents (**Figure 124a**). Self-assembly investigations within this trisamide in CB have shown that it also forms fibrillar structures, however, with apolar aliphatic periphery (**Figure 124b**). Because of this apolar aliphatic periphery, this compound should serve as a reference and the investigations should not show any shish-kebab superstructures.

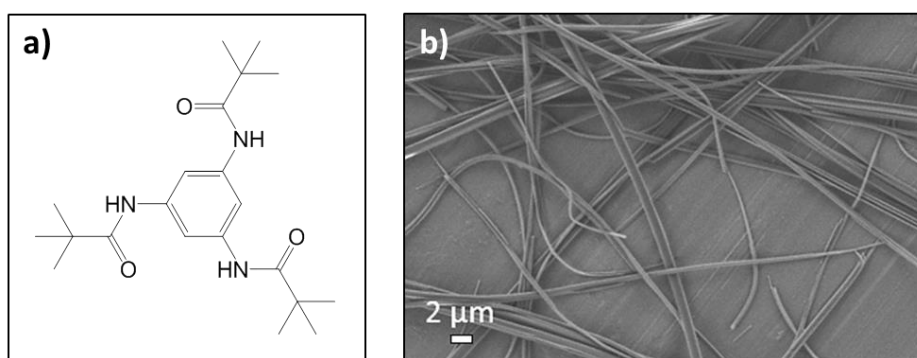


Figure 124: (a) Chemical structure of the commercially available nucleating agent Irgaclear XT 386. (b) SEM micrograph of supramolecular nanofibers of Irgaclear XT 386 prepared by self-assembly upon cooling in CB with a trisamide concentration of 300 ppm in solution.

5.3.2 Procedure for shish-kebab preparation

It is assumed that the effective nucleating agents are not only able to nucleate P3HT in the melted state but also nucleate P3HT in solution. Therefore, the preparation of the shish-kebab superstructures was kept very simple and proceeded as follows. First, the respective additive was self-assembled in chlorobenzene at a concentration of 100 ppm. The experimental setup to perform these tests can be compared to a simple batch cooling crystallizer. The respective additive is weighed in a 4 mL glass vial and then the appropriate amount of CB is added to get an additive concentration of 0.01 % by weight in solution. After five minutes of ultrasonic treatment, to obtain a homogeneous dispersion, the vial is heated up to the boiling point of CB (131 °C), under shaking. Once the additive is completely dissolved, the glass vial is cooled down to room temperature without active cooling. After the solution has cooled down to room temperature 1 wt.-% of neat P3HT with respect to chlorobenzene is added to the sample vial, so that the ratio of P3HT to the supramolecular nucleating agent amounts to 100:1. Subsequently heating of the sample up to 50 °C homogeneously dissolves the P3HT, whereas the self-assembled nanostructures retain its

initial shape. Afterwards the sample was cooled down to room temperature and allowed to rest for different time periods such as 4 hours, 24 hours and 7 days. Thin films were spin-coated both on glass substrates and silicon wafers and analysed via various microscopic techniques.

5.3.3 Microscopic investigations of shish-kebab superstructures

To analyse the shish-kebab superstructures produced in this work the microscopic techniques SEM, TEM and polarized optical microscopy were used.

SEM analysis

The SEM investigations were performed on thin films of P3HT shish-kebab superstructures with a thickness of approximately 100 nm. All samples have been sputtered with platinum (2.0 nm) before investigated.

Prior to the shish-kebab superstructure investigations the individual components are considered individually. Therefore, **Figure 125** shows the SEM images of a neat **P3HT-2** film and a single self-assembled **BA 2** fiber. The sample preparation was performed as described above, except that one main component each was omitted from the preparation. The storage period of the samples before spin-coating was 24 hours for each sample. The neat **P3HT-2** film corresponds to a conventional spin-coated P3HT film and does not show any unusual features or fiber-like morphologies (**Figure 125a**). The neat **BA 2** sample (**Figure 125b**) shows a single self-assembled fiber with a width of approximately 200 nm. The dimensions of the fiber are in the range of those fibers determined with the standard self-assembly studies CB.

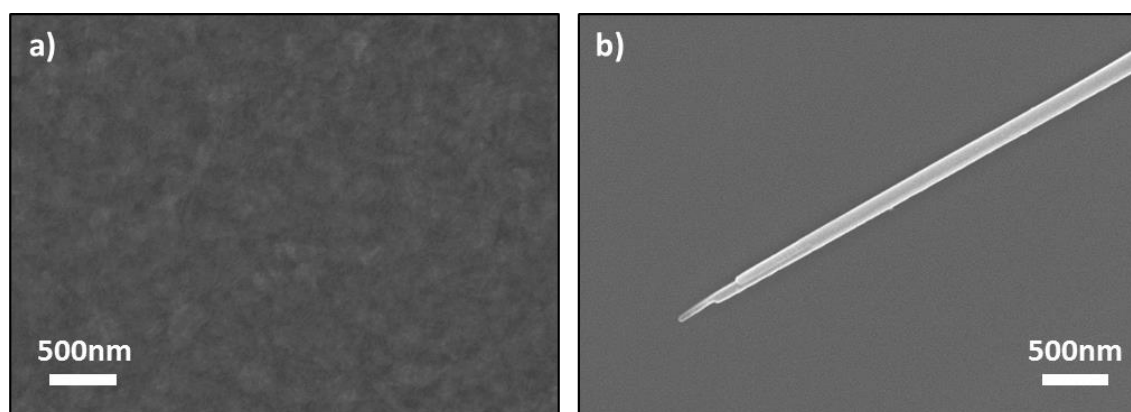


Figure 125: SEM images of a neat P3HT-2 film (a) and a neat BA 2 fiber (b) produced according to the method described in Chapter 5.3.2. The storage time before spin-coating was 24 hours each.

Figure 126 shows a SEM image of a sample consisting of **P3HT-2** and **BA 2** spin coated 24 hours after the preparation according to the method described in **Chapter 5.3.2**. A well-defined shish-kebab superstructure can be observed. Thereby the bisamide **BA 2** forms the

approximately 250 nm wide shish and the **P3HT-2** the kebabs. These P3HT kebabs are 500-1000 nm long and have a width of approximately 15 nm. Furthermore, a parallel alignment of the **P3HT-2** nanofibers is clearly evident. The distance of the kebabs between their origin at the shish, and hence the P3HT nucleation density, is about the diameter of the kebab fibers.

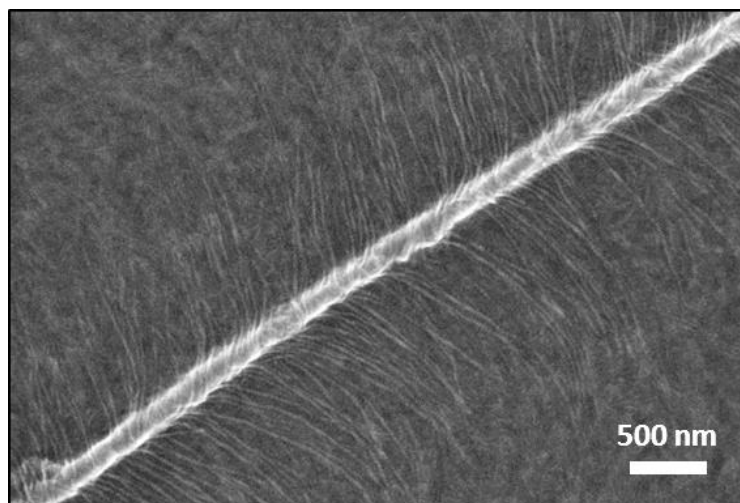


Figure 126: SEM image of a shish-kebab superstructure made of P3HT-2 and BA 2 according to the method described in Chapter 5.3.2. The P3HT-2 nanofibers (kebabs) are trans-crystallized on a self-assembled BA 2 nanofiber (shish). The amount of bisamide BA 2 was 1 wt.-% based on P3HT and the storage time before spin-coating of the sample was 24 hours.

In further studies, the processing parameters P3HT concentration in solution and storage time at room temperature before spin-coating were varied. In this manner, the influence of these processing parameters on the resulting shish-kebab structure especially on the fiber length of the kebabs is investigated. For the experiments three different P3HT concentrations in solution and two different storage times have been investigated. **Figure 127** shows a series of SEM images of samples prepared with these different parameters. The images compare samples that were spin-coated after 24 hours (**a, c, e**) and 7 days (**b, d, f**) of storage time at room temperature. Furthermore, the concentration of **P3HT-2** in solution was varied: 0.5 wt.-% (**a, b**), 1.0 wt.-% (**c, d**) and 2.0 wt.-% (**e, f**).

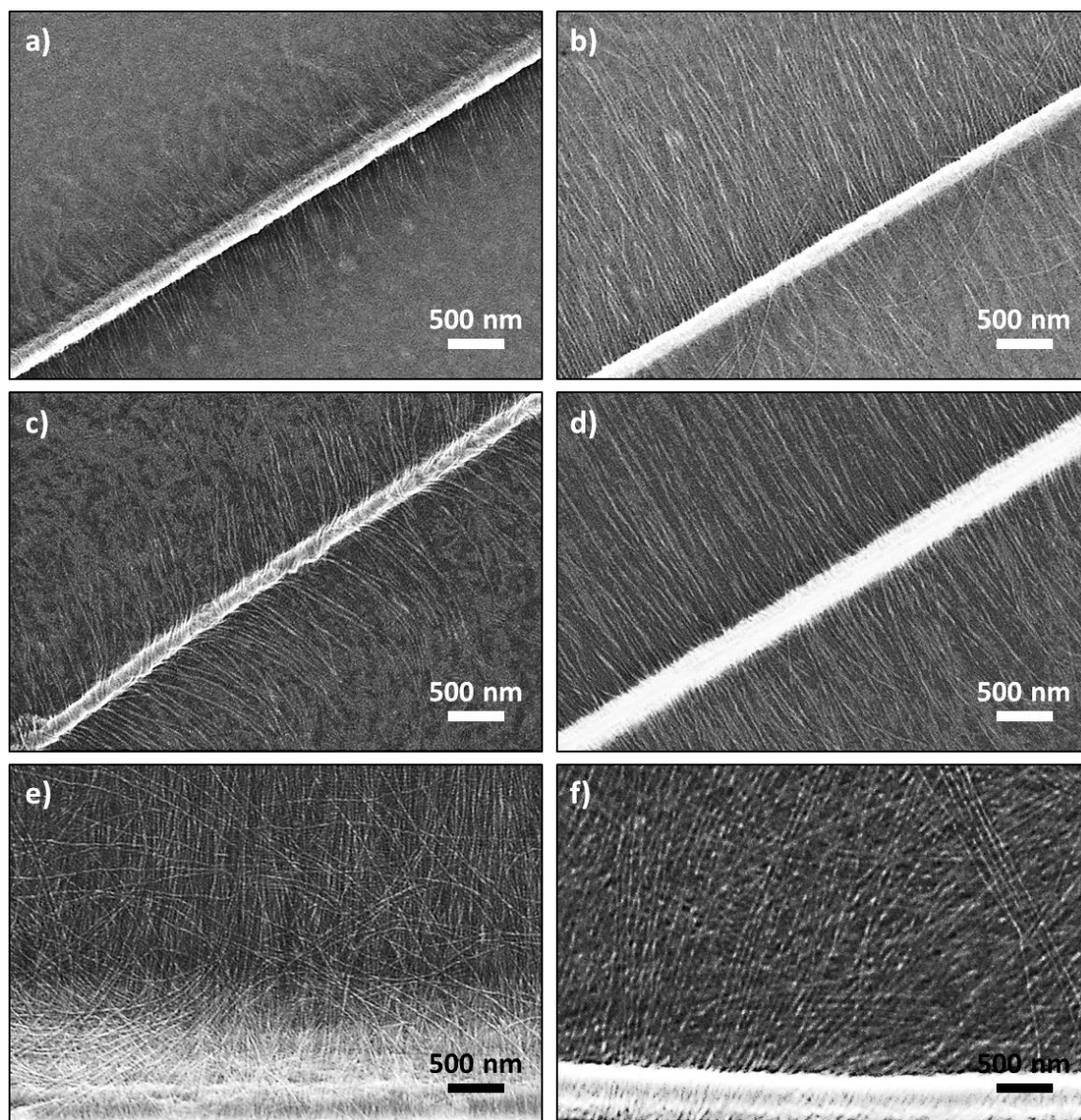


Figure 127: SEM images of P3HT-BA 2 shish-kebab structures. For the preparation of the samples the parameters P3HT-2 concentration in chlorobenzene and storage time before spin-coating were varied: (a, c, e) 24 hours storage time; (b, d, f) 7 days storage time. (a, b) 0.5 wt.-% P3HT-2 in CB, (c, d) 1 wt.-% P3HT-2 in CB, (e, f) 2 wt.-% P3HT-2 in CB. The concentration of BA 2 in CB was 0.01 wt.-% in each sample.

Comparing the fiber lengths of the kebabs in relation to the storage time of the samples before spin-coating, it is clearly evident that they become longer with increasing storage time. For instance, the kebab fiber length of the sample with the lowest **P3HT-2** concentration (0.5 wt.-%) amounts to 300-500 nm after 24 hours of storage time (**a**). After one week of storing at room temperature before spin-coating, the kebabs of this sample grow to more than 1.5 μm (**b**).

Identical observations can be made for the samples with 1 wt.-% (**c, d**). Only for the samples with the highest concentration of P3HT in solution such conclusions cannot be made, since the film already consists of kebab fiber mats for both the short and long storage time (**e, f**).

Comparing the samples of different concentrations with each other in terms of the kebab fiber lengths, it can be seen that the fiber lengths of the kebabs increase with increasing **P3HT-2** concentration in solution. This is partly due to the fact that more P3HT is available for epitaxial crystallization, but also because the solutions of the lower concentrations are more stable. Since all previous investigations of the shish-kebab structures have only included the bisamide **BA 2**, the remaining two additives (**BA 4** and **Irgaclear XT 386**) are now described in detail regarding their ability to form shish-kebab structures with **P3HT-2**.

Figure 128 shows the SEM image of a film with shish-kebab superstructure based on **P3HT2** and the bisamide **BA 4**. The film was processed via the method as described before.

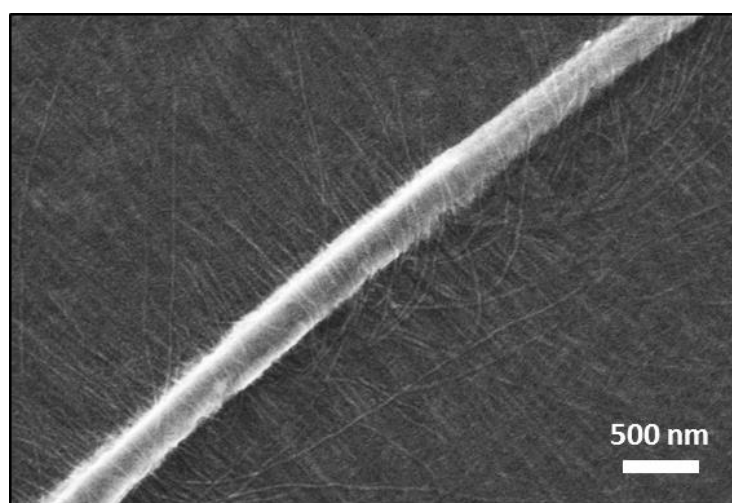


Figure 128: SEM image of a shish kebab structure composed of bisamide **BA 4** and **P3HT-2**. The concentration of **P3HT-2** in solution was 1 wt.-%, equally the concentration of **BA 4** regarding **P3HT-2**. The storage time before the film was spin-coated was seven days.

A shish-kebab superstructure, where **P3HT-2** forms the kebabs and **BA 4** forms the shish, can clearly be observed. The concentration of **P3HT-2** in solution was 1 wt.-%, the ratio of **P3HT-2** regarding the bisamide was 100:1, the storage time before the film was spin-coated was seven days. The nucleation density seems to be slightly lower for the shish-kebab structures containing **BA 4** than that of the corresponding samples of **BA 2**. However, the kebabs are much longer and hence lose their vertical alignment to the shish to some extent. The reason for the different structures could be attributed that **BA 2** is a more slightly effective nucleating agent for P3HT than **BA 4** (see **Chapter 4.4.2**). As a result, not the complete fiber surface of **BA 4** may be suitable for epitaxial crystallization of P3HT. The fewer P3HT kebabs that have formed, become longer over the same period of time.

Finally, shish kebab investigations were performed with the commercially available nucleating agent (for i-polypropylene) **Irgaclear XT 386** which was used as a reference. **Figure 129** shows

a SEM image of a film produced via the method described above. The trisamide concentration in CB was 0.01 wt.-%, the concentration of **P3HT-2** in solution was 1 wt.-%. The storage period after homogeneous dissolving of P3HT was seven days. The results show that the trisamide self-assembled in fibrous structures, like **BA 2** and **BA 4**. The shown fiber has a width of approximately 300 nm and a length of several hundred micrometers and can therefore act perfectly as shish for the epitaxial crystallization of the P3HT kebabs. However, even after seven days crystallization time in solution, no P3HT nanofibers can be observed. It is therefore assumed that **Irgaclear XT 386** is not or at least only a very poor nucleating agent for **P3HT-2**. This also corroborate that the nucleating agents **BA 2** and **BA 4** have a perfect epitaxial surface regarding P3HT.

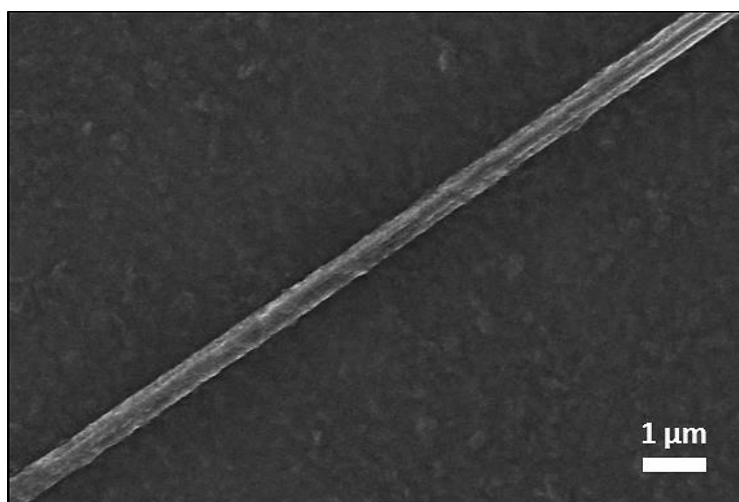


Figure 129: SEM image of a spin-coated film composed of self-assembled trisamide Irgaclear XT 386 and P3HT-2. The concentration of P3HT-2 in solution was 1 wt.-%, equally the concentration of Irgaclear XT 386 regarding P3HT-2. The storage time before the film was spin-coated was 7 days.

In order to determine if there is an influence of the molecular weight of P3HT on the resulting kebab fiber lengths, **P3HT-4** a highly defined P3HT was investigated. As mentioned before, this P3HT grade has a molecular weight of $24 \text{ kg}\cdot\text{mol}^{-1}$, which is about half the size of the previously discussed **P3HT-2**. Additionally, the PDI of 1.15 is clearly narrower and the regioregularity (>98 %) is higher than the values for **P3HT-2**.

Figure 130 shows the SEM image of a spin-coated film of **P3HT-4** and the bisamide **BA 2**. The film was produced in a similar way as described for the previous shish kebab films. The concentration of **P3HT-4** in CB was 1 wt.-%, the ratio of P3HT to the bisamide **BA 2** was 100:1 and the storage time before spin-coating amounts to 24 hours. The resulting shish kebab structures are already very pronounced after this short storage time in solution. The **P3HT-4** kebabs have a length of more than $5 \mu\text{m}$ and are therefore ten times longer than the corresponding kebabs of **P3HT-2** (**Figure 127**) at the same storage time. This result, which

shows that a lower molecular weight leads to longer kebab fibers, is in agreement to the results of Misra et al.^[276] However, the measured thicknesses of the kebab nanofibres of the different P3HT grades do not differ from each other. The fibers show a homogeneous width of about 15 nm. This contrasts with the results of Misra et al., but confirms the present basic theory that chain folding occurs for P3HT grades with molecular weights of more than $10 \text{ kg}\cdot\text{mol}^{-1}$ and that the P3HT nanofibers can therefore only be around 15 nm in thickness. The inset in **Figure 130** shows that a fiber mat has been formed. Accordingly, the nucleation density at the bisamide surface is very high. The majority of the **P3HT-4** nanofibers are present parallel to each other in a highly ordered fashion. The film morphology changes completely and sharply at a distance of about $5 \mu\text{m}$ away from the bisamide shish. After that, no nanofibers can be observed and only the typical features of the semi-crystalline P3HT film are present.

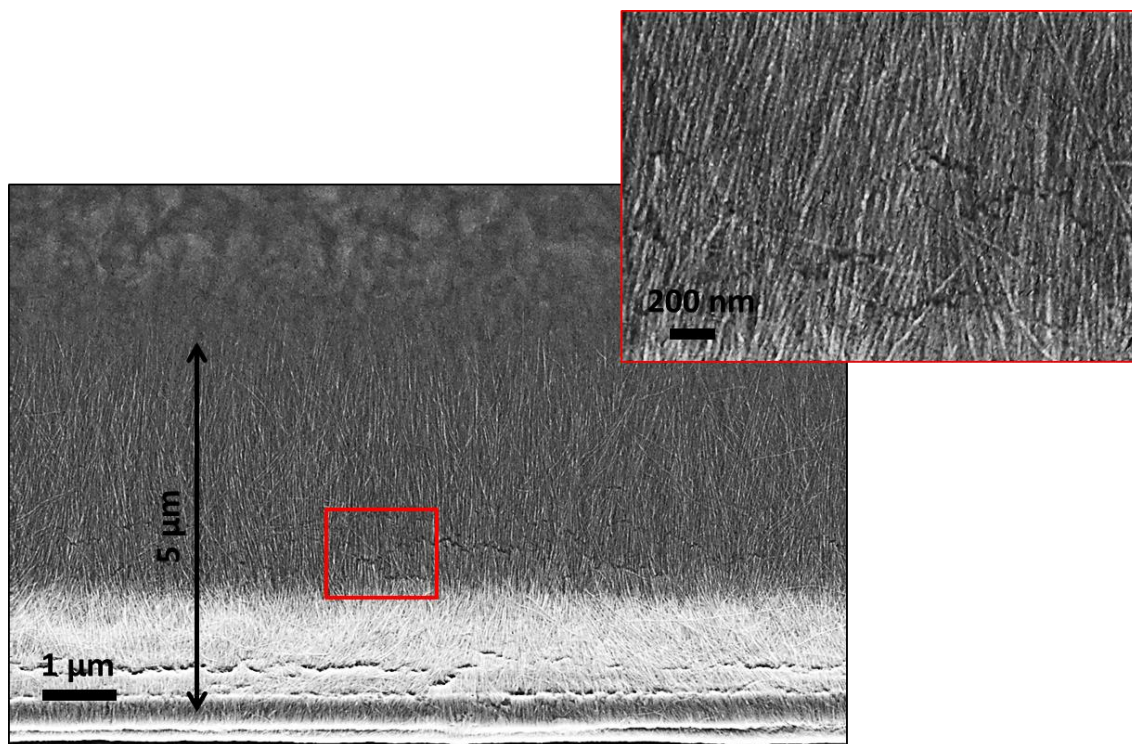


Figure 130: SEM image of a spin-coated film of P3HT-4 and the bisamide BA 2. The film was produced via the method described in Chapter 5.3.2. The concentration of P3HT-4 in CB was 1 wt.-%, equally the concentration of BA 2 regarding to P3HT-4. The storage time before spin-coating of the sample amounts to 24 hours. The inset shows a magnification of the parallel aligned P3HT-4 nanofibers.

In order to get insight on the surface topography at the locations of the shish-kebab structures, desktop SEM images were taken in topography mode. **Figure 131** shows such micrographs of **P3HT-4** and **BA 2** shish-kebab superstructures. The images clearly show that the surface topography is changing in dependency of the distance to the shish. Seven microns on both sides of the shish, a very homogeneous surface texture can be observed. In this area the epitaxially crystallized P3HT nanofibers are present (see **Figure 130**). The semi-crystalline

P3HT film next to the shish-kebabs shows a significantly higher surface roughness and no oriented areas.

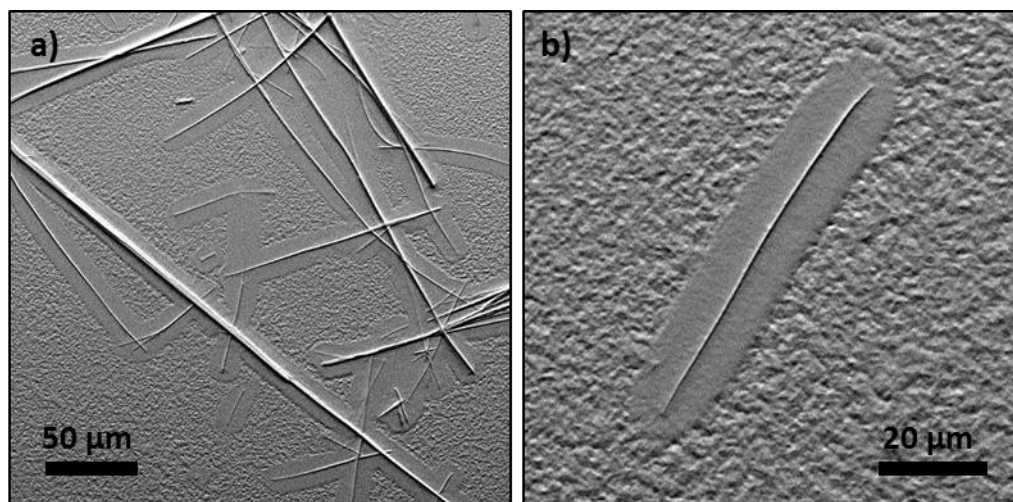


Figure 131: Desktop-SEM images in topography mode of shish-kebab structures comprising P3HT-4 kebabs and BA 2 shish: a) Representative b) magnification. Samples were prepared according to the method described in Chapter 5.3.2. The concentration of P3HT-4 in CB was 1 wt.-%, equally the concentration of BA 2 regarding to P3HT-4. The storage time before spin-coating amounts to 24 hours.

TEM and STEM investigations

The SEM has a sufficiently high resolution, but only scans the film surface. If the kebab fibers run into the film layer after a certain distance to the shish or if there are hidden P3HT fibers over the whole sample, they cannot be detected. Therefore, in order to be able to give a statement about the exact P3HT fiber lengths, samples must be prepared which can be analyzed by means of TEM.

TEM is extremely versatile and offers many highly complementary operating options. The combination of different complementary information helps to understand structural properties, such as preferred orientations, contact planes of polymer crystals and the dimensions of crystalline and amorphous regions, on different length scales. Accordingly, it is an ideal and unique method to detect the characteristic structures and morphological features in epitaxial polymer films and to reveal the crystallization and epitaxial growth mechanism. However, since most semiconducting polymers are highly radiation-sensitive, the radiation intensity must be kept low.^[113] Therefore, the film thickness, adjusted for standard TEM examinations, has to be in the range of 50 nm or thinner. In order to reduce the film thickness of the samples, on the one hand, the spinning speed can be increased drastically or the concentration of P3HT in solution can be reduced. The latter possibility was used in this work because a very high spin speed could possibly lead to too high a stress on the shish-kebab structures, which may lead to destroy the P3HT nanostructures. **Figure 132** shows the

dependence of the film layer thickness on the P3HT concentration in CB. A 50 nm thick layer is expected to be sufficient to perform TEM examinations. This film thickness can be achieved by a concentration of 0.5 wt.-% P3HT in solution with unchanged spin coating parameters. Considering the results of the concentration-dependent SEM investigations on **P3HT-2** (see **Figure 127**), it can be assumed, however, that the kebab fiber length also decreases with a lower **P3HT-2** concentration in solution.

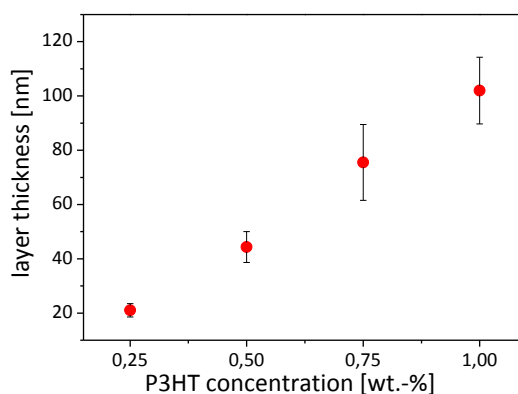


Figure 132: P3HT film layer thickness after spin-coating in dependency of the P3HT-2 concentration in chlorobenzene.

Figure 133 shows TEM images of shish kebab superstructures with **P3HT-2** and the bisamide **BA 2**. The concentration of **P3HT-2** in CB was 0.5 wt.-%. The ratio of P3HT to bisamide was 50:1 and the storage time after the solutions were prepared amounts to seven days.

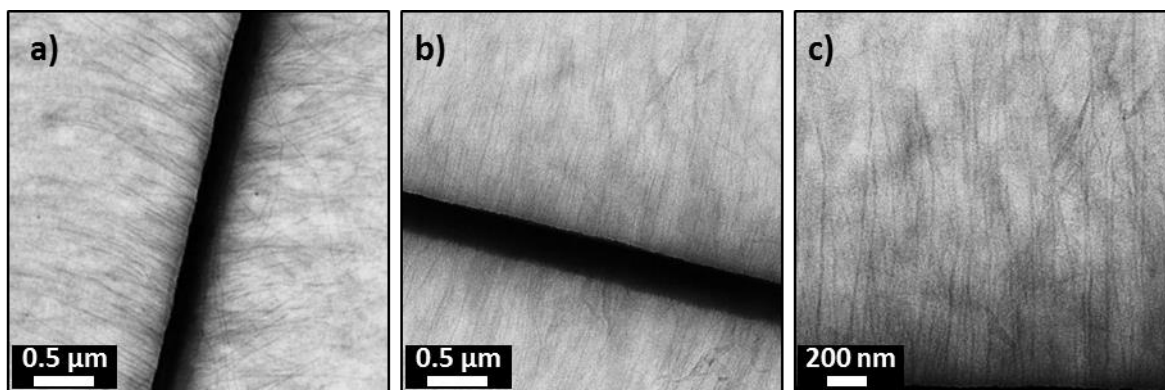


Figure 133: TEM images of shish-kebab structures comprising P3HT-2 kebabs and BA 2 shish: representatives (a, b), magnification (c). The concentration of P3HT-2 in CB amounts to 0.5 wt.-%, the ratio of P3HT-2 to BA 2 was 50:1 and the storage time before the samples were spin-coated amounts to seven days. For the production of the TEM samples, a water-soluble PEDOT:PSS film was first spin-coated onto a silicon wafer before the P3HT-bisamide film was coated onto it. The shish-kebab film was then floated in water, collected with a TEM grid and finally analyzed.

For the production of the TEM samples, a water-soluble PEDOT:PSS film, acting as a sacrificial layer, was first spin-coated onto a silicon wafer before the P3HT-bisamide film was coated onto it. The Shish kebab film was then, due to the dissolution of PEDOT:PSS, floated in water, collected with a TEM grid and finally analyzed. The TEM images show 300 nm wide **BA 2** shish and **P3HT-2** kebabs, which are about 1-1.5 μm long and about 15 nm wide. However, the contrast between the P3HT kebab fibers and the surrounding semi-crystalline P3HT film is

very low in order to be able to give more precise statements regarding the binding of the kebabs to the Shish or the nucleation density. In all probability, the total film thickness is still too high for efficient TEM investigations.

Another analysis method, which was carried out within this thesis, is scanning transmission electron microscopy (STEM). Due to the relationship to TEM, a layer thickness less than 100 nm is also crucial for this analyzing method. For the TEM samples presented above, the reduced film thickness was achieved by changing the P3HT concentration in solution. However, a reduced P3HT concentration in solution leads to shorter kebab fibers. In addition, for high-quality images it is advantageous if the disordered semi-crystalline P3HT film, that means all the P3HT except the P3HT-kebabs on the shish, could be removed during sample preparation. Therefore, the sample preparation was modified for the subsequent STEM measurements. Initially, the semi-crystalline part of the film should be removed from the shish-kebab structures using a chemical etching method. However, in this experiment, the entire film detached and therefore could not be analyzed. The following attempt was then to etch the untreated films by means of oxygen plasma. However, even with this approach, the desired result could not be achieved because the very sensitive P3HT nanofibers were damaged too much. Finally, the method of dilution was used again, but not in the manner as in the preparation of TEM samples. Instead, the initial concentration was set by default and the production of the shish kebab structures was carried out in solution as usual. However, after 24 hours of storing time in solution, the sample was not spin-coated but diluted by a factor of 200 with pure chlorobenzene, resulting in a total concentration of 0.005 wt.-% P3HT in CB. Immediately afterwards, a drop of the solution containing the shish-kebabs was added on top of a TEM grid. The resulting dried film was so thin that it was perfectly suited for STEM examinations. **Figure 134** shows the STEM images of the sample from **P3HT-4** with the bisamide **BA 2**. The almost maximum nucleation density is clearly visible. This again confirms that the bisamide **BA 2** is an excellent nucleating agent for **P3HT-4**. The kebab fibers are more than 5 μm long and, due to their length and high aspect ratio, are not available as rigid fibers but as bent flexible fibers. The average width of the fibers is 14 nm.

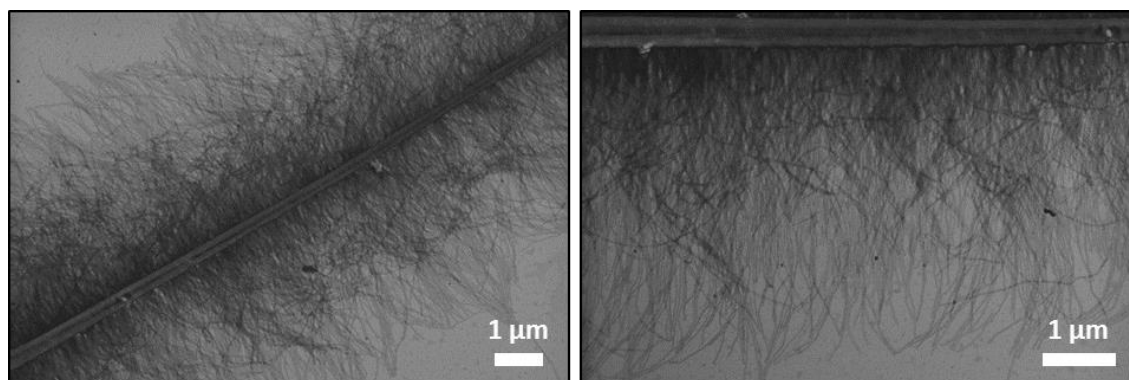


Figure 134: STEM images of shish-kebab structures comprising P3HT-4 kebabs and BA 2 shishs. The concentration of P3HT-4 in CB was 1 wt.-%, equally the concentration of BA 2 regarding to P3HT-4. The storage time before dilution of the solution by factor 200 amounts to 24 hours. Immediately afterwards the dilution a drop of the sample was added on top of a TEM grid and measured via STEM after drying of the film.

Polarized optical microscopy investigations

In order to identify both a possible anisotropic order and orientation of the crystalline P3HT domains over large distances, films were spin-coated on glass substrates and then examined via polarized optical microscopy. Furthermore, samples were prepared after different storage times in order to verify the SEM result above, that an increasing storage time leads to longer P3HT kebabs.

Figure 135 shows microscopic images of shish-kebab superstructures prepared from P3HT-2 and BA 2 as a function of different storage times before spin-coating. The sample in Figure 135a was processed immediately after homogenizing the P3HT-2 in solution. The image shows self-assembled crystalline bisamide fibers and the semi-crystalline P3HT film around them. After four hours of storage time before spin-coating, the crystalline areas around the bisamide fibers have increased marginally (Figure 135b). However, these small new crystalline regions can only be associated with ordered P3HT-2, which crystallizes epitaxially on the bisamide shishs, since the BA 2 fiber width does not change with increasing storage time. Furthermore, the morphology of the film beyond the bisamide fibers has not changed. Figure 135c shows a micrograph of a sample spin coated after 24 hours storage time. It can be observed that the crystalline areas around the BA 2 shishs have significantly enlarged and are now about 5-10 microns wide. These new crystalline areas also represent the formed and grown P3HT-2 kebabs.

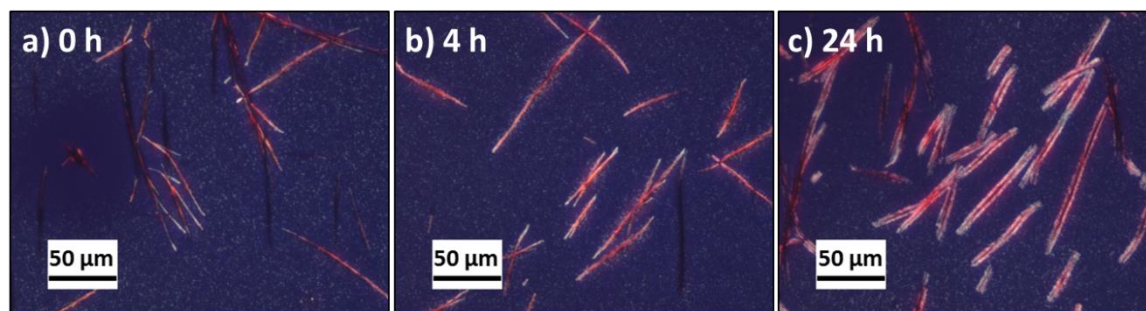


Figure 135: Cross polarized optical microscopy images of P3HT-2 films with self-assembled nanofibers of BA 2. The films were prepared by spin-coating of P3HT:additive solutions on clean glass substrates with a polymer:additive ratio of 1:0.01. The polymer:additive concentration in chlorobenzene was 1 wt.-%. The storage time before spin-coating of the samples was varied: (a) 0 h, (b) 4 h, (c) 24 h.

A further feature of this analyzing method is that the parallel alignment of the P3HT nanofibers can be verified. **Figure 136** shows images of a arrow-like shish-kebab superstructure formed from **P3HT-4** and **BA-2** recorded at different rotational positions.

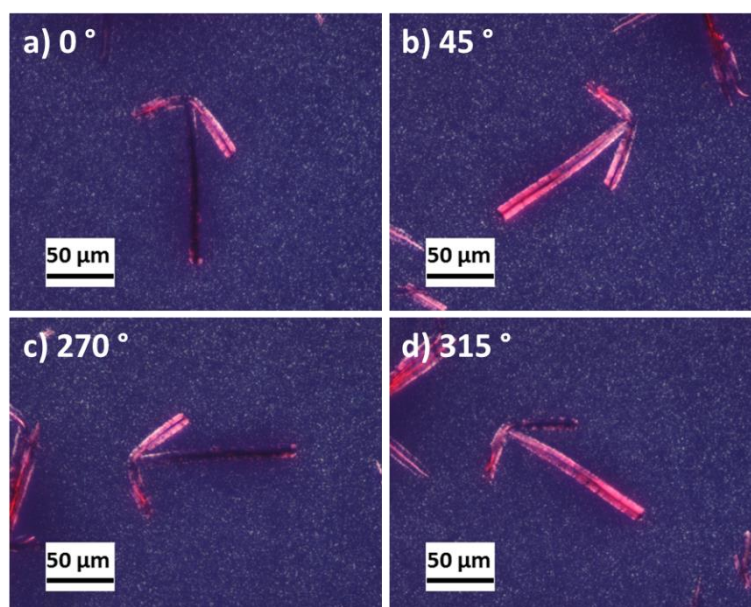


Figure 136: Cross polarized optical microscopy images of a P3HT-4 film with self-assembled nanofibers of BA 2 in dependency of the rotational position of the sample: (a) 0° , (b) 45° , (c) 270° and (d) 315° . The film was prepared by spin-coating of a P3HT-4:bisamide solution on a clean glass substrate with a polymer:additive ratio of 1:0.01. The polymer:additive concentration in chlorobenzene was 1 wt.-%. The storage time before spin-coating of the sample was 24 hours.

Figure 136a shows the longitudinal section of the arrow parallel to the polarizer. Since the **P3HT-4** chains are also crystallized in this direction, this part of the arrow is almost dark. If the sample is rotated by 45° , the previously extinguished crystalline part now forms a brightness maximum, as the crystalline areas are now perpendicular to the polarizer (**Figure 136b**). Further rotation of the sample leads every 45° alternately to a brightness maximum followed by a brightness minimum (**Figure 136c** and **d**). These results illustrate the presence of highly oriented **P3HT-4** kebabs. The remaining semi-crystalline part of the film is completely disordered and therefore no illumination angle dependencies exist. Furthermore, the sharp-

edged transitions between the kebab fibers and the semi-crystalline film signals that all kebab fibers have approximately the same length dimensions.

The prepared shish-kebab superstructures with highly oriented P3HT nanofibers allow for confocal photophysical investigations. The performed spatially resolved spectroscopic investigations along these P3HT nanofibers are described in detail in the following.

5.4 Spatially resolved spectroscopy along P3HT nanofibers

The measurements were performed by Sebastian Stäter at the department of “Spektroskopie of soft matter” of Dr. Richard Hildner and Professor Jürgen Köhler at the University of Bayreuth.

5.4.1 Setup for spatially resolved spectroscopy

The setup for the spectroscopic investigations is shown schematically in **Figure 137**. All measurements were performed at room temperature.

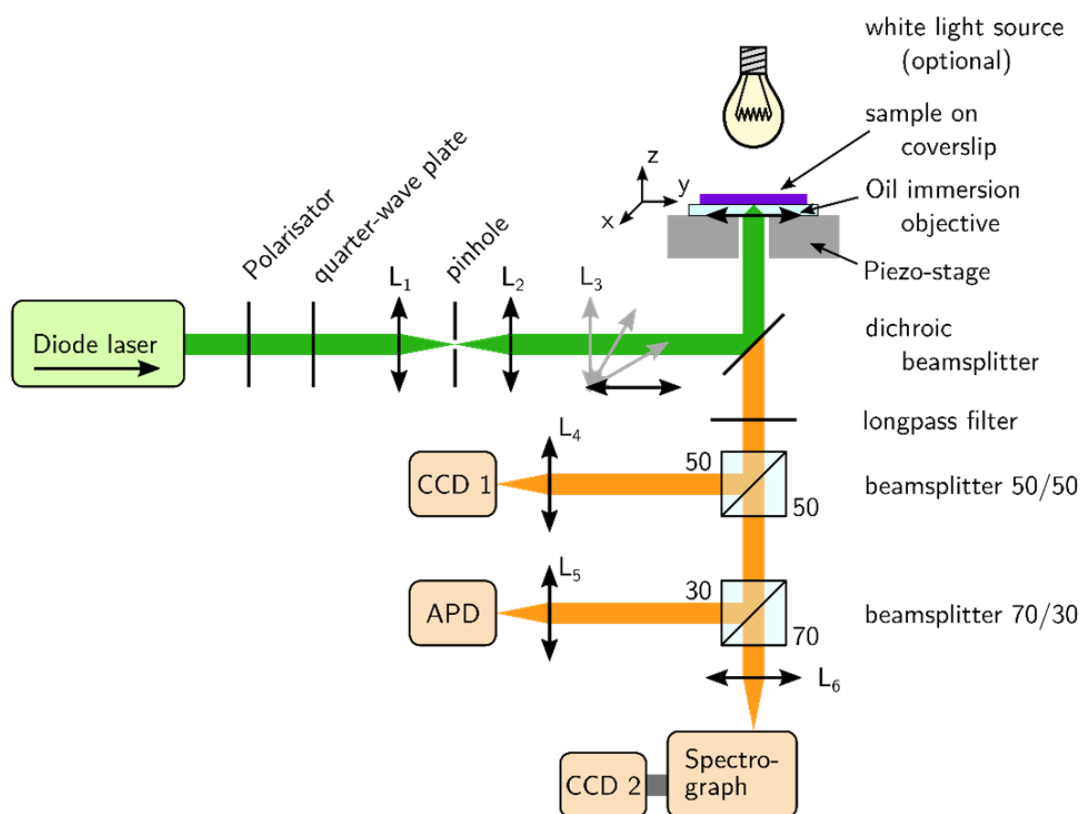


Figure 137: Experimental setup for bright field microscopy, epifluorescence microscopy, confocal spatially resolved emission and absorption spectroscopy as well as fluorescence lifetime measurements. The excitation beam path is shown in green, the different detection paths in orange. L1 to L6 denote collective lenses.

The versatile setup can be used for bright field, confocal microscopy and fluorescence microscopy. Spatially resolved, emission and absorption spectra can be recorded as well as

time-resolved and fluorescence measurements. The possible illumination and detection paths are explained in the following.

The excitation path is shown in green in **Figure 137**. The light source is a pulsed diode laser (LDH-P-FA 530L, PicoQuant) at a wavelength of $\lambda = 532 \pm 2$ nm. It can be operated at a pulse frequency of 40 MHz and has a pulse width of less than 100 ps. In principle, the laser emits linearly polarized light. Light with a different polarization is suppressed with a downstream polarizer. With a $\lambda/4$ platelet the linearly polarized beam can be transformed into circular or elliptical polarization. After that the beam passes a telescope consisting of the collecting lens L1, a pinhole with a diameter of 20 μm and the collecting lens L2. The telescope acts as a spatial filter and leads to a gaussian beam profile with which the lens is optimally illuminated. The wide-field lens L3 can be optionally introduced into the beam path. If the lens is not introduced into the beam path the excitation light is transmitted via a dichroitic beam splitter into an oil immersion lens and is focused on the sample. If the wide-field lens is introduced in the beam path, the excitation light shines defocused on the sample and thus leads to a wide field excitation. The excitation power was set to of $253 \text{ mW}\cdot\text{cm}^{-2}$ for wide field excitation experiments or $4 \text{ W}\cdot\text{cm}^{-2}$ for confocal excitation experiments and further reduced with gray filters if as required. The size of the confocally area is given by the diffraction limit. All measurements were performed on films, which have a thickness of about 100 nm. In addition, the refractive index of the sample differs slightly from the refractive index of the substrate and the immersion oil. The size of the excitation focus is thereby increased in the sample compared to the theoretical value. It is therefore estimated that the achieved spatial resolution is about 450 nm.

When the sample is excited a part of the emission signal passes through the lens. Spectral components with $\lambda > 532$ nm are transmitted through the dichroic beamsplitter. The remaining laser light scattered on the sample is filtered out by a long-pass filter. Non-polarizing beam splitters then split the signal into three different detection paths. The first detection path leads to the designated detector CCD1, a CCD camera ("Charge-Coupled-Device") from type Orca C4742-80-12AG from Hamamatsu. With a wide-field excitation epifluorescence microscopy can be performed and detected with this detection path. The second detection path leads to an avalanche photo diode (APD). This photo diode detects and counts individual photons and transmits the counting events to a counting card. The counting card also receives a synchronisation signal of the pulsed laser and can therefore be used for

time-resolved spectroscopy, in particular for fluorescence lifetime measuring. The third detection path leads into a spectrograph, in which a spectral splitting of the signal takes place with a dispersive lattice. The signal is detected by another CCD camera (CCD2).

In the setup, the detection takes place on the same side of the sample from which the excitation originates. In particular, the same lens is used for both beam paths. Therefore, it is a so-called reflected light fluorescence microscope (epifluorescence microscope).

As an alternative to excitation with the diode laser, wide-field illumination of the sample with a white-light source can be carried out. In this case the dichroic beam splitter and the long-pass filter are removed from the beam path. CCD1 can now be used for brightfield microscopy and CCD2 for recording transmission spectra without moving the sample. Thus, it is possible to seamlessly switch between fluorescence spectroscopy and transmission spectroscopy.

The setup described in this section was used for the brightfield and epifluorescence microscopy images presented in this work. Spatially resolved emission spectra at room temperature were measured with this setup by removing the wide-field lens L3 from the beam path. The location of the excitation can be determined by the comparison between focused excitation and wide field excitation. Spatially resolved absorption spectra were determined by illuminating with a white light source and converting transmission spectra into absorption spectra. In the following chapter the results of these investigations are presented.

5.4.2 Photophysical properties of P3HT superstructures

Here, we focused on the photophysical investigations of films of shish-kebab superstructures to study the sample preparation dependency on the resulting photophysical properties of the films. Only shish-kebab structures consisting of **P3HT-2** and the bisamide **BA 2** were studied spectroscopically. The sample preparation was performed as described in **Chapter 5.3.2**. All films were spin-coated on cleaned glass substrates. A total of three different types of samples were produced. Sample 1 (**S1**) was spin-coated 4 hours after the dissolution of P3HT in the sample vial with the self-assembled bisamide fibers. Sample 2 (**S2**) was spin-coated after 24 hours storage time and sample 3 (**S3**) after 47 days. All films originate from the same P3HT-**BA 2** mixture to determine the storage time dependency.

In the following, spatially resolved recorded emission and absorption spectra are presented, which allow for the investigation of the electronic structure of the sample. Fluorescence

microscopy was used to locate the shish kebab superstructures on the sample and shift them into the focus of excitation. In order to record emission spectra, the sample was then stimulated at a confocal level, achieving a spatial resolution of 450 nm. All emission spectra were corrected for reabsorption effects. Absorption spectra were recorded by illuminating the sample with a white light source. In these measurements, the spatial resolution in the x-direction results from the spectrometer gap and in the y-direction from a line-by-line scanning of the CCD2 chip. Absorption spectra are recorded from the transmission signal. Emission and absorption spectra are measured at the same location on the sample.

Figure 138a shows a schematic illustration of a spin coated P3HT film with a Shish-kebab superstructure in top view. The P3HT nanofibers have different lengths but uniform width and grow epitaxially from the bisamide surface. Since the P3HT kebabs have already formed in solution, they grew around the entire shish surface. Thus, the spin-coating of the film causes the fibers to overlap which is shown schematically in in-plane front view in **Figure 138b**. In addition, it can be seen that there is also unassembled P3HT between the individual kebabs. At a certain distance from the shish, only the semi-crystalline P3HT film is present.

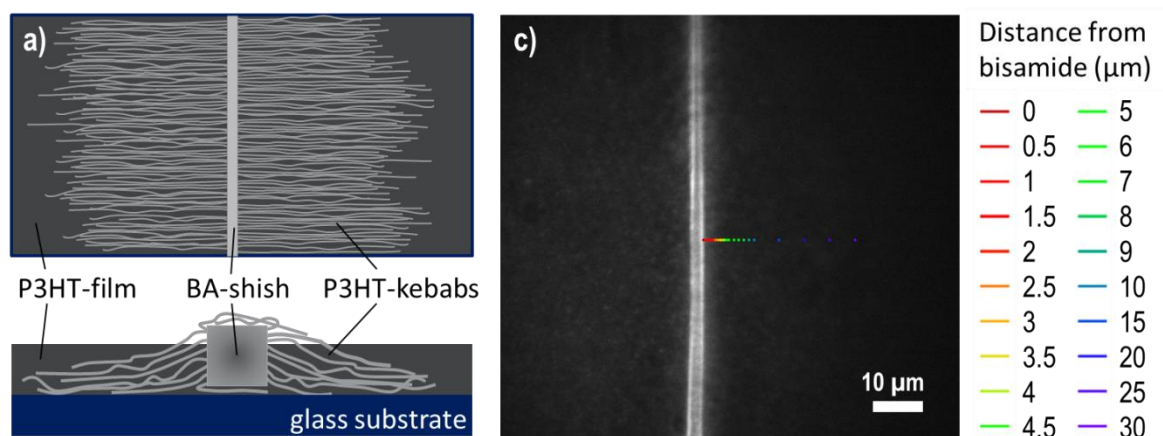


Figure 138: Schematic illustration of a spin coated P3HT film with a shish-kebab superstructure in top view (a) and in in-plane front view (b). Fluorescence microscope image of sample S2 comprising a BA 2 shish and P3HT kebabs (not visible) (c). The measuring positions at which the emission and absorption spectra are recorded were color-coded in the image. They are located at intervals of 0-30 μm to the shish. With increasing distances to the shish, the distance between the measuring points increases. The exact distances regarding the shish of the respective measuring points are listed next to the microscope image.

Figure 138c shows a fluorescence microscope image of the sample **S2** which is used as an example to explain how the different absorption and fluorescence spectra are produced. The 20 measuring positions are marked with colored dots in the fluorescence microscope image. Close to shish in the range from 0 to 5 μm the measuring positions have a distance of 500 nm to each other. For larger distances away from the shish the distance between the measuring

positions has also been increased. It should also be noted that the distance 0 μm corresponds to a measuring position at the intensity maximum of the double-strand structure and not to a measuring position in the middle of the shish.

Before discussing the results of the photophysical investigations, the energetic disorder in aggregated systems must first be considered for a better understanding of the spectra obtained. An indication of disorder in a system is an inhomogeneous linewidth σ . Assuming that the system has uncorrelated energetic disorder, each chromophore has a transition energy that deviates by a certain amount of the transient energy E_a (energy in excited state). Typically, the distribution of these deviations is Gaussian and defined by the inhomogeneous linewidth σ . For example, since the local dielectric environment of the molecules can influence the transition energies, it is useful to assume spatially correlated energetic disorder in tightly packed molecules. How many molecules the transition energies are correlated with is defined by the correlation length l_0 . Furthermore, the correlation parameter $\beta = \exp(-1/l_0)$ can be defined, which can take on values between 0 (no correlation) and 1 ($l_0 = \infty$). For $l_0 = \infty$, the transition energies within an aggregate are the same. However, if several aggregates are considered, the transition energies of each aggregate are again Gauss-distributed according to the inhomogeneous linewidth. In the case of absorption spectra, it is irrelevant to consider of correlated or uncorrelated disorder, since always an ensemble of aggregates has taken into account. As a result, the transition energies are via the linewidth Gauss distributed. However, the shape of the emission spectra of H-aggregated systems depends crucially on the linewidth σ and the correlation parameter β . For emission spectra, the relative intensities of the transitions is assumed to follow a Franck-Condon progression, as it is the case in an isolated molecule. Only the transition F_0 is prohibited if there is no disorder. If there is disorder in the system, the transition F_0 is weakly allowed by symmetry breaking. The intensity of the transition F_0 then increases with increasing disorder σ or decreasing correlation β . For extremely high disorder, the F_0 transition is quite permissible and assumes the same intensity as for isolated molecules. Furthermore, a decreasing exciton bandwidth W also leads to an increasing intensity of the transition F_0 .^[281–283]

In the following, the results of the photophysical investigations are presented and discussed. **Figures 139, 140** and **141** show a selection of the data obtained for the measurements. **Figure 139** was recorded on sample **S1** (4 h crystallization time), **Figure 140** on sample **S2** (24 h crystallization time) and **Figure 141** on sample **S3** (47 d crystallization time). The

different distances of the 20 measuring positions are visualized next to the corresponding microscope images. The color coding for emission and absorption spectra is the same as described above. Emission and absorption spectra of the same color have therefore been recorded at the same distances to the shish. The figures also shows the reference emission and absorption spectra of neat **P3HT-2** samples (black lines), which were prepared in the same manner. On the reference samples, five spatially resolved absorption and emission spectra were recorded at arbitrary locations of the films. The spectra obtained showed no dependence on the measuring position on the sample. So the spectra shown in the figures correspond to the mean of the five measurements. All emission spectra were normalized to their value at 715 nm ($E = 1.75$ eV), the absorption spectra in **Figure 141** were normalized to their value at 550 nm ($E = 2.25$ eV).

All emission spectra are located in the range of 830 – 600 nm ($1.5 \text{ eV} \leq E \leq 2.05 \text{ eV}$). Two high energy transitions appear to be around 660 nm (1.9 eV) and 715 nm (1.75 eV), respectively. These transitions are referred hereinafter as F_0 and F_1 . In the following, the variation of the emission spectra with increasing distance to the shish will be described for all samples.

The emission spectra of **S1** are shown in **Figure 139**. The course how the spectra evolves at different separate positions is illustrated by gray arrows. It can be seen that the ratio of the intensities of the transitions F_0 and F_1 initially increases for increasing distances to the shish up to a distance of 4.5 μm . For larger distances F_0/F_1 decreases again. For distances over 10 μm to the shish only a small variation of the emission spectrum takes place. It is noticeable that not only the relative intensity of the transition F_0 changes in the emission spectra, but also the high-energy edge of the spectrum changes its position. In particular, the high energy edge of the emission spectrum in **Figure 139** at the distance 0 μm (dark red line) is blueshifted by about 0.05 eV with respect to the edge of the emission spectrum at distance of 7 μm (green line). Likewise, a shift of the low-energy edge of the emission spectra relative to each other can be detected.

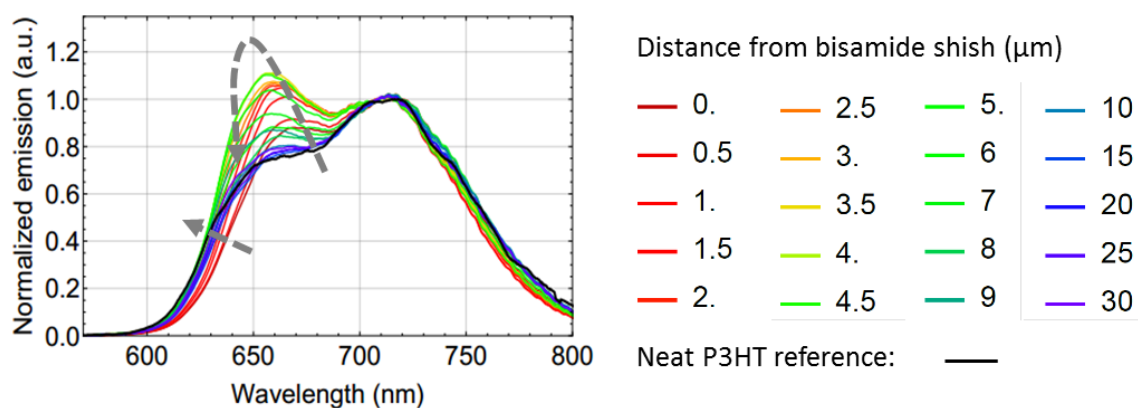


Figure 139: Spatial resolved emission spectra at different distances to the shish of a shish-kebab superstructure of sample **S1** (4 h crystallization time). The emission spectra are normalized to their value at $E = 1.75$ eV. The gray arrows visualize the course of the emission spectra as a function of the distance to the bisamide shish. The black line indicates the emission spectra of the comparative sample of neat P3HT.

The emission spectra of **S2** are shown in **Figure 140**. The course of the spectra is again illustrated by gray arrows. The figure shows that the dependence of the intensity ratios F_0/F_1 regarding to the distance to the shish is more pronounced than in **S1**. The ratio increases for **S2** up to a distance of 10 μm . Subsequently, a decrease is observed analogous **S1**, however, the final ratio is still above the initial value at Shish and well above the ratio of the neat P3HT reference sample (black line). Furthermore, the blueshift of the high-energy edge is much more intense compared to **S1**. In addition, a slight blueshift of F_1 can be observed.

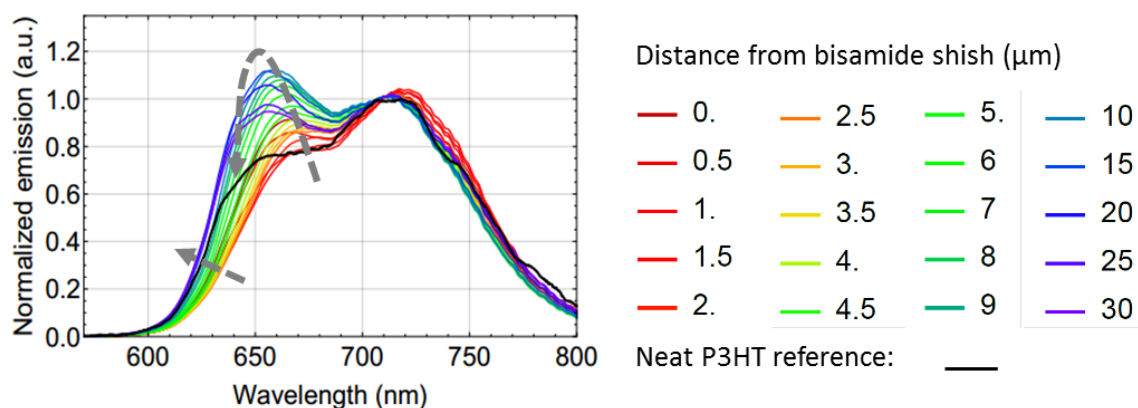


Figure 140: Spatial resolved emission spectra at different distances to the shish of a shish-kebab superstructure of sample **S2** (24 h crystallization time). The emission spectra are normalized to their value at $E = 1.75$ eV. The gray arrows visualize the course of the emission spectra as a function of the distance to the bisamide shish. The black line indicates the emission spectra of the comparative sample of neat P3HT.

In addition to the emission spectra, **Figure 141** also shows the recorded absorption spectra of **S3**. As expected, the absorption spectra show no differences in dependency on the distance of the measurement points to the shish. Since this is the case for all samples, the absorption spectra are only shown in this figure. The emission spectra show significant dependencies on distances to the shish. Thus, a continuous increase of the ratio F_0/F_1 can be observed. The final ratio quite accurate reflects the ratio of the neat P3HT reference sample. The continuous

blueshift of the low-energy flank is very pronounced for **S3**. As for **S2**, a blueshift of F_1 can also be observed for **S3**.

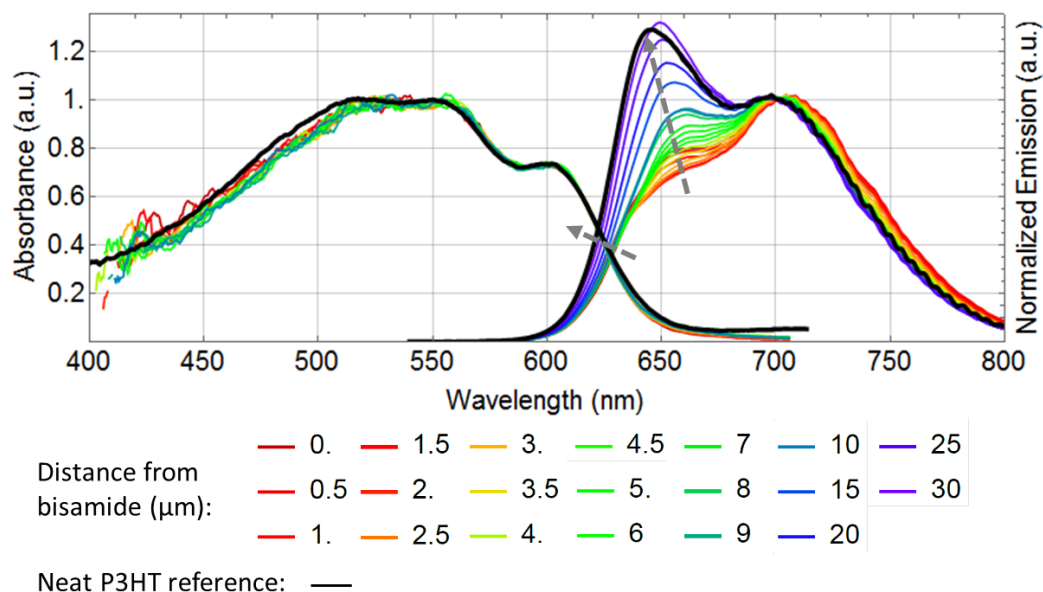


Figure 141: Spatial resolved emission spectra at different distances to the shish of a shish-kebab superstructure of sample **S3** (47 d crystallization time). The emission spectra are normalized to their value at $E = 1.75$ eV. The gray arrows visualize the course of the emission spectra as a function of the distance to the bisamide shish. The black line indicates the emission spectra of the comparative sample of neat P3HT.

In summary, all emission spectra of the samples containing the supramolecular nucleating agent **BA 2** reveal significant variations of relative peak intensities as function of distance from the bisamide fiber and that these different intensities are dependent on the manufacturing process of the samples. These observations of these different features were only possible by having highly ordered shish-kebab superstructures with significantly long P3HT fibers as well as with high resolution photophysical setup. Therefore, the electronic properties of P3HT-nanofibers can be tailored by processing conditions. Increasing emission at 650 nm indicates weaker interchain electronic coupling between neighbouring H-aggregated P3HT-chains. Furthermore, it can be assumed that the overall structural order along P3HT-nanofibers decreases as a function of distance from the bisamide fiber. One sign of this is the continuous blueshift of the emission spectra, which indicates that there is an increased fraction of P3HT-aggregates with more disordered side chains. Moreover, the decreasing electronic coupling indicates increasing disorder in backbone packing. Since the absorption spectra do not vary with the distance to the shish, it can be assumed that there is a fast and efficient energy transfer within the P3HT nanofibers towards emitting regions and that the emission is derived from small parts of excited P3HT nanofibers. Accordingly, it can be assumed that there may be an energy gradient along the P3HT nanofiber present.

6 Extended summary

Poly(3-hexylthiophene) (P3HT) as highly used semiconducting polymer has been an integral part in the field of organic electronics for decades. In this context it has earned itself a reputation as a model polymer for π -conjugated systems. Despite the intensive research, however, not all existing issues have been solved and open questions have not been clarified till date. For example, controlling the solid-state morphology and order of semi-crystalline films still represents a challenge today. There are a lot of proposed solutions, but these typically also increase the complexity of the overall system. A promising and straightforward approach to control the solid-state morphology is nucleation. For this reason, this work is dedicated to the nucleation of P3HT with supramolecular nucleating agents.

The first chapter describes in detail the design, synthesis and characterization of *pyridine-containing C₂-symmetric bisamides* and *C₃-symmetric trisamides*, which serve as *nucleating agents for P3HT*. These supramolecular building blocks were selected as they feature sufficient thermal stability and also have a potential to self-assemble under certain conditions into supramolecular nanostructures in a controlled manner. As substituents, various pyridine moieties have been used to provide an epitaxial surface for P3HT. In total, six different pyridine-containing trisamides and six pyridine-containing bisamides were synthesized by amidation reactions between different acid chlorides and amine derivatives, whereas most of those compounds are not described in literature. The structural variations of the investigated compounds involve the central core, the orientation of the amide bond, and the pyridine-containing peripheral substituents. These structural variations were necessary to study the influences of the chemical structure in particular on the nucleation ability on P3HT in a comprehensive manner. Exemplarily, **Figure 142** shows selected chemical structures of an investigated trisamide and a bisamide.

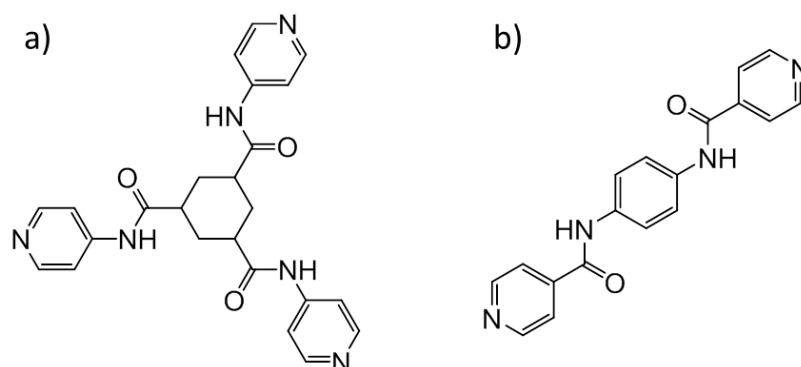


Figure 142: Chemical structures of N¹,N³,N⁵-tri(pyridin-4-yl)cyclohexane-1,3,5-tricarboxamide (a) and N,N'-(1,4-phenylene)diisonicotinamide (b).

Analytical methods such as $^1\text{H-NMR}$ spectroscopy, mass spectrometry and IR spectroscopy confirmed that all desired compounds were successfully synthesized in high purity. Thermal characterizations via thermogravimetric analyses, simultaneous differential thermal analyses and melting point measurements showed that nine of the twelve synthesized compounds have sufficient thermal stability to potentially be used as supramolecular nucleating agent for P3HT.

Comprehensive self-assembly investigations were performed with all of the compounds in chlorobenzene (CB) and ortho-dichlorobenzene (o-DCB). These solvents were selected since both are good solvents for P3HT and therefore will be used for the nucleation investigations and the shish-kebab production. It was found that four cyclohexane-based pyridine-containing trisamides can form fibrous nanostructures in o-DCB. The resulting nanofiber widths are highly concentration-dependent and can therefore be tailored in the range from 17 nm to 200 nm. For instance, **Figure 143a** shows as a SEM image of self-assembled nanofibers from the trisamide N,N',N'' -(cyclohexane-1,3,5-triyl)triisonicotinamide. Moreover, self-assembly studies performed in aqueous solutions using selected pyridine containing trisamides revealed that with these systems it was possible to generate stable supramolecular gels based on nanofibers. In contrast the trisamides, the pyridine-containing bisamides showed a significantly higher solubility in CB and o-DCB. In these studies it was found that the morphologies of the self-assembled objects were multifaceted. Besides to rigid fibrous-like 1D-nanostructures, as found for N,N' -(1,4-phenylene)-diisonicotinamide in o-DCB (**Figure 143b**), different sheet-like 2D-nanostructures could also be observed.

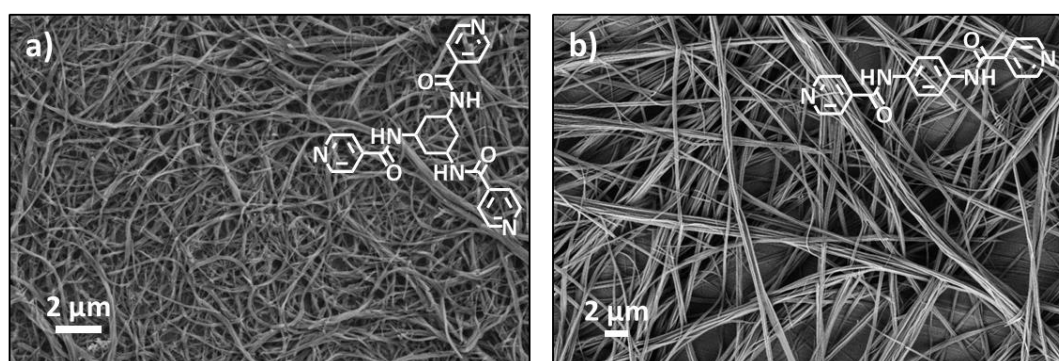


Figure 143: SEM micrographs of supramolecular nanofibers prepared by self-assembly upon cooling in o-DCB of N,N',N'' -(cyclohexane-1,3,5-triyl)triisonicotinamide (a) and N,N' -(1,4-phenylene)-diisonicotinamide (b). The trisamide and bisamide concentration in solution was 50 ppm each.

The second chapter deals with the *nucleation of P3HT* without and with various additives. Three different commercially available P3HT grades were selected, which vary with respect to molecular weight (M_w), regioregularity and polydispersity. These variations results in

significant differences of the thermal properties, such as melting temperature, crystallization temperature (T_c^0) and the respective enthalpies.

Self-nucleation experiments on thin P3HT films at temperatures where the number of P3HT nuclei is very small were performed to visualize the P3HT spherulites. In this way, highly ordered unexpected large spherulitic structures could be generated with macroscopic diameters of more than 500 μm . Via parameters such as annealing time, annealing temperature and layer thickness of the spin-coated P3HT film the size of the spherulites could be tuned. Such large spherulitic structures of P3HT prepared via isothermal melt annealing have not yet been reported in literature and are therefore subject of further photophysical investigations.

Self-nucleation experiments according to Lotz et al. and Richter et al on bulk P3HT were performed by means of differential scanning calorimetry (DSC) to determine the maximum crystallization temperature (T_c^{max}) of each grade. The largest difference between T_c^0 and T_c^{max} with a value of 9.1 $^{\circ}\text{C}$ showed the grade *RMI_001_EE2* from *Rieke Metals Incorporation*. Due to this rather large nucleation window, this grade was selected to investigate the nucleation behavior and the nucleation efficiency (NE) of the different pyridine-containing additives. In a first step to evaluate the nucleation capability of the nine thermally suitable pyridine-containing additives, these additives were blended with P3HT at a concentration of 1 wt.-% and investigated by means of DSC. With four of these additives a nucleating effect could be observed. It was found that only the 1,4-bisamides with 4-pyridine substituents are capable of nucleating P3HT. In contrast, the investigated pyridine-containing trisamides, despite being able to self-assemble in a fibrous manner, did not affect the crystallization temperature of P3HT. It can therefore be assumed that they do not provide an epitaxial surface for the P3HT nucleation. Concentration-dependent investigations with the 1,4-bisamides revealed that already after the addition of 0.025 wt.-% of additive, the T_c^{nuc} of P3HT increases strongly and reaches a plateau at an additive concentration above 0.25 wt.-%. Furthermore, the comparison of the respective NEs showed that 1,4-bisamides based on a benzene core are more efficient as nucleating agents for P3HT than bisamides based on a cyclohexane core. Notably, the highest NE with an outstanding value of about 94 % could be observed for the bisamide *N,N'-(1,4-phenylene)-diisonicotinamide* at a concentration of 0.25 wt.-%. In conclusion, this thesis presents for the first time very efficient nucleating agents for P3HT.

Temperature-dependend polarized optical microscopy investigations on P3HT bisamide films revealed that the nucleating agents dissolve in the P3HT melt and form supramolecular

nanostructures upon cooling before P3HT crystallization takes place and thus serving as heterogeneous nuclei. Isothermal investigations using DSC have shown that the addition of nucleating agents significantly reduces the crystallization half-time $T_{1/2}$. Furthermore, the data indicates that the nucleation mechanism which is present for neat P3HT does not change upon the addition of the supramolecular nucleating agents.

The third chapter deals with *highly ordered shish kebab superstructures* based on rigid fiber-like self-assembled 1,4-bisamides acting as shish and self-assembled P3HT nanofibers acting as kebabs (**Figure 144a**). The preparation of these shish-kebab superstructures was realized via a dispersion-based nucleation process at room temperature. Hereby, the dissolved P3HT crystallizes in a fibrous manner from the solid bisamide surface of a supramolecular nanofiber.

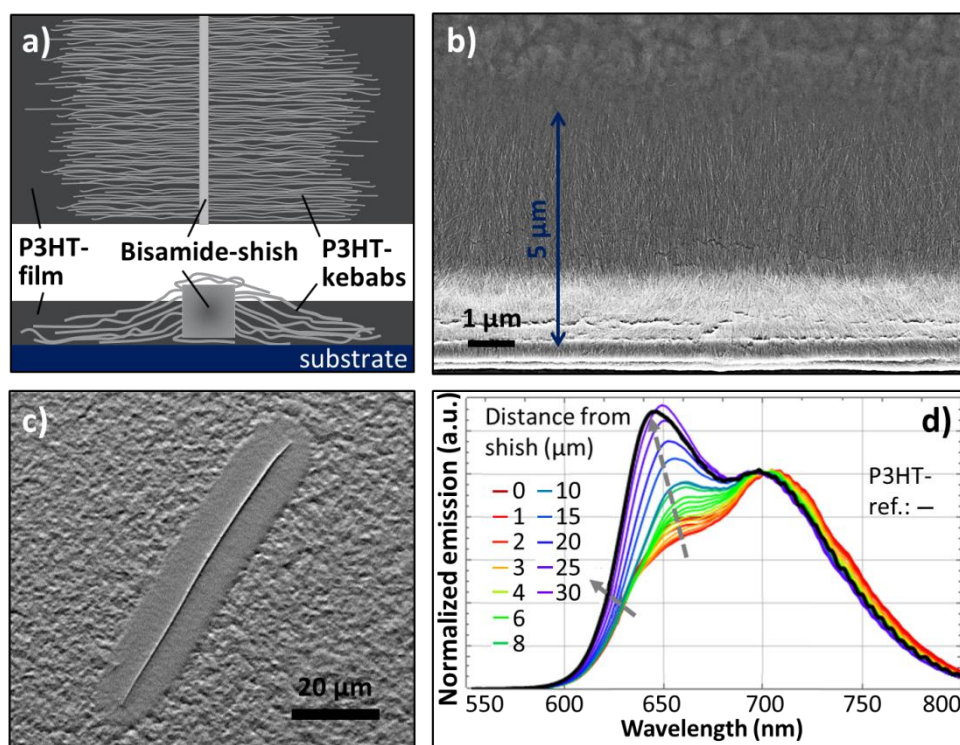


Figure 144: Schematic illustration of a thin P3HT film with a shish-kebab superstructure in top view and in in-plane front view (a). SEM image (b) and Desktop-SEM image in topography mode (c) of a shish-kebab superstructure comprising P3HT kebabs and a *N,N'*-(1,4-phenylene)diisonicotinamide shish. The concentration of P3HT in chlorobenzene was 1 wt.-%, equally the concentration of *N,N'*-(1,4-phenylene)diisonicotinamide regarding to P3HT. The aging time before spin-coating amounts to 24 hours each. Spatially resolved emission spectra at different distances to the shish of a shish-kebab superstructure of a 47 days old sample (d). The emission spectra were normalized to their value at $E = 1.75$ eV. The gray arrows visualize the course of the emission spectra as a function of the distance to the bisamide shish. The black line indicates the emission spectra of a comparative sample of neat P3HT.

Several processing parameters, such as the molecular weight of P3HT, the concentration of the P3HT in solution and aging time of the P3HT-additive dispersion were systematically varied to reveal their influences on the resulting P3HT nanofiber length. Subsequent film formation allows for the characterization and evaluation of the shish-kebab superstructures

via optical and electron microscopy (**Figure 144b** and **c**). It was found that each of the process parameters mentioned above has an enormous influence on the resulting P3HT kebab length and density. The results showed that P3HT with a lower molecular weight and at higher solution concentrations as well as extended aging times lead to significant longer kebab fibers and higher kebab densities. By systematically tuning these parameters, it was possible to prepare highly oriented and aligned P3HT fibers that were over five micrometer long and also had an enormous growth density. This high density of P3HT fibers confirms the very suitable epitaxially surface of the self-assembled additives and therefore the ultra high efficiency of the studied pyridine-containing 1,4-bisamide as nucleating agents for P3HT.

These unique shish kebab superstructures never realized before allowed us for the very first time, to perform spatially resolved photophysical spectroscopic investigations along P3HT nanofibers. Unexpectedly, these spectroscopic investigations revealed, that all emission spectra of the samples containing supramolecular nucleating agents feature variations of relative peak intensities as function of distance from the bisamide shish (**Figure 144d**). These different intensities are equivalent to variations of the structural and electronic order along P3HT nanofibers and are also dependent on the preparation process of the samples. These findings indicate that an energy gradient along the P3HT nanofiber can be formed just using one single species of conjugated polymers and by applying suitable processing conditions.

In summary, this work presents tailored supramolecular nucleating agents based on pyridine-containing bisamides which are highly efficient for the nucleation of P3HT in melted state and also in solution. Moreover, the formation of highly oriented P3HT nanofibers with a shish-kebab-like superstructure was demonstrated for the first time. Employing confocal imaging and spectroscopy, it could be found that the structural and electronic order along the P3HT nanofibers varies in a directed manner. Moreover, it was shown that this order can be controlled by applying proper processing protocols. Thus, controlling of the morphology of P3HT by means of nucleating agents paves the way to study and understand the charge and energy transport processes of P3HT shish-kebab superstructures.

7 Experimental

7.1 Materials and methods

The synthesis of the individual bis- and trisamides investigated in the course of this thesis was performed by Doris Hanft, Sandra Ganzleben, Jutta Failner and Rika Schneider. Characterization, analysis and evaluation were performed by my self.

All chemicals were commercially available and used without further purification, except of chlorobenzene and ortho-dichlorobenzene, which were purified by distillation prior the self-assembly investigations.

¹ H-NMR	NMR spectra were recorded on a Bruker AC spectrometer (300 MHz) using DMSO as solvent and internal standard. Chemical shifts are denoted in ppm relative. Multiplicities are indicated with s (singlet), d (doublet), t (triplet), dd (duplicated doublet) and m (multiplet).
MS	Mass Spectra (MS) were recorded on a FINNIGAN MAT 8500 spectrometer from Thermo Fisher Scientific using electron spray ionization (EI).
IR spectroscopy	Infrared (IR) spectra were recorded with a PerkinElmer Spectrum 100 FT-IR spectrometer in the range of 4000 cm ⁻¹ to 650 cm ⁻¹ .
TGA/SDTA	Thermogravimetric analysis (TGA) and simultaneous differential thermal analysis (SDTA) measurements were performed on a Mettler Toledo TGA/SDTA 851e. Data were recorded with a heating rate of 10 K·min ⁻¹ in the temperature range from 30 °C to 700 °C under nitrogen atmosphere.
Film fabrication	Thin films were prepared by spin coating on a Coros OP15 (Siemens) with a CONVAC 1001 and by doctor blading.
Film thickness	The thickness of spin coated polymer films was measured on a Dektak 3030 ST surface profilometer (Sloan Technologies) and on a Veeco Dektak 150.

SEM	<p>Scanning electron microscopy (SEM) investigations were performed on a Zeiss 1530 FESEM. Images were taken utilizing a SE2 or an in-lens detector and an accelerating voltage of 3 kV.</p> <p>Additionally, scanning electron micrographs were recorded on a Phenom Pro from Phenom-World BV with an accelerating voltage of 5 kV.</p> <p>All samples have been sputtered with platinum (2.0 nm) on a Sputter Coater 208HR (Cressington) before investigated.</p>
TEM	<p>Transmission electron microscopy was performed on a Zeiss CEM902 EFTEM electron microscope (CEM 902).</p>
T _m -determination	<p>The melting point system MP 90 from Mettler Toledo was used to determine the melting points of the pyridine-containing bis- and trisamides via haze analysis. Data were recorded with a heating rate of 10 K·min⁻¹ in a temperature range from 30 °C to 400 °C. The neat substances were filled into three measuring tubes and the mean value was determined from three measurements.</p>
DSC	<p>Differential scanning calorimetry (DSC) measurements were performed on a Perkin Elmer Diamond DSC and on a Mettler Toledo DSC 2. For the preparation of the DSC samples 3 wt.-% solutions of P3HT with and without additive in chlorobenzene were prepared. After removing the solvent in a vacuum oven at 100 °C for 12 hours 8-12 mg of the dried samples are weighed in aluminum pans and measured via DSC.</p> <p><u>Temperature profile for samples containing P3HT:</u></p> <ol style="list-style-type: none">1. Heating from 150 °C to 300 °C with a heating rate of 10 K·min⁻¹2. Isothermal holding for 5 min at 300 °C3. Cooling from 300 °C to 150 °C with a cooling rate of 10 K·min⁻¹ <p>For the <u>self-nucleation investigations</u>, two standard temperature profiles were measured at the beginning. Subsequently, the heating temperature is lowered to the endset of the melting range of the respective component and is maintained isothermally for 5 min. The sample is then cooled down to the starting temperature with a cooling rate of 10 K·min⁻¹. Afterwards, the maximum heating temperature for</p>

each successive run is decreased by one Kelvin. As a result, a shift in the crystallization temperature up to the maximum crystallization temperature can be observed.

For the stability measurements, the standard temperature profiles of the corresponding components were measured 10 times in a row and the enthalpy values were noted.

Temperature profile for the isothermal crystallization measurements:

1. Heating from 150 °C to 300 °C with a heating rate of 10 K·min⁻¹
2. Isothermal holding for 5 min at 300 °C
3. Cooling from 300 °C to 150 °C with a cooling rate of 10 K·min⁻¹
4. Heating from 150 °C to 300 °C with a heating rate of 10 K·min⁻¹
5. Isothermal holding for 5 min at 300 °C
6. Cooling from 300 °C to T_{iso} with a cooling rate of 10 K·min⁻¹
7. Isothermal holding at T_{iso} for 60 minutes

PL microscopy

Polarized light (PL) microscopy was performed on a Nikon Invers Diaphot TMD 300 optical microscope. The samples were prepared via spin-coating. Optical micrographs were recorded by a Nikon ACT-1 software using a Nikon DMX1200 digital camera.

7.2 Synthesis and characterization of pyridine-containing trisamides

7.2.1 N^1,N^3,N^5 Tri(pyridin-4-yl)benzene-1,3,5-tricarboxamide (TA 1)

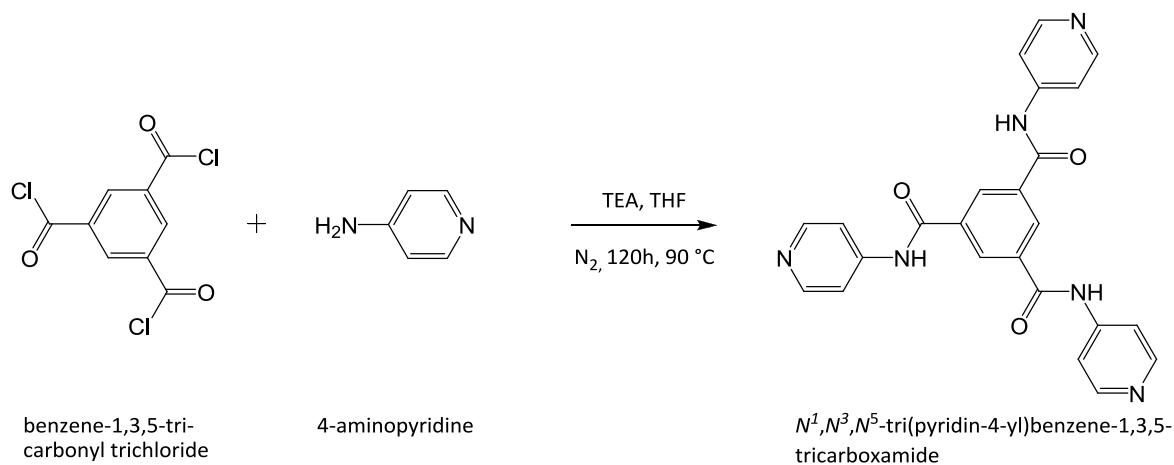


Figure 145: Reaction of benzene-1,3,5-tricarbonyl trichloride with 4-aminopyridine.

Synthesis:

1,60 g (6 mmol) of benzene-1,3,5-tricarbonyl trichloride

2,80 g (30 mmol) of 4-aminopyridine

80 mL of THF (abs.)

4,15 mL of triethylamine

4-Aminopyridine and TEA were mixed together with 80 mL of dried THF in a Schlenk flask. Benzene-1,3,5-tricarbonyl trichloride was then added under inert gas (N_2) and ice cooling. The reaction time was 120 hours at 90 °C. The white precipitate was then filtered off after cooling the suspension to room temperature, washed in a mixture of THF/ H_2O /Acetone and dried under high vacuum. The crude product then recrystallized in DMF/Acetone; filtered off and dried to get whitish crystals.

Characterization:

Yield: 0,75 g (29 %, as white crystals)

$^1\text{H-NMR}$: δ (ppm) = 10,95 (3H, s); 8,76 (3H, s); 8,43-8,63 (6H, m); 7,73-7,93 (6H, m)

MS: m/z (%): 438 (54, M^+); 345 (33); 318 (100); 250 (13); 223 (19); 195 (24); 121 (21); 75 (37)

TGA: 5 % mass loss at 379 °C

SDTA: T_m^1 : 379°C; T_m^2 : 400°C

Mp (MP90): T_m : 381 °C

IR: $\tilde{\nu}$ (cm^{-1}): 1683; 1589; 1507; 1414; 1330

7.2.2 N,N',N''(Benzene-1,3,5-triyl)triisonicotinamide (TA 2)

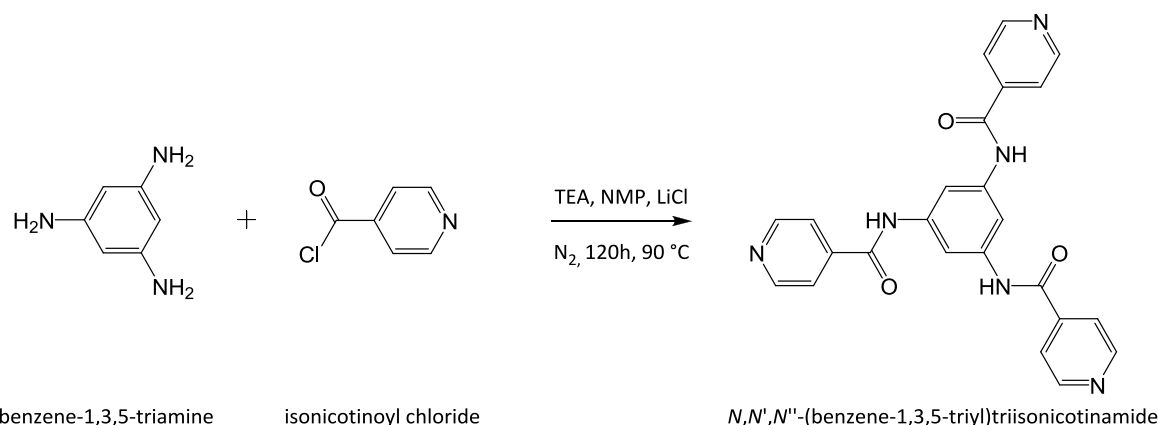


Figure 146: Reaction of benzene-1,3,5-triamine with isonicotinoyl chloride.

Synthesis:

0,73 g (6 mmol) of benzene-1,3,5-triamine

4,2 g (30 mmol) of isonicotinoyl chloride

80 mL of NMP (abs.)

4,15 mL of triethylamine

LiCl

Benzene-1,3,5-triamine, TEA and LiCl were mixed together with 80 mL of NMP in a Schlenk flask. The acid chloride was then added under inert gas (N_2) and ice cooling. The reaction time was 120 hours. The resulting dark brown suspension was precipitated in ice water and the precipitate was filtered off. The crude product was then recrystallized in DMF with a few drops of water, filtered off and dried at 140 °C under high vacuum to yield a yellowish powder.

Characterization:

Yield: 1,21 g (46 %, as yellowish powder)

$^1\text{H-NMR}$: δ (ppm) = 10,68 (3H, s); 8,74-8,86 (6H, m); 8,12 (3H, s); 7,84-7,94 (6H, m)

MS: m/z (%): 438 (53, M^+); 409 (9); 360 (8); 332 (24); 106 (100); 78 (71)

TGA: 5 % mass loss at 432 °C

SDTA: T_m : 448 °C

Mp (MP90): T_m : > 400 °C

IR: $\tilde{\nu}$ (cm^{-1}): 3157; 3071; 1667; 1622; 1555; 1427

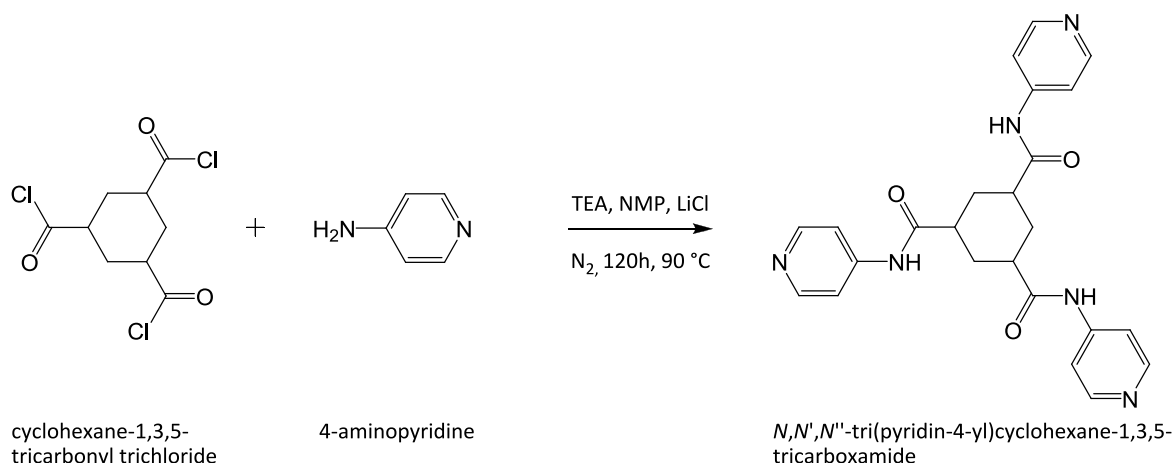
7.2.3 N¹,N³,N⁵-Tri(pyridin-4-yl)cyclohexane-1,3,5-tricarboxamide (TA 3)

Figure 147: Reaction of cyclohexane-1,3,5-tricarbonyl trichloride with 4-aminopyridine.

Synthesis:

2,68 g (10 mmol) of cyclohexane-1,3,5-tricarbonyl trichloride

4,64 g (49 mmol) of 4-aminopyridine

100 mL of NMP (abs.)

6,80 mL of triethylamine

LiCl

4-Aminopyridine, TEA and LiCl were mixed together with 100 mL of NMP in a Schlenk flask. The acid chloride was then added under inert gas (N₂) and ice cooling. The reaction time was 120 hours at 90 °C. The resulting reaction mixture was then precipitated in a mixture of 800 mL of ice water and NaCl. The solid is filtered off and dried. The resulting crude product was then dissolved in a small amount of hot DMF; precipitated in aqueous NaOH, filtered off and dried yielding a brownish powder.

Characterization:

Yield: 1,06 g (24 %, as brownish powder)

¹H-NMR: δ (ppm) = 10,28 (3H, s); 8,34-8,56 (6H, m); 7,48-7,68 (6H, m); 2,57-2,77 (3H, m); 1,97-2,17 (3H, m); 1,50-1,76 (3H, m)

MS: m/z (%): 444 (1, M⁺); 402 (2); 350 (100); 257 (53); 230 (17); 121 (38); 81 (93)

TGA: 5 % mass loss at 329 °C

SDTA: T_m: 345 °C

Mp (MP90): T_m: 335 °C

IR: $\tilde{\nu}$ (cm⁻¹): 3293; 1668; 1587; 1506; 1411

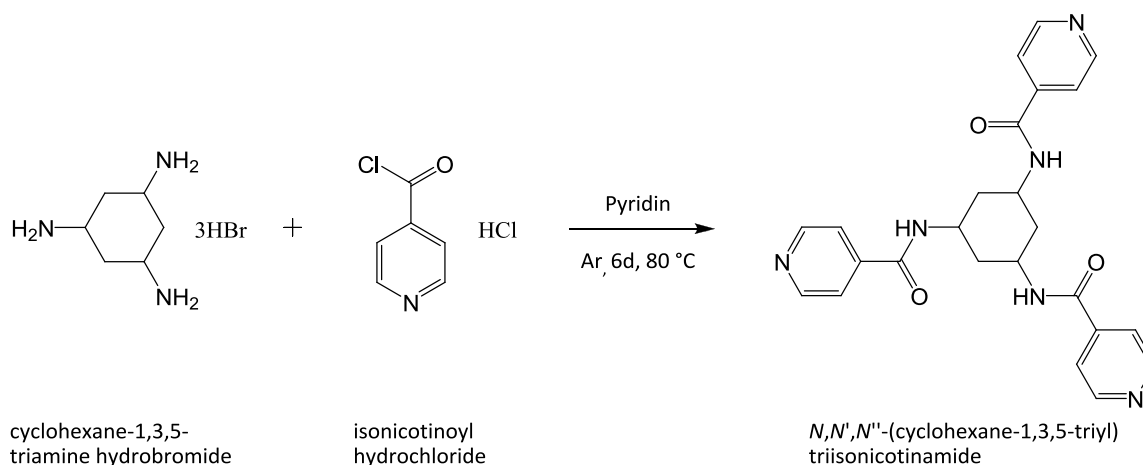
7.2.4 N,N,N'' -(Cyclohexane-1,3,5-triyl)triisonicotinamide (TA 4)

Figure 148: Reaction of cyclohexane-1,3,5-triamine hydrobromide with isonicotinoyl chloride hydrochloride.

Synthesis:

2 g (5 mmol) cis, cis-cyclohexane-1,3,5-triamine hydrobromide

4,78 g (26 mmol) isonicotinoyl chloride hydrochloride

50 mL pyridine

Cis,cis-cyclohexane-1,3,5-triamine hydrobromide was mixed with 50 mL of pyridine in a Schlenk flask. The acid chloride was then added under inert gas (Ar) and ice cooling. The reaction time was 6 days. The resulting black solution was then cooled to room temperature and concentrated in a rotary evaporator. The remaining brown solid was then dissolved in a $\text{H}_2\text{O}/\text{HCl}$ mixture. Afterwards KOH is added till a pH of 8 was reached. The resulting precipitate was filtered off; recrystallized in MeOH, filtered off and dried to yield a fine slightly yellowish powder.

Characterization:

Yield: 1,74 g (73 %, as yellowish powder)

$^1\text{H-NMR}$: δ (ppm) = 8,77 (3H, s); 8,64-8,82 (6H, m); 7,68-7,80 (6H, m); 3,90-4,16 (3H, m); 1,96-2,16 (3H, m); 1,40-1,64 (3H, m)

MS: m/z (%): 444 (3, M^+); 350 (3); 322 (16); 200 (45); 123 (63); 106 (100); 78 (90)

TGA: 5 % mass loss at 426 °C

SDTA: T_m^1 : 325°C; T_m^2 : 421°C

Mp: T_m : > 400 °C

IR (MP90): $\tilde{\nu}$ (cm^{-1}): 3291; 3038; 1671; 1643; 1531; 1408

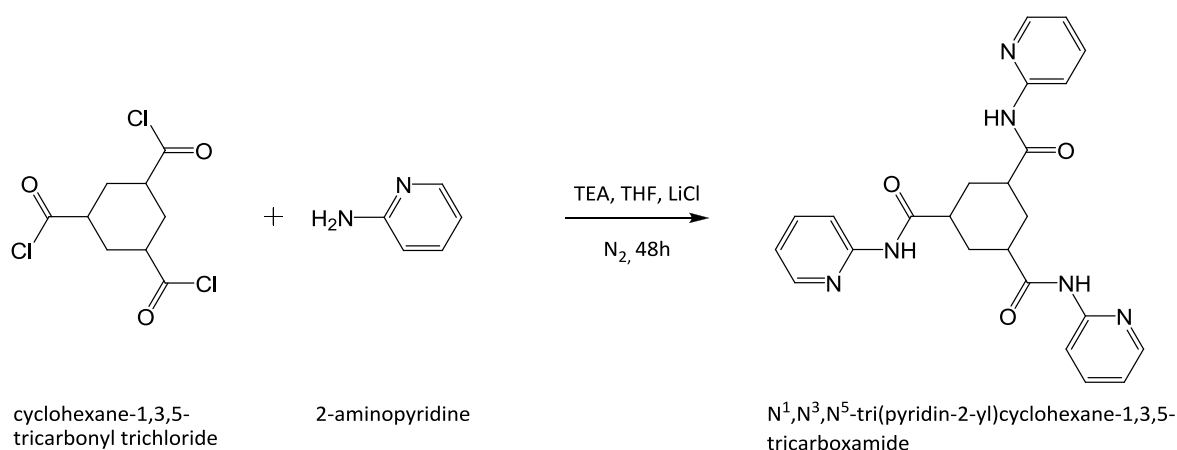
7.2.5 N¹,N³,N⁵-Tri(pyridin-2-yl)cyclohexane-1,3,5-tricarboxamide (TA 5)

Figure 149: Reaction of cyclohexane-1,3,5-tricarbonyl trichloride with 2-aminopyridine.

Synthesis:

3,25 g (12,0 mmol) of cis,cis-cyclohexane-1,3,5-tricarbonyl trichloride

3,71 g (39,0 mmol) of 2-aminopyridine

150 mL of THF (dried)

15 mL of triethylamine

LiCl

2-Aminopyridine, TEA and LiCl were mixed together with 150 mL of dried THF in a Schlenk flask. The acid chloride was then added under inert gas (N₂) and ice cooling. The reaction time was 48 hours. The resulting reaction mixture was concentrated in a rotary evaporator and then precipitated in 200 mL of water. The crude product was recrystallized in MeOH, filtered off and dried to yield a white powder.

Characterization:

Yield: 0,57 g (10 %, as white powder)

¹H-NMR: δ (ppm) = 10,45 (3H, s); 8,29-8,32 (3H, m); 8,07-8,10 (3H, m); 7,73-7,79 (3H, m); 7,06-7,10 (3H, m); 2,68-2,71 (3H, m); 1,95-1,97 (3H, m); 1,59-1,63 (3H, m)

MS: m/z (%): 444 (10, M⁺); 323 (58); 229 (39); 176 (67); 149 (46); 121 (72); 95 (100)

TGA: 5 % mass loss at 287 °C

SDTA: T_m: 284 °C

Mp (MP90): T_m: 280 °C

IR: $\tilde{\nu}$ (cm⁻¹): 3294; 1664; 1574; 1518; 1429; 1312

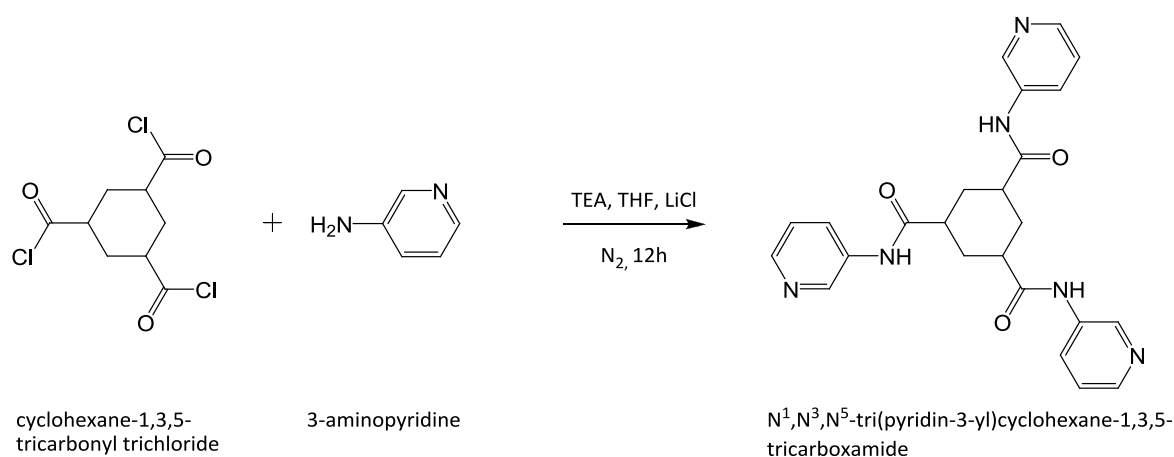
7.2.6 N¹,N³,N⁵-Tri(pyridin-3-yl)cyclohexane-1,3,5-tricarboxamide (TA 6)

Figure 150: Reaction of cyclohexane-1,3,5-tricarbonyl trichloride with 3-aminopyridine.

Synthesis:

3,25 g (12,0 mmol) of cis,cis-cyclohexane-1,3,5-tricarbonyl trichloride

3,71 g (39,0 mmol) of 3-aminopyridine

150 mL of THF (dried)

15 mL of triethylamine

LiCl

3-Aminopyridine, TEA and LiCl were mixed together with 150 mL of dried THF in a Schlenk flask. The acid chloride was then added under inert gas (N₂) and ice cooling. The reaction time was 12 hours. The resulting solid was precipitated in 200 mL of water, filtered off and dried to yield a white powder.

Characterization:

Yield: 2,77 g (51 %, as white powder)

¹H-NMR: δ (ppm) = 10,09 (3H, s); 8,66-8,82 (3H, m); 8,16-8,32 (3H, m); 7,96-8,12 (3H, m); 7,26-7,40 (3H, m); 2,52-2,68 (3H, m); 1,96-2,18 (3H, m); 1,58-1,80 (3H, m)

MS: m/z (%): 444 (18, M⁺); 323 (85); 229 (52); 176 (76); 149 (45); 121 (71); 95 (100)

TGA: 5 % mass loss at 377 °C

SDTA: T_m: 393 °C

Mp (MP90): T_m: 380 °C

IR: $\tilde{\nu}$ (cm⁻¹): 3259; 1659; 1587; 1525; 1480; 1421

7.3 Synthesis and characterization of pyridine-containing bisamides

7.3.1 N¹,N⁴-Di(pyridin-4-yl)terephthalamide (BA 1)

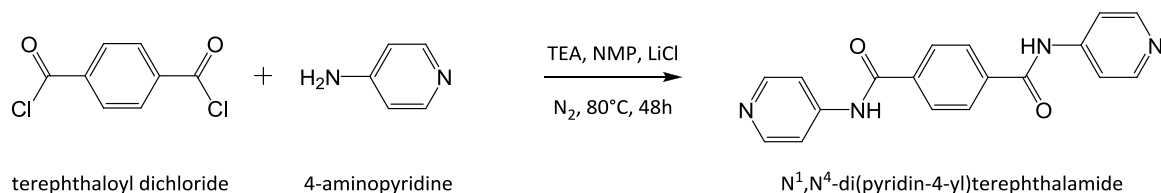


Figure 151: Reaction of terephthaloyl dichloride with 4-aminopyridine.

Synthesis:

2,53 g (12 mmol) of terephthaloyl dichloride

2,58 g (27 mmol) of 4-aminopyridine

50 mL of N-methyl-2-pyrrolidone

10 mL of triethylamine

LiCl

4-Aminopyridine, triethylamine (TEA) and LiCl were mixed together with 50 ml of NMP in a Schlenk flask. Terephthaloyl dichloride was then added under inert gas (N₂) and ice cooling. The reaction time was 48 hours at a temperature of 80 °C. The resulting reaction mixture was precipitated in ice water; the solid was filtered off and dried. The crude product thus obtained was then dissolved in dimethylsulfoxide (DMSO) and precipitated again in 500 ml of H₂O. The final product was finally dried at 60 °C under high vacuum to get a greyish powder.

Characterization:

Yield: 2,08 g (54 %, as greyish powder)

¹H-NMR: δ (ppm) = 10,77 (2H, s); 8,51 (4H, dd); 8,13 (4H, s); 7,81 (4H, dd)

MS: m/z (%): 318 (72, M⁺); 225 (100); 198 (25); 104 (45); 76 (23)

TGA: 5 % mass loss at 384 °C

SDTA: T_m: 385 °C

Mp (MP90): T_m: 378 °C

IR: $\tilde{\nu}$ (cm⁻¹): 1689; 1593; 1513; 1418; 1328

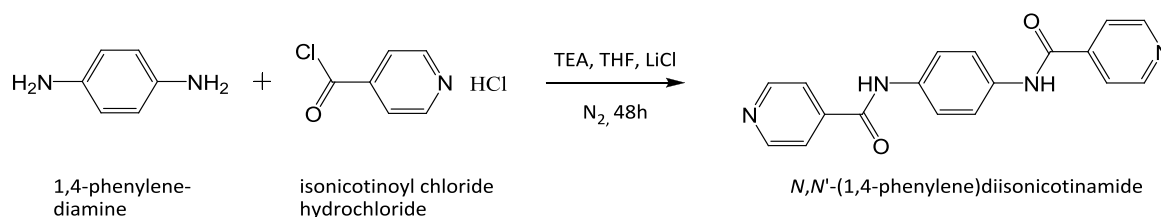
7.3.2 *N,N'*-(1,4-Phenylene)diisonicotinamide (BA 2)

Figure 152: Reaction of 1,4-phenylenediamine with isonicotinoyl chloride hydrochloride.

Synthesis:

0,5 g (4,6 mmol) of 1,4-phenylenediamine

1,81 g (10,1 mmol) of isonicotinoyl chloride hydrochloride

50 mL of THF (dried)

5 mL of triethylamine

1,4-Phenylenediamine and TEA were mixed together with 50 mL of dried THF in a Schlenk flask. The acid chloride was then added under inert gas (N₂) and ice cooling. The reaction time was 48 hours. The resulting reaction mixture was concentrated in a rotary evaporator and the residues were extracted in ethyl acetate (EA). The solid was then extracted in MeOH. Finally, the crude product was recrystallized in DMF with a few drops of H₂O to get a whitish powder.

Characterization:

Yield: 0,48 g (33 %, as whitish powder)

¹H-NMR: δ (ppm) = 10,55 (2H, s); 8,74-8,84 (4H, m); 7,83-7,93 (4H, m); 7,78 (4H, s)

MS: m/z (%): 318 (100, M⁺); 240 (12); 212 (12); 106 (99); 78 (84); 51 (20)

TGA: 5 % mass loss at 372 °C

SDTA: T_m: 331 °C

Mp (MP90): T_m: 330 °C

IR: $\tilde{\nu}$ (cm⁻¹): 3330; 1645; 1545; 1520; 1410

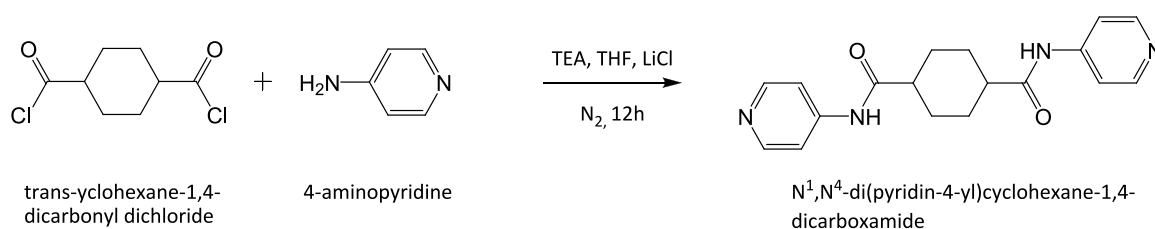
7.3.3 N¹,N⁴-Di(pyridin-4-yl)cyclohexane-1,4-dicarboxamide (BA 3)

Figure 153: Reaction of trans-cyclohexane-1,4-dicarbonyl dichloride with 4-aminopyridine.

Synthesis:

2,34 g (11,1 mmol) of trans-cyclohexane-1,4-dicarbonyl dichloride

2,31 g (24,6 mmol) of 4-aminopyridine

100 mL of THF (dried)

10 mL of triethylamine

LiCl

4-Aminopyridine, triethylamine (TEA) and LiCl were mixed together with 50 ml of NMP in a Schlenk flask. The acid chloride was then added under inert gas (N₂) and ice cooling. The reaction time was 12 hours at room temperature. The resulting reaction mixture was precipitated in ice water; the solid was filtered off and dried. The crude product was then recrystallized in DMSO, filtered and dried under high vacuum to yield a white powder.

Characterization:

Yield: 2,32 g (64 %, as white powder)

¹H-NMR: δ (ppm) = 10,29 (2H, s); 8,40 (4H, dd); 8,57 (4H, dd); 2,25-2,45 (2H, m); 1,80-2,10 (4H, m); 1,35-1,60 (4H, m)

MS: m/z (%): 324 (51, M⁺); 231 (16); 203 (100); 121 (52); 95 (77); 81 (43)

TGA: 5 % mass loss at 386 °C

SDTA: T_m: 406 °C

Mp (MP90): T_m: > 400 °C

IR: $\tilde{\nu}$ (cm⁻¹): 1695; 1594; 1512; 1418; 1376

7.3.4 N,N'-(Cyclohexane-1,4-diyl)diisonicotinamide (BA 4)

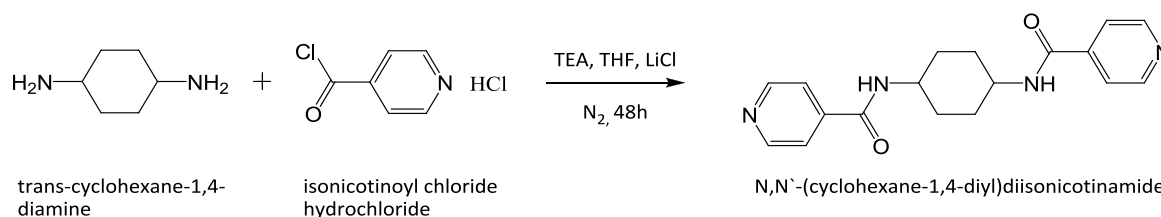


Figure 154: Reaction of trans-cyclohexane-1,4-diamine with isonicotinoyl chloride hydrochloride.

Synthesis:

1 g (8,7 mmol) of trans-cyclohexane-1,4-diamine

3,42 g (19,2 mmol) of isonicotinoyl chloride hydrochloride

100 mL of THF (dried)

10 mL of triethylamine

LiCl

Trans-cyclohexane-1,4-diamine, TEA and LiCl were mixed together with 100 mL of dried THF in a Schlenk flask. The acid chloride was then added under inert gas (N₂) and ice cooling. The reaction time was 48 hours at room temperature. The resulting reaction mixture was precipitated in ice water; the solid was filtered off and dried. The crude product was then recrystallized in 30 mL of DMSO, filtered and dried under high vacuum to get a white powder.

Characterization:

Yield: 0,75 g (27 %, as white powder)

¹H-NMR: δ (ppm) = 8,72 (4H, dd); 8,59 (2H, d); 7,74 (4H, dd); 3,65-2,90 (2H, m); 1,80-2,05 (4H, m); 1,35-1,60 (4H, m)

MS: m/z (%): 324 (6, M⁺); 218 (15); 202 (100); 123 (99); 106 (95); 78 (75); 51 (20)

TGA: 5 % mass loss at 350 °C

SDTA: T_m: 364 °C

Mp (MP90): T_m: 361 °C

IR: $\tilde{\nu}$ (cm⁻¹): 3312; 2947; 1640; 1529; 1490; 1412

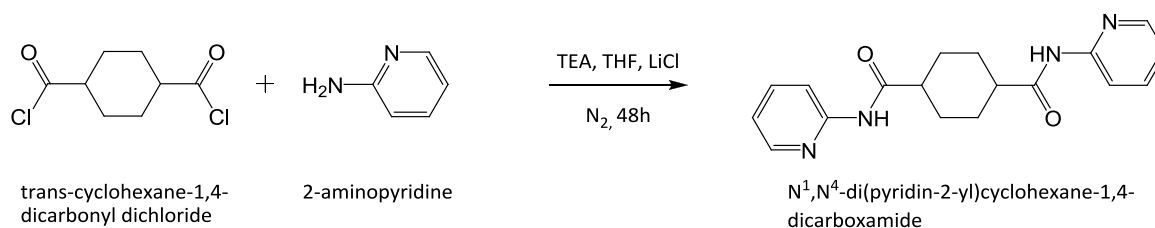
7.3.5 N¹,N⁴-Di(pyridin-2-yl)cyclohexane-1,4-dicarboxamide (BA 5)

Figure 155: Reaction of trans-cyclohexane-1,4-dicarbonyl dichloride with 2-aminopyridine.

Synthesis:

3 g (14,3 mmol) of trans-cyclohexane-1,4-dicarbonyl dichloride

2,97 g (31,0 mmol) of 2-aminopyridine

100 mL of THF (dried)

10 mL of triethylamine

LiCl

2-Aminopyridine, TEA and LiCl were mixed together with 100 mL of dried THF in a Schlenk flask. The acid chloride was then added under inert gas (N₂) and ice cooling. The reaction time was 48 hours at room temperature. The resulting reaction mixture was concentrated in a rotary evaporator and the crude product is extracted with 200 mL of methanol. For further purification, the solid was boiled in a mixture of NaOH/H₂O, subsequently filtered and dried yielding a white powder.

Characterization:

Yield: 0,92 g (20 %, as white powder)

¹H-NMR: δ (ppm) = 10,42 (2H, s); 8,26-8,34 (2H, m); 8,09 (2H, d); 7,70-7,80 (2H, m); 7,04-7,12 (2H, m); 2,51-2,55 (2H, m); 1,75-2,05 (4H, m); 1,30-1,60 (4H, m)

MS: m/z (%): 324 (94, M⁺); 203 (100); 185 (21); 149 (21); 121 (40); 95 (97); 78 (39)

TGA: 5 % mass loss at 307 °C

SDTA: T_m: 318 °C

Mp (MP90): T_m: 314 °C

IR: $\tilde{\nu}$ (cm⁻¹): 3238; 1669; 1575; 1529; 1433

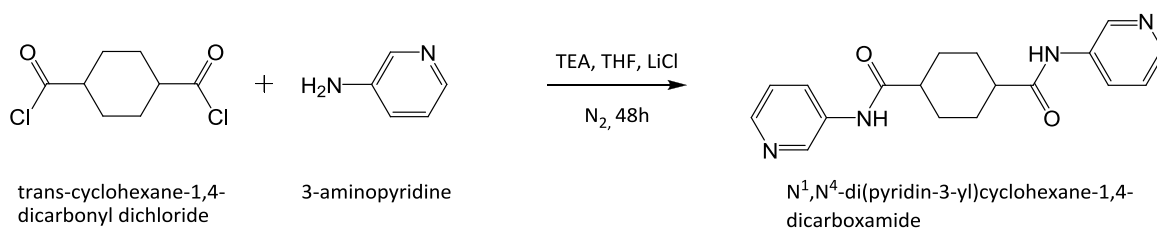
7.3.6 N¹,N⁴-Di(pyridin-3-yl)cyclohexane-1,4-dicarboxamide (BA 6)

Figure 156: Reaction of trans-cyclohexane-1,4-dicarbonyl dichloride with 3-aminopyridine.

Synthesis:

3 g (14,3 mmol) of trans-cyclohexane-1,4-dicarbonyl dichloride

2,97 g (31,0 mmol) of 3-aminopyridine

100 mL of THF (dried)

10 mL of triethylamine

LiCl

3-Aminopyridine, TEA and LiCl were mixed together with 100 mL of dried THF in a Schlenk flask. The acid chloride was then added under inert gas (N₂) and ice cooling. The reaction time was 48 hours. The resulting reaction mixture was concentrated in a rotary evaporator and the crude product was extracted with 200 mL of methanol. Since the product was not completely pure, this was subsequently extracted in acetone, yielding a white powder.

Characterization:

Yield: 3,01 g (64 %, as white powder)

¹H-NMR: δ (ppm) = 10,12 (2H, s); 8,76 (2H, d); 8,18-8,30 (2H, m); 7,98-8,10 (2H, m); 7,26-7,40 (2H, m); 2,26-2,46 (2H, m); 1,84-2,04 (4H, m); 1,38-1,60 (4H, m)

MS: m/z (%): 324 (88, M⁺); 231 (47); 203 (100); 149 (8); 121 (72); 95 (49); 81 (52)

TGA: 5 % mass loss at 307 °C

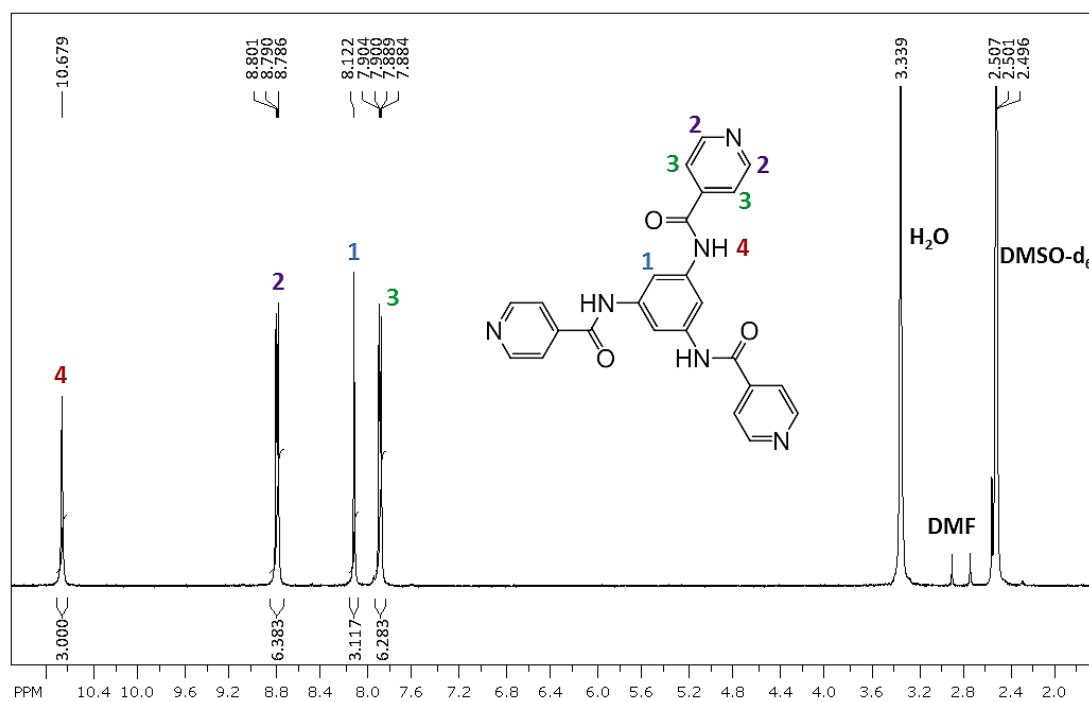
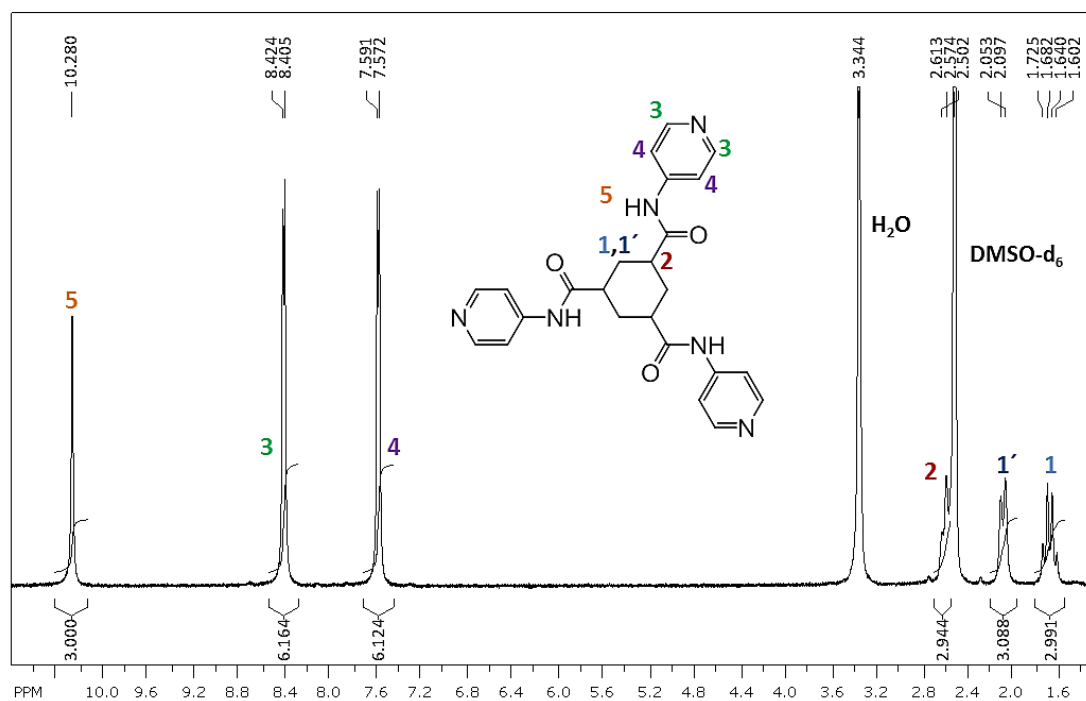
SDTA: T_m: 324 °C

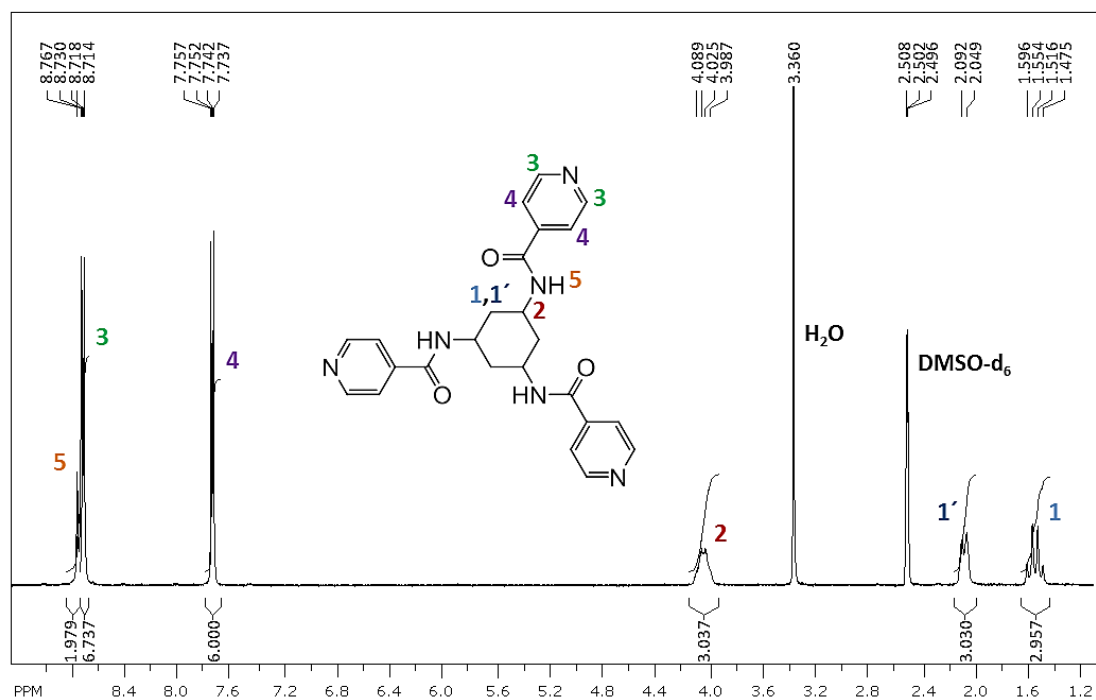
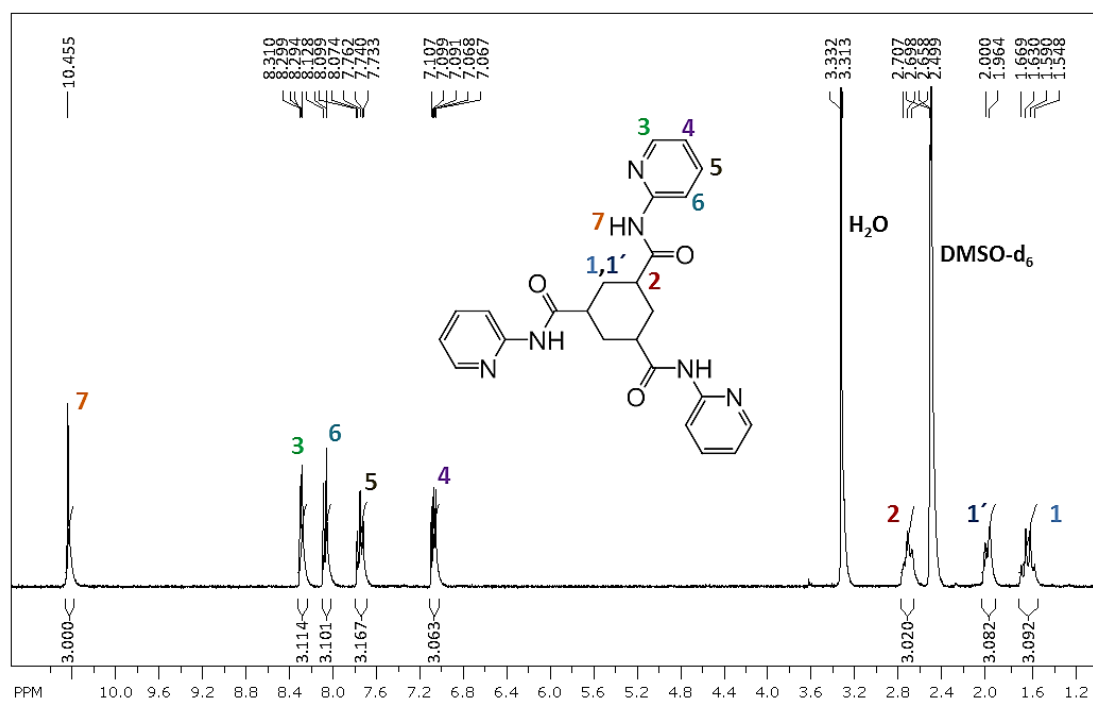
Mp (MP90): T_m: 293 °C

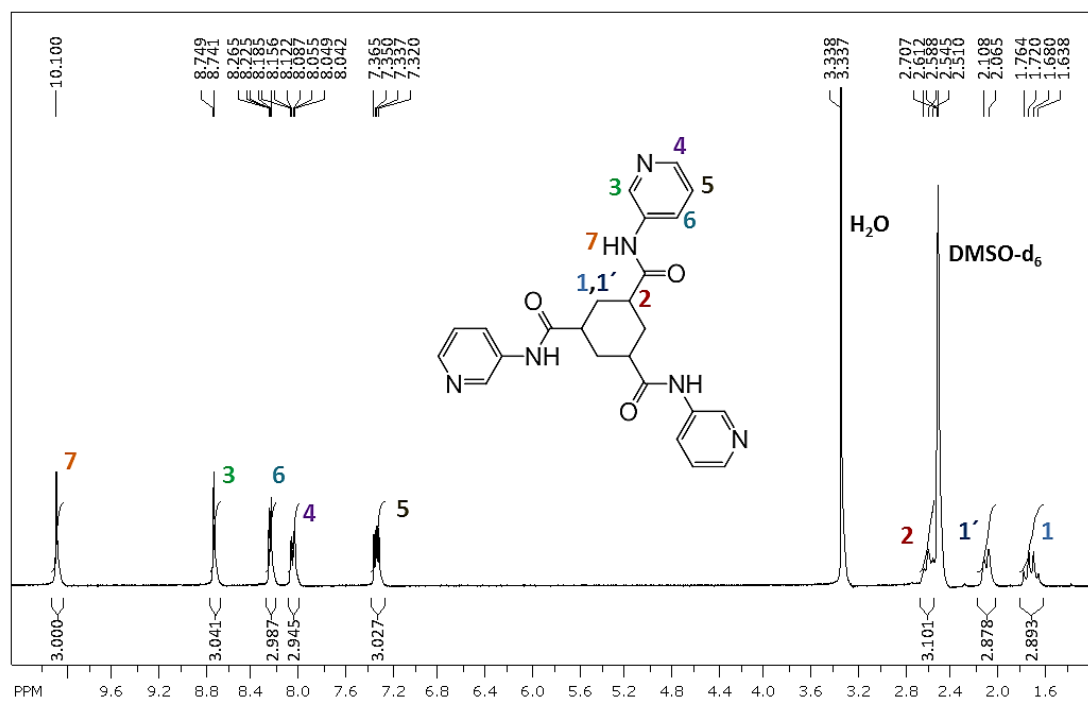
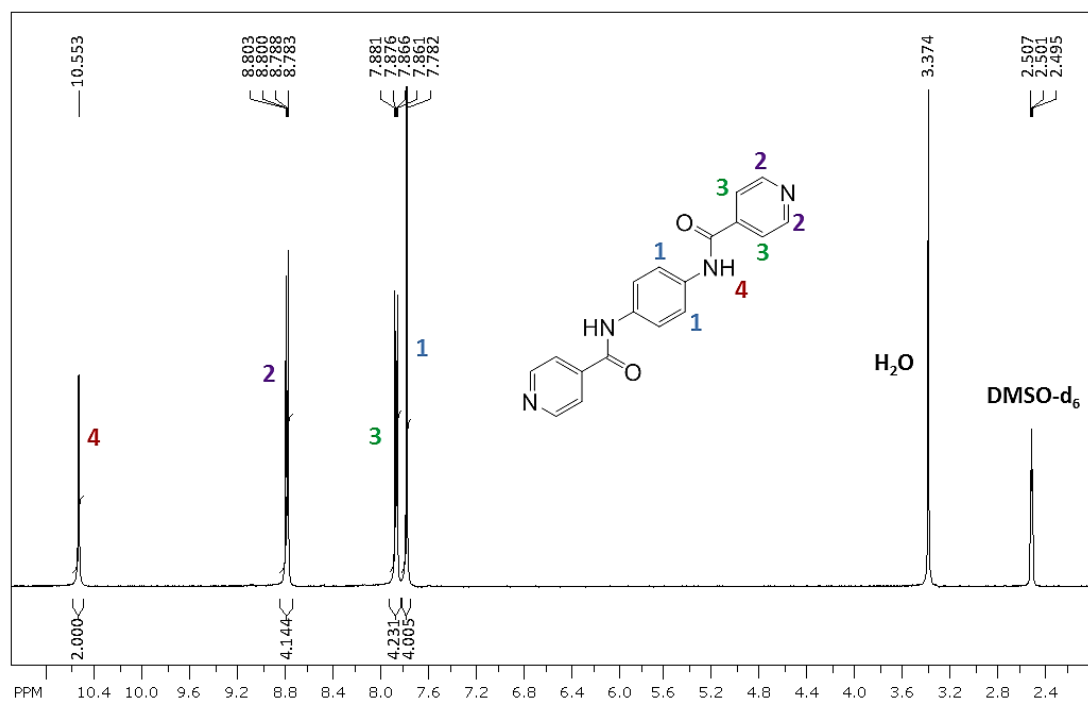
IR: $\tilde{\nu}$ (cm⁻¹): 1683; 1581; 1535; 1422

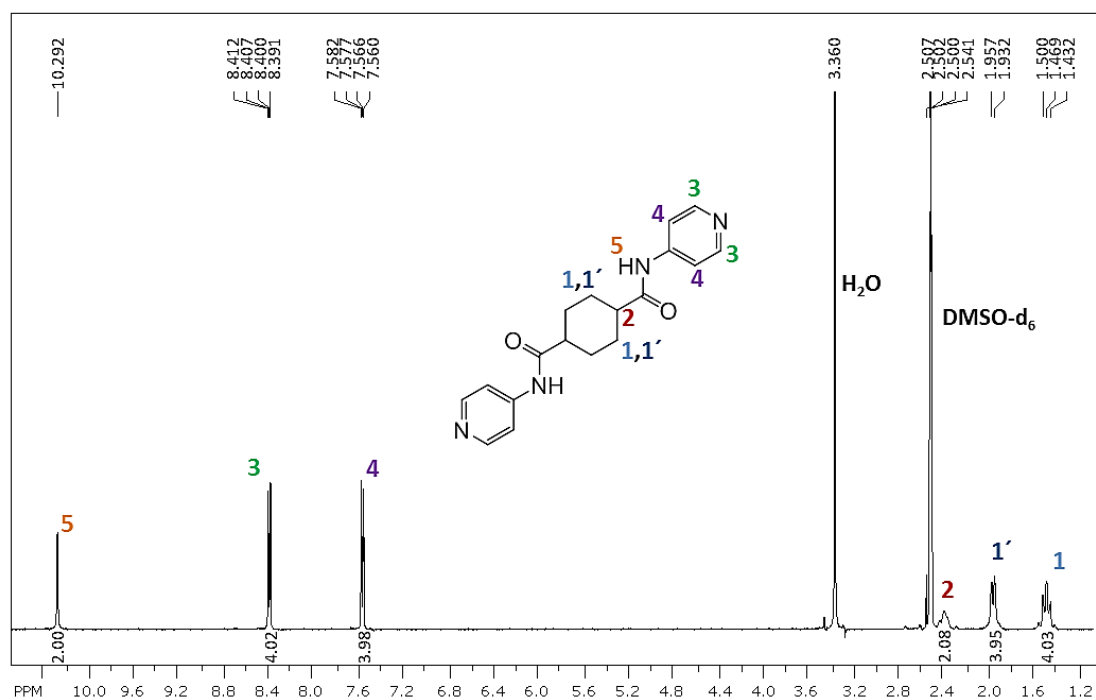
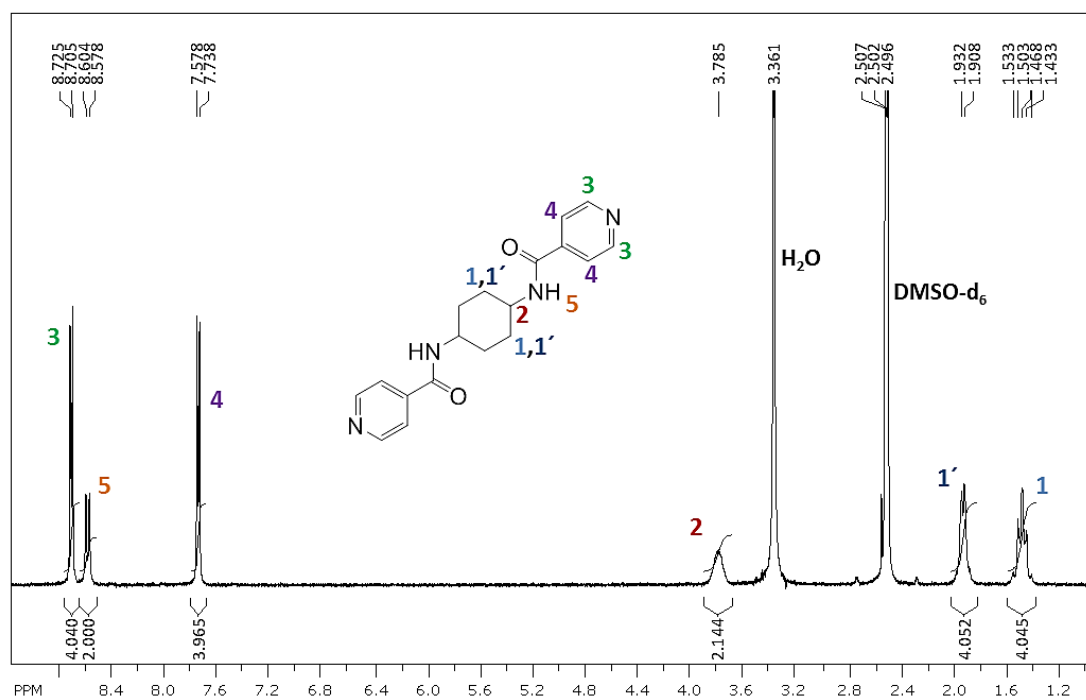


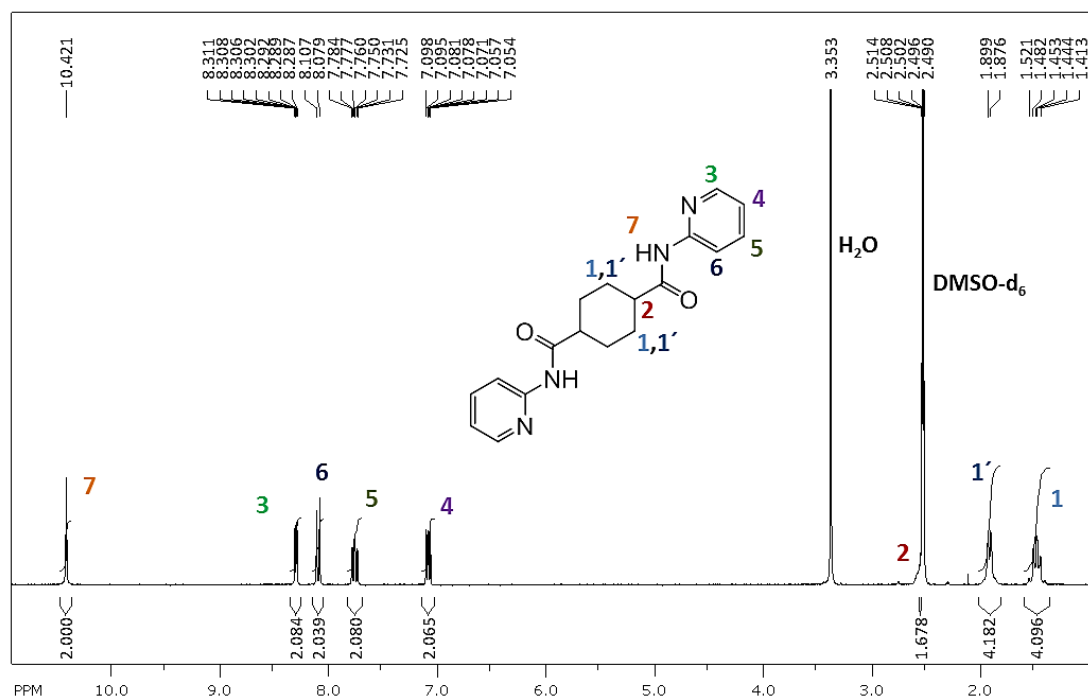
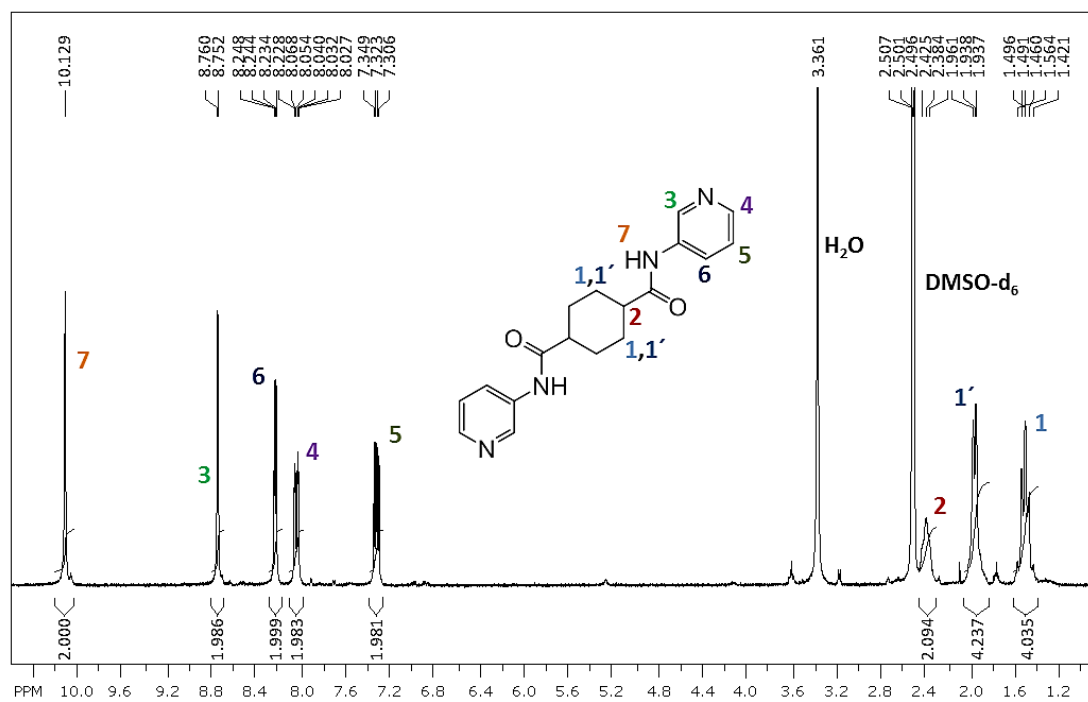
8 Appendix

8.1 $^1\text{H-NMR}$ spectra of bis- and trisamidesFigure 157: $^1\text{H-NMR}$ spectra of TA 2 in DMSO.Figure 158: $^1\text{H-NMR}$ spectra of TA 3 in DMSO.

Figure 159: ¹H-NMR spectra of TA 4 in DMSO.Figure 160: ¹H-NMR spectra of TA 5 in DMSO.

Figure 161: ¹H-NMR spectra of TA 6 in DMSO.Figure 162: ¹H-NMR spectra of BA 2 in DMSO.

Figure 163: $^1\text{H-NMR}$ spectra of BA 3 in DMSO.Figure 164: $^1\text{H-NMR}$ spectra of BA 4 in DMSO.

Figure 165: $^1\text{H-NMR}$ spectra of BA 5 in DMSO.Figure 166: $^1\text{H-NMR}$ spectra of BA 6 in DMSO.

8.2 Mass spectra of bis- and trisamides

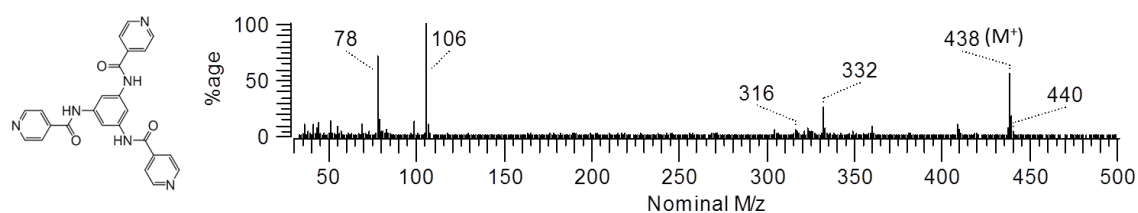


Figure 167: Mass spectra of TA 2.

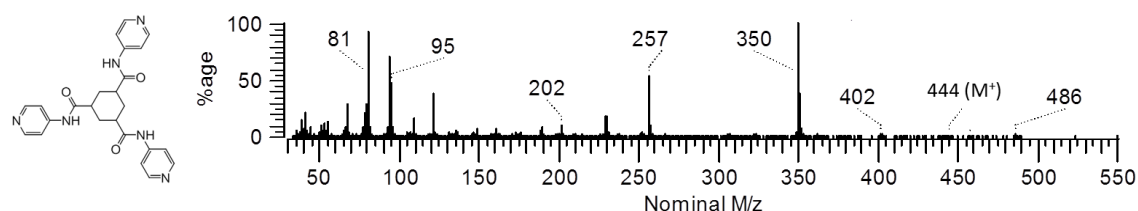


Figure 168: Mass spectra of TA 3.

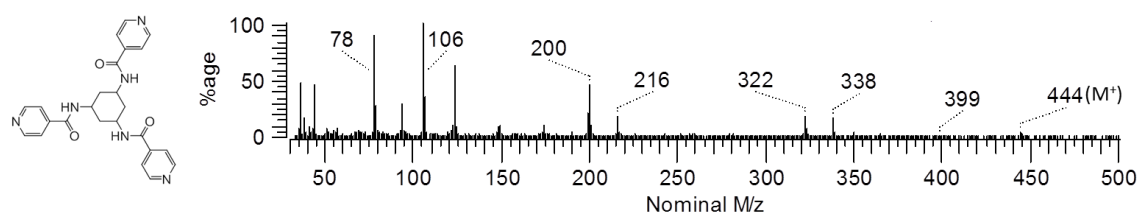


Figure 169: Mass spectra of TA 4.

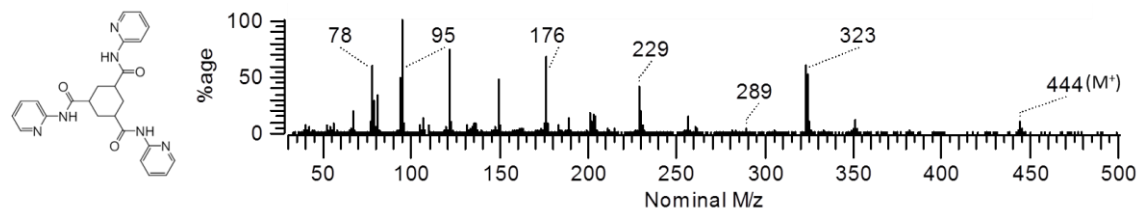


Figure 170: Mass spectra of TA 5.

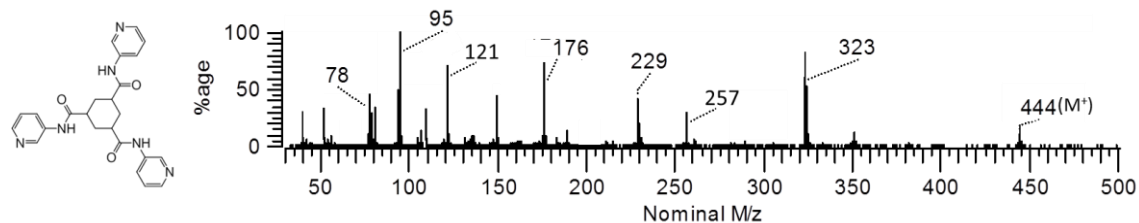


Figure 171: Mass spectra of TA 6.

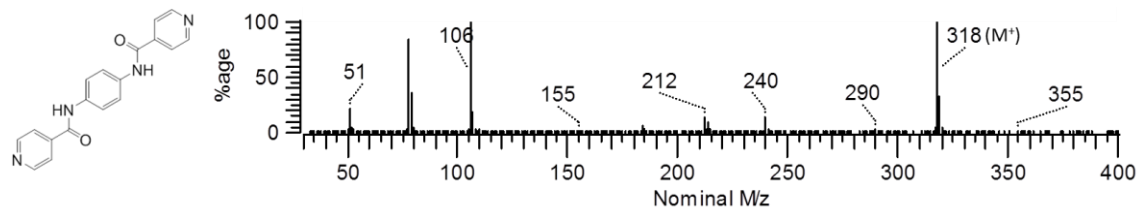


Figure 172: Mass spectra of BA 2.

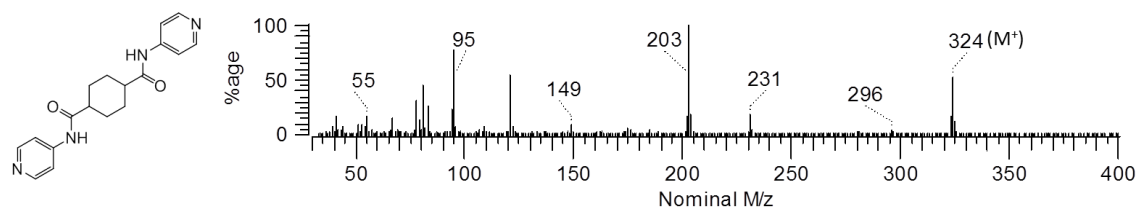


Figure 173: Mass spectra of BA 3.

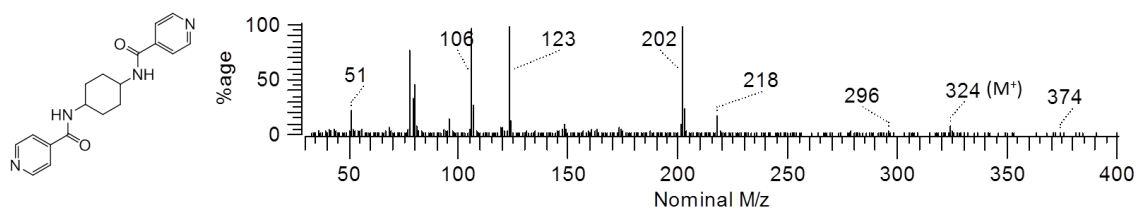


Figure 174: Mass spectra of BA 4.

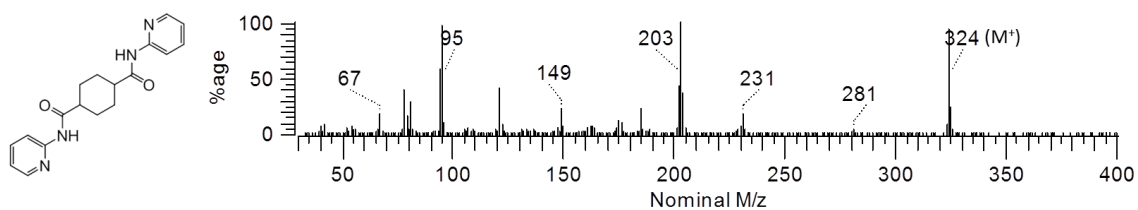


Figure 175: Mass spectra of BA 5.

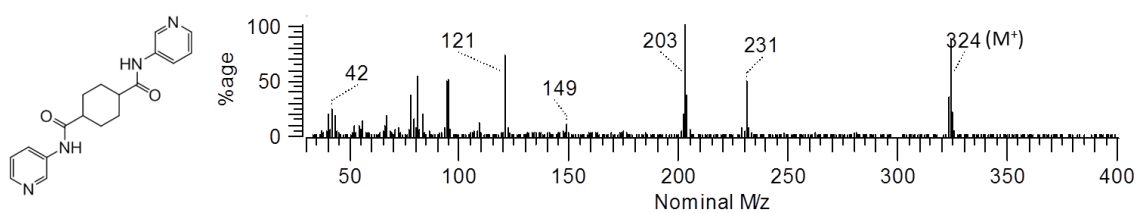


Figure 176: Mass spectra of BA 6.

8.3 Fourier-transform infrared spectra

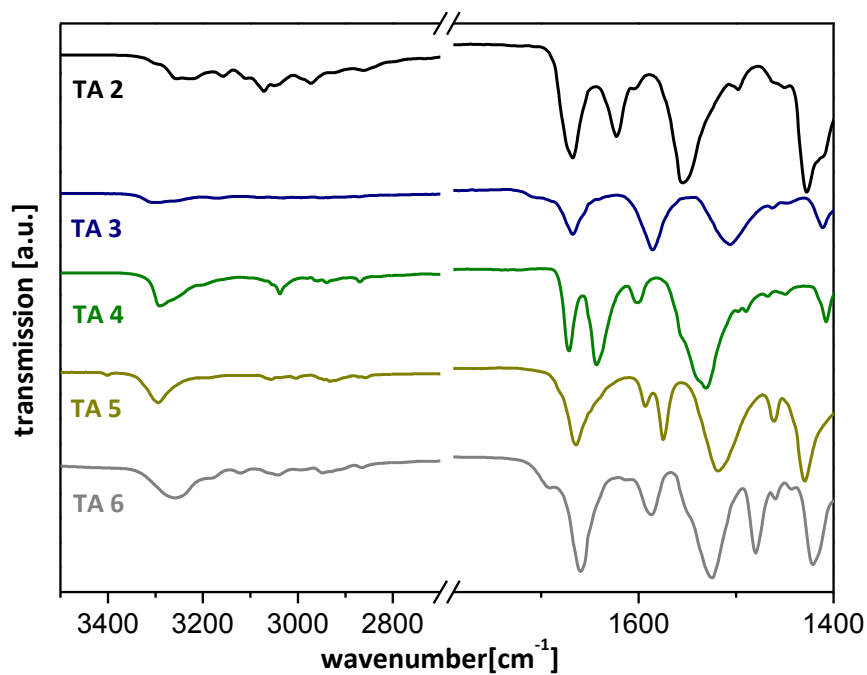


Figure 177: FT-IR spectra of TA 2 – TA 6 recorded with a Perkin Elmer Spectrum 100 FT-IR spectrometer in the range of 3500 cm^{-1} to 1400 cm^{-1} .

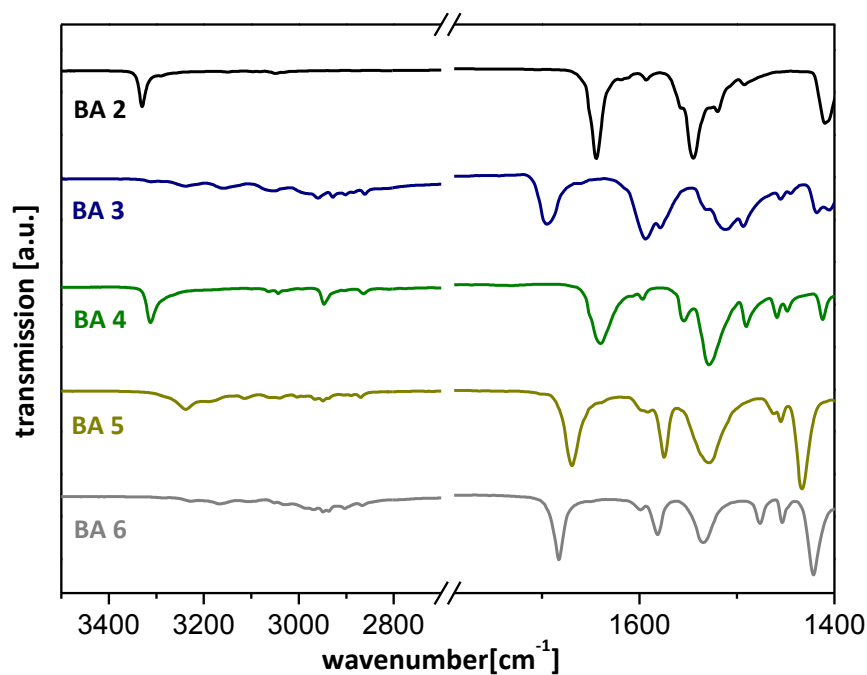


Figure 178: FT-IR spectra of BA 2 – BA 6 recorded with a Perkin Elmer Spectrum 100 FT-IR spectrometer in the range of 3500 cm^{-1} to 1400 cm^{-1} .

8.4 TGA and SDTA thermograms

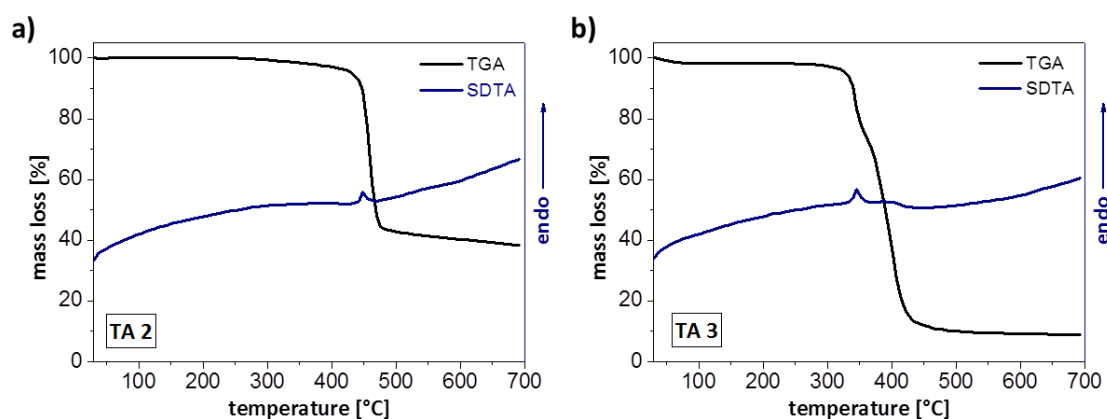


Figure 179: Thermograms of the thermogravimetric analysis (black) and the SDTA (blue) of TA 2 (a) and TA 3 (b). Data were recorded with a heating rate of $10 \text{ K}\cdot\text{min}^{-1}$ in the temperature range from $30 \text{ }^\circ\text{C}$ to $700 \text{ }^\circ\text{C}$ under nitrogen atmosphere.

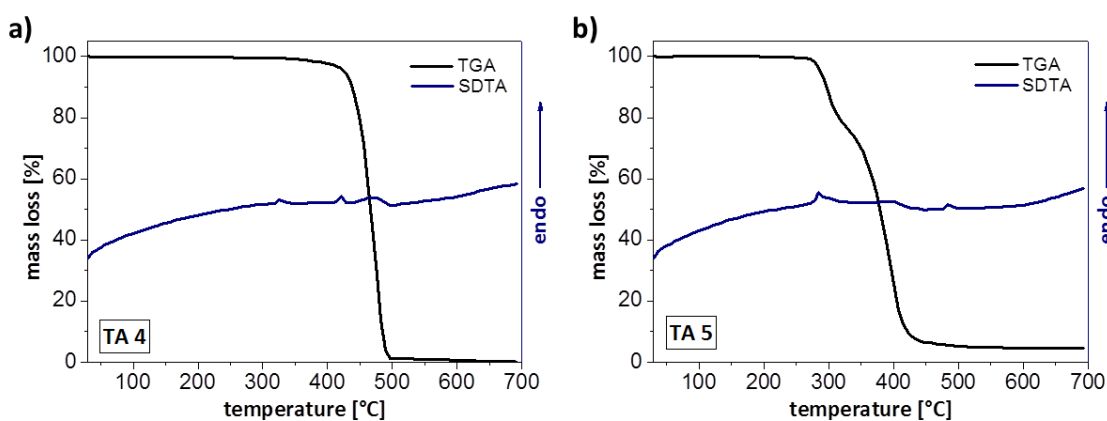


Figure 180: Thermograms of the thermogravimetric analysis (black) and the SDTA (blue) of TA 4 (a) and TA 5 (b). Data were recorded with a heating rate of $10 \text{ K}\cdot\text{min}^{-1}$ in the temperature range from $30 \text{ }^\circ\text{C}$ to $700 \text{ }^\circ\text{C}$ under nitrogen atmosphere.

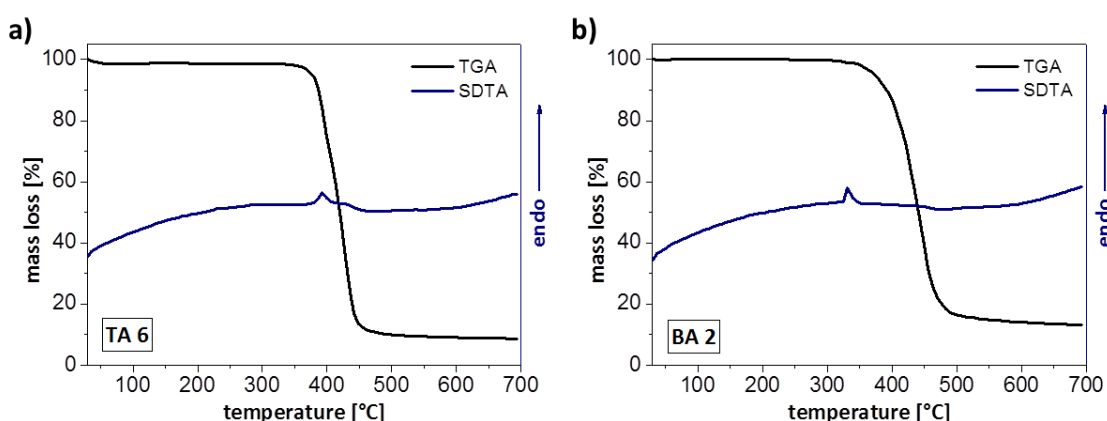


Figure 181: Thermograms of the thermogravimetric analysis (black) and the SDTA (blue) of TA 6 (a) and BA 2 (b). Data were recorded with a heating rate of $10 \text{ K}\cdot\text{min}^{-1}$ in the temperature range from $30 \text{ }^\circ\text{C}$ to $700 \text{ }^\circ\text{C}$ under nitrogen atmosphere.

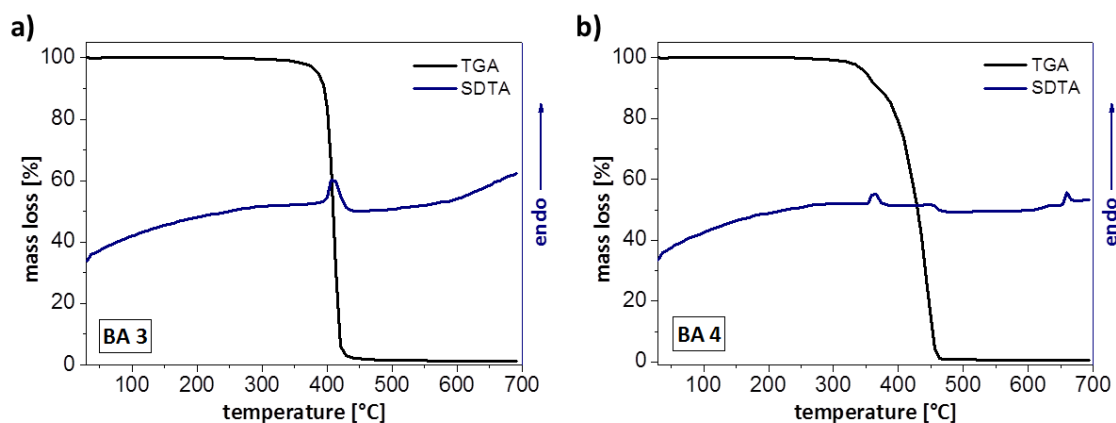


Figure 182: Thermograms of the thermogravimetric analysis (black) and the SDTA (blue) of BA 3 (a) and BA 4 (b). Data were recorded with a heating rate of $10 \text{ K}\cdot\text{min}^{-1}$ in the temperature range from $30 \text{ }^\circ\text{C}$ to $700 \text{ }^\circ\text{C}$ under nitrogen atmosphere.

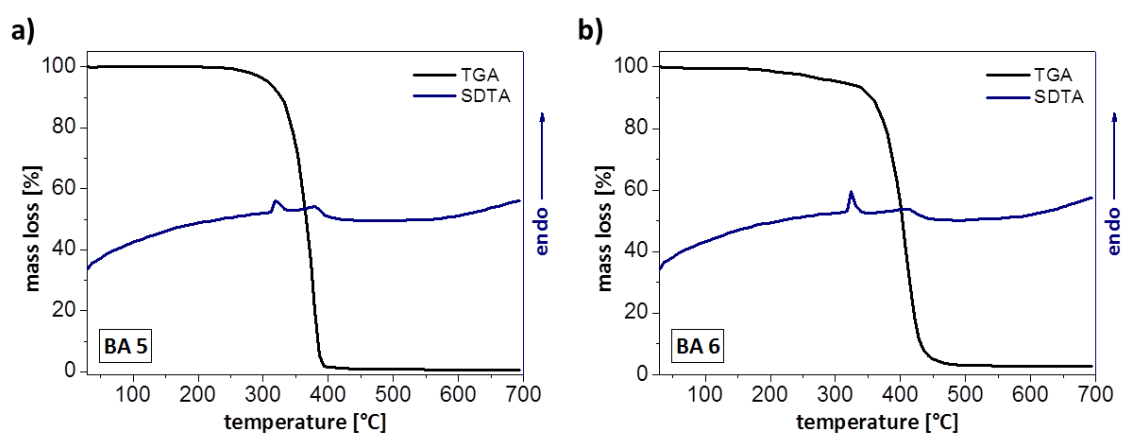


Figure 183: Thermograms of the thermogravimetric analysis (black) and the SDTA (blue) of BA 5 (a) and BA 6 (b). Data were recorded with a heating rate of $10 \text{ K}\cdot\text{min}^{-1}$ in the temperature range from $30 \text{ }^\circ\text{C}$ to $700 \text{ }^\circ\text{C}$ under nitrogen atmosphere.

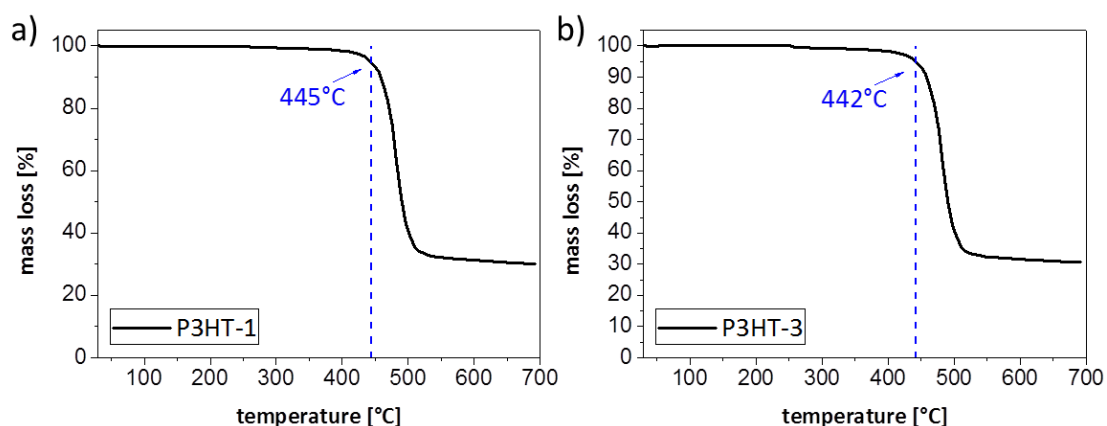


Figure 184: Thermogravimetric analysis thermograms of P3HT-1 (a) and P3HT-3 (b). TGA data were recorded with a heating rate of $10 \text{ K}\cdot\text{min}^{-1}$ in a temperature range from $30 \text{ }^\circ\text{C}$ to $700 \text{ }^\circ\text{C}$ under nitrogen atmosphere. The inserted dashed blue lines indicate 5 % mass loss up to the current temperature.

9 References

- (1) Troshin, P. A.; Sariciftci, N. S. *Supramolecular Chemistry for Organic Photovoltaics*; John Wiley & Sons, **2012**.
- (2) Bundesministerium für Wirtschaft und Energie (BMWi). Erneuerbare Energien in Zahlen: Nationale und internationale Entwicklung im Jahr 2015, **2015**.
- (3) Battaglia, C.; Cuevas, A.; Wolf, S. de. High-efficiency crystalline silicon solar cells: Status and perspectives. *Energy Environmental Science* **2016**, *9*, 1552–1576.
- (4) Shaheen, S. E.; Ginley, D. S.; Jabbour, G. E. Organic-Based Photovoltaics: Toward Low-Cost Power Generation. *MRS Bulletin* **2005**, *30*, 10–19.
- (5) Metz A. International Technology Roadmap for Photovoltaic: Results 2015, Seventh Edition, **2016**.
- (6) Heliatek GmbH. Press Release Heliatek WEF Technology Pioneer, **2015**.
- (7) Liao, H.-C.; Ho, C.-C.; Chang, C.-Y.; Jao, M.-H.; Darling, S. B.; Su, W.-F. Additives for morphology control in high-efficiency organic solar cells. *Materials Today* **2013**, *16*, 326–336.
- (8) Pivrikas, A.; Neugebauer, H.; Sariciftci, N. S. Influence of processing additives to nano-morphology and efficiency of bulk-heterojunction solar cells: A comparative review. *Solar Energy* **2011**, *85*, 1226–1237.
- (9) Chang, L.; Lademann, H. W. A.; Bonekamp, J.-B.; Meerholz, K.; Moulé, A. J. Effect of Trace Solvent on the Morphology of P3HT: PCBM Bulk Heterojunction Solar Cells. *Advanced Functional Materials* **2011**, *21*, 1779–1787.
- (10) Müller, C.; Bergqvist, J.; Vandewal, K.; Tvingstedt, K.; Anselmo, A. S.; Magnusson, R.; Alonso, M. I.; Moons, E.; Arwin, H.; Campoy-Quiles, M. *et al.* Phase behaviour of liquid-crystalline polymer/fullerene organic photovoltaic blends: Thermal stability and miscibility. *Journal of Materials Chemistry* **2011**, *21*, 10676.
- (11) Bull, T. A.; Pingree, L. S. C.; Jenekhe, S. A.; Ginger, D. S.; Luscombe, C. K. The role of mesoscopic PCBM crystallites in solvent vapor annealed copolymer solar cells. *ACS nano* **2009**, *3*, 627–636.
- (12) Søndergaard, R.; Hösel, M.; Angmo, D.; Larsen-Olsen, T. T.; Krebs, F. C. Roll-to-roll fabrication of polymer solar cells. *Materials Today* **2012**, *15*, 36–49.
- (13) Griffini, G.; Douglas, J. D.; Piliago, C.; Holcombe, T. W.; Turri, S.; Fréchet, J. M. J.; Mynar, J. L. Long-term thermal stability of high-efficiency polymer solar cells based on photocrosslinkable donor-acceptor conjugated polymers. *Advanced Materials* **2011**, *23*, 1660–1664.
- (14) Knauer, P. S. Crosslinkable low bandgap polymers for organic solar cells. Dissertation, Universität Bayreuth, **2016**.
- (15) Cheng, Y.-J.; Hsieh, C.-H.; Li, P.-J.; Hsu, C.-S. Morphological Stabilization by In Situ Polymerization of Fullerene Derivatives Leading to Efficient, Thermally Stable Organic Photovoltaics. *Advanced Functional Materials* **2011**, *21*, 1723–1732.
- (16) Lee, J. U.; Jung, J. W.; Emrick, T.; Russell, T. P.; Jo, W. H. Morphology control of a polythiophene-fullerene bulk heterojunction for enhancement of the high-temperature stability of solar cell performance by a new donor-acceptor diblock copolymer. *Nanotechnology* **2010**, *21*, 105201.

- (17) Lee, J. U.; Jung, J. W.; Emrick, T.; Russell, T. P.; Jo, W. H. Synthesis of C60-end capped P3HT and its application for high performance of P3HT/PCBM bulk heterojunction solar cells. *Journal of Materials Chemistry* **2010**, *20*, 3287.
- (18) Liu, H.-W.; Chang, D.-Y.; Chiu, W.-Y.; Rwei, S.-P.; Wang, L. Fullerene bisadduct as an effective phase-separation inhibitor in preparing poly(3-hexylthiophene)-[6,6]-phenyl-C61-butyric acid methyl ester blends with highly stable morphology. *Journal of Materials Chemistry* **2012**, *22*, 15586.
- (19) Bertho, S.; Haeldermans, I.; Swinnen, A.; Moons, W.; Martens, T.; Lutsen, L.; Vanderzande, D.; Manca, J.; Senes, A.; Bonfiglio, A. Influence of thermal ageing on the stability of polymer bulk heterojunction solar cells. *Solar Energy Materials and Solar Cells* **2007**, *91*, 385–389.
- (20) Zhang, Y.; Yip, H.-L.; Acton, O.; Hau, S. K.; Huang, F.; Jen, A. K.-Y. A Simple and Effective Way of Achieving Highly Efficient and Thermally Stable Bulk-Heterojunction Polymer Solar Cells Using Amorphous Fullerene Derivatives as Electron Acceptor. *Chemistry of Materials* **2009**, *21*, 2598–2600.
- (21) Padinger F., Rittberger S., Sariciftci N. Effects of Postproduction Treatment on Plastic Solar Cells. *Advanced Functional Materials* **2003**, 85–88.
- (22) Lindqvist, C.; Bergqvist, J.; Feng, C.-C.; Gustafsson, S.; Bäcke, O.; Treat, N. D.; Bounioux, C.; Henriksson, P.; Kroon, R.; Wang, E. *et al.* Fullerene Nucleating Agents: A Route Towards Thermally Stable Photovoltaic Blends. *Advanced Energy Materials* **2014**, *4*, 1301437.
- (23) Treat, N. D.; Nekuda Malik, J. A.; Reid, O.; Yu, L.; Shuttle, C. G.; Rumbles, G.; Hawker, C. J.; Chabiny, M. L.; Smith, P.; Stingelin, N. Microstructure formation in molecular and polymer semiconductors assisted by nucleation agents. *Nature materials* **2013**, *12*, 628–633.
- (24) Varga, J.; Mudra, I.; Ehrenstein, G. W. Highly active thermally stable [beta]-nucleating agents for isotactic polypropylene. *Journal of Applied Polymer Science* **1999**, *74*, 2357–2368.
- (25) Kim, Y. C.; Kim, C. Y.; Kim, S. C. Crystallization characteristics of isotactic polypropylene with and without nucleating agents. *Polymer Engineering & Science* **1991**, *31*, 1009–1014.
- (26) Kristiansen, M.; Werner, M.; Tervoort, T.; Smith, P.; Blomenhofer, M.; Schmidt, H.-W. The Binary System Isotactic Polypropylene/Bis(3,4-dimethylbenzylidene)sorbitol: Phase Behavior, Nucleation, and Optical Properties. *Macromolecules* **2003**, *36*, 5150–5156.
- (27) Blomenhofer, M.; Ganzleben, S.; Hanft, D.; Schmidt, H.-W.; Kristiansen, M.; Smith, P.; Stoll, K.; Mäder, D.; Hoffmann, K. “Designer” Nucleating Agents for Polypropylene. *Macromolecules* **2005**, *38*, 3688–3695.
- (28) Wang, H.; Li, C.-C.; Ke, Y.-C.; Zhang, D.; Li, Z.-Y. Effects of rosin-type clarifying agent on the crystallization and compatibility of polypropylene and low density polyethylene. *Journal of Applied Polymer Science* **2006**, *99*, 1568–1575.
- (29) Abraham, F.; Ganzleben, S.; Hanft, D.; Smith, P.; Schmidt, H.-W. Synthesis and Structure-Efficiency Relations of 1,3,5-Benzenetrisamides as Nucleating Agents and Clarifiers for Isotactic Poly(propylene). *Macromolecular Chemistry and Physics* **2010**, *211*, 171–181.
- (30) Zhang, X.; Zhang, D.; Liu, T. Influence of Nucleating Agent on Properties of Isotactic Polypropylene. *Energy Procedia* **2012**, *17*, 1829–1835.

- (31) Simanke, A. G.; Azeredo, A. P. d.; Lemos, C. d.; Mauler, R. S. Influence of nucleating agent on the crystallization kinetics and morphology of polypropylene. *Polímeros* **2016**, *26*, 152–160.
- (32) Lehn, J. M. Cryptates: Inclusion complexes of macropolycyclic receptor molecules. *Pure and Applied Chemistry* **1978**, *50*, 1.
- (33) Lehn, J.-M. Supramolecular Chemistry—Scope and Perspectives Molecules, Supermolecules, and Molecular Devices (Nobel Lecture). *Angewandte Chemie* **1988**, *27*, 89–112.
- (34) Vögtle, F. *Supramolekulare Chemie*; B. G. Teubner: Stuttgart, **1992**.
- (35) Varshey, D. B.; Sander, J. R. G.; Friscic, T.; MacGillivray L. R. *Supramolecular Interactions: Supramolecular Chemistry: From Molecules to Nanomaterials*; John Wiley & Sons, **2012**.
- (36) Lehn, J.-M. Perspectives in Supramolecular Chemistry—From Molecular Recognition towards Molecular Information Processing and Self-Organization. *Angewandte Chemie International Edition in English* **1990**, *29*, 1304–1319.
- (37) Lehn, J.-M. Supramolecular polymer chemistry - scope and perspectives. *Polymer International* **2002**, *51*, 825–839.
- (38) Lehn, J.-M. From supramolecular chemistry towards constitutional dynamic chemistry and adaptive chemistry. *Chemical Society reviews* **2007**, *36*, 151–160.
- (39) Fischer, E. Einfluss der Configuration auf die Wirkung der Enzyme. *Berichte der deutschen chemischen Gesellschaft* **1894**, 2985–2993.
- (40) Villiers, A.; Hebd, C. R. Sur la transformation de la fécula en dextrine par le ferment butyrique. *Comptes rendus de l'Académie des sciences* **1891**, 435–437.
- (41) Steed, J. W.; Gale, P. A. *Supramolecular chemistry: From molecules to nanomaterials*, 1st edition; Wiley: Hoboken, NJ, **2012**.
- (42) Vögtle, F.; Löhr, H.-G.; Franke, J.; Worsch, D. Host/Guest Chemistry of Organic Onium Compounds-Catharates, Crystalline Complexes, and Molecular Inclusion Compounds in Aqueous Solution. *Angewandte Chemie International Edition* **1985**, 727–742.
- (43) Gloe, K.; Heßke, H.; Lindoy L. F. Supramolekulare Chemie: Vom Einzelmolekül zur komplexen Funktionseinheit. *Wissenschaftliche Zeitung der Technischen Universität Dresden* **2007**, 32–38.
- (44) Stoddart, J. F.; Lindoy, L. F.; Atkinson, I. M. *Self Assembly in Supramolecular Systems*; Royal Society of Chemistry: Cambridge, **2000**.
- (45) Maitland, G. C. *Intermolecular forces: Their origin and determination*; Clarendon Press: Oxford, **1981**.
- (46) Alcock, N. *Bonding and structure: structural principles in inorganic and organic chemistry*; Ellis Horwood series in inorganic chemistry 1990: 1; Horwood: New York, **1990**.
- (47) Buckingham, A. D.; Legon, A. C.; Roberts, S. M. *Principles of Molecular Recognition*; Springer Netherlands: Dordrecht, **1993**.
- (48) Schalley, C. A. *Analytical methods in supramolecular chemistry*; Wiley-VCH: Weinheim, **2007**.
- (49) Steed, J. W.; Atwood, J. L. *Supramolecular chemistry*, 2nd edition; Wiley: Chichester, UK, **2009**.
- (50) McCord, P. *Inter- and intramolecular forces and their energy values*. <https://ch301.cm.utexas.edu/pdfs/im-forces.pdf> (accessed **March 14, 2019**).

9 References

- (51) Garratt, P. J.; Ibbett, A. J.; Ladbury, J. E.; O'Brien, R.; Hursthouse, M. B.; Abdul Malik, K. M. Molecular design using electrostatic interactions. 1. Synthesis and properties of flexible tripodand tri- and hexa-cations with restricted conformations. Molecular selection of ferricyanide from ferrocyanide. *Tetrahedron* **1998**, *54*, 949–968.
- (52) Ma, J. C.; Dougherty, D. A. The Cation– π Interaction. *Chemical reviews* **1997**, *97*, 1303–1324.
- (53) Anslyn, E. V.; Dougherty, D. A. *Modern physical chemistry*; University Science: Sausalito, California, **2004**.
- (54) Ilioudis, C. A.; Tocher, D. A.; Steed, J. W. A highly efficient, preorganized macrobicyclic receptor for halides based on CH- and NH-anion interactions. *Journal of the American Chemical Society* **2004**, *126*, 12395–12402.
- (55) Gamez, P. The anion– π interaction: Naissance and establishment of a peculiar supramolecular bond. *Inorganic Chemistry Frontiers* **2014**, *1*, 35–43.
- (56) Rosokha, Y. S.; Lindeman, S. V.; Rosokha, S. V.; Kochi, J. K. Halide recognition through diagnostic "anion- π " interactions: molecular complexes of Cl⁻, Br⁻, and I⁻ with olefinic and aromatic π receptors. *Angewandte Chemie International Edition* **2004**, *43*, 4650–4652.
- (57) Schottel, B. L.; Chifotides, H. T.; Shatruck, M.; Chouai, A.; Pérez, L. M.; Bacsá, J.; Dunbar, K. R. Anion- π interactions as controlling elements in self-assembly reactions of Ag(I) complexes with π -acidic aromatic rings. *Journal of the American Chemical Society* **2006**, *128*, 5895–5912.
- (58) Canceill, J.; Lacombe, L.; Collet, A. Water-soluble cryptophane binding lipophilic guests in aqueous solution. *Journal of the Chemical Society, Chemical Communications* **1987**, 219.
- (59) Morokuma, K. Why do molecules interact?: The origin of electron donor-acceptor complexes, hydrogen bonding and proton affinity. *Accounts of chemical research* **1977**, *10*, 294–300.
- (60) Muehldorf, A. V.; van Engen, D.; Warner, J. C.; Hamilton, A. D. Aromatic-aromatic interactions in molecular recognition: A family of artificial receptors for thymine that shows both face-to-face and edge-to-face orientations. *Journal of the American Chemical Society* **1988**, *110*, 6561–6562.
- (61) Hunter, C. A.; Sanders, J. K. M. The nature of π - π interactions. *Journal of the American Chemical Society* **1990**, *112*, 5525–5534.
- (62) Matthews, R. P.; Welton, T.; Hunt, P. A. Competitive π interactions and hydrogen bonding within imidazolium ionic liquids. *Physical chemistry chemical physics* **2014**, *16*, 3238–3253.
- (63) Jeffrey, G. A. *An introduction to hydrogen bonding*; Topics in physical chemistry; Oxford Univ. Press: New York, **1997**.
- (64) Pimentel, G.; McClellan, A. *Hydrogen bond*; Nabu Press, **1960**.
- (65) van Oss, C. J.; Absolom, D. R.; Neumann, A. W. Applications of net repulsive van der Waals forces between different particles, macromolecules, or biological cells in liquids. *Colloids and Surfaces* **1980**, *1*, 45–56.
- (66) Sethi, M. S.; Satake, M. *Chemical bonding*; Discovery Publishing House: New Delhi, **1992**.
- (67) Tschumper, G. S. *Reliable Electronic Structure Computations for Weak Noncovalent Interactions in Clusters* 26; John Wiley & Sons, Inc: Hoboken, NJ, **2008**.

- (68) Lehn, J.-M. Perspektiven der Supramolekularen Chemie – von der molekularen Erkennung zur molekularen Informationsverarbeitung und Selbstorganisation. *Angewandte Chemie* **1990**, *102*, 1347–1362.
- (69) Whitesides, G.; Mathias, J.; Seto, C. Molecular self-assembly and nanochemistry: A chemical strategy for the synthesis of nanostructures. *Science* **1991**, *254*, 1312–1319.
- (70) Yonath, A. Polar bears, antibiotics, and the evolving ribosome (Nobel Lecture). *Angewandte Chemie (International ed. in English)* **2010**, *49*, 4341–4354.
- (71) Barboiu, M.; Lehn, J.-M. Dynamic chemical devices: modulation of contraction/extension molecular motion by coupled-ion binding/pH change-induced structural switching. *Proceedings of the National Academy of Sciences of the United States of America* **2002**, *99*, 5201–5206.
- (72) Wang, Y.; Xu, H.; Zhang, X. Tuning the Amphiphilicity of Building Blocks: Controlled Self-Assembly and Disassembly for Functional Supramolecular Materials. *Adv. Mater.* **2009**, *21*, 2849–2864.
- (73) Schneider, H.-J.; Strongin, R. M. Supramolecular interactions in chemomechanical polymers. *Accounts of chemical research* **2009**, *42*, 1489–1500.
- (74) Ercole, F.; Davis, T. P.; Evans, R. A. Photo-responsive systems and biomaterials: Photochromic polymers, light-triggered self-assembly, surface modification, fluorescence modulation and beyond. *Polym. Chem.* **2010**, *1*, 37–54.
- (75) Fenske, T.; Korth, H.-G.; Mohr, A.; Schmuck, C. Advances in switchable supramolecular nanoassemblies. *Chemistry (Weinheim an der Bergstrasse, Germany)* **2012**, *18*, 738–755.
- (76) Maggini, L.; Bonifazi, D. Hierarchised luminescent organic architectures: design, synthesis, self-assembly, self-organisation and functions. *Chemical Society reviews* **2012**, *41*, 211–241.
- (77) Atwood, J. L.; Steed, J. W. *Encyclopedia of Supramolecular Chemistry*; CRC Press, **2004**.
- (78) Gautieri, A.; Vesentini, S.; Redaelli, A.; Buehler, M. J. Hierarchical structure and nanomechanics of collagen microfibrils from the atomistic scale up. *Nano letters* **2011**, *11*, 757–766.
- (79) JARVIS, M. C. Self-assembly of plant cell walls. *Plant Cell Environ* **1992**, *15*, 1–5.
- (80) Klug, A. The tobacco mosaic virus particle: structure and assembly. *Philosophical transactions of the Royal Society of London. Series B, Biological sciences* **1999**, *354*, 531–535.
- (81) Philp, D.; Stoddart, J. F. Self-Assembly in Natural and Unnatural Systems. *Angew. Chem. Int. Ed. Engl.* **1996**, *35*, 1154–1196.
- (82) L. F. Lindoy, I. M. Atkinson. Self-Assembly in Supramolecular Systems. In *Self Assembly in Supramolecular Systems*; Stoddart, J. F., Lindoy, L. F., Atkinson, I. M., Eds.; Royal Society of Chemistry: Cambridge, **2000**.
- (83) Whitesides, G. M.; Grzybowski, B. Self-assembly at all scales. *Science (New York, N.Y.)* **2002**, *295*, 2418–2421.
- (84) Shirakawa, H.; Louis, E. J.; MacDiarmid, A. G.; Chiang, C. K.; Heeger, A. J. Synthesis of electrically conducting organic polymers: Halogen derivatives of polyacetylene, (CH) *x*. *J. Chem. Soc., Chem. Commun.* **1977**, 578.

9 References

- (85) Sista, P.; Luscombe, C. K. Progress in the Synthesis of Poly (3-hexylthiophene). In *P3HT Revisited – From Molecular Scale to Solar Cell Devices*; Ludwigs, S., Ed.; Advances in Polymer Science; Springer Berlin Heidelberg: Berlin, Heidelberg, **2014**; pp 1–38.
- (86) Tourillon, G. Stability of Conducting Polythiophene and Derivatives. *J. Electrochem. Soc.* **1983**, *130*, 2042.
- (87) Yamamoto, T.; Sanechika, K.; Yamamoto, A. Preparation of thermostable and electric-conducting poly(2,5-thienylene). *J. Polym. Sci. B Polym. Lett. Ed.* **1980**, *18*, 9–12.
- (88) Yamamoto, T.; Sanechika, K.-i.; Yamamoto, A. Preparation and Characterization of Poly(thienylene)s. *BCSJ* **1983**, *56*, 1497–1502.
- (89) Sato, M.; Morii, H. Nuclear magnetic resonance studies on electrochemically prepared poly(3-dodecylthiophene). *Macromolecules* **1991**, *24*, 1196–1200.
- (90) McCullough, R. D.; Lowe, R. D. Enhanced electrical conductivity in regioselectively synthesized poly(3-alkylthiophenes). *J. Chem. Soc., Chem. Commun.* **1992**, 70.
- (91) Chen, T. A.; Rieke, R. D. The first regioregular head-to-tail poly(3-hexylthiophene-2,5-diyl) and a regiorandom isopolymer: Nickel versus palladium catalysis of 2(5)-bromo-5(2)-(bromozincio)-3-hexylthiophene polymerization. *J. Am. Chem. Soc.* **1992**, *114*, 10087–10088.
- (92) Loewe, R. S.; Khersonsky, S. M.; McCullough, R. D. A Simple Method to Prepare Head-to-Tail Coupled, Regioregular Poly(3-alkylthiophenes) Using Grignard Metathesis. *Adv. Mater.* **1999**, *11*, 250–253.
- (93) Miyakoshi, R.; Yokoyama, A.; Yokozawa, T. Catalyst-transfer polycondensation. mechanism of Ni-catalyzed chain-growth polymerization leading to well-defined poly(3-hexylthiophene). *Journal of the American Chemical Society* **2005**, *127*, 17542–17547.
- (94) Bronstein, H. A.; Luscombe, C. K. Externally initiated regioregular P3HT with controlled molecular weight and narrow polydispersity. *Journal of the American Chemical Society* **2009**, *131*, 12894–12895.
- (95) Roncali, J. Conjugated poly(thiophenes): Synthesis, functionalization, and applications. *Chem. Rev.* **1992**, *92*, 711–738.
- (96) Perepichka, I. F.; Perepichka, D. F.; Meng, H.; Wudl, F. Light-Emitting Polythiophenes. *Adv. Mater.* **2005**, *17*, 2281–2305.
- (97) Yamamoto, T. Molecular assembly and properties of polythiophenes. *NPG Asia Mater* **2010**, *2*, 54–60.
- (98) Okamoto, K.; Luscombe, C. K. Controlled polymerizations for the synthesis of semiconducting conjugated polymers. *Polym. Chem.* **2011**, *2*, 2424.
- (99) Sista, P.; Ghosh, K.; Martinez, J. S.; Rocha, R. C. Polythiophenes in Biological Applications. *j. nanosci. nanotech.* **2014**, *14*, 250–272.
- (100) Bhatt, M. P.; Magurudeniya, H. D.; Rainbolt, E. A.; Huang, P.; Dissanayake, D. S.; Biewer, M. C.; Stefan, M. C. Poly(3-Hexylthiophene) Nanostructured Materials for Organic Electronics Applications. *j. nanosci. nanotech.* **2014**, *14*, 1033–1050.
- (101) Snyder, C. R.; Henry, J. S.; DeLongchamp, D. M. Effect of Regioregularity on the Semicrystalline Structure of Poly(3-hexylthiophene). *Macromolecules* **2011**, *44*, 7088–7091.

- (102) Thurn-Albrecht, T.; Thomann, R.; Heinzl, T.; Hugger, S. Semicrystalline morphology in thin films of poly(3-hexylthiophene). *Colloid & Polymer Science* **2004**, *282*, 932–938.
- (103) Brinkmann, M.; Rannou, P. Effect of Molecular Weight on the Structure and Morphology of Oriented Thin Films of Regioregular Poly(3-hexylthiophene) Grown by Directional Epitaxial Solidification. *Adv. Funct. Mater.* **2007**, *17*, 101–108.
- (104) Wu, Z.; Petzold, A.; Henze, T.; Thurn-Albrecht, T.; Lohwasser, R. H.; Sommer, M.; Thelakkat, M. Temperature and Molecular Weight Dependent Hierarchical Equilibrium Structures in Semiconducting Poly(3-hexylthiophene). *Macromolecules* **2010**, *43*, 4646–4653.
- (105) Prosa, T. J.; Winokur, M. J.; Moulton, J.; Smith, P.; Heeger, A. J. X-ray structural studies of poly(3-alkylthiophenes): An example of an inverse comb. *Macromolecules* **1992**, *25*, 4364–4372.
- (106) Brinkmann, M.; Rannou, P. Molecular Weight Dependence of Chain Packing and Semicrystalline Structure in Oriented Films of Regioregular Poly(3-hexylthiophene) Revealed by High-Resolution Transmission Electron Microscopy. *Macromolecules* **2009**, *42*, 1125–1130.
- (107) Koch, F. P. V.; Heeney, M.; Smith, P. Thermal and structural characteristics of oligo(3-hexylthiophene)s (3HT)_n, n = 4–36. *Journal of the American Chemical Society* **2013**, *135*, 13699–13709.
- (108) Kim, D. H.; Han, J. T.; Park, Y. D.; Jang, Y.; Cho, J. H.; Hwang, M.; Cho, K. Single-Crystal Polythiophene Microwires Grown by Self-Assembly. *Adv. Mater.* **2006**, *18*, 719–723.
- (109) Rahimi, K.; Botiz, I.; Stingelin, N.; Kayunkid, N.; Sommer, M.; Koch, F. P. V.; Nguyen, H.; Coulembier, O.; Dubois, P.; Brinkmann, M. *et al.* Controllable processes for generating large single crystals of poly(3-hexylthiophene). *Angewandte Chemie (International ed. in English)* **2012**, *51*, 11131–11135.
- (110) Malik, S.; Nandi, A. K. Crystallization mechanism of regioregular poly(3-alkyl thiophene)s. *J. Polym. Sci. B Polym. Phys.* **2002**, *40*, 2073–2085.
- (111) Pascui, O. F.; Lohwasser, R.; Sommer, M.; Thelakkat, M.; Thurn-Albrecht, T.; Saalwächter, K. High Crystallinity and Nature of Crystal–Crystal Phase Transformations in Regioregular Poly(3-hexylthiophene). *Macromolecules* **2010**, *43*, 9401–9410.
- (112) Lee, C. S.; Dadmun, M. D. Important thermodynamic characteristics of poly(3-hexyl thiophene). *Polymer* **2014**, *55*, 4–7.
- (113) Brinkmann, M.; Hartmann, L.; Kayunkid, N.; Djurado, D. Understanding the Structure and Crystallization of Regioregular Poly(3-hexylthiophene) from the Perspective of Epitaxy. In *P3HT Revisited – From Molecular Scale to Solar Cell Devices*; Ludwigs, S., Ed.; Advances in Polymer Science; Springer Berlin Heidelberg: Berlin, Heidelberg, **2014**; pp 83–106.
- (114) Tremel, K.; Ludwigs, S. Morphology of P3HT in Thin Films in Relation to Optical and Electrical Properties. In *P3HT Revisited – From Molecular Scale to Solar Cell Devices*; Ludwigs, S., Ed.; Advances in Polymer Science; Springer Berlin Heidelberg: Berlin, Heidelberg, **2014**; pp 39–82.
- (115) Ihn, K. J.; Moulton, J.; Smith, P. Whiskers of poly(3-alkylthiophene)s. *J. Polym. Sci. B Polym. Phys.* **1993**, *31*, 735–742.
- (116) Liu, J.; Arif, M.; Zou, J.; Khondaker, S. I.; Zhai, L. Controlling Poly(3-hexylthiophene) Crystal Dimension: Nanowhiskers and Nanoribbons. *Macromolecules* **2009**, *42*, 9390–9393.

9 References

- (117) Kohn, P.; Rong, Z.; Scherer, K. H.; Sepe, A.; Sommer, M.; Müller-Buschbaum, P.; Friend, R. H.; Steiner, U.; Hüttner, S. Crystallization-Induced 10-nm Structure Formation in P3HT/PCBM Blends. *Macromolecules* **2013**, *46*, 4002–4013.
- (118) Brinkmann, M. Structure and morphology control in thin films of regioregular poly(3-hexylthiophene). *J. Polym. Sci. B Polym. Phys.* **2011**, *49*, 1218–1233.
- (119) Prosa, T. J.; Winokur, M. J.; McCullough, R. D. Evidence of a Novel Side Chain Structure in Regioregular Poly(3-alkylthiophenes). *Macromolecules* **1996**, *29*, 3654–3656.
- (120) Meille, S. V.; Romita, V.; Caronna, T.; Lovinger, A. J.; Catellani, M.; Belobrzeckaja, L. Influence of Molecular Weight and Regioregularity on the Polymorphic Behavior of Poly(3-decylthiophenes). *Macromolecules* **1997**, *30*, 7898–7905.
- (121) Koch, F. P. V.; Heeney, M.; Smith, P. Thermal and structural characteristics of oligo(3-hexylthiophene)s (3HT)_n, n = 4–36. *Journal of the American Chemical Society* **2013**, *135*, 13699–13709.
- (122) Cardona, C. M.; Li, W.; Kaifer, A. E.; Stockdale, D.; Bazan, G. C. Electrochemical considerations for determining absolute frontier orbital energy levels of conjugated polymers for solar cell applications. *Advanced materials (Deerfield Beach, Fla.)* **2011**, *23*, 2367–2371.
- (123) Trznadel; Pron; Zagorska; Chrzaszcz; Pielichowski. Effect of Molecular Weight on Spectroscopic and Spectroelectrochemical Properties of Regioregular Poly(3-hexylthiophene). *Macromolecules* **1998**, *31*, 5051–5058.
- (124) Skompska, M.; Szkurlat, A. The influence of the structural defects and microscopic aggregation of poly(3-alkylthiophenes) on electrochemical and optical properties of the polymer films: Discussion of an origin of redox peaks in the cyclic voltammograms. *Electrochimica Acta* **2001**, *46*, 4007–4015.
- (125) Dang, M. T.; Hirsch, L.; Wantz, G. P3HT: PCBM, Best Seller in Polymer Photovoltaic Research. *Adv. Mater.* **2011**, *23*, 3597–3602.
- (126) Brabec, C. J.; Dyakonov, V.; Parisi, J.; Sariciftci, N. S. *Organic Photovoltaics*; Springer Berlin Heidelberg: Berlin, Heidelberg, **2003**.
- (127) Dennler, G.; Scharber, M. C.; Brabec, C. J. Polymer-Fullerene Bulk-Heterojunction Solar Cells. *Adv. Mater.* **2009**, *21*, 1323–1338.
- (128) Proctor, C. M.; Kuik, M.; Nguyen, T.-Q. Charge carrier recombination in organic solar cells. *Progress in Polymer Science* **2013**, *38*, 1941–1960.
- (129) Brabec, C. J.; Heeney, M.; McCulloch, I.; Nelson, J. Influence of blend microstructure on bulk heterojunction organic photovoltaic performance. *Chemical Society reviews* **2011**, *40*, 1185–1199.
- (130) Elsenbaumer, R. L.; Jen, K. Y.; Oboodi, R. Processible and environmentally stable conducting polymers. *Synthetic Metals* **1986**, *15*, 169–174.
- (131) Nekuda Malik, J. A.; Treat, N. D.; Abdelsamie, M.; Yu, L.; Li, R.; Smilgies, D.-M.; Amassian, A.; Hawker, C. J.; Chabynyc, M. L.; Stingelin, N. Controlling the Solidification of Organic Photovoltaic Blends with Nucleating Agents. *Organic Photonics and Photovoltaics* **2014**, *2*, DOI: 10.2478/oph-2014-0006.

- (132) Sharenko, A.; Treat, N. D.; Love, J. A.; Toney, M. F.; Stingelin, N.; Nguyen, T.-Q. Use of a commercially available nucleating agent to control the morphological development of solution-processed small molecule bulk heterojunction organic solar cells. *J. Mater. Chem. A* **2014**, *2*, 15717–15721.
- (133) Amos, S. E. *Plastics additives handbook*, 6. ed.; Hanser: Munich, Cincinnati, Ohio, **2009**.
- (134) Sperling, L. H. *Introduction to physical polymer science*, Fourth edition; Wiley: Hoboken, N.J., **2006**.
- (135) Milner, S. T. Polymer crystal–melt interfaces and nucleation in polyethylene. *Soft matter* **2011**, *7*, 2909.
- (136) Lechner, M. D.; Gehrke, K.; Nordmeier, E. H. *Makromolekulare Chemie: Ein Lehrbuch für Chemiker, Physiker, Materialwissenschaftler und Verfahrenstechniker*, 5. Aufl. 2014; SpringerLink : Bücher; Springer Spektrum: Berlin, Heidelberg, **2014**.
- (137) Menges, G.; Michaeli, W.; Haberstroh, E.; Schmachtenberg, E. *Menges Werkstoffkunde Kunststoffe*, 6. Aufl.; Hanser: München, **2011**.
- (138) Costantino, A.; Pettarin, V.; Viana, J.; Pontes, A.; Pouzada, A.; Frontini, P. Microstructure of PP/clay Nanocomposites Produced by Shear Induced Injection Moulding. *Procedia Materials Science* **2012**, *1*, 34–43.
- (139) Schmidt, H.-W.; Blomenhofer, M.; Stoll, K.; Meier, H. Resin compositions with reduced haze containing amide compounds as nucleating agents. Patent: WO 2004072168.
- (140) G.H. Meeten. *Optical properties of polymers*; Elsevier Applied Science: London, **op. 1986**.
- (141) Hoffmann, K.; Huber, G.; Mäder, D. Nucleating and clarifying agents for polyolefins. *Macromol. Symp.* **2001**, *176*, 83–92.
- (142) Kersch, M.; Pischke, L.; Schmidt, H.-W.; Altstädt, V. Influence of trisamide-based additives on the morphological and mechanical properties of isotactic polypropylene. *Polymer* **2014**, *55*, 3227–3233.
- (143) M. Blomenhofer. *Nukleierungsmittel und Clarifier für isotaktisches Polypropylen auf Basis von 1,3,5-Benzoltricarbonsäureamiden, 5-Aminoisophthalamiden und 3,5-Diaminobenzamiden*, **2003**.
- (144) Ferrage, E.; Martin, F.; Boudet, A.; Petit, S.; Forty, G.; Jouffret, F.; Micoud, P.; Parseval, P. de; Salvi, S.; Bourgerette, C. *et al.* Talc as nucleating agent of polypropylene: morphology induced by lamellar particles addition and interface mineral-matrix modelization. *Journal of Materials Science* **2002**, 1561–1573.
- (145) Hosier, I. L.; Alamo, R. G.; Lin, J. S. Lamellar morphology of random metallocene propylene copolymers studied by atomic force microscopy. *Polymer* **2004**, *45*, 3441–3455.
- (146) Poon, B.; Rogunova, M.; Chum, S. P.; Hiltner, A.; Baer, E. Classification of homogeneous copolymers of propylene and 1-octene based on comonomer content. *Journal of Polymer Science Part B: Polymer Physics* **2004**, *42*, 4357–4370.
- (147) Shakoar, A.; Thomas, N. L. Talc as a nucleating agent and reinforcing filler in poly(lactic acid) composites. *Polymer Engineering & Science* **2014**, *54*, 64–70.
- (148) Yang, J.; Huang, L.; Zhang, Y.; Chen, F.; Fan, P.; Zhong, M.; Yeh, S. A New Promising Nucleating Agent for Polymer Foaming: Applications of Ordered Mesoporous Silica Particles in Polymethyl Methacrylate Supercritical Carbon Dioxide Microcellular Foaming. *Industrial & Engineering Chemistry Research* **2013**, *52*, 14169–14178.

- (149) Ou, C. F.; Ho, M. T.; Lin, J. R. The Nucleating Effect of Montmorillonite on Crystallization of PET/Montmorillonite Nanocomposite. *Journal of Polymer Research* **2003**, *10*, 127–132.
- (150) Stein, R. S.; Misra, A.; Yuasa, T.; Khambatta, F. Recent studies of light scattering from polymer films. *Pure and Applied Chemistry* **1977**, *49*, 915–928.
- (151) Beck, H. N.; Ledbetter, H. D. DTA study of heterogeneous nucleation of crystallization in polypropylene. *Journal of Applied Polymer Science* **1965**, *9*, 2131–2142.
- (152) Beck, H. N. Heterogeneous nucleating agents for polypropylene crystallization. *Journal of Applied Polymer Science* **1967**, *11*, 673–685.
- (153) Zhao, Y.; Vaughan, A. S.; Sutton, S. J.; Swingler, S. G. On the crystallization, morphology and physical properties of a clarified propylene/ethylene copolymer. *Polymer* **2001**, *42*, 6587–6597.
- (154) Schmidt, H.-W.; Smith, P.; Blomenhofer, M. Polypropylene resin compositions, trimesic acid derivatives and their preparation. Patent: WO 2002046300.
- (155) Maeder, D.; Hoffmann, K.; Schmidt, H.-W. α -Nucleating agents for crystalline polypropylenes containing β -form crystals. Patent: WO 2003102069.
- (156) Shepard, T. A.; Delsorbo, C. R.; Louth, R. M.; Walborn, J. L.; Norman, D. A.; Harvey, N. G.; Spontak, R. J. Self-organization and polyolefin nucleation efficacy of 1,3:2,4-di-p-methylbenzylidene sorbitol. *Journal of Polymer Science Part B: Polymer Physics* **1997**, *35*, 2617–2628.
- (157) Libster, D.; Aserin, A.; Garti, N. Advanced nucleating agents for polypropylene. *Polymers for Advanced Technologies* **2007**, *18*, 685–695.
- (158) Thierry, A.; Straupé, C.; Wittmann, J.-C.; Lotz, B. Organogelators and Polymer Crystallisation. *Macromol. Symp.* **2006**, *241*, 103–110.
- (159) Wunderlich, B. *Thermal analysis of polymeric materials*; Springer: Berlin, **2005**.
- (160) F. Richter. *Supramolecular polymer additives to improve the crystallization behavior and optical properties of polybutylene terephthalate and polyamides*, **2013**.
- (161) Fillon, B.; Wittmann, J. C.; Lotz, B.; Thierry, A. Self-nucleation and recrystallization of isotactic polypropylene (α phase) investigated by differential scanning calorimetry. *J. Polym. Sci. B Polym. Phys.* **1993**, *31*, 1383–1393.
- (162) Fillon, B.; Lotz, B.; Thierry, A.; Wittmann, J. C. Self-nucleation and enhanced nucleation of polymers. Definition of a convenient calorimetric “efficiency scale” and evaluation of nucleating additives in isotactic polypropylene (α phase). *J. Polym. Sci. B Polym. Phys.* **1993**, *31*, 1395–1405.
- (163) Brinkmann, M.; Wittmann, J.-C. Orientation of Regioregular Poly(3-hexylthiophene) by Directional Solidification: A Simple Method to Reveal the Semicrystalline Structure of a Conjugated Polymer. *Adv. Mater.* **2006**, *18*, 860–863.
- (164) Liu, J.; Zou, J.; Zhai, L. Bottom-up Assembly of Poly(3-hexylthiophene) on Carbon Nanotubes: 2D Building Blocks for Nanoscale Circuits. *Macromolecular rapid communications* **2009**, *30*, 1387–1391.
- (165) Brédas, J.-L.; Beljonne, D.; Coropceanu, V.; Cornil, J. Charge-transfer and energy-transfer processes in pi-conjugated oligomers and polymers: a molecular picture. *Chemical reviews* **2004**, *104*, 4971–5004.

- (166) Haedler, A. T.; Kreger, K.; Issac, A.; Wittmann, B.; Kivala, M.; Hammer, N.; Köhler, J.; Schmidt, H.-W.; Hildner, R. Long-range energy transport in single supramolecular nanofibres at room temperature. *Nature* **2015**, *523*, 196–199.
- (167) Matsunaga, Y.; Miyajima, N.; Nakayasu, Y.; Sakai, S.; Yonenaga, M. Design of Novel Mesomorphic Compounds: N, N', N''-Trialkyl-1,3,5-benzenetricarboxamides. *BCSJ* **1988**, *61*, 207–210.
- (168) Lightfoot, M. P.; Mair, F. S.; Pritchard, R. G.; Warren, J. E. New supramolecular packing motifs: Π -stacked rods encased in triply-helical hydrogen bonded amide strands. *Chem. Commun.* **1999**, 1945–1946.
- (169) Kristiansen, M.; Smith, P.; Chanzy, H.; Baerlocher, C.; Gramlich, V.; McCusker, L.; Weber, T.; Pattison, P.; Blomenhofer, M.; Schmidt, H.-W. Structural Aspects of 1,3,5-Benzenetrisamides—A New Family of Nucleating Agents. *Crystal Growth & Design* **2009**, *9*, 2556–2558.
- (170) Cantekin, S.; de Greef, Tom F A; Palmans, A. R. A. Benzene-1,3,5-tricarboxamide: a versatile ordering moiety for supramolecular chemistry. *Chemical Society reviews* **2012**, *41*, 6125–6137.
- (171) Du, X.; Zhou, J.; Shi, J.; Xu, B. Supramolecular Hydrogelators and Hydrogels: From Soft Matter to Molecular Biomaterials. *Chemical reviews* **2015**, *115*, 13165–13307.
- (172) Fan, E.; Yang, J.; Geib, S. J.; Stoner, T. C.; Hopkins, M. D.; Hamilton, A. D. Hydrogen-bonding control of molecular aggregation: Self-complementary subunits lead to rod-shaped structures in the solid state. *J. Chem. Soc., Chem. Commun.* **1995**, 1251.
- (173) Sakamoto, A.; Ogata, D.; Shikata, T.; Hanabusa, K. Controlled Large Macrodipoles in a Supramolecular Polymer of Tri-3,7-dimethyloctyl- cis -1,3,5-cyclohexanetricarboxamide in n -Decane. *Macromolecules* **2005**, *38*, 8983–8986.
- (174) García, F.; Korevaar, P. A.; Verlee, A.; Meijer, E. W.; Palmans, A. R. A.; Sánchez, L. The influence of π -conjugated moieties on the thermodynamics of cooperatively self-assembling tricarboxamides. *Chemical communications (Cambridge, England)* **2013**, *49*, 8674–8676.
- (175) Bernet, A.; Albuquerque, R. Q.; Behr, M.; Hoffmann, S. T.; Schmidt, H.-W. Formation of a supramolecular chromophore: A spectroscopic and theoretical study. *Soft matter* **2012**, *8*, 66–69.
- (176) Liu, G.-F.; Zhu, L.-Y.; Ji, W.; Feng, C.-L.; Wei, Z.-X. Inversion of the Supramolecular Chirality of Nanofibrous Structures through Co-Assembly with Achiral Molecules. *Angewandte Chemie (International ed. in English)* **2016**, *55*, 2411–2415.
- (177) Smulders, M. M. J.; Filot, I. A. W.; Leenders, J. M. A.; van der Schoot, P.; Palmans, A. R. A.; Schenning, Albertus P H J; Meijer, E. W. Tuning the extent of chiral amplification by temperature in a dynamic supramolecular polymer. *Journal of the American Chemical Society* **2010**, *132*, 611–619.
- (178) Ishioka, Y.; Minakuchi, N.; Mizuhata, M.; Maruyama, T. Supramolecular gelators based on benzenetricarboxamides for ionic liquids. *Soft matter* **2014**, *10*, 965–971.
- (179) Zhou, Y.; Xu, M.; Yi, T.; Xiao, S.; Zhou, Z.; Li, F.; Huang, C. Morphology-tunable and photoresponsive properties in a self-assembled two-component gel system. *Langmuir : the ACS journal of surfaces and colloids* **2007**, *23*, 202–208.
- (180) Camerel, F.; Faul, C. F. J. Combination of ionic self-assembly and hydrogen bonding as a tool for the synthesis of liquid-crystalline materials and organogelators from a simple building blockElectronic

supplementary information (ESI) available: IR, NMR, DSC and TGA data of the organic core and complexes. See <http://www.rsc.org/suppdata/cc/b3/b303552b>. *Chem. Commun.* **2003**, 1958.

(181) Misslitz, H.; Kreger, K.; Schmidt, H.-W. Supramolecular nanofiber webs in nonwoven scaffolds as potential filter media. *Small (Weinheim an der Bergstrasse, Germany)* **2013**, *9*, 2053–8, 2025.

(182) Weiss, D.; Skrybeck, D.; Misslitz, H.; Nardini, D.; Kern, A.; Kreger, K.; Schmidt, H.-W. Tailoring Supramolecular Nanofibers for Air Filtration Applications. *ACS applied materials & interfaces* **2016**, *8*, 14885–14892.

(183) Kluge, D.; Abraham, F.; Schmidt, S.; Schmidt, H.-W.; Fery, A. Nanomechanical properties of supramolecular self-assembled whiskers determined by AFM force mapping. *Langmuir : the ACS journal of surfaces and colloids* **2010**, *26*, 3020–3023.

(184) Kluge, D.; Singer, J. C.; Neubauer, J. W.; Abraham, F.; Schmidt, H.-W.; Fery, A. Influence of the molecular structure and morphology of self-assembled 1,3,5-benzenetrisamide nanofibers on their mechanical properties. *Small (Weinheim an der Bergstrasse, Germany)* **2012**, *8*, 2563–2570.

(185) Kreger, K.; Wolfer, P.; Audorff, H.; Kador, L.; Stingelin-Stutzmann, N.; Smith, P.; Schmidt, H.-W. Stable holographic gratings with small-molecular trisazobenzene derivatives. *Journal of the American Chemical Society* **2010**, *132*, 509–516.

(186) Probst, C.; Meichner, C.; Audorff, H.; Walker, R.; Kreger, K.; Kador, L.; Schmidt, H.-W. Improving holographic writing performance of photo-orientable azobenzene polymers by molecular glasses. *J. Polym. Sci. Part B: Polym. Phys.* **2016**, *54*, 2110–2117.

(187) Probst, C.; Meichner, C.; Kreger, K.; Kador, L.; Neuber, C.; Schmidt, H.-W. Athermal Azobenzene-Based Nanoimprint Lithography. *Advanced materials (Deerfield Beach, Fla.)* **2016**, *28*, 2624–2628.

(188) Mohmeyer, N.; Müller, B.; Behrendt, N.; Hillenbrand, J.; Klaiber, M.; Zhang, X.; Smith, P.; Altstädt, V.; Sessler, G. M.; Schmidt, H.-W. Nucleation of isotactic polypropylene by triphenylamine-based trisamide derivatives and their influence on charge-storage properties. *Polymer* **2004**, *45*, 6655–6663.

(189) Mohmeyer, N.; Behrendt, N.; Zhang, X.; Smith, P.; Altstädt, V.; Sessler, G. M.; Schmidt, H.-W. Additives to improve the electret properties of isotactic polypropylene. *Polymer* **2007**, *48*, 1612–1619.

(190) Abraham, F.; Kress, R.; Smith, P.; Schmidt, H.-W. A New Class of Ultra-Efficient Supramolecular Nucleating Agents for Isotactic Polypropylene. *Macromol. Chem. Phys.* **2013**, *214*, 17–24.

(191) Abraham, F.; Schmidt, H.-W. 1,3,5-Benzenetrisamide based nucleating agents for poly(vinylidene fluoride). *Polymer* **2010**, *51*, 913–921.

(192) Richter, F.; Schmidt, H.-W. Supramolecular Nucleating Agents for Poly(butylene terephthalate) Based on 1,3,5-Benzenetrisamides. *Macromol. Mater. Eng.* **2013**, *298*, 190–200.

(193) Kubas, H.; Schäfer, M.; Bauder-Wüst, U.; Eder, M.; Oltmanns, D.; Haberkorn, U.; Mier, W.; Eisenhut, M. Multivalent cyclic RGD ligands: influence of linker lengths on receptor binding. *Nuclear medicine and biology* **2010**, *37*, 885–891.

(194) Rajakumar, P.; Anandhan, R.; Manoj, D.; Santhanalakshmi, J. Synthesis, H² PO⁴⁻ and Pd²⁺ ion sensing and gold nanoparticle encapsulation of ferrocenyldendrimers by a green chemistry approach. *RSC Adv* **2014**, *4*, 4413–4419.

- (195) Lee, J.; Farha, O. K.; Roberts, J.; Scheidt, K. A.; Nguyen, S. T.; Hupp, J. T. Metal-organic framework materials as catalysts. *Chemical Society reviews* **2009**, *38*, 1450–1459.
- (196) Ranjbar, Z. R.; Morsali, A. Preparation of silver nanostructure from silver(I) coordination polymer and fabrication of nano silver(I) bromide by reverse micelles technique. *Synthetic Metals* **2011**, *161*, 1449–1455.
- (197) Hanabusa, K.; Koto, C.; Kimura, M.; Shirai, H.; Takechi, A. Remarkable Viscoelasticity of Organic Solvents Containing Trialkyl-1,3,5-benzenetricarboxamides and Their Intermolecular Hydrogen Bonding. *Chem. Lett.* **1997**, *26*, 429–430.
- (198) Jana, P.; Paikar, A.; Bera, S.; Maity, S. K.; Haldar, D. Porous organic material from discotic tricarboxamide: side chain-core interactions. *Organic letters* **2014**, *16*, 38–41.
- (199) Karmakar, A.; Oliver, C. L.; Platero-Prats, A. E.; Laurila, E.; Öhrström, L. Crystal structures and hydrogen bond analysis of five amino acid conjugates of terephthalic and benzene-1,2,3-tricarboxylic acids. *CrystEngComm* **2014**, *16*, 8243–8251.
- (200) Jung, S. H.; Jeon, J.; Kim, H.; Jaworski, J.; Jung, J. H. Chiral arrangement of achiral Au nanoparticles by supramolecular assembly of helical nanofiber templates. *Journal of the American Chemical Society* **2014**, *136*, 6446–6452.
- (201) Kumar, D. K.; Jose, D. A.; Dastidar, P.; Das, A. Nonpolymeric Hydrogelators Derived from Trimesic Amides. *Chem. Mater.* **2004**, *16*, 2332–2335.
- (202) Rajput, L.; Biradha, K. Crystalline forms of 1,3,5-benzene-tri(pyridinyl)carboxamides: Isolated site hydrates as polymorphs and solvates. *Journal of Molecular Structure* **2011**, *991*, 97–102.
- (203) Luo, X.-Z.; Jia, X.-J.; Deng, J.-H.; Zhong, J.-L.; Liu, H.-J.; Wang, K.-J.; Zhong, D.-C. A microporous hydrogen-bonded organic framework: exceptional stability and highly selective adsorption of gas and liquid. *Journal of the American Chemical Society* **2013**, *135*, 11684–11687.
- (204) Hong, S.; Zou, Y.; Moon, D.; Lah, M. S. An unprecedented twofold interpenetrating (3,4)-connected 3-D metal-organic framework. *Chemical communications (Cambridge, England)* **2007**, 1707–1709.
- (205) Tzeng, B.-C.; Chen, B.-S.; Yeh, H.-T.; Lee, G.-H.; Peng, S.-M. Self-assembly of N,N',N''-tris(4-pyridyl)trimesic amide and N,N',N''-tris(3-pyridyl)trimesic amide with Ag I or Cd II ions. *New J. Chem.* **2006**, *30*, 1087–1092.
- (206) Tzeng, B.-C.; Chiu, T.-H.; Chen, B.-S.; Lee, G.-H. Novel single-crystal-to-single-crystal anion exchange and self-assembly of luminescent d(10) metal (Cd(II), Zn(II), and Cu(I)) complexes containing C(3)-symmetrical ligands. *Chemistry (Weinheim an der Bergstrasse, Germany)* **2008**, *14*, 5237–5245.
- (207) Zhao, X.; Mao, C.; Luong, K. T.; Lin, Q.; Zhai, Q.-G.; Feng, P.; Bu, X. Framework Cationization by Preemptive Coordination of Open Metal Sites for Anion-Exchange Encapsulation of Nucleotides and Coenzymes. *Angewandte Chemie (International ed. in English)* **2016**, *55*, 2768–2772.
- (208) Zhong, J.-L.; Jia, X.-J.; Liu, H.-J.; Luo, X.-Z.; Hong, S.-G.; Zhang, N.; Huang, J.-B. Self-assembled metallogels formed from N,N',N''-tris(4-pyridyl)trimesic amide in aqueous solution induced by Fe(III)/Fe(II) ions. *Soft matter* **2016**, *12*, 191–199.

- (209) Lee, H. H.; Jung, S. H.; Park, S.; Park, K.-M.; Jung, J. H. A metal–organic framework gel with Cd²⁺ derived from only coordination bonds without intermolecular interactions and its catalytic ability. *New J. Chem.* **2013**, *37*, 2330.
- (210) Jung, J. H.; Moon, S.-J.; Ahn, J.; Jaworski, J.; Shinkai, S. Controlled supramolecular assembly of helical silica nanotube-graphene hybrids for chiral transcription and separation. *ACS nano* **2013**, *7*, 2595–2601.
- (211) Gong, W.-t.; Hiratani, K. A novel amidepyridinium-based tripodal fluorescent chemosensor for phosphate ion via binding-induced excimer formation. *Tetrahedron Letters* **2008**, *49*, 5655–5657.
- (212) Kitson, P. J.; Marshall, R. J.; Long, D.; Forgan, R. S.; Cronin, L. 3D printed high-throughput hydrothermal reactionware for discovery, optimization, and scale-up. *Angewandte Chemie (International ed. in English)* **2014**, *53*, 12723–12728.
- (213) Dang, L.-l.; Li, J.-q.; Liu, S.-j.; Luo, M.-b.; Luo, F. A new acylamide MOF showing uncommon ten-fold interpenetration. *Inorganic Chemistry Communications* **2014**, *45*, 30–32.
- (214) Lin, R.-G.; Cao, G.-J.; Lin, J.-D.; Wang, Y.-L. A novel 3-fold interpenetration metal–organic framework with tunable luminescence and selective adsorption of CO₂ properties. *New J. Chem.* **2015**, *39*, 9075–9078.
- (215) Rajput, L.; Sarkar, M.; Biradha, K. Assembling one-dimensional coordination polymers into three-dimensional architectures via hydrogen bonds. *J Chem Sci* **2010**, *122*, 707–720.
- (216) Yao, W.-T.; Luo, M.-b.; Feng, X.-F.; Meng, P.-P.; Gong, L.-L.; Luo, F. Construction of structural diversity and fine-tuned porosity in acylamide MOFs by a synthetic approach. *New J. Chem.* **2016**, *40*, 2021–2027.
- (217) Lee, C.-H.; Huang, H.-Y.; Liu, Y.-H.; Luo, T.-T.; Lee, G.-H.; Peng, S.-M.; Jiang, J.-C.; Chao, I.; Lu, K.-L. Cooperative effect of unsheltered amide groups on CO₂ adsorption inside open-ended channels of a zinc(II)-organic framework. *Inorganic chemistry* **2013**, *52*, 3962–3968.
- (218) Lee, C.-H.; Wu, J.-Y.; Lee, G.-H.; Peng, S.-M.; Jiang, J.-C.; Lu, K.-L. Correlation of Mesh Size of Metal–Carboxylate Layer with Degree of Interpenetration in Pillared-Layer Frameworks. *Crystal Growth & Design* **2014**, *14*, 5608–5616.
- (219) Sarkar, M.; Biradha, K. Amide-to-Amide Hydrogen Bonds in the Presence of a Pyridine Functionality: Crystal Structures of Bis(pyridinecarboxamido)alkanes. *Crystal Growth & Design* **2006**, *6*, 202–208.
- (220) Rajput, L.; Singha, S.; Biradha, K. Comparative Structural Studies on Homologues of Amides and Reverse Amides: Unprecedented 4-fold Interpenetrated Quartz Network, New β -Sheet, and Two-Dimensional Layers. *Crystal Growth & Design* **2007**, *7*, 2788–2795.
- (221) Safarifard, V.; Rodríguez-Hermida, S.; Guillerm, V.; Imaz, I.; Bigdeli, M.; Azhdari Tehrani, A.; Juanhuix, J.; Morsali, A.; Casco, M. E.; Silvestre-Albero, J. *et al.* Influence of the Amide Groups in the CO₂ /N₂ Selectivity of a Series of Isostructural, Interpenetrated Metal–Organic Frameworks. *Crystal Growth & Design* **2016**, *16*, 6016–6023.
- (222) Wang, X.-L.; Sha, X.-T.; Liu, G.-C.; Chen, N.-L.; Gong, C.-H.; Qu, Y. Assembly, Structures, and Properties of a Series of Metal-Organic Coordination Polymers Derived from a Semi-rigid Bis-pyridyl-bis-amide Ligand. *Z. anorg. allg. Chem.* **2015**, *641*, 1274–1281.

- (223) Wang, X.-L.; Mu, B.; Lin, H.-Y.; Liu, G.-C. Three new two-dimensional metal-organic coordination polymers derived from bis(pyridinecarboxamide)-1,4-benzene ligands and 1,3-benzenedicarboxylate: Syntheses and electrochemical property. *Journal of Organometallic Chemistry* **2011**, *696*, 2313–2321.
- (224) Lin, H.-Y.; Liu, P.; Wang, X.-L.; Mu, B.; Sui, F.-F.; Liu, G.-C. Two New 3-D Supramolecular Complexes Based on Tetradentate Carboxylate Linker and Bis-pyridyl-bis-amide Ligand: Syntheses, Structures and Electrochemical Properties. *J Chem Crystallogr* **2013**, *43*, 44–50.
- (225) Weilandt, T.; Troff, R. W.; Saxell, H.; Rissanen, K.; Schalley, C. A. Metallo-supramolecular self-assembly: the case of triangle-square equilibria. *Inorganic chemistry* **2008**, *47*, 7588–7598.
- (226) Wang, X.; Li, J.; Hu, H.; Lin, H.; Tian, A.; Chen, Y. Two New Organic–Inorganic Hybrids Based on [SiW₁₂O₄₀]⁴⁻ Anion: Hydrothermal Syntheses, Crystal Structures, and Electrochemical Properties. *J Inorg Organomet Polym* **2010**, *20*, 361–368.
- (227) Wang, X.; Lin, H.; Mu, B.; Tian, A.; Liu, G. Encapsulation of discrete (H₂O)₁₂ clusters in a 3D three-fold interpenetrating metal-organic framework host with (3,4)-connected topology. *Dalton transactions (Cambridge, England : 2003)* **2010**, *39*, 6187–6189.
- (228) Pansanel, J.; Jouaiti, A.; Ferlay, S.; Hosseini, M. W.; Planeix, J.-M.; Kyritsakas, N. Molecular tectonics: Generation of 1- and 2-D copper coordination networks by positional isomeric tectons based on a phenylenediamine backbone bearing two isonicotinoyl moieties. *New J. Chem.* **2006**, *30*, 683.
- (229) Luo, F.; Zheng, J.-m.; Batten, S. R. Unprecedented (3,4)-connected metal–organic frameworks (MOFs) with 3-fold interpenetration and considerable solvent-accessible void space. *Chem. Commun.* **2007**, *119*, 3744.
- (230) Sheykhani, M.; Rashidi Ranjbar, Z.; Morsali, A.; Heydari, A. Minimisation of E-Factor in the synthesis of N-hydroxylamines: The role of silver(I)-based coordination polymers. *Green Chem.* **2012**, *14*, 1971.
- (231) Ranjbar, Z. R.; Morsali, A. Solid state irreversible anion-exchange on one-dimensional silver(I) coordination polymer nanostructures. *Inorganica Chimica Acta* **2012**, *382*, 171–176.
- (232) Pansanel, J.; Jouaiti, A.; Ferlay, S.; Wais Hosseini, M.; Planeix, J.-M.; Kyritsakas, N. Molecular tectonics: Generation of 2-D molecular networks by combination of coordination and hydrogen bonds. *New J. Chem.* **2006**, *30*, 71–76.
- (233) Zhang, Y.; Hao, J.-J.; Zhou, H. Tetra-kis(nitrato-κ(2)O,O')N,N'-1,4-phenyl-enebis(pyridine-4-carboxamide)-κN(1)(4-{4-(pyridine-4-carboxamido-κN(1))phen-ylcarbamo-yl}pyridin-1-ium)neodymium(III). *Acta crystallographica. Section E, Structure reports online* **2012**, *68*, m459.
- (234) Huang, S.-L.; Lin, Y.-J.; Li, Z.-H.; Jin, G.-X. Self-assembly of molecular Borromean rings from bimetallic coordination rectangles. *Angewandte Chemie (International ed. in English)* **2014**, *53*, 11218–11222.
- (235) Zhang, L.; Lin, L.; Liu, D.; Lin, Y.-J.; Li, Z.-H.; Jin, G.-X. Stacking Interactions Induced Selective Conformation of Discrete Aromatic Arrays and Borromean Rings. *Journal of the American Chemical Society* **2017**, *139*, 1653–1660.
- (236) Wu, T.; Gong, Y.; Qin, J.; Wu, X.; Cao, R. Syntheses, Crystal Structures, and Photoluminescence Properties of Three Bis-acylamide Compounds. *Z. anorg. allg. Chem.* **2012**, *638*, 438–442.

- (237) Huang, S.-y.; Li, J.-q.; Wu, X.-l.; Zhang, X.-m.; Luo, M.-b.; Luo, F. A novel 4-connected binodal Moganite net with three-fold interpenetration. *Inorganic Chemistry Communications* **2014**, *39*, 1–4.
- (238) Wang, X.-L.; Mu, B.; Lin, H.-Y.; Yang, S.; Liu, G.-C.; Tian, A.-X.; Zhang, J.-W. Assembly and properties of transition-metal coordination polymers based on semi-rigid bis-pyridyl-bis-amide ligand: effect of polycarboxylates on the dimensionality. *Dalton transactions (Cambridge, England : 2003)* **2012**, *41*, 11074–11084.
- (239) Lin, H.; Sui, F.; Liu, P.; Wang, X.; Liu, G. Synthesis, Crystal Structures and Properties of Two 3D Cd II and Zn II Complexes with a 3-Fold Interpenetrating Feature. *Bulletin of the Korean Chemical Society* **2013**, *34*, 2138–2142.
- (240) Lin, H.; Rong, X.; Liu, G.; Wang, X.; Wang, X.; Duan, S. Fluorescent sensing and electrocatalytic properties of three Zn(II)/Co(II) coordination complexes containing two different dicarboxylates and two various bis(pyridyl)-bis(amide) ligands. *Journal of Molecular Structure* **2016**, *1119*, 396–403.
- (241) Ramani, R.; Srivastava, J.; Alam, S. Application of model-free kinetics to the thermal and thermo-oxidative degradation of poly(3-hexyl thiophene). *Thermochimica Acta* **2010**, *499*, 34–39.
- (242) Lu, G. H.; Li, L. G.; Yang, X. N. Achieving Perpendicular Alignment of Rigid Polythiophene Backbones to the Substrate by Using Solvent-Vapor Treatment. *Adv. Mater.* **2007**, *19*, 3594–3598.
- (243) Lu; Li; Yang. Morphology and Crystalline Transition of Poly(3-butylthiophene) Associated with Its Polymorphic Modifications. *Macromolecules* **2008**, *41*, 2062–2070.
- (244) Crossland, E. J. W.; Rahimi, K.; Reiter, G.; Steiner, U.; Ludwigs, S. Systematic Control of Nucleation Density in Poly(3-Hexylthiophene) Thin Films. *Adv. Funct. Mater.* **2011**, *21*, 518–524.
- (245) Crossland, E. J. W.; Tremel, K.; Fischer, F.; Rahimi, K.; Reiter, G.; Steiner, U.; Ludwigs, S. Anisotropic charge transport in spherulitic poly(3-hexylthiophene) films. *Advanced materials (Deerfield Beach, Fla.)* **2012**, *24*, 839–844.
- (246) Müller, C.; Aghamohammadi, M.; Himmelberger, S.; Sonar, P.; Garriga, M.; Salleo, A.; Campoy-Quiles, M. One-Step Macroscopic Alignment of Conjugated Polymer Systems by Epitaxial Crystallization during Spin-Coating. *Adv. Funct. Mater.* **2013**, *23*, 2368–2377.
- (247) Ye, Z.; Cui, H.; Yang, X.; Qiu, F. Charge injection promoted electrohydrodynamic instabilities in poly(3-hexylthiophene) thin films. *J. Mater. Chem. C* **2015**, *3*, 1949–1956.
- (248) Sepe, A.; Rong, Z.; Sommer, M.; Vaynzof, Y.; Sheng, X.; Müller-Buschbaum, P.; Smilgies, D.-M.; Tan, Z.-K.; Le Yang; Friend, R. H. *et al.* Structure formation in P3HT/F8TBT blends. *Energy Environ. Sci.* **2014**, *7*, 1725–1736.
- (249) Yuan, N.; Huo, H. 1,2,3,4-Bis(p-methylbenzylidene sorbitol) accelerates crystallization and improves hole mobility of poly(3-hexylthiophene). *Nanotechnology* **2016**, *27*, 06LT01.
- (250) McCulloch, I.; Heeney, M.; Chabinyc, M. L.; DeLongchamp, D.; Kline, R. J.; Cölle, M.; Duffy, W.; Fischer, D.; Gundlach, D.; Hamadani, B. *et al.* Semiconducting Thienothiophene Copolymers: Design, Synthesis, Morphology, and Performance in Thin-Film Organic Transistors. *Adv. Mater.* **2009**, *21*, 1091–1109.

- (251) Vakhshouri, K.; Gomez, E. D. Effect of Crystallization Kinetics on Microstructure and Charge Transport of Polythiophenes. *Macromolecular rapid communications* **2012**, *33*, 2133–2137.
- (252) Bechara, R.; Leclerc, N.; Lévêque, P.; Richard, F.; Heiser, T.; Hadziioannou, G. Efficiency enhancement of polymer photovoltaic devices using thieno-thiophene based copolymers as nucleating agents for polythiophene crystallization. *Appl. Phys. Lett.* **2008**, *93*, 13306.
- (253) Deribew, D.; Pavlopoulou, E.; Fleury, G.; Nicolet, C.; Renaud, C.; Mognier, S.-J.; Vignau, L.; Cloutet, E.; Brochon, C.; Cousin, F. *et al.* Crystallization-Driven Enhancement in Photovoltaic Performance through Block Copolymer Incorporation into P3HT: PCBM Blends. *Macromolecules* **2013**, *46*, 3015–3024.
- (254) Yang, Z.; Lu, H. Nonisothermal crystallization behaviors of poly(3-hexylthiophene)/reduced graphene oxide nanocomposites. *J. Appl. Polym. Sci.* **2013**, *128*, 802–810.
- (255) Avrami, M. Kinetics of Phase Change. I General Theory. *The Journal of Chemical Physics* **1939**, *7*, 1103–1112.
- (256) Berson, S.; De Bettignies, R.; Bailly, S.; Guillerez, S. Poly(3-hexylthiophene) Fibers for Photovoltaic Applications. *Adv. Funct. Mater.* **2007**, *17*, 1377–1384.
- (257) Sun, S.; Salim, T.; Wong, L. H.; Foo, Y. L.; Boey, F.; Lam, Y. M. A new insight into controlling poly(3-hexylthiophene) nanofiber growth through a mixed-solvent approach for organic photovoltaics applications. *J. Mater. Chem.* **2011**, *21*, 377–386.
- (258) Samitsu, S.; Shimomura, T.; Heike, S.; Hashizume, T.; Ito, K. Effective Production of Poly(3-alkylthiophene) Nanofibers by means of Whisker Method using Anisole Solvent: Structural, Optical, and Electrical Properties. *Macromolecules* **2008**, *41*, 8000–8010.
- (259) Zhao, K.; Xue, L.; Liu, J.; Gao, X.; Wu, S.; Han, Y.; Geng, Y. A new method to improve poly(3-hexylthiophene) (P3HT) crystalline behavior: decreasing chains entanglement to promote order-disorder transformation in solution. *Langmuir : the ACS journal of surfaces and colloids* **2010**, *26*, 471–477.
- (260) Kiriy, N.; Jähne, E.; Adler, H.-J.; Schneider, M.; Kiriy, A.; Gorodyska, G.; Minko, S.; Jehnichen, D.; Simon, P.; Fokin, A. A. *et al.* One-Dimensional Aggregation of Regioregular Polyalkylthiophenes. *Nano Lett.* **2003**, *3*, 707–712.
- (261) Li, L.; Lu, G.; Yang, X. Improving performance of polymer photovoltaic devices using an annealing-free approach via construction of ordered aggregates in solution. *J. Mater. Chem.* **2008**, *18*, 1984.
- (262) Park, Y. D.; Lee, H. S.; Choi, Y. J.; Kwak, D.; Cho, J. H.; Lee, S.; Cho, K. Solubility-Induced Ordered Polythiophene Precursors for High-Performance Organic Thin-Film Transistors. *Adv. Funct. Mater.* **2009**, *19*, 1200–1206.
- (263) Kim, B.-G.; Kim, M.-S.; Kim, J. Ultrasonic-assisted nanodimensional self-assembly of poly-3-hexylthiophene for organic photovoltaic cells. *ACS nano* **2010**, *4*, 2160–2166.
- (264) Guo, Y.; Jiang, L.; Ma, X.; Hu, W.; Su, Z. Poly(3-hexylthiophene) monolayer nanowhiskers. *Polym. Chem.* **2013**, *4*, 4308.
- (265) Guo, Y.; Han, Y.; Su, Z. Ordering of poly(3-hexylthiophene) in solution and on substrates induced by concentrated sulfuric acid. *The journal of physical chemistry. B* **2013**, *117*, 14842–14848.

- (266) Lobov, G. S.; Zhao, Y.; Marinins, A.; Yan, M.; Li, J.; Sugunan, A.; Thylén, L.; Wosinski, L.; Östling, M.; Toprak, M. S. *et al.* Size Impact of Ordered P3HT Nanofibers on Optical Anisotropy. *Macromol. Chem. Phys.* **2016**, *217*, 1089–1095.
- (267) Wittmann, J. C.; Smith, P. Highly oriented thin films of poly(tetrafluoroethylene) as a substrate for oriented growth of materials. *Nature* **1991**, *352*, 414–417.
- (268) Nagamatsu, S.; Takashima, W.; Kaneto, K.; Yoshida, Y.; Tanigaki, N.; Yase, K.; Omote, K. Backbone Arrangement in “Friction-Transferred” Regioregular Poly(3-alkylthiophene)s. *Macromolecules* **2003**, *36*, 5252–5257.
- (269) Hartmann, L.; Tremel, K.; Uttiya, S.; Crossland, E.; Ludwigs, S.; Kayunkid, N.; Vergnat, C.; Brinkmann, M. 2D Versus 3D Crystalline Order in Thin Films of Regioregular Poly(3-hexylthiophene) Oriented by Mechanical Rubbing and Epitaxy. *Adv. Funct. Mater.* **2011**, *21*, 4047–4057.
- (270) Zhu, R.; Kumar, A.; Yang, Y. Polarizing organic photovoltaics. *Advanced materials (Deerfield Beach, Fla.)* **2011**, *23*, 4193–4198.
- (271) Ward, M. D. Bulk Crystals to Surfaces: Combining X-ray Diffraction and Atomic Force Microscopy to Probe the Structure and Formation of Crystal Interfaces. *Chem. Rev.* **2001**, *101*, 1697–1726.
- (272) Brinkmann, M.; Chandezon, F.; Pansu, R. B.; Julien-Rabant, C. Epitaxial Growth of Highly Oriented Fibers of Semiconducting Polymers with a Shish-Kebab-Like Superstructure. *Adv. Funct. Mater.* **2009**, *19*, 2759–2766.
- (273) Jimison, L. H.; Toney, M. F.; McCulloch, I.; Heeney, M.; Salleo, A. Charge-Transport Anisotropy Due to Grain Boundaries in Directionally Crystallized Thin Films of Regioregular Poly(3-hexylthiophene). *Adv. Mater.* **2009**, *21*, 1568–1572.
- (274) Liu, J.; Moo-Young, J.; McInnis, M.; Pasquinelli, M. A.; Zhai, L. Conjugated Polymer Assemblies on Carbon Nanotubes. *Macromolecules* **2014**, *47*, 705–712.
- (275) Misra, R. D. K.; Depan, D.; Challa, V. S. A.; Shah, J. S. Supramolecular structures fabricated through the epitaxial growth of semiconducting poly(3-hexylthiophene) on carbon nanotubes as building blocks of nanoscale electronics. *Physical chemistry chemical physics : PCCP* **2014**, *16*, 19122–19129.
- (276) Challa, V. S. A.; Nune, K. C.; Misra, R. D. K. The impact of molecular weight on nanoscale supramolecular structure of semiconducting poly(3-hexylthiophene) on carbon nanotubes and photophysical properties. *Materials Technology* **2016**, *31*, 477–481.
- (277) Yan, H.; Yan, Y.; Yu, Z.; Wei, Z. Self-Assembling Branched and Hyperbranched Nanostructures of Poly(3-hexylthiophene) by a Solution Process. *J. Phys. Chem. C* **2011**, *115*, 3257–3262.
- (278) Bu, L.; Pentzer, E.; Bokel, F. A.; Emrick, T.; Hayward, R. C. Growth of polythiophene/perylene tetracarboxydiimide donor/acceptor shish-kebab nanostructures by coupled crystal modification. *ACS nano* **2012**, *6*, 10924–10929.
- (279) Huang, W.; Markwart, J. C.; Briseno, A. L.; Hayward, R. C. Orthogonal Ambipolar Semiconductor Nanostructures for Complementary Logic Gates. *ACS nano* **2016**, *10*, 8610–8619.

- (280) Zhang, X.; Yuan, N.; Ding, S.; Wang, D.; Li, L.; Hu, W.; Bo, Z.; Zhou, J.; Huo, H. Growth and carrier-transport performance of a poly(3-hexylthiophene)/1,2,3,4-bis(p-methylbenzylidene) sorbitol hybrid shish-kebab nanostructure. *J. Mater. Chem. C* **2017**, *5*, 3983–3992.
- (281) Spano, F. C. Modeling disorder in polymer aggregates: the optical spectroscopy of regioregular poly(3-hexylthiophene) thin films. *The Journal of Chemical Physics* **2005**, *122*, 234701.
- (282) Spano, F. C.; Clark, J.; Silva, C.; Friend, R. H. Determining exciton coherence from the photoluminescence spectral line shape in poly(3-hexylthiophene) thin films. *The Journal of Chemical Physics* **2009**, *130*, 74904.
- (283) Paquin, F.; Yamagata, H.; Hestand, N. J.; Sakowicz, M.; Bérubé, N.; Côté, M.; Reynolds, L. X.; Haque, S. A.; Stingelin, N.; Spano, F. C. *et al.* Two-dimensional spatial coherence of excitons in semicrystalline polymeric semiconductors: Effect of molecular weight. *Phys. Rev. B* **2013**, *88*, DOI: 10.1103/PhysRevB.88.155202.



(Eidesstattliche) Versicherungen und Erklärungen

(§ 9 Satz 2 Nr. 3 PromO BayNAT)

Hiermit versichere ich eidesstattlich, dass ich die Arbeit selbständig verfasst und keine anderen als die von mir angegebenen Quellen und Hilfsmittel benutzt habe (vgl. Art. 64 Abs. 1 Satz 6 BayHSchG).

(§ 9 Satz 2 Nr. 3 PromO BayNAT)

Hiermit erkläre ich, dass ich die Dissertation nicht bereits zur Erlangung eines akademischen Grades eingereicht habe und dass ich nicht bereits diese oder eine gleichartige Doktorprüfung endgültig nicht bestanden habe.

(§ 9 Satz 2 Nr. 4 PromO BayNAT)

Hiermit erkläre ich, dass ich Hilfe von gewerblichen Promotionsberatern bzw. -vermittlern oder ähnlichen Dienstleistern weder bisher in Anspruch genommen habe noch künftig in Anspruch nehmen werde.

(§ 9 Satz 2 Nr. 7 PromO BayNAT)

Hiermit erkläre ich mein Einverständnis, dass die elektronische Fassung meiner Dissertation unter Wahrung meiner Urheberrechte und des Datenschutzes einer gesonderten Überprüfung unterzogen werden kann.

(§ 9 Satz 2 Nr. 8 PromO BayNAT)

Hiermit erkläre ich mein Einverständnis, dass bei Verdacht wissenschaftlichen Fehlverhaltens Ermittlungen durch universitätsinterne Organe der wissenschaftlichen Selbstkontrolle stattfinden können.

.....
Ort, Datum, Unterschrift